IDENTIFICATION AND SYNTHESIS OF SEISMIC GROUND MOTION IN STRUCTURAL RESPONSE ANALYSES(Dissertation_全文)

AUTHOR(S):

Kiyono, Junji

IDENTIFICATION AND SYNTHESIS OF SEISMIC GROUND MOTION IN STRUCTURAL RESPONSE ANALYSES

Junji KIYONO

IDENTIFICATION AND SYNTHESIS OF SEISMIC GROUND MOTION IN STRUCTURAL RESPONSE ANALYSES

Junji KIYONO

Disaster Prevention Research Institute
Kyoto University

1992

SUMMARY

The subject of this dissertation is on the identification and simulation of seismic ground motions for static and dynamic analyses of structural responses. Information about local conditions, the travel path, and source mechanisms must be obtained before seismic ground motions can be synthesized. The parameters that affect earthquake motion first are identified, after which seismic ground motions are synthesized from them.

A procedure is developed by which to identify the real input motion to a structure or its foundation. The Kalman filter is used to estimate the input motion from the structural response and structural parameters.

The nature of the local site condition is investigated. The dispersion curve of the phase velocities is derived from observed data by deconvolution combined with the Kalman filter. The shape of an irregular interface is identified from the mean powers and spatial correlation coefficients. A simple procedure by which the relative displacements on non-uniform soil layers can be calculated is proposed by replacing a basin model with a layered media model.

Estimation of the peak value for seismic load is a requisite for the assessment of input ground motion. A simplified analytical method is presented with which to predict peak accelerations near the source region where the effect of the fault extent can not be ignored. Seismic hazard is evaluated by the joint use of historical earthquake and active fault data with Bayes' theorem. The procedure developed is used to introduce the attenuation equation of peak acceleration. The risk spectrum at the bed rock level is obtained from the attenuation of the response spectrum.

A method to identify the rupture process of a fault is proposed that is based on deconvolution of trains of impulses. Much information about fault rupture mechanisms, including the rupture velocity, starting point of rupture, direction of rupture propagation, and rise time can be obtained from deconvoluted impulses with this method.

Lastly, a procedure for synthesizing ground motion that uses earthquake and microearthquake records is presented. The recorded waveforms were analyzed by the AR-MA (autoregressive-moving average) process, after which regression analyses of the AR-MA parameters derived from each record were made. A statistical simulation model for microearthquake motion then was developed. The statistical Green function is superposed to synthesize large earthquake motion, and a new scaling law is proposed for the superposing of microearthquakes.

ACKNOWLEDGEMENTS

This dissertation presents the results of eight years of study after my completion of the master's course at the Faculty of Engineering, Kyoto University. I here wish to acknowledge the supervision, guidance, support, encouragement, and assistance received from professors, colleagues, and friends.

I am deeply grateful to Professor Kenzo Toki of the Disaster Prevention Research Institute, Kyoto University for his expert supervision of my research, scholarly guidance, wholehearted support, and continuous encouragement. Professor Toki taught me how to extract important information from analyses and experiments and how to see the results in terms of the whole, as well as how to make judgements based on engineering concerns. He has provided not only a research position but a splendid environment in which to conduct earthquake engineering research.

Particular thanks also are due Professor Tadanobu Sato of the Disaster Prevention Research Institute, Kyoto University who introduced me to this field of research. Throughout my years of study, Professor Sato has provided useful suggestions, technical advice, and stimulating discussions on all aspects of the subjects covered in this dissertation as well as unstinting support and encouragement.

I am particularly indebted to Professor Hiroyuki Kameda of the Disaster Prevention Research Institute, Kyoto University, for his constructive suggestions and critical reading of the manuscript. I wish also to thank Professor Fusanori Miura of the Faculty of Engineering, Yamaguchi University for his enthusiastic support and encouragement of my dissertation research.

I am deeply indebted to Professor Yoshikazu Yamada of the Faculty of Engineering, Kyoto University, Professor Hirokazu Iemura of the Faculty of Engineering, Kyoto University, Dr. Masata Sugito of the Faculty of Engineering, Kyoto University, Professor Shigeru Noda of the Faculty of Engineering, Tottori University, and Mr. Kazuyuki Izuno of the Faculty of Engineering, Kyoto University for their many discussions of my work and the constructive suggestions made during joint seminars and various meetings on earthquake engineering. Dr. Sugito encouraged me to write my dissertation as quickly as possible.

I also wish to express my appreciation to Professor Tohru Shibata of the Faculty of Engineering, Kyoto University, Professor Toshihisa Adachi of the Faculty of Engineering, Kyoto University, Professor Hideo Sekiguchi of the Faculty of Engineering, Kyoto

University, Dr. Mamoru Mimura of the Disaster Prevention Research Institute, Kyoto University, and Dr. Atsushi Iizuka of the Faculty of Engineering, Kanazawa University for their informative suggestions and advice about soil mechanics.

Thank also are due to Mr. Joji Ejiri of Ohbayashi Corporation, Dr. Akira Murakami of the Faculty of Agriculture, Kyoto University, Messrs. Sumio Sawada and Takao Kagawa of the Geo-research Institute of the Osaka Soil Test Laboratory, Dr. Yoshio Sunasaka of Kajima Corporation, Mr. Michiyasu Terada of Kumagai Co. Ltd., Mr. Takashi Yoshimura of Shimizu Construction Co. Ltd., Dr. Kunihiko Fuchida of Yatsushiro College of Technology, Dr. Etsuo Saito of Fujita Corporation, and Dr. Osamu Maruyama of Musashi Institute of Technology for their frequent, stimulating and helpful discussions of my work, as well as to Mr. Hideaki Kishimoto of Japan Computer Consultants for his suggestions and help with the computer management and programing. The assistance of Professor Kojiro Irikura and Dr. Tomotaka Iwata of the Disaster Prevention Research Institute, Kyoto University who provided many important ideas and information about seismology is also greatly appreciated.

The very significant contributions made by several generations of students in Professor Toki's laboratory; in particular, those of Mr. Hiroshi Watanabe of the Public Works Institute of the Ministry of Construction, Mr. Toshikazu Matsuoka of Aoki Construction Co. Ltd., Mr. Kazuhiko Ichihara of Sato Kogyo Co. Ltd., Mr. Jiro Wakabayashi of Maeda Construction Co. Ltd., Mr. Tsutomu Nishioka of the Hanshin Expressway Public Corporation, Mr. Takashi Saito of Mitsui Corporation, Mr. Hirotaka Takeuchi of Hazama Co. Ltd., Mr. Haruhiro Mizutani of the Hanshin Expressway Public Corporation, Mr. Kazuya Fujimura of the Graduate School of Kyoto University, and Dr. N. K. Garmroudi, former doctoral course student of our laboratory also are acknowledged.

I thank my many colleagues in Professor Toki's laboratory for their provocative discussions and support. Thanks also are due the members of the Association of Young Earthquake Research Engineers, for their stimulating assessments of my research. I especially want to thank Mr. Hiroshi Iwamae, former manager of the Rugby Football Club, the Athletic Association, Kyoto University, for his interest in my career and encouragement to complete my dissertation. I also am deeply indebted to Ms. Yuko Takii for typing the manuscript and to Ms. Patricia Yamada for editing both this dissertation and the publications on which it is based.

Lastly, I thank my wife, Mariko, and my elder brother Atsunobu and his wife Etsuko for their abiding understanding and support. I dedicate this dissertation to my late father, Sojiro, and to my mother, Sueko, in token of my gratitude for their belief in my abilities and constant support during my years of study.

TABLE OF CONTENTS

CHAPTER 1

INTRODUCTION

1.1 General Remarks

The best of human history has been highlighted by creativeness, the design and construction of civil structures providing a good example of human creativity. The erection of such structures calls for the incorporation of safety measures in order to ensure the safety of human beings. Natural disasters such as earthquakes, floods, typhoons, volcanic eruptions, and tornadoes are major threats to this safety. The main engineering countermeasure against these natural hazards is the estimation of what is a reasonable and reliable external force input to civil structures. If this input is overestimated, the design expense may render a project uneconomical; but, if underestimated, human lives may be endangered. In the case of earthquakes, the determination of input ground motion is one of the most important factors in making dynamic analyses for the assessment of the earthquake-resistant properties of structures. A sophisticated analytical procedure with which to determine input ground motion therefore is required.

The objective of this study was to develop rational methodologies for determining input ground motion in order to make dynamic response analyses of civil engineering structures. The estimation of seismic ground motion, which includes not only the time history of seismic motion, but the extreme and mean values of seismic motion, depends on the fault mechanism, seismicity of the region, soil properties at the site, and the effect of the interaction between the soil and the structure. That is, the earthquake ground motion parameters are affected by the source, travel path, and local conditions, thus requiring knowledge of geology, seismology, and of geotechnical and structural engineering. The seismic source problem has been seen in terms of the explanation of fault mechanisms. Accurate estimation of source parameters is difficult because there is much uncertainty in sizes, locations, and rupture processes of future earthquakes. For engineering purposes, therefore, the fault should be modeled in a simple manner using simple parameters. In particular, as

there is little information about earthquake ground motion near the fault, analyses are needed that account for the extension of the fault. The concept of the path also changes. The epicentral distance utilized in the widely used attenuation laws assumes that the point source and its definitions are very clear and uniquely determined. But, if the fault extent is considered, the epicentral distance becomes an obscure parameter. Moreover, the damping effect along the path has to be thoroughly investigated.

The soil properties, subsurface soil conditions, and shape of the interfaces in layered media are all important factors. The site conditions markedly affect the estimation of ground motion. The problem of soil-structure interaction also is one of the most important factors in analyzing the dynamic characteristics of structures. Although there are few records pertaining to soil-structure interaction, the effects of that interaction have been incorporated in the structural designs. Development of a balanced procedure that considers the source, path, site, and interaction effects is required to make a valid estimation of ground motion.

1.2 Review of Previous Studies

Various methods for the determination of earthquake ground motion have been proposed. The most widely used procedure is a statistical approach based on engineering concerns. Physical factors such as the peak ground motion and response spectral parameters are expressed empirically on the basis of the magnitude, epicentral distance, and geological conditions at the site. This approach is independent of the physical condition of the source. Kanai [1], Esteva [2], Katayama [3], Trifnac [4], Blume [5], Goto and Kameda [6], Donovan [7], the Public Work Research Institute of the Ministry of Construction [8] and various other research groups have developed prediction models based on statistical regression analyses of the model parameters. These models have been extended to predict nonstationary earthquake ground motion (Kameda and Sugito [9]), and nonlinear amplification effects have been incorporated. Theoretical and semi-empirical approaches also have been used over the past twenty years.

These studies have played important roles in the assessment of seismic intensity of ground motion subject to the aseismic design of a construction project. Collection of all the available data and pertinent judgements are required in the engineering stance. In seismology, a clear elucidation of phenomena occurring in source and path are important. A fault model firstly was developed based on this seismological concerns.

Among the source parameters that affect ground motion are the source dimensions, source depth, direction of rupture propagation, and the radiation pattern. Haskell [10] investigated the correlations of the fault parameters with geological and seismological data and proposed a fault model called by his name. This model simulates fault motion and the seismic wave on the basis of fault parameters: the length of the fault, L; the width,W; rupture velocity, v_r; rise time, τ; and dislocation, D. Aki [11] simulated the near-field wave with this model and showed there is good agreement with the observed records. Thereafter, many studies were done, of which Kanamori and Anderson [12] expressed the stress condition and rupture dimension at a source by using the seismic moment.

A representative semi-empirical method was proposed by Hartzell [13]. It uses the so-called empirical Green function. Hartzell used a record of a small event as a Green function to simulate a large event because, if an aftershock is assumed to be a Green function (which contains all the information along the traveling path), a large earthquake that has occurred at the same fault can be synthesized by superposing small events according to the scaling law. The merits of this method is that the simulated waves of large events agree well with the observed records and that complicated numerical calculations based on the theory of elastic waves are not needed.

In Japan, Irikura [14], Mikumo [15], Kobayashi and Midorikawa [16], and Iida [17] have made pioneering studies. Irikura [18] proposed a method for predicting the ground motion for a postulated large earthquake by combining the empirical Green function technique with the earthquake similarity law. Synthesized waves, in general, can not be used to simulate high frequency components; therefore, a revised model has been proposed. Many other problems such as selection of the Green function, correction of the radiation pattern, and the damping effect of the path, however, remain.

In the theoretical model, ground displacement, the velocity or acceleration is calculated from known static and dynamic parameters such as the fault size, dip, strike, dislocation, rupture propagation, rupture velocity, and rise time. The initial studies were based on the dislocation theory in elastic media ([19], [20]). With the introduction of this theory, the earthquake fault model came to be accepted as the expression of a double couple model which predicts far-field, long period ground motion. As it was not enough to predict the near-field motion when the media are layered, various models such as one which locates the fault in the elastic half space with layered media ([21], [22]) and a stochastic model ([23], [24]) which explains the factors contributing to high frequency components were established.

It is still difficult to estimate high frequency, strong ground motion of engineering importance. Madariaga [25] reported that high frequency components are generated when

crack propagation of constant velocity suddenly stops at the edge of the fault. Das and Aki [26], and Papageorgiou and Aki [27] proposed a barrier model in order to interpret the source complexity of a large event. Lay and Kanamori [28] proposed a simplified fault model that incorporates asperity and barrier aspects on the fault. Mikumo and Miyatake [29] calculated seismic waves numerically taking into account barrier aspects. These fault models significantly have influenced to the engineering field. But, the problems with this method are that (i) the physical parameters of the source and path are too complicated to generate high frequency motion and (ii) much time is needed to calculate motion that is of engineering use, for which the period is about one second and the wave length several hundred meters.

In the engineering field, Midorikawa et al. [30] proposed a method for calculating spectra of incident waves from seismic bed rock in the near-field with regard to fault rupture. For the design of large-scaled structures such as long span bridges, high-rise buildings and oil tanks, Inoue et al. [31] estimated relatively long-period ground motions with a fault dislocation theory. Yamada and Noda [32] considered the attenuation of earthquake ground motions excited from point dislocation sources for estimating large near-field earthquakes. Kawakami [33] used a fault model to evaluate the deformation of tunnel structures in a focal region. Yamada and Noda [34] proposed a fault model for estimating the relative ground motions induced by surface waves. Iida and Hakuno [35] synthesized the record of a large earthquake from a record of a small earthquake used as a Green function and studied the complexity of the large event. Toki and Miura [36] and Toki and Sawada [37] simulated fault rupture mechanisms using the two- and three-dimensional finite element methods. Other studies on earthquake prediction and estimations of the response spectra also have been published ([38], [39]).

The factors attributable to the path effects are geometric spreading, internal friction, inhomogeneity of the media, and phase conversion of the propagation waves. Attenuation of the media can be considered by the use of two factors; geometric spreading and internal friction, which are expressed in terms of the distance to the source and the Q-value. The other factors are not easily quantified. Various definitions have been proposed for the distance between the site and the source, the epicentral distance, hypocentral distance, distances to the energy center, and to the closest point of the conservative fault. Misusage of these expressions causes analytical errors. The frequency dependence of Q has been studied as an internal friction phenomena. The characteristics of attenuation are obtained from the inversion of S-waves or by analysis of the coda parts of seismograms. In Japan, Iwata and Irikura [40], as well as Sato [41] have identified the Q-value from the S-wave by means of the inversion method. Aki [42], Umino [43], Tsujiura [44], Sato [45], Akamatsu

[46], and Hoshiba [47] all have published reports on the calculated coda Q-value that expresses the scattering and damping effect in an area that includes the source and site. At present, the distance and Q-value are the only parameters used in expressions to describe the path effects on seismic ground motion.

Site effects include many factors: subsurface conditions such as the assessment of bed rock, properties of the layered media, irregularities in interfaces, and topographic variation, as well as soil-structure interaction when structures are present. Various studies have pointed out that the local subsurface conditions significantly affect ground motion. Early studies assessed the influence of subsurface conditions and compared analytical results with recorded motions (Idriss [48], Seed [49], Tsai [50]). More systematic analyses of recorded motions are now being made. The main analytical procedure used with layered media is multiple reflection analysis ([51], [52]); but, layered media present irregular interfaces which affect ground motion. Many procedures for assessing an irregular profile have been proposed. Early studies originated the integral equation method ([53], [54], [55], [56], [57], [58]). Numerical analyses that parallel the analytical method also have been developed ([59], [60], [61]). These methods mainly deal with the behavior of the body wave. Recently, long and extended structures have been constructed on irregular topographic sites under which irregular interfaces exist (Ohtuki [62]). Therefore, the behavior of ground motion for both body and surfaces wave inputs must be discussed. The above factors are included in the site effect and contribute to the spatial variation of ground motion. This spatial variability due to wave propagation is known as the wave passage effect. Knowledge of the phase velocity of the seismic wave, in particular, is indispensable when making seismic response analyses of structures in which the relative deformation between two supporting points is crucial.

The motion experienced by the foundation of a structure during an earthquake may differ substantially from the free-field ground motion. This is the soil-structure interaction phenomenon. Many theoretical and experimental studies have been made on the dynamics of soil-structure interaction. The comparison of a structure embedded in soil with a similar structure founded on rock shows that the seismic motion at the base of the structure is affected in two ways; the geometric averaging of seismic input motion called 'kinematic interaction' (Housner [63], Yamahara [64], [65]), and the 'inertial interaction' caused by the inertial load applied to the structure. Early studies based on the elastic wave theory were theoretical analyses of foundation structures in elastic space (Tajimi [66], Kobori [67], Goto [68]) and experiments on foundation structures (Hakuno [69], Toki [70]). Thereafter, numerical procedures such as the FEM (Harada [71], Toki and Miura [72]), the substructure method (Wolf [73], Luco [74], Takemiya [75]), and the complex stiffness

model based on elastic wave theory (Harada [76]) became widespread. It is now recognized that there is a relation between FEM analysis and mass-spring models.

1.3 Outline of This Dissertation

In view of the problems described above, this dissertation assesses totally balanced input ground motion on the basis of the following points:

(1) development of a method for identifying structural parameters and ground motion input to structure
(2) identification of the seismic wave that affects kinematic interaction in a soil-structure system
(3) investigation of the effects of wave propagation and site conditions on ground motion; i.e., detection of the apparent phase velocity of the seismic wave and identification of layered media that have irregular boundaries
(4) estimation of peak ground motion taking into account the source, path, and site effects
(5) synthesizing ground motion for structural response analyses.

In chapter 2, structural parameters and the effective input motions are identified. A versatile model that conveniently expresses nonlinear restoring force characteristics is adopted, and model parameters are identified using the extended Kalman filter technique. Effective input motion is estimated by the use of the parameters and responses identified, the procedure being extended to the identification of the input ground motions of a multi-input system.

In chapter 3, both amplitude and phase problems of the propagating waves are investigated. Several methods for calculating the appropriate phase velocity from a seismic wave are compared, and a new technique that incorporates the Kalman filter is developed. The dynamic responses of a site are affected by the shape of the interfaces of the layered media. The shape of an irregular interface is identified by taking into account the spatial variation in ground motion. Ground motion in layered media that have irregular interfaces is simulated by the discrete wave number method. The relative displacement between two observation points is modeled by spatial correlation. The autocorrelation function is modeled by replacing a simple basin with two sets of layered media.

In chapter 4, a simplified analytical procedure is developed with which to estimate the peak ground motion and which takes into account the fault extent. This procedure is an improvement on unrealistic usage in previous studies in which the epicentral distance is used to express the distance between the source region and the site. The theoretical distri-

bution of peak accelerations for many earthquakes is established and compared with observed accelerations. Incorporation of the time effect when an earthquake occurs in the region concerned is done by making a seismic risk analysis based on historical earthquake records and active fault data. The risk spectrum at the base rock level is proposed.

In chapter 5, the source parameters and fault rupture process are identified by deconvolution. The Kalman filter is applied to deconvolute a seismic wave into a system response function and a train of impulses. Earthquake motions are simulated statistically by the AR-MA process. A prediction model for an aseismic design is presented that considers strong ground motion at short epicentral distances.

References

[1] Kanai, K. Improved Empirical Equations for the Characteristics of Strong Earthquake Motions, Proc. 5th Japan Earthq. Eng. Symp., pp.1-4, 1966 (in Japanese with English abstract).

[2] Esteva, L. and R. Villaverde. Seismic Risk, Design Spectra, and Structural Reliability, Proc. 5th World Conf. on Earthq. Eng., Vol.2, pp.2586-2597, 1973.

[3] Katayama, T. Statistical Analysis of Peak Accelerations of Recorded Earthquake Motions, Research Report, Institute of Industrial Science, University of Tokyo, Vol.26, No.1, pp.81-91, 1974 (in Japanese).

[4] Trifnac, M. D. Preliminary Analysis of the Peaks of Strong Earthquake Ground Motion - Dependence of Peaks on Earthquake Magnitude, Epicentral Distance, and Recording Site Conditions, Bull. Seism. Soc. Am., Vol.66, No.1, pp.189-220, 1976.

[5] Blume, J. A. The SAM Procedure for Site-Acceleration-Magnitude Relationships, Proc. 6th World Conf. on Earthq. Eng., Vol. I, pp.416-422, 1977.

[6] Goto, H., H. Kameda, N. Imanishi and O. Hashimoto. Statistical Analysis of Earthquake Ground Motion with the Effect of Frequency-content Correction, Proc. 5th Japan Earthq. Eng. Symp., pp.49-56, 1978 (in Japanese with English abstract).

[7] Donovan, N. C. and A. E. Bornstein. Uncertainties in Seismic Risk Procedures, Jour. Geotech. Eng. Div., ASCE, Vol.84, No.SM3, pp.1730-1 - 1730-23.

[8] Kawashima, K., K. Aizawa and K. Takahashi. Attenuation of Peak Ground Motions and the Absolute, Acceleration Response Spectra, Report of the Public Works Research Institute, Ministry of Construction, Vol.166, 1985 (in Japanese with English abstract).

[9] Kameda, H., M. Sugito and T. Asamura. Simulated Earthquake Motions for Magnitude, and Local Soil Conditions, Proc. 7th World Conf. on Earthq. Eng., Istanbul, Vol.2, pp.295-302, 1980.

[10] Haskell, N. A. Total Energy and Energy Spectral Density of Elastic Wave Radiation from Propagating Faults, Bull. Seism. Soc. Am, Vol.54, No.6, pp.1811-1841,

[11] Aki, K. Seismic Displacements Near a Fault, Jour. Geophys. Res., Vol.73, No.16, pp.5359-5375, 1968.

[12] Kanamori, H. and D. L. Anderson. Theoretical Basis of Some Empirical Relations in Seismology, Bull. Seism. Soc. Am, Vol.65, pp.1073-1095, 1975.

[13] Hartzell, S. Earthquake Aftershocks as Green's Functions, Geophys. Res. Letters, Vol.5, No.1, pp.1-4, 1978.

[14] Irikura, K. and I. Muramatu. Synthesis of Strong Ground Motions from Large Earthquakes Using Observed Seismograms of Small Events, Proc. of 3rd International Earthquake, Microzonation Conference, Vol.1, pp.447-458, 1982.

[15] Mikumo, T. Estimation of Strong Ground Motion During Large Earthquakes Using Observed Seismograms of Small Events: Predicting Damage from a Large Earthquake in the Tokai District, Final Technical Report of Research Group for the Study of Natural Disaster (in Japanese).

[16] Kobayashi, H. and S. Midorikawa. A Semi-Empirical Method for Estimating Response Spectra of Near-field Ground Motions with Regard to Fault Rupture, Proc. 7th European Conf. Earthquake Engineering, pp.161-166, 1982.

[17] Iida, M. and M. Hakuno. The Synthesis of the Acceleration Wave in a Great Earthquake by Small Earthquake Records, Proc. JSCE, No.329, pp.57-68, 1983.

[18] Irikura, K. Semi-empirical Estimation of Strong Ground Motion, During Large Earthquakes, Bull. Disas. Prev. Res. Insti., Kyoto University, Vol.33-2, No.298, pp.63-104, 1983.

[19] Maruyama, T. On the Force Equivalents of Dynamic Elastic Dislocations with Reference to the Earthquake Mechanism, B. E. R. I., Vol.41, pp.467-486, 1963.

[20] Burridge, R. and L. Knopoff. Body Force Equivalents for Seismic Dislocations, Bull. Seism. Soc. Am, Vol.54, No.6, pp.1875-1888, 1964.

[21] Yamada, Y. and S. Noda. Prediction of Long-Period (2 to 20 sec) Ground Motions from a Hypothetical Great Earthquake along the Nankai Trough, Journal of Japan Society for Natural Disaster Science, Vol.5, No.1, pp.31-55 (in Japanese with English abstract).

[22] Matumura, L., K. Kudo and E. Shima. Distribution of Ground-motion Amplification Factors as a Function of Period (3-15 sec) in Japan, Bull. Earthq. Res. Inst., Univ. of Tokyo, Vol.59,1984.

[23] Suzuki, Y. and T. Hirasawa. Strong Motions from a Stochastic Model of Faulting, Proc. 8th World Conf. on Earthq. Eng., Vol.II, pp.481-488, 1984.

[24] Izutani, Y. A Statistical Model for Prediction of Quasi-realistic, Strong Ground Motion, Jour. of Physics of Earthquake, 29, pp.537-557, 1981.

[25] Madariaga, R. High-Frequency Radiation from Crack (Stress-Drop) Models of Earthquake Faulting, Geophys. J. Roy. Astron. Soc., Vol.51, pp.625-652, 1977.

[26] Das, S. and K. Aki. Fault Plane with Barriers: A Versatile Earthquake Model, Jour. Geophys. Res., Vol.82, pp.5648-5670, 1977.

[27] Papageorgiou, A. S. and K. Aki. A Specific Barrier Model for the Quantitative Description of Inhomogeneous Faulting and the Prediction of Strong Ground Motion: I. Description of the model, Bull. Seism. Soc. Am., Vol.73, No.3, pp.693-722, 1983.

[28] Lay, T. and H. Kanamori. Earthquake Doublets in the Solomon Islands, Phys. Earth Planet. Int., Vol.21, pp.283-304, 1980.

[29] Mikumo, T. and T. Miyatake. Dynamic Rupture Process on a Three Dimensional Fault with Non-uniform Friction and Near-field Seismic Waves, Geophys. J. R. Astr. Soc., Vol.54, pp.417-738, 1978.

[30] Midorikawa, S. and H. Kobayashi. On the Estimation of Strong Earthquake Motions with Regard to Fault Rupture, Proc. 2nd Inter. Conf. Microzonation, Vol.2, pp.825-836, 1978.

[31] Inoue, R. Studies on Design Earthquakes in the Period Range of 2 to 20 sec: A Review, Proc. JSCE, No.374, pp.1-23, 1986 (in Japanese with English abstract).

[32] Yamada, Y. and S. Noda. Theoretical Considerations on Attenuation of Earthquake, Ground Motions Excited from Point Dislocation Source, Proc. JSCE, Vol.323, pp.15-28, 1982 (in Japanese with English abstract).

[33] Kawakami, H. and Y. Sato. Effect of Deformation of Seismic Waves on Estimated Value of Ground Relative Displacement or Strain, Proc. JSCE, Vol.337, pp.37-46, 1983 (in Japanese with English abstract).

[34] Yamada, Y. and S. Noda. Theoretical Attempt for Estimating Relative Ground Motions Induced by Surface Waves, Proc. JSCE, No.335, pp.41-50, 1983 (in Japanese with English abstract).

[35] Iida, M. and M. Hakuno. Study on Complexity of Large Earthquakes, Proc. of JSCE, Structural Engineering/ Earthquake, Engineering, Vol.1, No.2, pp.47-57, 1984.

[36] Toki, K. and F. Miura. Simulation of a Fault Rupture Mechanism by a Two-dimensional Finite Element Method, J. Phys. Earthquake, Vol.33, No.6, pp.485-511, 1985.

[37] Toki, K. and S. Sawada. Simulation of the Fault Rupture Process and Near, Field Ground Motion by the Three-Dimensional Finite, Element Method, Proc. 9th World Conf. on Earthq. Eng., Vol.II, pp.751-756, 1988.

[38] Sato, R. Strong Ground Motion from an irregular Fault Model: Study of Short-Period Behavior in Fault Motion and Estimation of Input Seismic Motion, Final Technical Report of the Research Group for the Study of Natural Disaster, Vol.A-59-3, pp.117-138, 1984 (in Japanese).

[39] Toki, K., T. Sato and J. Kiyono. Synthesizing Design Ground Motions from Microearthquake Records, Proc. JSCE, Struc. Eng./ Earthq. Eng., Vol.2, No.2, pp.177-187, 1985.

[40] Iwata, T. and K. Irikura. Separation of Source, Propagation and Site Effects from Observed S Waves, Zisin 2, No.39, pp.579-593, 1986 (in Japanese).

[41] Sato, H. Regional Study of Coda Q^{-1} in the Kanto-Tokai District, Japan, Zisin 2, Vol.39, pp.241-249, 1986 (in Japanese with English abstract).

[42] Aki, K. Analysis of the Seismic Coda of Local Earthquake as Scattered waves, J. Geophys. Res., 74, pp.615-631, 1969.

[43] Umino, N. and A. Hasegawa. Three-dimensional Qs Structure in the Northeastern Japan Arc, Zisin 2, No.39, pp.241-249, 1986 (in Japanese with English abstract).
[44] Tsujiura, M. Special Analysis of the Coda Waves from Local Earthquakes, Bull. Earthq. Res. Inst.,Univ. of Tokyo, 53, pp.1-48, 1978.

[45] Sato, H. and S. Matumura. Q-value (2-32Hz) of S-waves in the Kanto District, Zisin, 33, pp.541-543, 1980 (in Japanese).

[46] Akamatu, J. Seismic Observation at the Sumiyama Seismic Station(2)- On the Natures of Attenuation and Spectra of Coda Parts of Local Earthquakes, Annuals Disas. Prev. Res. Inst., Kyoto University, Vol.23B-1, pp.107-114, 1980 (in Japanese with English abstract).

[47] Hoshiba, K. Regional Study of Coda Q^{-1} in the Kyushu District, Japan, Abstracts of Annual Convention of the Seism. Soc. of Japan, 1987.

[48] Idriss, I. M. and H. B. Seed. An Analysis of Ground Motions During the 1957 San Francisco earthquake , Bull. Seism. Soc. Am., Vol.58, No.6, pp.2013-2032, 1968.

[49] Seed, H. B. and I. M. Idriss. Influence of Soil Conditions on Ground Motions During Earthquakes, Jour. Soil Mech. and Foundation Division, ASCE, Vol.95, No.sm1, pp.99-137, 1969.

[50] Tsai, N. C. and G. W. Housner. Calculation of a Surface Motion of a Layered Half-Space, Bull. Seism. Soc. Am., Vol.60 , No.5 , pp.1625-1651, 1970.

[51] Aki, K. and P. G. Richards. Quantitative Seismology, Theory and Methods, W. H. Freeman and Company, Vol.1, 1980, pp.144-151.

[52] Haskell, N. A. The Dispersion of Surface Waves Multilayered Media, Bull. Seism. Soc. Am., Vol.60, No.1, pp.89-104, 1970.

[53] Aki, K. and K. L. Larner. Surface Motion of a Layered Medium having an Irregular Interface Due to Incident Plane SH Waves , J. Geophys. Res, Vol.75, pp.933-954, 1970.

[54] Bouchon, M. Effect of Topography on Surface Motions, Bull. Seism. Soc. Am, Vol.63, pp.615-632, 1973.

[55] Trifunac, M. D. Scattering of Plane SH-Waves by a Semi-cylindrical Canyon, Earthq. Eng. and Struc. Dyn., Vol.1, pp.267-281, 1973.

[56] Wong, W. L. and M. D. Trifunac. Scattering of Plane SH-Waves by a Semi-elliptical Canyon, Earthq. Eng. and Struc. Dyn., Vol.3, pp.157-169, 1974.

[57] Wong, H. L. and P. C. Jennings. Effect of Canyon Topographies on Strong Ground Motion, Bull. Seism. Soc. Am, Vol.65, pp.1239-1257, 1975.

[58] Wong, H. L. Diffraction of P, SV, and Rayleigh Waves by Surface Topographies, Report No. CE 79-05, Dept. of Civil Eng., University of Southern California, Los Angeles, 1979.

[59] Boore, D. M., K. Larner and K. Aki. A Comparison of Two Independent Methods for the Solution of Wave-Scattering Problems, J. Geophys. Res., No.76, pp.588-569, 1971.

[60] Boore, D. M. A Note on the Effect of Simple Topography on Seismic SH Waves, Bull. Seism. Soc. Am., Vol.62, pp.275-284, 1972.

[61] Ilan, A., A. Ungar and A. Alterman. An Improved Representation of Boundary Conditions in Finite Difference Scheme for Seismological Problems, Geophys. J. R. Astr. Soc., No.43, pp.727-745, 1975.

[62] Ohtsuki, A., H. Yamahara and K. Harumi. Effect of Topographies and Subsurface Inhomogeneities on Surface Motions for Incident SV-waves, Proc. 6th Japan Earthq. Eng. Symp., pp.433-440, 1982.

[63] Housner, G. W. Interaction of Building and Ground During an Earthquake, Bull. Seism. Soc. Am., Vol.47, No.3, pp.179-186, 1957.

[64] Yamahara, H. Input loss of Earthquake Ground Motions and Waves (I), Proc. Architectural Institute of Japan, No.165, pp.61-66, 1969 (in Japanese).

[65] Yamahara, H. Input loss of Earthquake Ground Motions and Waves (II), Proc. Architectural Institute of Japan, No.167, pp.25-30, 1970 (in Japanese).

[66] Tajimi, H. Dynamic Analysis of Structures Supported on Deep Foundations, Proc. 2nd Japan Earthq. Eng. Symp., pp.255-260, 1966 (in Japanese).

[67] Kobori, T., R. Minai and T. Suzuki. Vibrational Characteristics of Sub-Structures Embedded in a Layered Medium, Annuals Disas. Prev. Res. Inst., Kyoto University, No.19-B, pp.219-244, 1976 (in Japanese with English abstract).

[68] Goto, H., K. Toki, and S. Takada. On the Vibrational Characteristics of Foundation Structures in the Ground, Annuals Disas. Prev. Res. Inst., Kyoto University, No.14A, pp.263-282, 1971 (in Japanese with English abstract).

[69] Hakuno, M. and Y. Nojiri. An Experiment on Dynamical Properties of a Well Foundation, Proc. JSCE, No.170, pp.1-21, 1969 (in Japanese with English title).

[70] Toki, K. and A. Komatsu. Seismic Response of Well Foundation, Proc. JSCE, No.281, pp.29-40, 1979 (in Japanese with English title).

[71] Harada, T., K. Kubo and T. Katayama. Dynamic Soil-structure Interaction Analysis by Continual Formulation Method, Research Report, Institute of Industrial Science, Univ. of Tokyo, Vol.29, No.5, 1981 (in Japanese).

[72] Toki, K., T. Sato and F. Miura. Separation and Sliding Between Soil and Structure during Strong Ground Motion, Earthq. Eng. and Struc. Dyn., Vol.9, pp.263-277, 1981.

[73] Wolf, J. P. Dynamic Soil-Structure Interaction, Prentice-Hall, 1985.

[74] Luco, J. E. On the Relation between Radiation and Scattering Problems for Foundations Embedded in an Elastic Half-space, Soil. Dyn. and Earthq. Eng, Vol.5, pp.97-101, 1986.

[75] Takemiya, H. and Y. Yamada. Layered Soil-pile-structure Dynamic Interaction, Earthq. Eng. Struc. Dyn., Vol.9, pp.437-457, 1981.

[76] Harada, T., K. Kubo and T. Katayama. Fundamentals of Dynamic Soil-Structure Interaction Analysis, Proc. JSCE, No.334, pp.173-176, 1983 (in Japanese with English title).

CHAPTER 2

IDENTIFICATION OF GROUND MOTION INPUT TO A STRUCTURE

2.1 General Remarks

The relation between the input and output motion for a structural system is shown in Fig.2.1. Input motion corresponds to the ground motion induced by an earthquake, microtremor, or mechanical vibration; whereas, output motion is the response of a structural system due to that input. Both the input and output motions are used to identify the dynamic properties of a structure, the output motion and the system parameters being needed to derive the input motion.

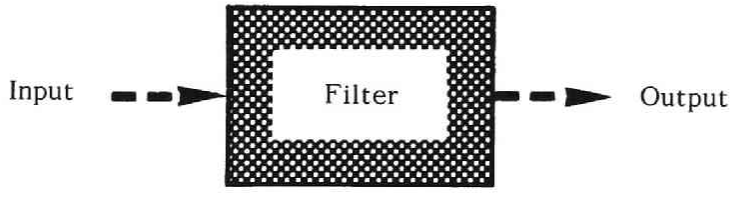

Fig. 2.1 Relation between input and output motion.

A procedure here is developed by which to identify such structural parameters as the natural frequency and damping constant and by which to estimate input motion from the seismic response time series of the structure alone. Kalman filter analysis, a method that updates the estimated value at each time step by incorporating new observation data, is used in this procedure. Toki and Sato [1] developed a method for identifying structural parameters that uses an AR-MA process based on white noise input for a linear system. It has proved useful for detecting the dynamic parameters of structural systems; but, as the input motion is assumed to be white noise, it can not be used when the input characteristics are

uncertain. Hoshiya and Saito [2, 3] used an extended Kalman filter with a dynamic structural system to solve the identification problem. They proposed a weighted global iteration procedure to obtain fast convergency to the optimum solution and the stability of that solution. In addition, they studied the sensitivity of the initial condition to the convergency. Hoshiya and Maruyama [4] developed a method by which to identify the parameters of a versatile hysteretic model by the use of an extended Kalman filter. In the geomechanics field, Murakami and Hasegawa [5] proposed a new back analysis method which uses Kalman Filter-Finite Elements to determine the optimal location of observation nodal points. All these procedures require both input and output data. The method described here differs in that the system parameters are identified from output data alone.

There have been only a few earthquake engineering studies [6, 7] whose objectives were to estimate input motion from the structural response because input motion is known when analyzing seismic response, and earthquake engineers usually are interested in estimating the response of a structure. It is necessary, however, to identify the real motion input to a structure or its foundation because there is much uncertainty as to the contact point between the soil and a structure. This is related to the idea of effective input. The Kalman error filter, developed by Ott and Meder [8], has been used to estimate input motion from the structural response and structural parameters. This method is here extended so that the input motion can be calculated from the estimation error obtained in the Kalman filter algorithm. The model proposed has three masses and three degrees of freedom. Its responses are assumed to be recorded in each mass.

2.2 Identification of Restoring Force Characteristics and Structural Parameters

2.2.1 Identification by the Kalman Filter

The determination of the state of a system from measurements contaminated by noise is called filtering. The filtering theory was first established by N. Wiener [9], who regarded the signal and noise as a stochastic process and proposed what is called the Wiener filter. Later, in the 1960s, Kalman and Bucy [10] formulated and derived the Kalman filter using orthogonal projection. Wiener's filtering theory is called a classical stochastic system theory because the process is continuous and is dealt with in the frequency domain. The Kalman filter processes data sequentially and correlates well with the change in state. The stochastic process of the Kalman filter can be applied to discrete sys-

tems. It has become a useful means of filtering due to the rapid increase in the use of digital computers.

As the Kalman filter processes data sequentially, based on orthogonal projection and minimum error criteria, it needs the dynamic characteristics of a linear filter, the stochastic characteristics of noise, *a priori* information about the initial values, and observed data given sequentially. The linear dynamic system is described by the linear vector differential equation

$$\frac{d\mathbf{x}(t)}{dt}=\mathbf{A}\cdot\mathbf{x}(t)+\mathbf{B}\cdot\mathbf{w}(t) \tag{2.1}$$

The continuous linear observations are given in Eq.(2.2).

$$\mathbf{y}(t)=\mathbf{H}\cdot\mathbf{x}(t)+\mathbf{v}(t) \tag{2.2}$$

in which $\mathbf{x}$, $\mathbf{w}$, $\mathbf{y}$, and $\mathbf{v}$ are n-,m-, p-, and the p-vector state, and $\mathbf{A}$, $\mathbf{B}$, and $\mathbf{H}$ are the $n \times n$, $n \times m$ and $p \times n$ constant matrices. Eqs.(2.1) and (2.2) are continuous equations. Because the data obtained usually are discrete, it is preferable to discretize the system. To convert the continuous system to a discrete one, $e^{-\mathbf{A}t}$ is multiplied in Eq.(2.1).

$$\frac{d}{dt}(\mathbf{x}e^{-\mathbf{A}t}) = \mathbf{B}\ \mathbf{w}\ e^{-\mathbf{A}t} \tag{2.3}$$

The integral from t_0 to t in Eq.(2.3) yields

$$\mathbf{x}(t) = \mathbf{x}(t_0)\ e^{-\mathbf{A}(t-t_0)} + \int_{t_0}^{t} \mathbf{B}\ \mathbf{w}(p)\ e^{\mathbf{A}(t-p)}\ dp \tag{2.4}$$

Suppose the following step functions;

$$\begin{gathered} t_0 \rightarrow k\Delta t,\quad t \rightarrow (k+1)\Delta t \\ \mathbf{w}(t) = \mathbf{w}(k\Delta t) = \mathbf{w}(k),\quad \mathbf{x}(t) = \mathbf{x}(k\Delta t) = \mathbf{x}(k) \\ k\Delta t \le t < (k+1)\Delta t \end{gathered} \tag{2.5}$$

From Eqs.(2.4) and (2.5)

$$\mathbf{x}(k+1) = \mathbf{x}(k)\, e^{\mathbf{A}\Delta t} + \int_{k\Delta t}^{(k+1)\Delta t} e^{\mathbf{A}p}\, dp\, \mathbf{B}\, \mathbf{w}(p) \tag{2.6}$$

Eq.(2.6) can be rewritten

$$\mathbf{x}(k+1) = \Phi \cdot \mathbf{x}(k) + \mathbf{G} \cdot \mathbf{w}(k) \tag{2.7}$$

in which

$$\Phi = e^{\mathbf{A}\Delta t}, \quad \mathbf{G} = \int_{k\Delta t}^{(k+1)\Delta t} e^{\mathbf{A}p}\, dp\, \mathbf{B} \tag{2.8}$$

The discrete systems of Eqs.(2.1) and (2.2) then are

$$\begin{aligned} \mathbf{x}(k+1) &= \Phi \cdot \mathbf{x}(k) + \mathbf{G} \cdot \mathbf{w}(k) \\ \mathbf{y}(k) &= \mathbf{H} \cdot \mathbf{x}(k) + \mathbf{v}(k) \end{aligned} \tag{2.9}$$

If k and k+1 are replaced by t-1 and t, the discrete linear system becomes

$$\mathbf{X}_t = \Phi_{t|t-1} \mathbf{X}_{t-1} + \mathbf{G}\mathbf{W}_{t-1} \tag{2.10}$$

$$\mathbf{Y}_t = \mathbf{H}\mathbf{X}_t + \mathbf{V}_t \tag{2.11}$$

in which $\mathbf{X}_t$ is the n-dimensional state estimate vector at t; $\mathbf{Y}_t$ the p-dimensional observation vector at t; $\mathbf{W}$ and $\mathbf{V}$ the m- and p-dimensional Gaussian white noise with $E\{\mathbf{W}_s \mathbf{W}_t^T\} = \mathbf{Q}\, \delta_{st}$, and $E\{\mathbf{V}_s \mathbf{V}_t^T\} = \mathbf{R}\, \delta_{st}$, where E represents the expectation and δ Kronecker's delta; Φ the state transition matrix with the dimensions $n \times n$; $\mathbf{H}$ the measurement matrix with the dimensions $p \times n$; and $\mathbf{G}$ the system noise matrix with the dimensions $n \times m$. If the governing differential equations are transformed to Eq.(2.3) and Eq.(2.4) by the appropriate modeling, the identification problem can be solved by use of the Kalman filter algorithm shown in Fig 2.2 [11].

Steps (2) and (3) are called the time update algorithm and steps (5) and (6) the measurement update algorithm. $\mathbf{x}_{t|t}$ and $\mathbf{x}_{t+1|t}$ are the filtering and prediction estimates. The filtering estimate, $\mathbf{x}_{t|t}$, is the optimum value at t when data up to t are given. The

prediction estimate, $\mathbf{x}_{t+1|t}$, is the optimum value at t+1 when data up to t are given. The state estimate, $\mathbf{x}_{t+1|t}$, is computed from $\mathbf{x}_{t|t}$ in step (2). The next filtering estimate, $\mathbf{x}_{t+1|t+1}$, is calculated from $\mathbf{x}_{t+1|t}$ after incorporating the observation, $\mathbf{y}_{t+1}$. The Kalman gain matrix is determined in this process by minimizing the difference between the estimate, $\hat{\mathbf{x}}_t$, and the exact value, $\mathbf{x}_t$.

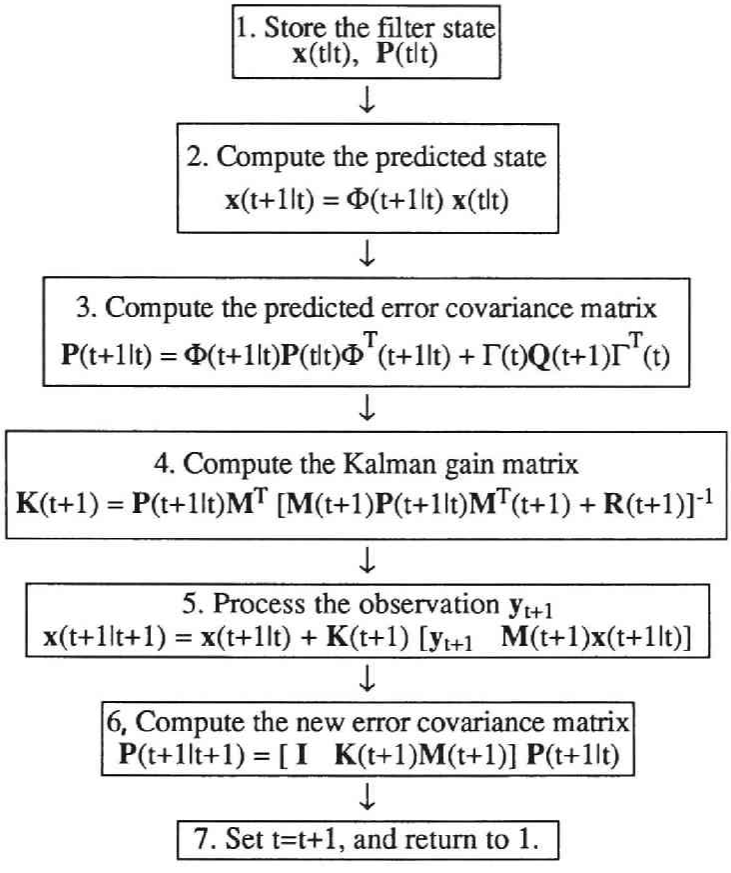

Fig. 2.2 Kalman filter algorithm (after Jazwinski [11])

When the above algorithm is executed, $\mathbf{x}_{t|t}$ often diverges as the matrices do not keep symmetric and positive definite characteristics because of rounding off errors. To avoid this, a U-D filter which keeps the symmetric and positive definite characteristics of matrix **P** is adopted.

Consider the equation of motion for a nonlinear one-degree-of-freedom system;

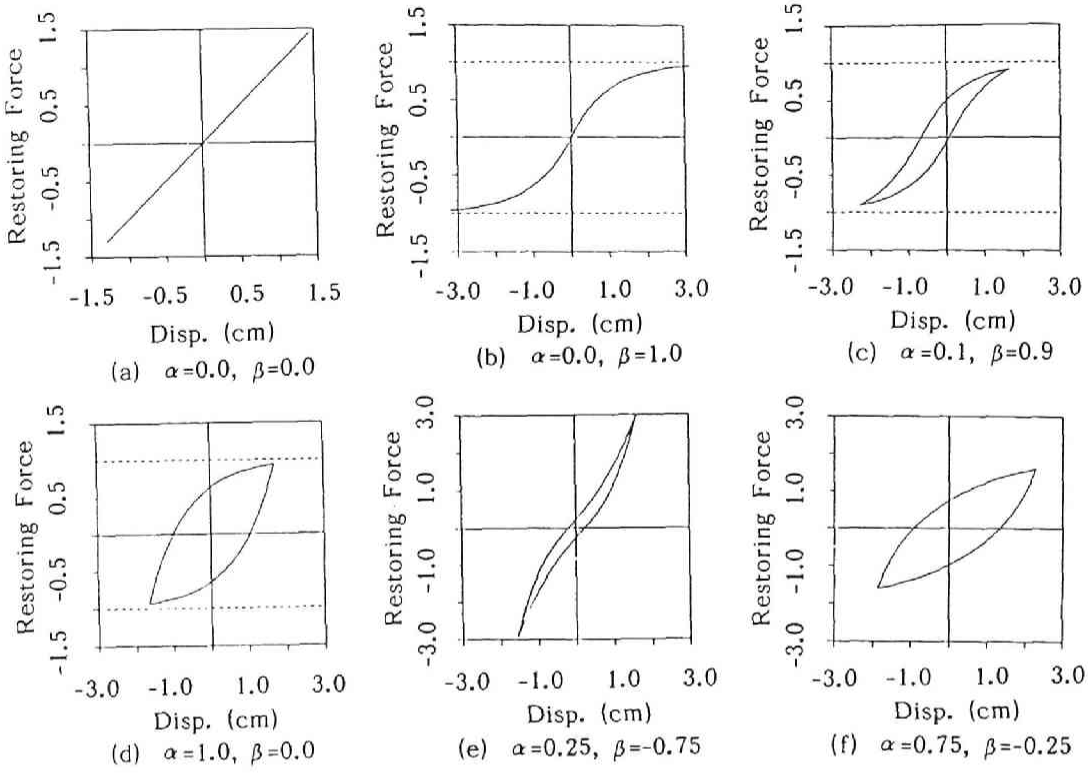

Fig. 2.3 Hysteretic loops, the versatile model (n=1).

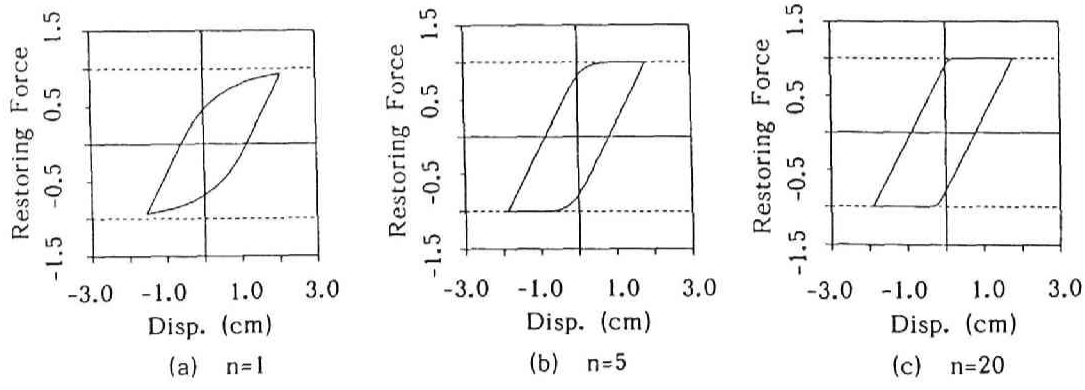

Fig. 2.4 Hysteretic loops for various *n*.

$$m\ddot{y} + c\dot{y} + z(y) = -m\ddot{u} \qquad (2.12)$$

in which m is the mass, c the coefficient of damping, z the restoring force, and ü the input acceleration. The nonlinear restoring force model is the versatile model proposed by Wen [12]. It is flexible and can be adjusted to various hysteretic models by the use of a few parameters. The governing equations for this model are

$$\dot{z} = -\alpha|\dot{y}|z^n \quad \beta\dot{y}|z^n| + k\dot{y} \quad \text{for odd } n \qquad (2.13)$$

$$\dot{z} = -\alpha|\dot{y}|z^{n-1}|z| \quad \beta\dot{y}z^n + k\dot{y} \quad \text{for even } n \qquad (2.14)$$

in which n, α and β are the parameters that control the shape of the hysteretic loop, and k is the tangential stiffness at the restoring force z=0.

To investigate the effect of the parameters on the shape of the hysteretic loop, the response time history is calculated by fixing the values of parameters at k=1 and n=1. The natural circular frequency is, ω, and the amplitude of the input sine-wave 1.0. The time step for the calculation is 0.01 sec, and the numerical integration used is the Runge-Kutta method. The hysteretic loops for various combinations of α and β are shown in Fig.2.3. When $\alpha=\beta=0$, the loop is linear. $\alpha>0$ and $\beta>0$ correspond to nonlinear elastic hardening, and $\alpha>0$ and $\beta<0$ to nonlinear elastic softening. When the ratio of α to β is small, the shape of the hysteretic loop becomes narrow.

The hysteretic loops for various values of n are shown in Fig.2.4. The values of k, α, and β are fixed at k=1, and $\alpha=\beta=0.5$. As the value of n increases, the shape comes close to the perfect elasto-plastic type of bi-linear model. When the hysteretic loop is the softening type ($\alpha>0$, $\beta>0$), the asymptote is $z = \pm (k/|\alpha+\beta|)^{1/n}$. The asymptotes of the hysteretic loops in Fig.2.3 (a), (c), (d) and Fig.2.4 are z=1. The shape is shown to be flexibly changed by varying only a few parameters.

2.2.2 Formulation for the Identification

The model of nonlinear multi-degree-of-freedom system (super-structure: two-degrees-of-freedom, foundation structire: two-degrees-of-freedom) that contains the rocking motion of the foundation is shown in Fig.2.5. The equation of motion is

$$\mathbf{M}\ddot{\mathbf{y}} + \mathbf{C}\dot{\mathbf{y}} + \mathbf{T}\mathbf{z} = -\mathbf{M}\mathbf{v}\ddot{u} \qquad (2.15)$$

where

$$\mathbf{M} = \begin{bmatrix} m_1 & 0 & 0 & 0 \\ 0 & m_2 & 0 & 0 \\ 0 & 0 & m_3 & 0 \\ 0 & 0 & 0 & m_4 \end{bmatrix} \tag{2.16}$$

$$\mathbf{C} = \begin{bmatrix} c_1 & -c_1 & 0 & -H_1'c_1 \\ -c_1 & c_1+c_2 & -c_2 & H_1'c_1-H_2'c_2 \\ 0 & -c_2 & c_2+c_3 & H_2'c_2-H_3'c_3 \\ -H_1'c_1 & H_1'c_1-H_2'c_2 & H_2'c_2-H_3'c_3 & c_4+\sum_{i=1}^{4} H_i'c_i \end{bmatrix} \tag{2.17}$$

$$\mathbf{T} = \begin{bmatrix} 1 & 0 & 0 & 0 \\ -1 & 1 & 0 & 0 \\ 0 & -1 & 1 & 0 \\ -H_1' & -H_2' & -H_3' & 1 \end{bmatrix} \tag{2.18}$$

$$\mathbf{v} = \{ \ 1 \quad 1 \quad 1 \quad 0 \ \}^T \tag{2.19}$$

$$\mathbf{y} = \{ \ y_1 \quad y_2 \quad y_3 \quad \phi \ \}^T \tag{2.20}$$

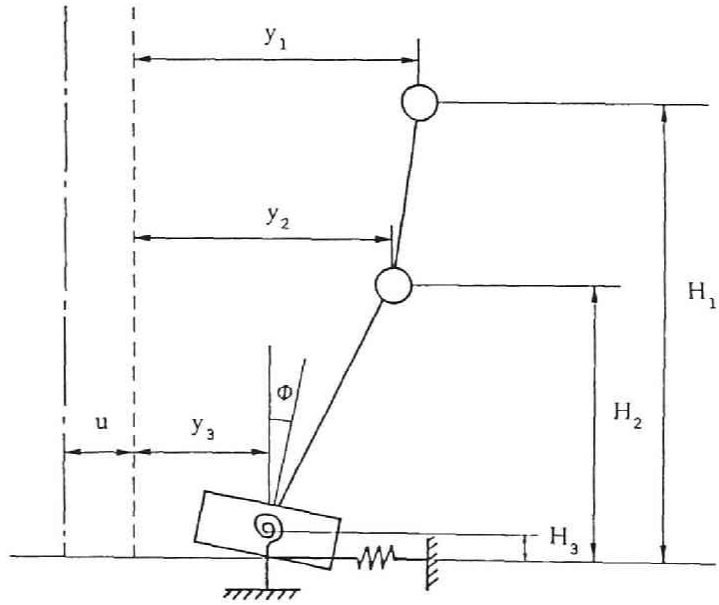

Fig. 2.5 The nonlinear multi-degree-of-freedom system model.

in which H'_i is H_i-H_{i+1}; m_i (i=1,2,3) the gravity of the mass, i; m_4 the inertia moment of the foundation; c_i the damping coefficient between mass i and mass i+1; z_i the restoring force between mass i and mass i+1; and y_i the relative displacement of mass i to that of the ground.

The dynamic system is modeled by combining the equation of motion and the equation of versatile restoring force which has been linearized by Taylor expansion. The response is derived from this combined equation by use of the linear acceleration method.

$\mathbf{y}_{t+1}$ and $\dot{\mathbf{y}}_{t+1}$ in the linear acceleration method are

$$\dot{\mathbf{y}}_{t+1} = \dot{\mathbf{y}}_t + \frac{\Delta t}{2}(\ddot{\mathbf{y}}_t + \ddot{\mathbf{y}}_{t+1}) \tag{2.21}$$

$$\mathbf{y}_{t+1} = \mathbf{y}_t + \Delta t\dot{\mathbf{y}}_t + \frac{\Delta t^2}{3}\ddot{\mathbf{y}}_t + \frac{\Delta t^2}{6}\ddot{\mathbf{y}}_{t+1} \tag{2.22}$$

in which Δt is the time interval.

A versatile restoring force model is constructed by making $\mathbf{z}$ and $\mathbf{y}$ satisfy the differential equation Eq.(2.13) or Eq.(2.14).

$$z^i_{t+1} = \frac{1}{\gamma}(k+\gamma z^i_t)\exp\left\{\gamma(\delta^i_{t+1}-\delta^i_t) - k\right\} \tag{2.23}$$

in which δ_t^i is the difference between the relative displacement of masses i and i+1, and the rocking displacement at time t. The nonlinear restoring force is dependent on δ_t. By linearizing Eq.(2.23) by Taylor expansion of the exponential term

$$\begin{aligned}\mathbf{z}_{t+1} &= \mathbf{z}_t + \Gamma_z(\delta_{t+1}-\delta_{t+1}) \\ &= \mathbf{z}_t + \Gamma_z\mathbf{T}^T(\mathbf{y}_{t+1}-\mathbf{y}_{t+1})\end{aligned} \tag{2.24}$$

in which $\mathbf{T}$ is the transfer matrix between $\mathbf{y}$ and δ, and Γ_z is given as

$$\Gamma_z = \begin{bmatrix} \ddots & & 0 \\ & k+\gamma z^i_t & \\ 0 & & \ddots \end{bmatrix} \tag{2.25}$$

When an input motion (such as the response acceleration, velocity or displacement) is given, $\ddot{y}$, $\dot{y}$, $\ddot{y}$, n, c/m, k/m, α, and β can be identified. Moreover, if the restoring force,

z, is known, $\ddot{y}$, $\dot{y}$, $\ddot{y}$, z, m, c, k, α, and β can be identified. The former is called 'formulation 1', the latter 'formulation 2'.

(1) Formulation 1

The parameters to be identified are

$$\alpha = \{\alpha_1\ \alpha_2\ \alpha_3\ \alpha_4\}^T \tag{2.26}$$

$$\beta = \{\beta_1\ \beta_2\ \beta_3\ \beta_4\}^T \tag{2.27}$$

$$\mathbf{c_m} = \{c_1/m_1\ c_2/m_2\ c_3/m_3\ c_4/m_4\}^T \tag{2.28}$$

$$\mathbf{k_m} = \{k_1/m_1\ k_2/m_2\ k_3/m_3\ k_4/m_4\ k_1/m_2\ k_2/m_3\ k_3/m_4\}^T \tag{2.29}$$

Unknown parameters c_1/m_2, c_2/m_3 and c_3/m_4 that should be exist in Eq.(2.28) are reduced by the following relation;

$$\frac{c_{n-1}}{m_n} = \frac{k_{n-1}/m_n}{k_{n-1}/m_{n-1}} \cdot \frac{c_{n-1}}{m_{n-1}} \tag{2.30}$$

The state estimate vector for the state equation (Eq.(2.10)) is

$$\mathbf{X} = \{\ddot{y}\ \dot{y}\ y\ \eta\ \alpha\ \beta\ \mathbf{c_m}\ \mathbf{k_m}\}^T \tag{2.31}$$

in which η is defined as z/k.

From Eq.(2.24),

$$\eta_{t+1} = \eta_t + \Gamma_\eta \mathbf{T}^T(\mathbf{y}_{t+1} - \mathbf{y}_t) + \mathbf{w}_t \tag{2.32}$$

in which $\mathbf{w}_t$ is noise vector and the diagonal matrix Γ_η is

$$\Gamma_\eta = \begin{bmatrix} \ddots & & 0 \\ & 1+\gamma\eta_t^i & \\ 0 & & \ddots \end{bmatrix} \tag{2.33}$$

Solving Eqs.(2.15), (2.21), (2.22) and (2.32) for $\ddot{y}$ to derive the state estimate equation gives

$$\mathbf{D}_1 = \mathbf{I} + \frac{\Delta t}{2}\mathbf{C_M} + \frac{\Delta t^2}{3}\mathbf{K_M}\,\Gamma_\eta\,\mathbf{T}^T$$

$$\mathbf{D}_1^{-1}\,(\mathbf{C_M} + \Delta t\,\mathbf{K_M}\,\Gamma_\eta\,\mathbf{T}^T)\,\dot{\mathbf{y}}_t$$

$$\mathbf{D}_1^{-1}\,\mathbf{K}_M\,\eta_t - \mathbf{D}_1^{-1}\quad \mathbf{K}_M\,\mathbf{w}_t - \mathbf{v}\,\ddot{u}_{t+1} \tag{2.34}$$

in which

$$\mathbf{D}_1 = \mathbf{I} + \frac{\Delta t}{2}\mathbf{C}_M + \frac{\Delta t^2}{3}\mathbf{K}_M\,\Gamma_\eta\,\mathbf{T}^T \tag{2.35}$$

$$\mathbf{C}_M = \mathbf{M}^{-1}\mathbf{C} \tag{2.36}$$

$$\mathbf{K}_M = \mathbf{M}^{-1}\mathbf{T}\mathbf{K} \tag{2.37}$$

$\mathbf{C}_M$ and $\mathbf{K}_M$ are described by the unknown parameters c/m and k/m. The state transition matrix $\Phi_{t+1|t}$ (of which the *ij* th-component is Φ_{ij}) is calculated by

$$\Phi_{ij} = \frac{\partial f_i}{\partial X_j} \tag{2.38}$$

in which f is the following nonlinear function of the state equation for the extended Kalman filter [13];

$$\mathbf{X}_{t+1} = f(\mathbf{X}_t) + \mathbf{w}_t \tag{2.39}$$

(3) Formulation 2

The parameters to be identified are

$$\alpha = \{\alpha_1\ \alpha_2\ \alpha_3\ \alpha_4\}^T \tag{2.40}$$

$$\beta = \{\beta_1\ \beta_2\ \beta_3\ \beta_4\}^T \tag{2.41}$$

$$\mathbf{m} = \{m_1\ m_2\ m_3\ m_4\}^T \tag{2.42}$$

$$\mathbf{c} = \{c_1\ c_2\ c_3\ c_4\}^T \tag{2.43}$$

$$\mathbf{k} = \{k_1\ k_2\ k_3\ k_4\}^T \tag{2.44}$$

Solving Eqs.(2.15), (2.21), (2.22) and (2.32) for $\ddot{\mathbf{y}}$

$$\begin{aligned}\ddot{\mathbf{y}}_{t+1} = &-\mathbf{D}_2^{-1}\left(\frac{\Delta t}{2}\mathbf{C} + \frac{\Delta t^2}{3}\mathbf{K}\Gamma_\eta\mathbf{T}^T\right)\ddot{\mathbf{y}}_t \\ &-\mathbf{D}_2^{-1}\left(\mathbf{C} + \Delta t\,\mathbf{K}\Gamma_\eta\mathbf{T}^T\right)\dot{\mathbf{y}}_t \\ &-\mathbf{D}_2^{-1}\,\mathbf{T}\mathbf{z}_t - \mathbf{D}_2^{-1}\quad \mathbf{T}^T\,\mathbf{w}_t - \mathbf{D}_2\,\mathbf{M}\mathbf{v}\,\ddot{u}_{t+1}\end{aligned} \tag{2.45}$$

$$\mathbf{D}_2 = \mathbf{M} + \frac{\Delta t}{2}\mathbf{C} + \frac{\Delta t^2}{3}\mathbf{K}\Gamma_\eta \mathbf{T}^T \qquad (2.46)$$

in which $\mathbf{K}=\mathbf{T}[k_i]$, and **M**, **C**, and **K** are expressed by the unknown parameters m, c and k in the state variables. The state transition matrix is calculated from formulation 1.

(3) Formulation verification

For a case study, the restoring characteristics of a nonlinear multi-degree-of-freedom system are identified. The nonlinear two-degree-of-freedom, sway-rocking model is shown in Fig.2.6. The model parameters are listed in Table 2.1. Input motion is simulated by multiplying the evolutionary function by white noise for which the frequency range is 0.1 10 Hz. The input accelerogram has a peak at 2.5 sec. The response waves from the model, with 10% white noise of their r.m.s values added, are used as the observed data.

Table 2.1 Model parameters

	Mass M	Damping Coeff. C	Stiffness K	α	β
Sway	0.1 (ton)	0.2 (tf*s/cm)	30 (tf/cm)	2.0	0.5
Rocking	1000 (ton*cm)	3000 (tf*cm*s/rad)	500000 (tf*cm/rad)	300	50

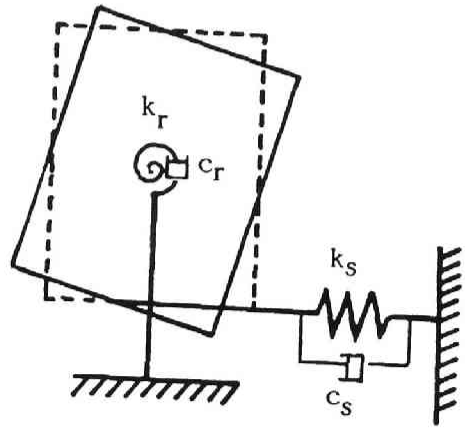

Fig. 2.6 The nonlinear two-degrees-of-freedom, sway-rocking model.

Model parameters are identified for six cases: In case 1 the response acceleration, velocity, and displacement of sway motion; in case 2 the response acceleration, velocity, and displacement of rocking motion; in case 3 the response velocities and displacements of both the sway and rocking motions; in case 4 the response velocity displacement and restoring force of the sway motion; in case 5 the response velocity, displacement, and restoring moment of the rocking motion; and in case 6 the response velocities, displacements, restoring force and moment of both the sway and rocking motions. Cases 1, 2 and 3 are identified by formulation 1; cases 4, 5 and 6 by formulation 2. The respective results are shown in Tables 2.2 and 2.3.

Table 2.2 shows that the results of the identification of parameters c and β in case 2 are not accurate. In all the cases, parameter β is not identified accurately. Because parameter β directly controls the shape of the hysteretic loop of softening or hardening, the identified parameter β fluctuates more than the other parameters. Table 2.3 shows the results obtained with formulation 2 in which either the response of swaying or the rocking motion is observed. The accuracy of the results is better than that obtained with formulation 1 (Table 2.2).

Table 2.2 Identification results (formulation 1)

	k_1/m_1	k_2/m_2	k_1/m_2	c_1/m_1	c_2/m_2	α_1	α_2	β_1	β_2
case 1	299.9	489.3	0.031	1.833	2.894	1.988	305.6	0.43	6.77
case 2	264.0	503.4	0.026	2.648	0.882	2.295	311.5	-0.14	28.20
case 3	293.7	487.6	0.029	2.001	2.623	2.015	309.1	0.32	18.99
Ex.Val.	300.0	500.0	0.030	2.000	3.000	2.000	300.0	0.50	50.00

Table 2.3 Identification results (formulation 2)

	k_1	k_2	c_1	c_2	α_1	α_2	β_1	β_2
case 4	30.25	492028	0.207	2748	1.996	312.3	0.549	21.78
case 5	30.75	499282	0.195	3478	1.912	293.3	0.668	61.40
case 6	30.36	489763	0.208	3014	1.949	303.6	0.559	36.78
Ex.Val.	30.00	500000	0.200	3000	2.000	300.0	0.500	50.00

2.2.3 Identification of Nonlinear Restoring Force Characteristics

(1) Application to a hybrid experiment

Nonlinear restoring characteristics are identified by applying the developed procedure to experimental data. Although a number of methods for soil-structure interaction are known, they lose accuracy when test results from small models are interpreted for actual systems. Analytical idealization; a time domain, numerical integration scheme; large scale modeling; and a pseudo-dynamic testing (PDT) method were used to develop a hybrid method for the study of the seismic nonlinear behavior of soil-structure interaction. In the experiment, three foundations (surface, shallow-embedded, and caisson) were used whose mechanical characteristics had been determined through static and dynamic tests. Analytical soil-structure interaction models were constructed on the bases of these characteristics, and the resulting equations of motion were utilized in the pseudo-dynamic tests.

An algorithm in which PDT is adopted was constructed in order to study the seismic non-linear behavior of soil-structure systems and their frequency dependence. When carefully conducted, results obtained from pseudo-dynamic tests have been shown to be reliable and more accurate than results of other analytical and experimental methods. A flowchart of the procedure is shown in Fig.2.7.

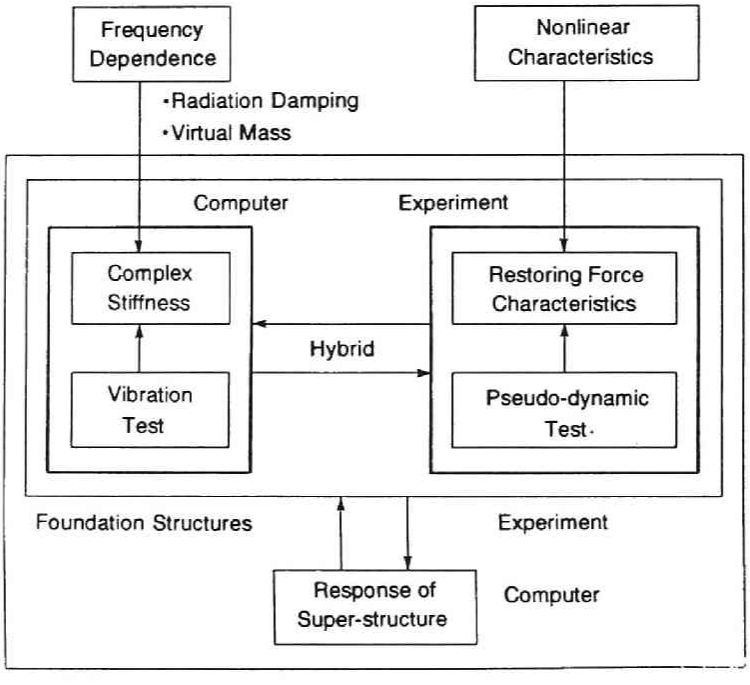

Fig. 2.7 Flow in the hybrid experiment.

The algorithm is called HENESSI, which stands for Hybrid Experiments on Non-linear Earthquake-induced Soil-Structure Interaction [14, 15, 16]. The procedure starts with large scale modeling after mathematical discretization of the soil-structure system. Lumped parameter discretization leads to a governing system of second-order ordinary differential equations for dynamic equilibrium. Static and forced dynamic vibration tests are made using these equations, from which the mechanical characteristics of the system are determined. In the numerical computations, the static stiffness evaluated by static tests is used as the initial stiffness. Frequency-dependent dynamic characteristics are determined through the phase delay study of forced vibration tests. Using these results, the complex frequency-dependent stiffness matrix of the system is constructed in the frequency domain. Then, using Hilbert and inverse Fourier transformations, a time-history-dependent pseudo-force is established. Although in the PDT only the developed non-linear static restoring force characteristics are accounted for, in HENESSI frequency dependence is present and dynamic non-linear behavior can be studied for a system whose frequency dependency is not changed appreciably by local non-linearity.

The foundation model to be identified is the surface foundation shown at left in Fig.2.8. Only two degrees of freedom were assigned for the systems. In the hybrid analysis, the structural system is considered to be an assembly of structural elements interconnected at the center of gravity where the mass is assumed to be concentrated (Fig.2.9). The deformation state of this idealized discrete parameter system is determined by the sway and rocking modes chosen as the two degrees of freedom at the center of gravity. For simplicity, in this first stage global non-linearities due to free-field soil responses and kinematic interaction effects are neglected.

Given a discrete parameter model of the system, the equations of dynamic equilibrium can be stated in matrix form as

$$\mathbf{M}\ddot{\mathbf{X}}_1 + \mathbf{C}\dot{\mathbf{X}}_1 + \mathbf{K}\mathbf{X}_1 = \mathbf{M}\ddot{\mathbf{u}} \tag{2.47}$$

in which $\mathbf{M}$ is the lumped mass matrix, $\mathbf{C}$ the viscous damping matrix, $\mathbf{K}$ the stiffness matrix, $\mathbf{X}_1$ the displacement vector, and $-\mathbf{M}\ddot{\mathbf{u}}$ the inertial force vector. The dots denote differentiation with respect to time. Recalling that in the PDT the system's developed restoring force is measured experimentally during each step of the on-line numerical procedure, the last term on the left side in Eq.(2.47) is replaced by the measured, developed static restoring forces, $\mathbf{F}$, in the actuators during the test. Therefore the equations of motion for the system under seismic excitation take the form;

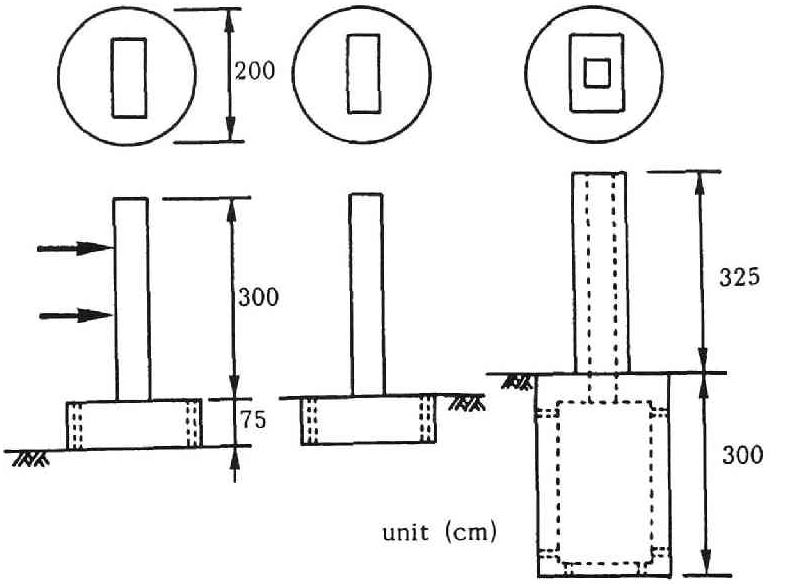

Fig. 2.8 The three foundations used in the hybrid experiment.

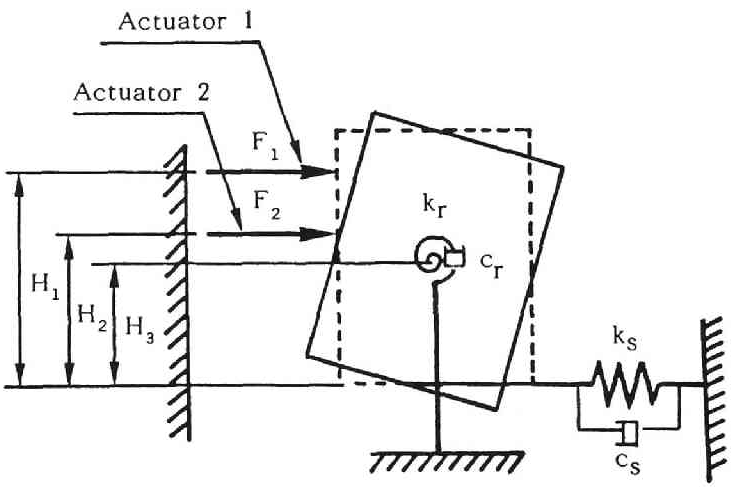

Fig. 2.9 Sway-rocking model for the three foundation.

$$M\ddot{X}_1 + C\dot{X}_1 + F = M\ddot{u} \qquad (2.48)$$

The input motion used is Taft EW, and the peak accelerations are normalized to 180 and 300 gal. The interval is 0.02 sec, and the duration 20 sec (1000 steps). The displacements and reaction forces of two actuators are measured.

(2) Results of identification

The response acceleration, velocity, displacement of sway and rocking motion, and the restoring forces can be used as observation data. As the restoring forces are given, formulation 2 is used. The value of the mass and inertial moment are the same as in the hybrid experiment calculation.

The model to be identified is the surface foundation, and the input acceleration is the Taft 180 gal record (Fig.2.10). Displacement of the spring and the restoring force of sway and rocking are shown in Fig.2.11 (left: sway, right: rocking). The upper part shows the displacement and rotation angle, and the lower part the force and moment. The observed and identified hysteretic loops are shown in Fig.2.12 (upper: observed loops, lower: identified ones). The left part corresponds to the sway motion and the right part to the rocking motion. The identified restoring force amplitude is somewhat underestimated. This is because the additional noise is filtered out by the effect of the covariance matrix of observation noise in the Kalman filter algorithm. This noise may be generated from the actuator. As the actuator gradually moves to the target it checks overshoot. This fluctuation of force or displacement affects noise generation.

The slope of the secant stiffness of the rocking hysteretic loop degrades with time. The changes with time of the unknown parameters, k, c, α, and β of the sway and rocking motions are shown in Fig.2.13. The tangential stiffness, k, of the rocking motion becomes small with time, which also shows the degradation of stiffness.

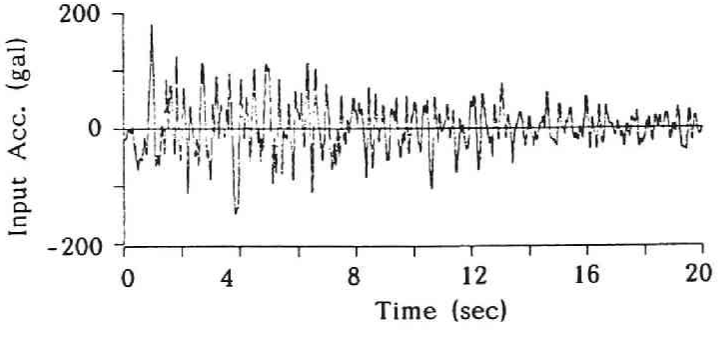

Fig. 2.10 Input ground motion (Taft 180 gal).

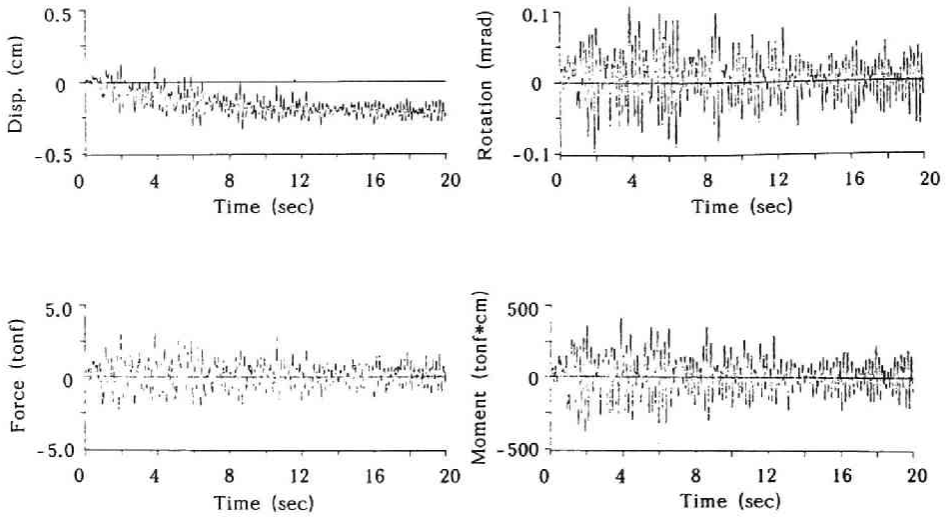

Fig. 2.11 Displacement and restoring force time histories for sway and rocking.

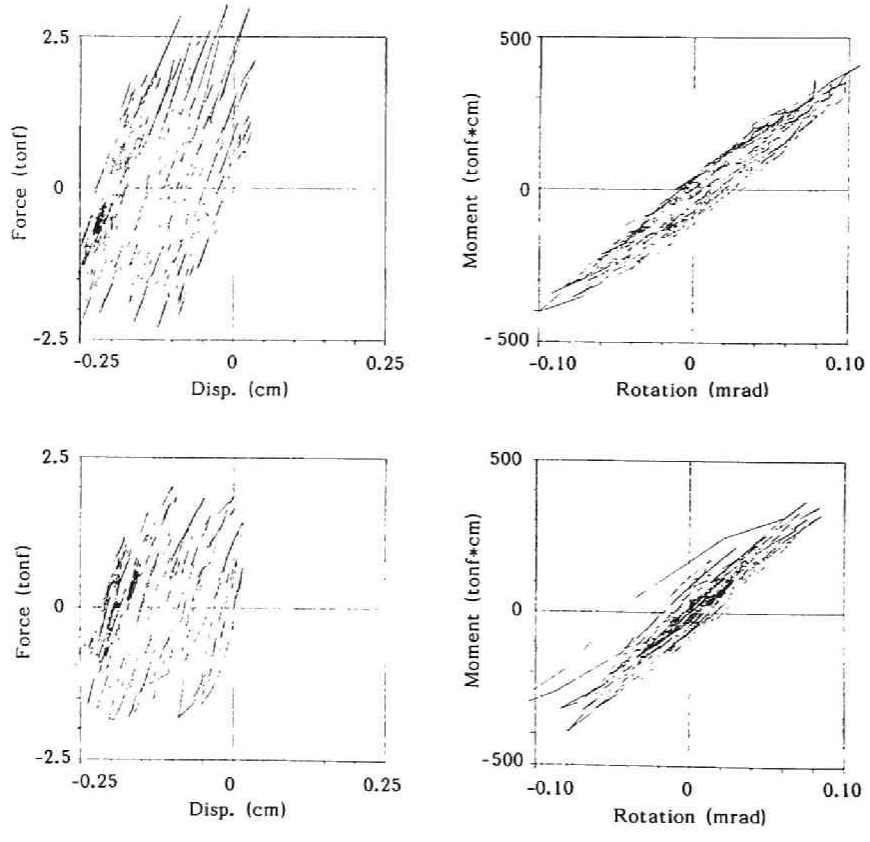

Fig. 2.12 Comparison of observed (upper) and identified (lower) hysteretic loops for the sway (left) and rocking (right) motions.

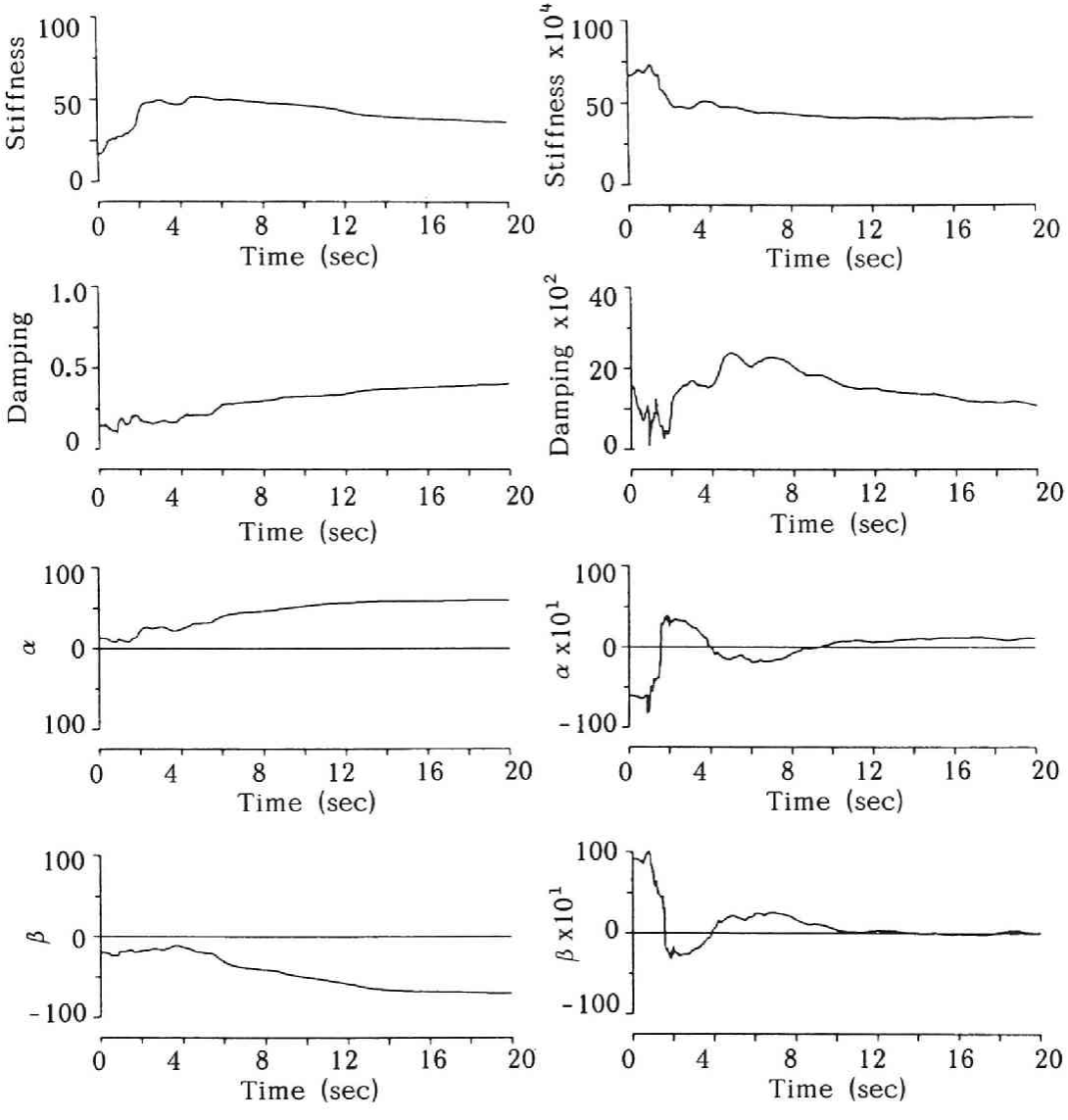

Fig. 2.13 Time histories of the identified model parameters (k, c, α, and β)

2.2.4 Identification of Structural Parameters

A 3-story structural model is shown in Fig.2.14. It is a system with three degrees of freedom, for which displacement or velocity response time histories are assumed to be obtained at each mass. When the structure is represented as a lumped mass model with springs and dashpots, its motion is governed by a differential equation that is the same as Eq.(2.47). **M**, **C**, and **K** are given by

$$\mathbf{M} = \begin{bmatrix} m_1 & 0 & 0 \\ 0 & m_2 & 0 \\ 0 & 0 & m_3 \end{bmatrix} \tag{2.49}$$

$$\mathbf{C} = \begin{bmatrix} c_1+c_2 & -c_2 & 0 \\ -c_2 & c_2+c_3 & -c_3 \\ 0 & -c_3 & c_3 \end{bmatrix} \tag{2.50}$$

$$\mathbf{K} = \begin{bmatrix} k_1+k_2 & -k_2 & 0 \\ -k_2 & k_2+k_3 & -k_3 \\ 0 & -k_3 & k_3 \end{bmatrix} \tag{2.51}$$

The state variables corresponding to Eqs.(2.10) and (2.11) are

$$\mathbf{X} = \{\mathbf{X}_1\ \mathbf{X}_2\ \mathbf{X}_3\ \mathbf{X}_4\}^T \tag{2.52}$$

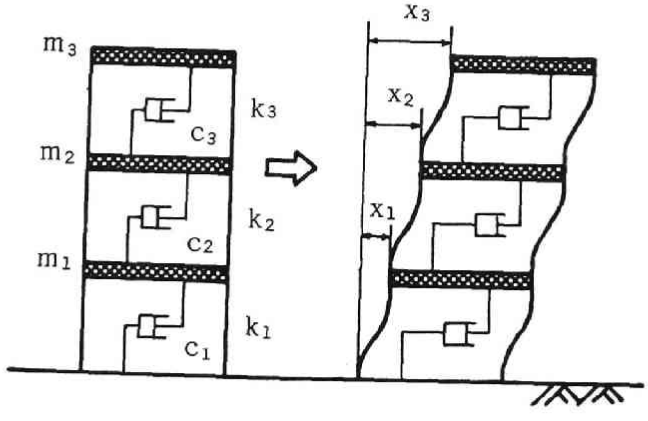

Fig. 2.14 Structural model.

in which

$$\mathbf{X}_1 = \{x_1\ x_2\ x_3\}^T \tag{2.53}$$

$$\mathbf{X}_2 = \{\dot{x}_1\ \dot{x}_2\ \dot{x}_3\}^T \tag{2.54}$$

$$\mathbf{X}_3 = \{k_1/m_1\ k_1/m_2\ k_1/m_3\ k_2/m_2\ k_3/m_3\} \tag{2.55}$$

$$\mathbf{X}_4 = \{c_1/m_1\ c_2/m_2\ c_3/m_3\}^T \tag{2.56}$$

The first differentiation of the state variables, written from Eqs.(2.47) and (2.52), is

$$\dot{\mathbf{X}} = \begin{Bmatrix} \dot{\mathbf{X}}_1 \\ \dot{\mathbf{X}}_2 \\ \dot{\mathbf{X}}_3 \\ \dot{\mathbf{X}}_4 \end{Bmatrix} = \begin{Bmatrix} \mathbf{X}_2 \\ -\mathbf{M}^{-1}\mathbf{C}\mathbf{X}_2 - \mathbf{M}^{-1}\mathbf{K}\mathbf{X}_1 - \ddot{\mathbf{u}} \\ \mathbf{0} \\ \mathbf{0} \end{Bmatrix} \tag{2.57}$$

The structural parameters can now be identified by the method proposed by Hoshiya and Saito [2]. The parameters which must be identified are the stiffness, $\mathbf{X}_3$, and damping, $\mathbf{X}_4$. The value for each mass also is unknown, but the number of variables in the state variable, $\mathbf{X}_4$, can be condensed by use of the relation [2]

$$\frac{c_1}{m_2} = \frac{(c_1/m_1)(k_1/m_2)}{k_1/m_1}, \qquad \frac{c_1}{m_3} = \frac{(c_1/m_1)(k_1/m_3)}{k_1/m_1} \tag{2.58}$$

The continuous differential equation, Eq.(2.57), is rewritten

$$\frac{d\mathbf{X}}{dt} = \mathbf{f} \tag{2.59}$$

By use of the following relation, the continuous equation is discretized, and the state transition matrix [2] mentioned before (Eqs.[2.38] and [2.39]) is obtained;

$$a_{ij} = \frac{\partial f_i}{\partial x_i} \tag{2.60}$$

$$\Phi = \mathbf{I} + \Delta t\ \mathbf{A} + \frac{\Delta t^2}{2!}\mathbf{A}^2 \tag{2.61}$$

in which a_{ij} is the *ij*th-component of matrix A, f_i the component of vector **f**, and Δt the time interval.

Even when ground motion stops after an earthquake, a structure continues to oscillate because of free vibration. Because the right side of Eq.(2.47) becomes zero during free vibration, the equation of motion is

$$\mathbf{M}\ddot{\mathbf{X}}_1 + \mathbf{C}\dot{\mathbf{X}}_1 + \mathbf{K}\mathbf{X}_1 = 0 \tag{2.62}$$

Therefore, the system parameters are identified by eliminating the input term incorporated in the state variable. The right side of Eq.(2.57) is replaced by

$$\begin{Bmatrix} \mathbf{X}_2 \\ -\mathbf{M}^{-1}\mathbf{C}\mathbf{X}_2 \quad \mathbf{M}^{-1}\mathbf{K}\mathbf{X}_1 \\ 0 \\ 0 \end{Bmatrix} \tag{2.63}$$

The components of the observation matrix vary depending on the type of record selected. Displacement or velocity records are used as observation data. Displacement records were selected, for which the observation matrix is

$$\mathbf{H} = \begin{bmatrix} 1 & 0 & 0 & 0 \cdots 0 \\ 0 & 1 & 0 & 0 \cdots 0 \\ 0 & 0 & 1 & 0 \cdots 0 \end{bmatrix} \tag{2.64}$$

Table 2.4 Structural model parameters

	mass 1	mass 2	mass 3
mass: mi (tonf)	10	10	10
damping coeff.: s_i (tf*sec/m)	40	40	30
spring const.: k_i (tf/m)	3000	2000	1000

In solving for the unknown parameters included in the state variables, a weighted global iteration procedure [2] is used to obtain a stable solution regardless of the initial conditions. This procedure accelerates the convergence speed by multiplying the estimated error covariance with weight and renews the initial condition with global iteration. To decide the number of global iterations the process of convergence was investigated. The model is the same as in Fig.2.14. Its structural parameters are given in Table 2.4. The input time history is shown in Fig.2.15.

The input motion is simulated by multiplying the white noise by an evolutionary function. The response time histories for each story are shown in Fig.2.16 (a), (b), (c). In order to use as observed time histories of structural responses, these waves are combined with white noise of the intensity of 5% of the mean square value of the response wave observed at the first story. The input motion is identified by regarding the calculated displacement responses with noise to be observed records. The process of convergence k_i/m_i (i=1,2,3) was checked to confirm the stability of the solution. These parameters are identified for the two seconds from 12 to 10 sec time history of response. This process, given in Fig.2.17, shows that a stable solution is obtained in a few global iterations. The parameters do not, however, converge to the exact value. This is because convergence is affected by the beginning time of filtration, the filtering period, and the ratio of the signal to the noise level. In this case, the upper story has a smaller response noise ratio. The weight W=20 was used for assuming the number of global iterations to be 4 - 6. The covariance of the observation error, R, was chosen to be between 10^{-6} and 10^{-2}.

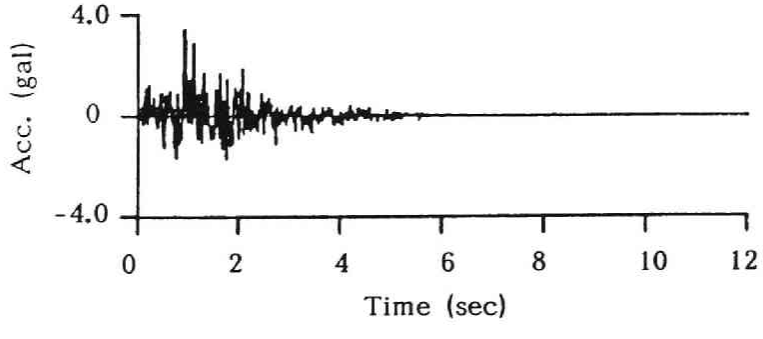

Fig. 2.15 Input ground acceleration.

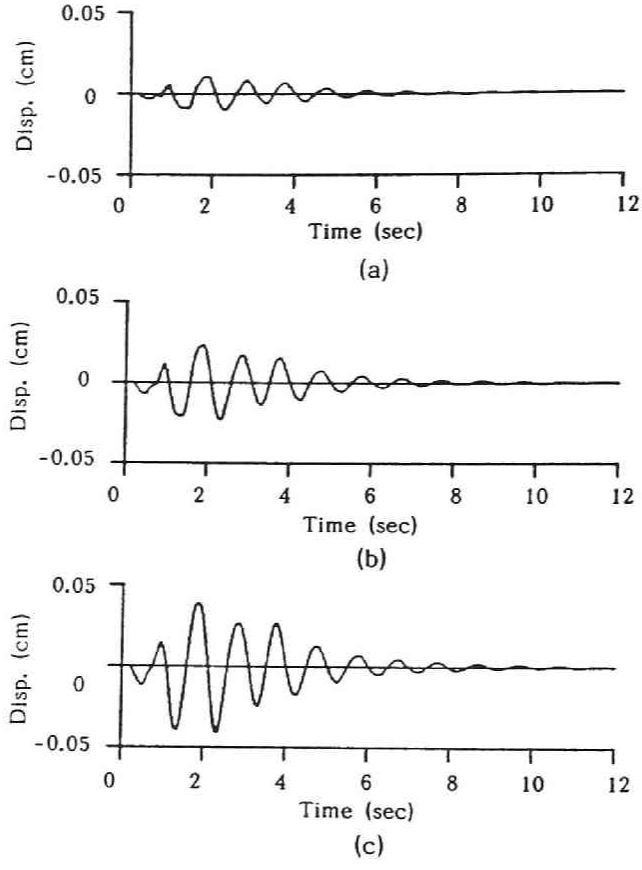

Fig. 2.16 Response displacement at each story of the 3-story structure.

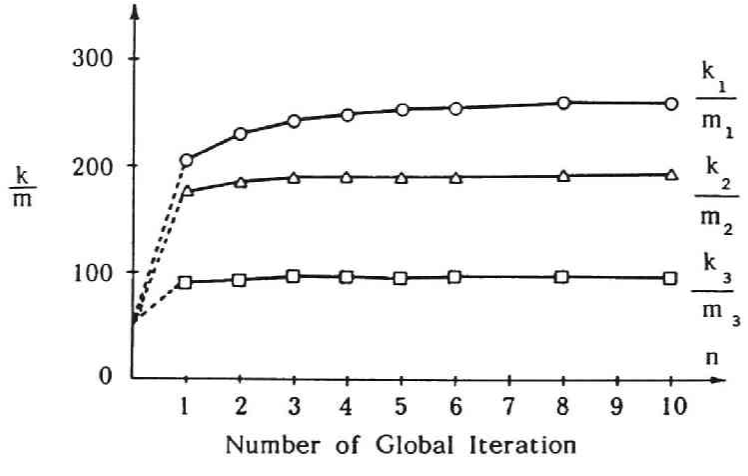

Fig. 2.17 Convergence process of {k/m} for the number of global iterations.

It is difficult to determine the exact time at which input motion becomes zero from the response time history. To surmount this difficulty, the free vibration part of the response time history was used as the input to the Kalman filter and was filtered inversely for the time axis. Fig.2.18 (a), (b) shows the identification obtained by filtering the record for the portion from t_b to t_e, t_b representing the beginning and t_e the end of filtration. In this figure, (a) corresponds to the parameter of stiffness k/m and (b) to the damping c/m. The abscissas are t_e. The line parallel to the t_e axis expresses the exact value. The results are not effected by the choice of the beginning time, t_b. In this case, the time range that gives reliable values for the identified parameters is 12 - 6 sec. Even unknown parameters can be identified from a rough estimate of t_b which represents a response amplitude of close to zero. A filtering period of only a few seconds is sufficient.

The input time history from 12 sec back to zero is shown at the bottom of (a) and (b) in Fig.2.18. In comparison with the upper three identified values, the deviation of the estimated value from the exact one becomes large about the time when the effect of the input motion is included in the response time history.

Because noise information is needed when using the Kalman filter, the value of the noise covariance must be estimated in advance. The accuracy of this identification was examined by using the initial value that coincides with the exact value (Fig.2.19). The parameter examined is damping, c_1/m_1. In this case, the identified results do not deviate from the exact value. Filtering starts from 12 sec and continues inversely on the time axis. The observation error covariance, R, which represents the covariance of noise added to the observation value in Eq.(2.2) or Eq.(2.11), must be very small in the time range in which the effect of the input motion can be ignored. The identified results, however, gradually diverge from the exact value as filtering proceeds. If the value of R is made larger, the identified results again coincide with the exact value. But, even when a large value is assumed for R, the initial value can not be maintained beyond 6 sec. This is because the input motion affects the response time history even if the input amplitude is small. This small amplitude, however, can be buried in the inherent noise. When the amplitude of the input motion is so small as to be negligible, a very small value can be assigned to R. When the inverse filtering time passes 10 sec and the input motion can no longer be ignored, a larger value for R can be chosen and the effect of that motion eliminated. By making the value of R large, the identified values can be kept constant only up to 6 sec without deviation from the initial value. This explains why the identified values become unreliable after 6 sec (Fig.2.18).

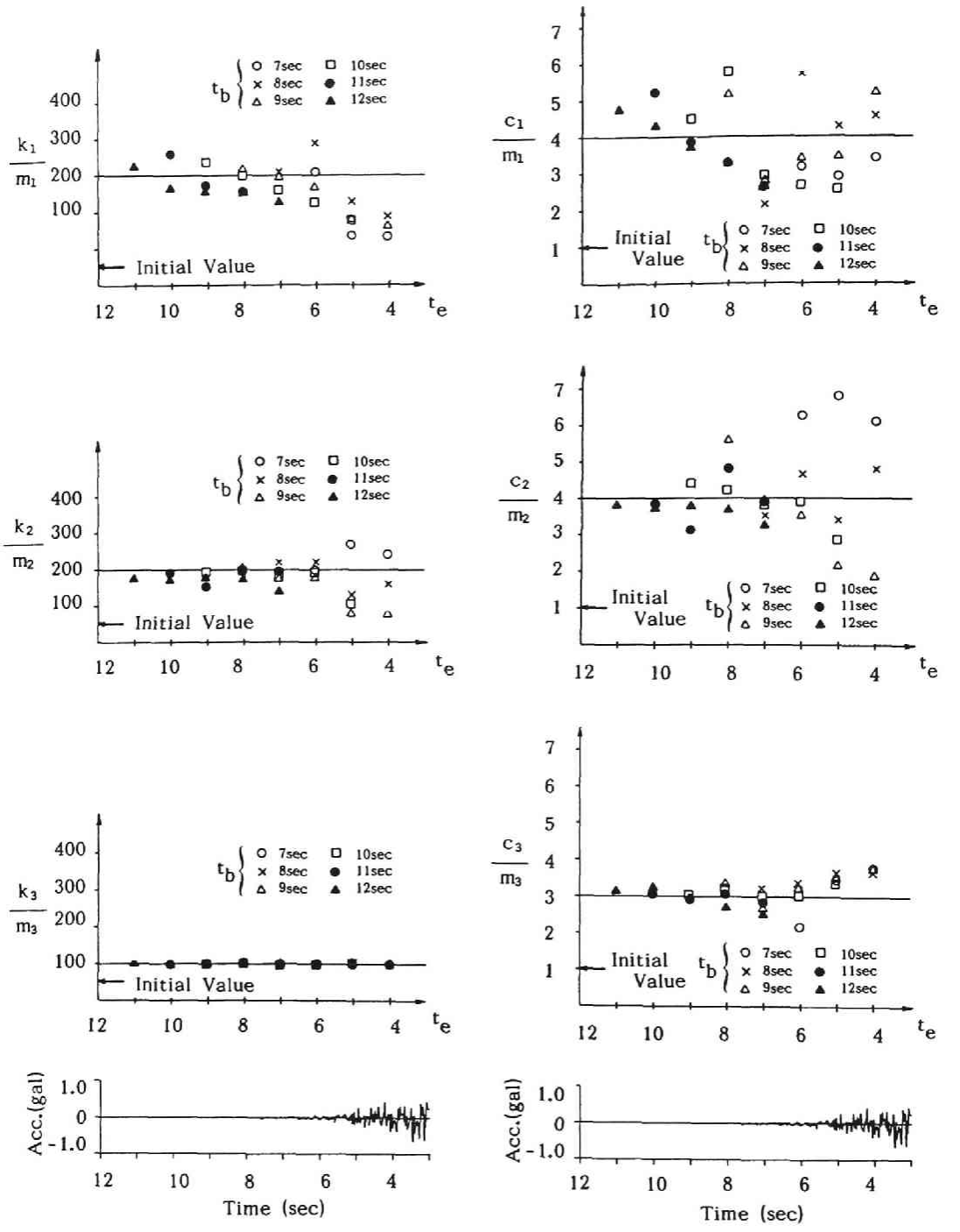

(a) Stiffness (b) Damping

Fig. 2.18 Relation between the identified results and t_b, t_e.

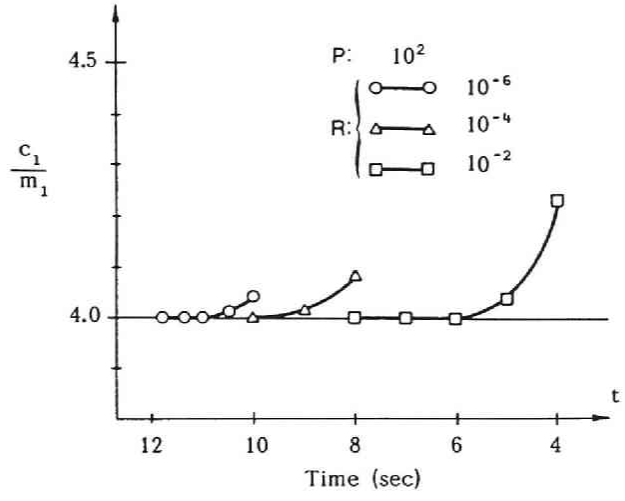

Fig. 2.19 Transition of the identification results for various observation error covariances, Rs.

2.3 Estimation of Input Ground Motion

2.3.1 Equation for the Error Filter

Once the structural parameters have been identified from the response alone, the input time history can be calculated by using both the identified parameters and responses [17].

Consider the system

$$\dot{\mathbf{X}}(t) = \mathbf{A}\mathbf{X}(t) + \mathbf{u}(t) \tag{2.65}$$

$$\mathbf{y}(t) = \mathbf{H}\mathbf{X}(t) + \mathbf{v}(t) \tag{2.66}$$

Assuming that $\mathbf{X}(t)$ and $\mathbf{u}(t)$ are step functions, multiplying Eq.(2.65) by e^{-At} gives

$$\mathbf{X}_t = \Phi_{t|t-1}\mathbf{X}_{t-1} + \mathbf{h}_{t-1} \tag{2.67}$$

$$\mathbf{Y}_t = \mathbf{H}_t\mathbf{X}_t + \mathbf{V}_t \tag{2.68}$$

$\mathbf{h}_t$ in Eq.(2.67) is given by

$$\mathbf{h}_{t-1} = \int_{t-\Delta t}^{t} \Phi(t,\tau)\, \mathbf{u}(\tau)\, d\tau \tag{2.69}$$

As u(t) is the step function, the numerical integration of Eq.(2.69) becomes

$$\mathbf{h}_{t-1} = \Phi\, \mathbf{u}\, \Delta t \tag{2.70}$$

Eq.(2.67) is rewritten

$$\mathbf{h}_{t-1} = \mathbf{X}_t - \Phi_{t|t-1}\mathbf{X}_{t-1} \tag{2.71}$$

Because the exact value of $\mathbf{X}_t$ is unknown, $\mathbf{X}_t$ and $\Phi_{t|t-1}\mathbf{X}_t$ are replaced with $\mathbf{X}(t|t)$ and $\mathbf{X}(t|t-1)$ in Fig. 2.2. Eq.(2.71) is rewritten

$$\mathbf{h}_{t-1} = \mathbf{X}(t|t) \quad \mathbf{X}(t|t-1) \tag{2.72}$$

The input motion, u(t), is obtained by substituting Eq.(2.72) in Eq.(2.70).

$$\mathbf{u} = \frac{1}{\Delta t}\Phi^{-1}\{\mathbf{X}(t|t) \quad \mathbf{X}(t|t-1)\} \tag{2.73}$$

2.3.2 Method of Analysis and Results

The equation of motion for the model shown in Fig.2.14 is represented by Eq.(2.47). The matrices **M**, **C**, and **K** are given by Eqs.(2.49), (2.50) and (2.51). Rewriting the upper two rows of Eq.(2.57), the state equation becomes

$$\begin{Bmatrix} \dot{\mathbf{X}}_1 \\ \dot{\mathbf{X}}_2 \end{Bmatrix} = \begin{bmatrix} 0 & \mathbf{I} \\ -\mathbf{M}^{-1}\mathbf{K} & -\mathbf{M}^{-1}\mathbf{C} \end{bmatrix} \begin{Bmatrix} \mathbf{X}_1 \\ \mathbf{X}_2 \end{Bmatrix} + \begin{Bmatrix} 0 \\ -\ddot{\mathbf{u}} \end{Bmatrix} \tag{2.74}$$

In section **2.2**, the input term $-\ddot{\mathbf{u}}$ is incorporated in the state transition matrix with the unknown parameter. Here the independent term has been set up as the input term. The observation equation is given by

$$\mathbf{Y} = \mathbf{H} \begin{Bmatrix} \mathbf{X}_1 \\ \mathbf{X}_2 \end{Bmatrix} + \mathbf{V} \tag{2.75}$$

If the equation of motion is expressed as Eq.(2.71) and calculations are done with the Kalman filter algorithm shown in Fig.2.2, the input motion is obtained from Eq.(2.73).

The structural parameters used to estimate the input motion are given in Table 2.5, the exact values being in the bottom row. The parameters in cases 1 and 2 are the identified results obtained by use of the response time history shown in Fig.2.16. Case 1 corresponds to results obtained by filtering the record from 12 to 10 sec, and case 2 by filtering it from 10 to 8 sec. The maximum error for the identified parameters is about 10%. The input motions estimated with these parameters are shown in Fig.2.20, the similarity of the waveforms is such that individual waves can not be distinguished at a glance. Comparisons of the times corresponding to peak acceleration, the shapes of the waveforms, and the duration of each wave shows that any differences present are negligible.

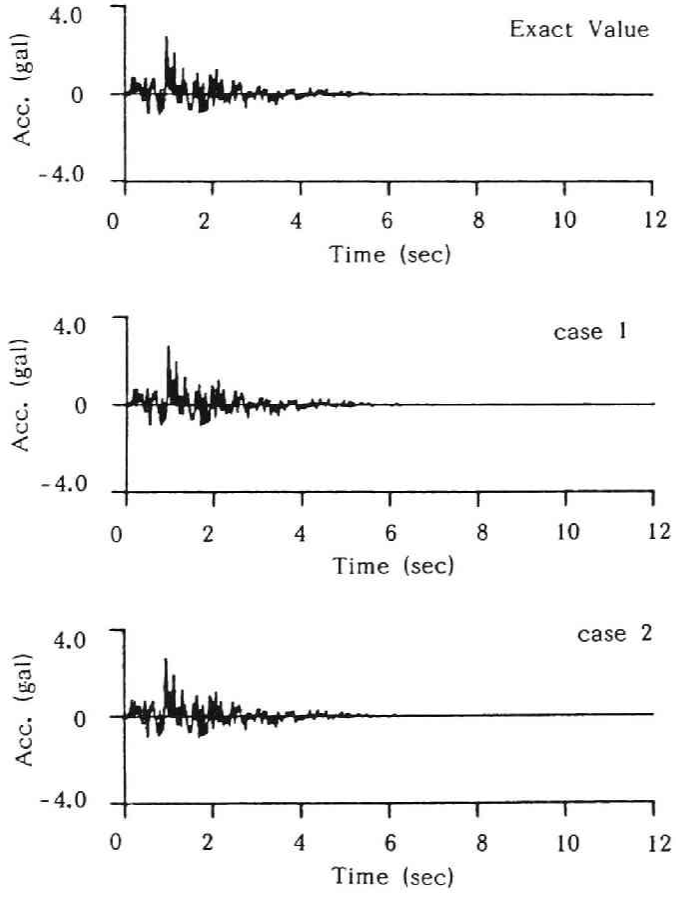

Fig. 2.20 Estimated input motions.

Table 2.5 Structural parameters used to estimate input motion

	k_1/m_1	k_1/m_2	k_1/m_3	k_2/m_2	k_3/m_3	c_1/m_1	c_2/m_2	c_3/m_3
case 1 (12-10s)	257.	287.	339.	174.	99.	3.75	3.78	3.11
case 1 (10-8s)	306.	284.	298.	191.	98.	5.82	4.18	3.40
Exact Value	300.	300.	300.	200.	100.	4.00	4.00	3.00

Table 2.6 Identified structural parameters

	k_1/m_1	k_1/m_2	k_1/m_3	k_2/m_2	k_3/m_3	c_1/m_1	c_2/m_2	c_3/m_3
El Centro (60-55s)	270.	311.	308.	200.	99.	3.97	3.99	3.03
Taft (60-55s)	264.	305.	307.	199.	100.	3.55	4.01	3.01

The El Centro (1941) and Taft (1952) records were used as input accelerations in the model shown in Fig.2.14. The structural parameters were identified and the input motion estimated from the obtained responses alone. The structural parameters identified are shown in Table 2.6. The input motion was estimated using these parameters. The input accelerogram of the El Centro record and its Fourier spectrum are shown in Fig.2.21 (a), (b). The response at each mass is shown in Fig.2.22 (a), (b), (c). The accelerogram and Fourier spectrum of the Taft record correspond to Fig.2.23 (a), (b) and the responses to Fig.2.24 (a), (b), (c).

The estimated input motions and Fourier spectra are given in Figs.2.25 and 2.26. Structural parameters were identified for 5 seconds; from 60 to 55 sec. A comparison with the original time histories shows that the results are in good agreement for the evolution of the waveform, the time corresponding to the peak acceleration, and the duration. But, beyond 10 Hz, high frequency spectral components show deviation. The explanation for this is that the noise contained in the response signal is assumed to be Gaussian white noise, and its spectral level is flat. The Kalman filter eliminates noise from the contaminated signal in the time domain. If the white noise component in the spectrum is reduced logarithmically, the relatively small amplitude component (beyond 10 Hz in Figs.2.25 and 2.26) must decrease markedly.

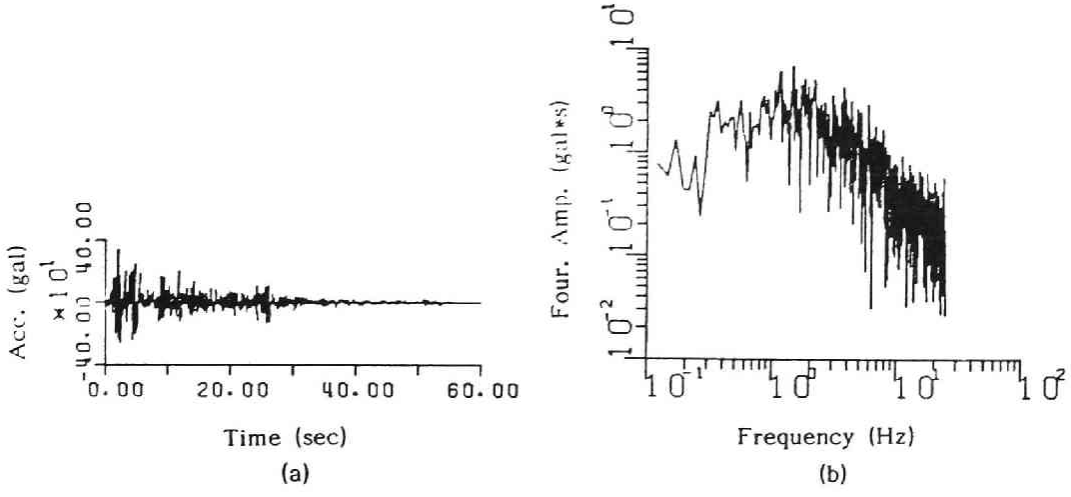

Fig. 2.21 The input accelerogram and its Fourier spectrum. (El Centro)

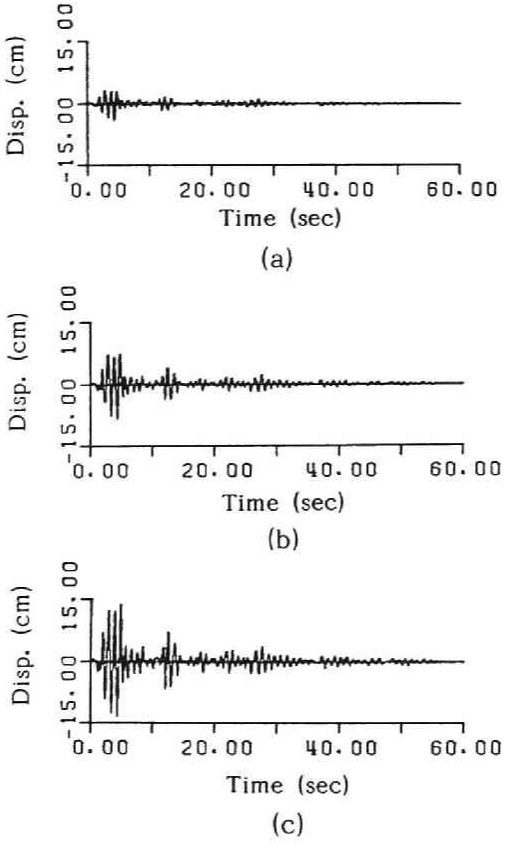

Fig. 2.22 Response displacement at each mass. (El Centro)

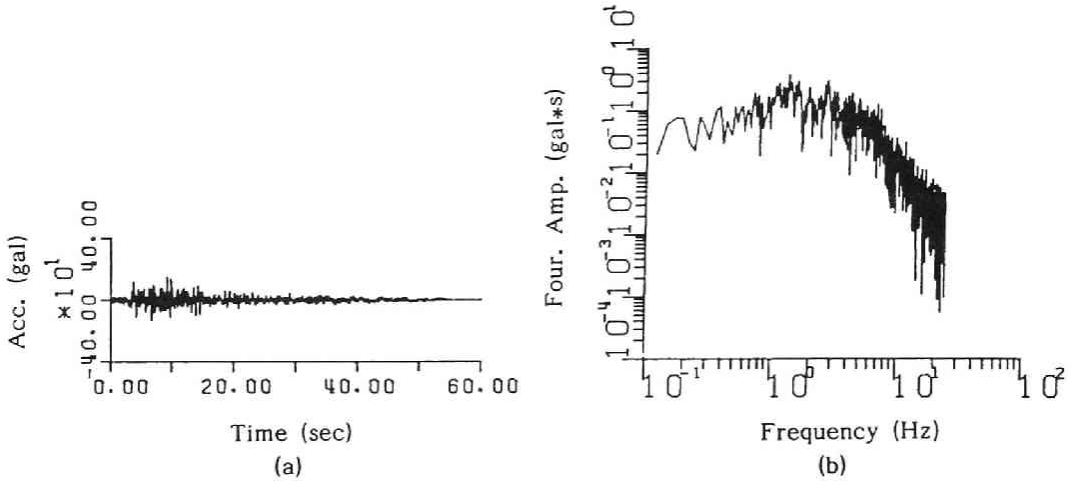

Fig. 2.23 The input accelerogram and its Fourier spectrum. (Taft)

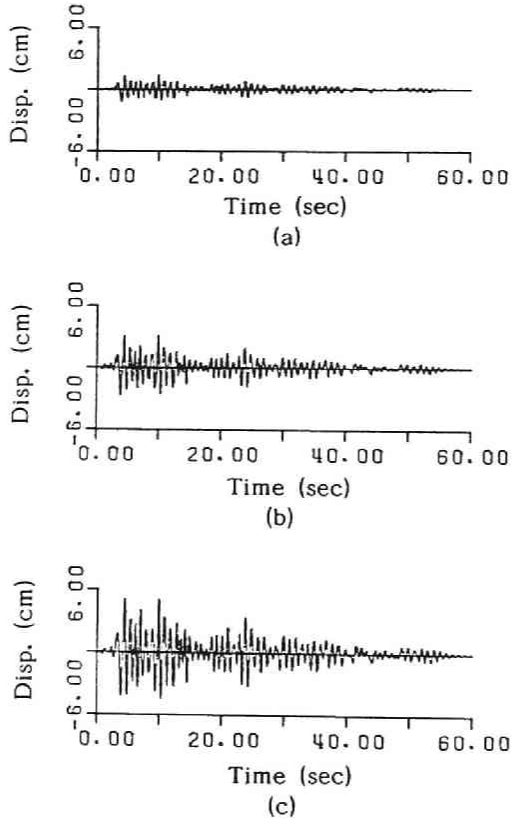

Fig. 2.24 Response displacement at each mass. (Taft)

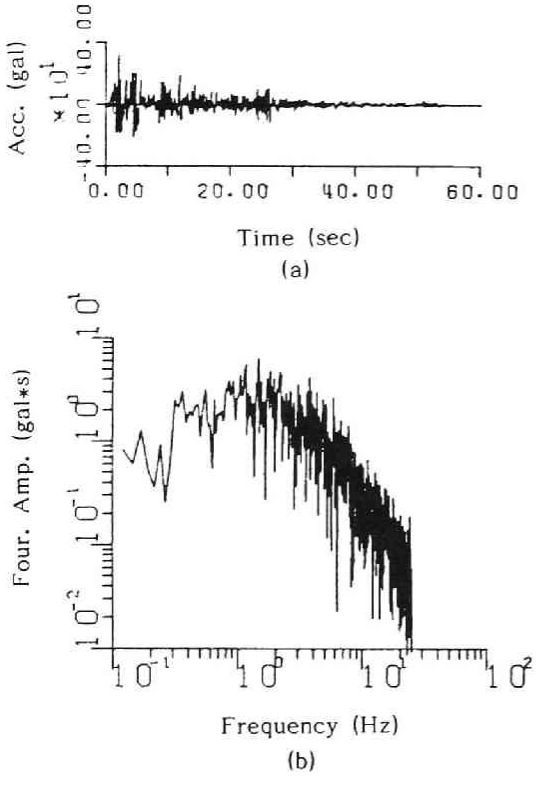

Fig. 2.25 The estimated input motion and its Fourier spectrum. (El Centro)

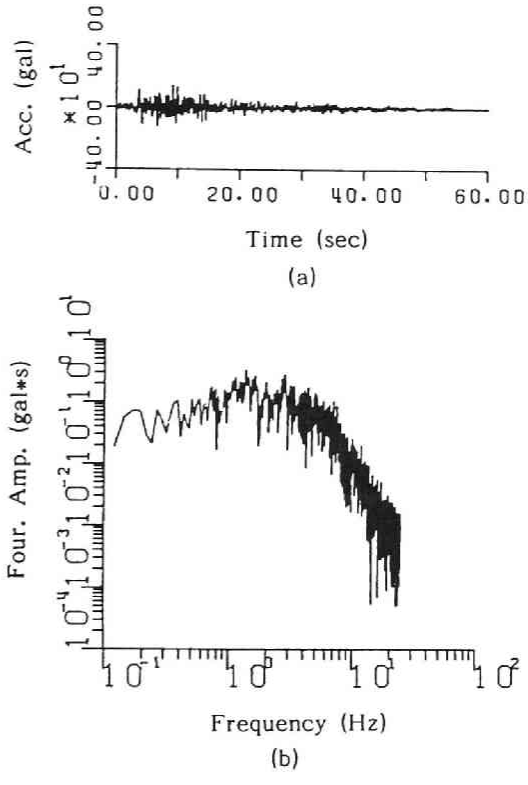

Fig. 2.26 The estimated input motion and its Fourier spectrum. (Taft)

The peak acceleration values and corresponding times for the original and estimated waves are given in Table 2.7 for the El Centro and Taft records. The differences in peak accelerations are 4% (El Centro) and 5% (Taft) of the values for the original waves; unremarkable differences. Although peak acceleration is somewhat underestimated, the corresponding times for acceleration coincide. The decrease in the high frequency component therefore has very little effect on the identification of the input motion.

Table 2.7 Peak accelerations and the times corresponding to the original and estimated waves

		Recorded Motion	Estimated Accelerogram
El Centro	Peak Acc. (gal)	341.7	328.1
	Time of Occurrence (sec)	2.41	2.41
Taft	Peak Acc. (gal)	152.7	145.3
	Time of Occurrence (sec)	9.12	9.12

2.3.3 Extension to a Multi-input System

When a structure extends a long distance, the system experiences different motion at each point during an earthquake. Estimation of multi-input motions therefore is of great importance to the seismic safety evaluation of lifelines. In this section, a multi-input system is formulated and the input motions identified. The possibility of identification is investigated for two cases; one in which the output waves are observed at all the points of the discrete system, and one in which they are observed at selected points.

The lifeline structural model that expresses the soil-structure system is shown in Fig.2.27. The discretized mass of the structural system is m_j (j=1,..., n), the damping coefficient, c_j, and the spring constant k_j. The mass receives the ground motion, z_j, through the linear spring, s_j, and dashpot, d_j [18]. The equation of motion about the mass, m_j, is

$$m_j\ddot{u}_j + c_{j-1}(\dot{u}_j-\dot{u}_{j-1}) - c_j(\dot{u}_{j+1}-\dot{u}_j) + k_{j-1}(u_j-u_{j-1}) - k_j(u_{j+1}-u_j) + s_j(u_j-z_j) + d_j(\dot{u}_j-\dot{z}_j) = 0 \qquad (2.76)$$

The equation is rewritten in matrix form as

$$\mathbf{M\ddot{u}} + \mathbf{C\dot{u}} + \mathbf{Ku} - \mathbf{D\dot{z}} - \mathbf{Sz} = \{0\} \qquad (2.77)$$

in which **M** is the diagonal mass matrix; **C** the band matrix composed of c_j and d_j; **K** the band matrix composed of k_j and s_j; and **D**, **S** the diagonal matrix composed of d_j and s_j.

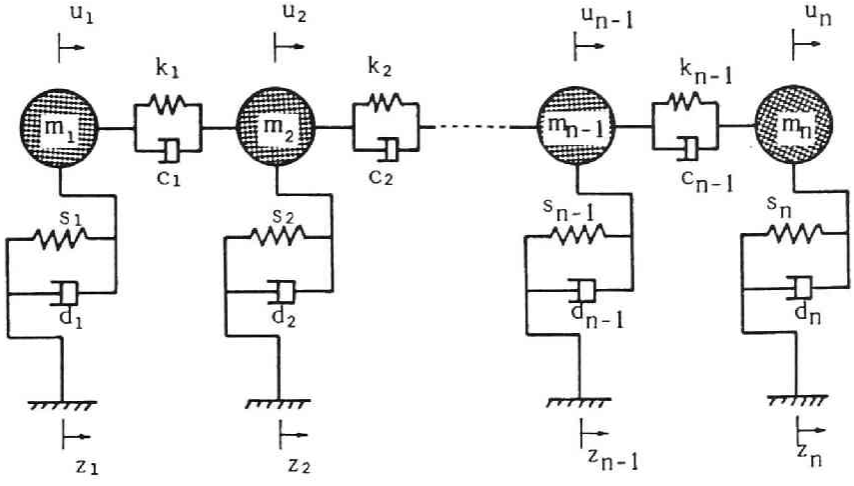

Fig. 2.27 Model of the multi-input system.

Assuming that the displacement u_j (j=1,..., n) expresses a response when z_j acts on the system statically, the following equation is obtained from Eq.(2.77).

$$\mathbf{K}\bar{\mathbf{u}} - \mathbf{S}\mathbf{z} = \{0\} \tag{2.78}$$

From the above definition of $\bar{\mathbf{u}}$, $\mathbf{u}(t)$ is

$$\mathbf{u}(t) = \bar{\mathbf{u}} + \mathbf{y}(t) \tag{2.79}$$

in which $\mathbf{y}(t)$ is the relative displacement of each mass to the input point. By substituting Eq.(2.79) in (2.77) and using the relation of Eq.(2.78), Eq.(2.77) becomes

$$\mathbf{M}\ddot{\bar{\mathbf{u}}} + \mathbf{M}\ddot{\mathbf{y}} + \mathbf{C}\dot{\bar{\mathbf{u}}} + \mathbf{C}\dot{\mathbf{y}} + \mathbf{K}\mathbf{y} = \mathbf{D}\dot{\mathbf{z}} \tag{2.80}$$

From Eq.(2.78)

$$\bar{\mathbf{u}} = \mathbf{K}^{-1}\mathbf{S}\mathbf{z} \tag{2.81}$$

Substituting Eq.(2.81) in Eq.(2.80), the equation of motion is

$$\mathbf{M}\ddot{\mathbf{y}} + \mathbf{C}\dot{\mathbf{y}} + \mathbf{K}\mathbf{y} = -\mathbf{M}\mathbf{K}^{-1}\mathbf{S}\ddot{\mathbf{z}} + \left\{\mathbf{D}-\mathbf{C}\mathbf{K}^{-1}\mathbf{S}\right\}\dot{\mathbf{z}} \tag{2.82}$$

If the system has the same input motion at the fixed bases, the matrices product, $\mathbf{K}^{-1}\mathbf{S}$, becomes unit **I**. Assuming the second term of right side in Eq.(2.28) to be negligible, the equation is rewritten

$$\mathbf{M}\ddot{\mathbf{y}} + \mathbf{C}\dot{\mathbf{y}} + \mathbf{K}\mathbf{y} = -\mathbf{M}\{1\}\ddot{z}_0 \tag{2.83}$$

This corresponds to the well-known equation that describes relative displacement. From the above equations, the system responses can be calculated even if the input motion differs at each point. A comparison of Eqs.(2.77) and (2.82) shows that Eq.(2.77) is the equation for the displacement and velocity inputs, and Eq.(2.82) the equation for the velocity and acceleration inputs. An alternative equation therefore must be chosen in order to estimate input motion. In this section, Eq.(2.82) which is based on the relative displacement to the soil $\mathbf{y}$ and $\dot{\mathbf{y}}$, is amended

$$\begin{Bmatrix}\mathbf{y}\\ \dot{\mathbf{y}}\end{Bmatrix} = \begin{Bmatrix}\mathbf{X}_1\\ \mathbf{X}_2\end{Bmatrix} = \mathbf{X} \tag{2.84}$$

Eq.(2.82) thus becomes

$$\begin{Bmatrix}\dot{\mathbf{X}}_1\\ \dot{\mathbf{X}}_2\end{Bmatrix} = \begin{bmatrix} 0 & \mathbf{I} \\ -\mathbf{M}^{-1}\mathbf{K} & -\mathbf{M}^{-1}\mathbf{C}\end{bmatrix}\begin{Bmatrix}\mathbf{X}_1\\ \mathbf{X}_2\end{Bmatrix} + \begin{Bmatrix}0\\ -\mathbf{K}^{-1}\mathbf{S}\ddot{\mathbf{z}}+\mathbf{M}^{-1}\left\{\mathbf{D}-\mathbf{C}\mathbf{K}^{-1}\mathbf{S}\right\}\dot{\mathbf{z}}\end{Bmatrix} \tag{2.85}$$

The second term is replaced with

$$\mathbf{f} = \begin{Bmatrix}0\\ -\mathbf{K}^{-1}\mathbf{S}\ddot{\mathbf{z}}+\mathbf{M}^{-1}\left\{\mathbf{D}-\mathbf{C}\mathbf{K}^{-1}\mathbf{S}\right\}\dot{\mathbf{z}}\end{Bmatrix} \tag{2.86}$$

Consequently, **f** in Eq.(2.86) is estimated as the input motion for the object system. The input acceleration is calculated by integrating Eq.(2.86) by the linear acceleration method.

The input ground motions for the multi-input system are estimated from the formulation. The model is a four-degrees-of-freedom one which corresponds to the case of n=4 in Fig.2.27. The model parameters are shown in Table 2.8.

Table 2.8 Model parameters for the four-degrees-of-freedom system

	mass 1	mass 2	mass 3	mass 4
mass: m_i ($tf*sec^2/m$)	6.0	4.0	8.0	10.0
Damping: d_i ($tf*sec/m$)	4.0	2.0	4.0	6.0
Spring: s_i (tf/m)	4000	2000	4000	6000

Damping: c_j ($tf*sec/m$)	3.0	3.0	3.0
Spring: k_j (tf/m)	2000	2000	2000
Span: L_j (m)	100	100	100

(1) Input ground motions

Input ground motions to the multi-input system are simulated by taking into account the phase delay and dispersion characteristics of the propagation wave (see Chapter 4) for the observed strong motion. A wave propagating from point A to point B, for which the distance is L, is considered. Using the Fourier transform of the accelerogram at point A, the amplitude and phase of the wave at the frequency f_k are a_{kA} and ϕ_{kA}. As the velocity of the dispersed wave, $v(f_k)$, depends on the frequency, the propagation time, $T(f_k)$, from the point A to B, is $L/v(f_k)$. The phase delay at point B, ϕ_{kB}, is $2\pi f_k T(f_k)$, and the amplitude, a_{kB}, is equal to a_{kA} if the damping caused by wave propagation is assumed to be negligible. Therefore the accelerogram at point B is obtained by the use of the inverse Fourier transform.

In this section, multi-input motions are synthesized by changing the phase of the strong motion recorded at El Centro during the 1940 Imperial Valley earthquake (Fig.2.28). The wave propagates from point 1 to 4. The dispersion curve of this wave is shown in Fig.2.29. The time history of the input acceleration of mass 1 is shown in Fig.2.30 (a). The accelerograms calculated at masses 2, 3, and 4 are shown in Fig.2.30 (b), (c), (d). As velocitigrams also are necessary for the identification, the accelerograms in Fig.2.30 are integrated in the frequency domain. The calculated response displacements of the four-degrees-of-freedom system are shown in Fig.2.31 (a), (b), (c) and (d).

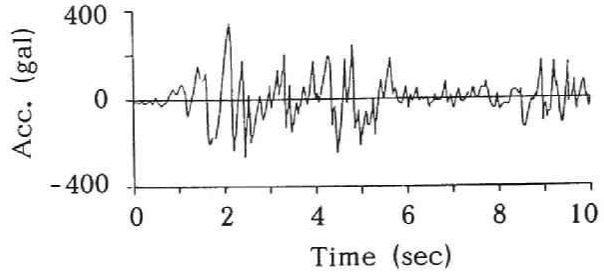

Fig. 2.28 Input motion. (El Centro)

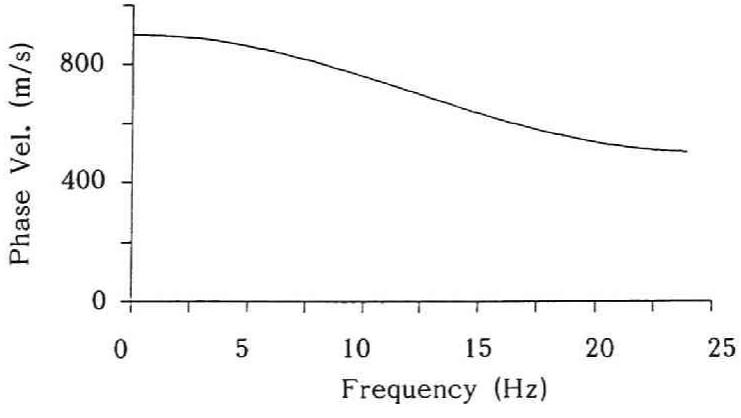

Fig. 2.29 Assumed dispersion curve.

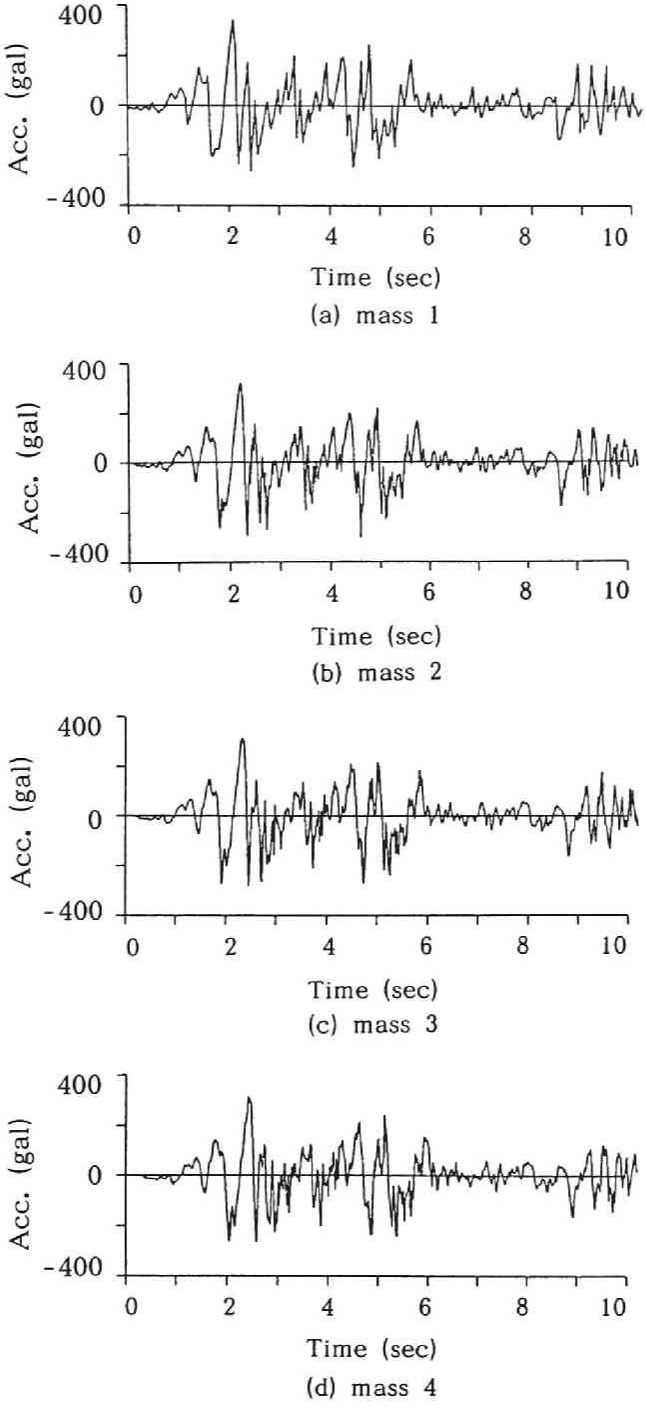

Fig. 2.30 Input accelerations for the four-degrees-of-freedom, multi-input system.

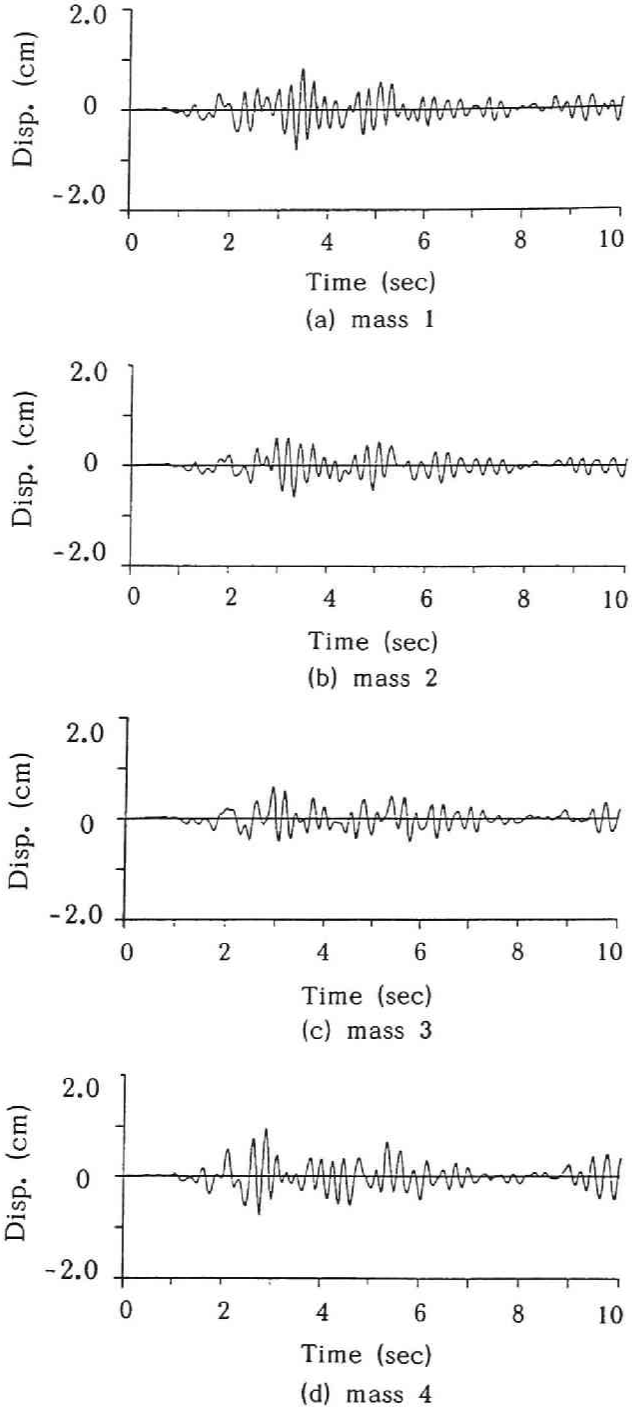

Fig. 2.31 Response displacements for the four-degrees-of-freedom, multi-input system.

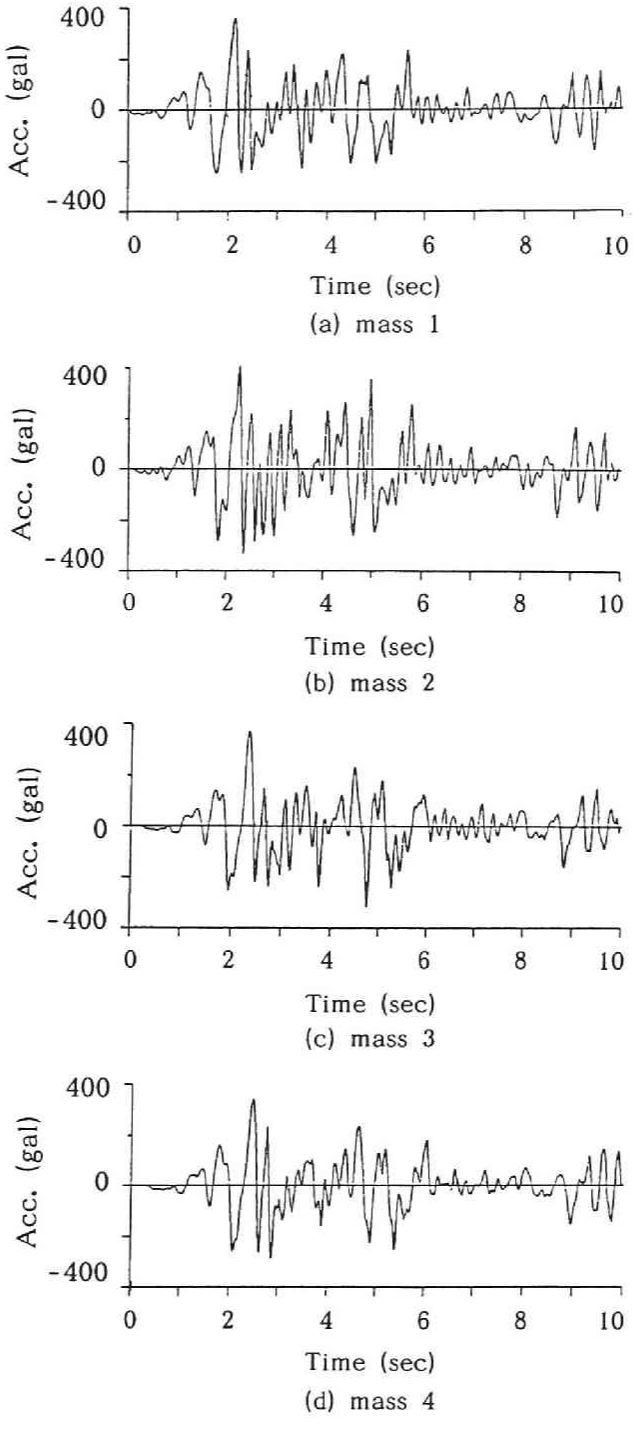

Fig. 2.32 Identified input accelerations.

(2) Estimation of input motion (responses observed at all mass points)

The response displacements observed at all the masses are used to estimate the input motion inversely. The observation equation is

$$\mathbf{Y} = \begin{bmatrix} 1 & 0 & 0 & 0 & 0 \cdots 0 \\ 0 & 1 & 0 & 0 & 0 \cdots 0 \\ 0 & 0 & 1 & 0 & 0 \cdots 0 \\ 0 & 0 & 0 & 1 & 0 \cdots 0 \end{bmatrix} \mathbf{X} + \mathbf{R} \tag{2.87}$$

The state equation is Eq.(2.85). The respective initial values of the error covariance matrix, p**I**; the system noise, q; and the observation noise, r, are 100, 1.0×10^{3}, and 1.0×10^{-5} *a priori* . The estimated quantity is **f** in Eq.(2.86); but, the input motion vector, **z**, is calculated by solving the differential equation, Eq.(2.86). The estimated accelerations are shown in Fig.2.32, and the Fourier spectra of the accelerograms of mass 1 in Fig.2.33, (a) being the spectrum of the exact input motion and (b) that of the estimated one. High-frequency components above 5 6 Hz are eliminated as observation and system noises. This information is given *a priori* . As the degree of freedom increases, it is more difficult to assess the system and the observation noise. But the time of occurrence of the peak acceleration and the phase aspects are in good agreement with those of the original waves. Even if p, q, and r are arbitrarily chosen, the estimated waves are almost same. These parameters therefore do not affect the estimated results.

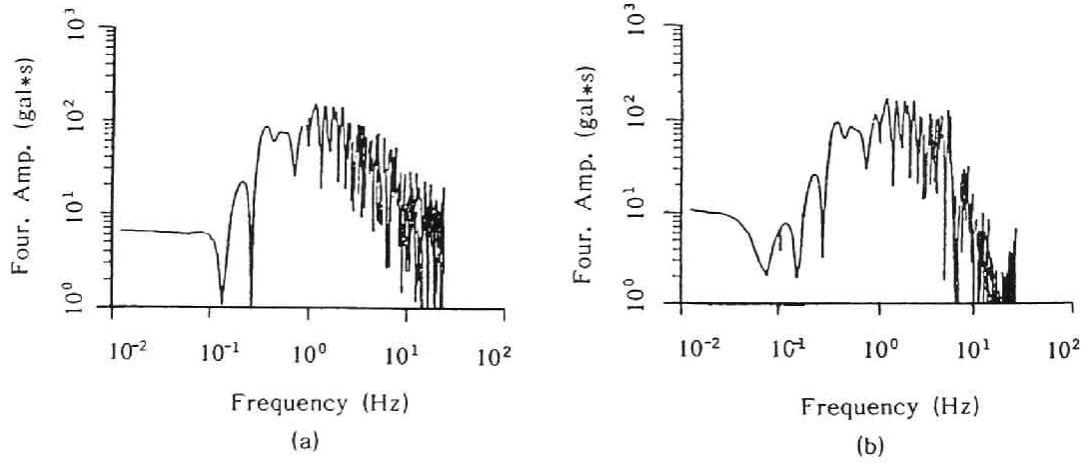

Fig. 2.33 Fourier spectra of the accelerograms of mass 1.
(a) exact input motion, (b) estimated input motion

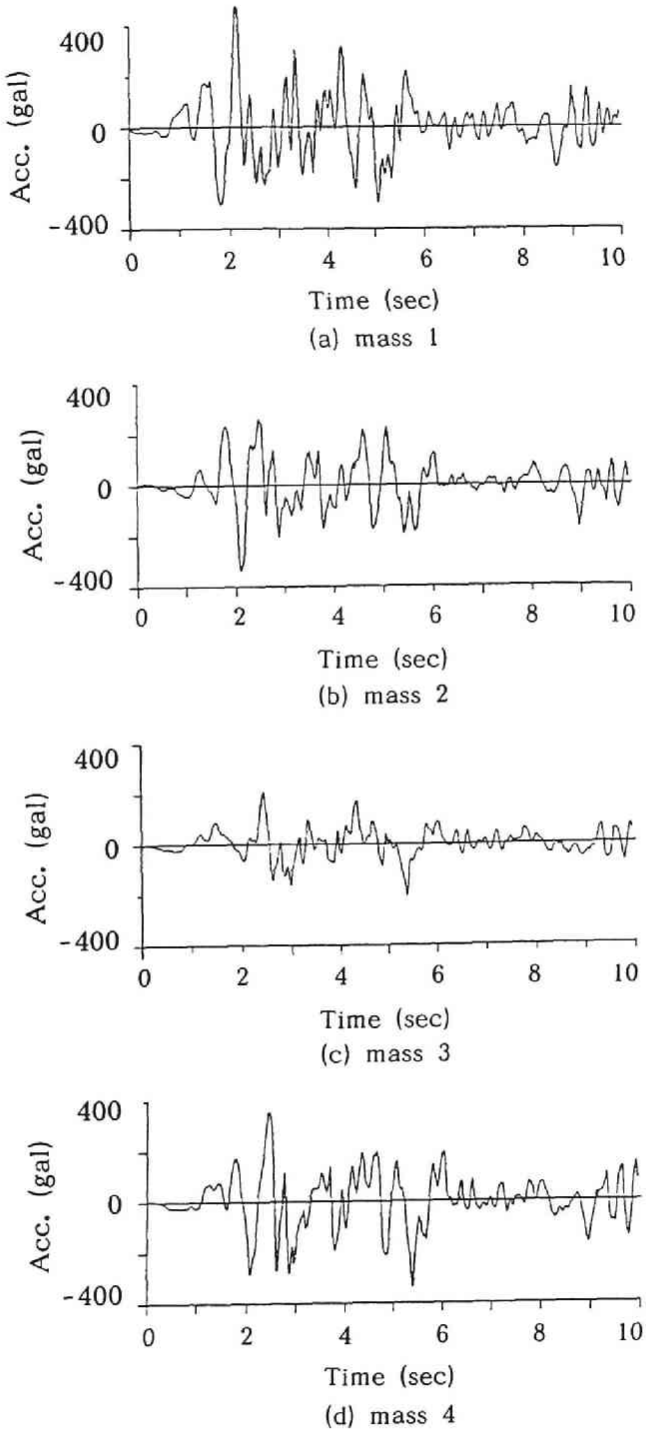

Fig. 2.34 Identified input accelerations.

(3) Estimation of input motion (responses observed at selected mass points)

The responses at masses 2 and 3 are unknown. In this case, the observation equation, Eq.(2.87), can not be used as is. A new observation equation is written using the response displacement of masses 1 and 4;

$$\mathbf{Y} = \begin{bmatrix} 1 & 0 & 0 & 0 & 0 \cdots 0 \\ 0 & 0 & 0 & 1 & 0 \cdots 0 \end{bmatrix} \mathbf{X} + \mathbf{R} \tag{2.88}$$

The estimated input motions from Eqs.(2.85) and (2.88) are shown in Fig.2.34. The initial values of the parameters p_0, q, and r are the same as in case (2). The figure shows that the accuracy of the estimated waves at points not observed is not good as compared with the accuracy for points with observation records. This is because the improvement of the state variables is not accurate in the innovation algorithm. The estimation of the input motion at the point at which the response is observed is, however, fairly good even if the number of observations is smaller than the number of degrees of freedom.

2.4 Conclusions

In this chapter, a procedure has been established with which to identify nonlinear structural dynamic characteristics and to estimate input motion. The procedure used and results are as follows:

(1) The EK-WGI method was used to identify the nonlinear restoring force. It was shown to be valid for solving nonlinear identification problems.

(2) Two formulations (formulation 1: an input motion is given, formulation 2: an input motion and the restoring force are given) were developed with which to identify nonlinear systems. The formulation 2 which incorporates restoring forces observed through an experiment gives accurate identification results.

(3) The parameters that control the restoring force are identified by the use of data from a hybrid experiment on soil-structure interaction. The response displacement and restoring force are filtered by the Kalman filter which eliminates the additional noise.

(4) Structural parameters can be identified from the coda part of the response time history alone, without information on the input motion. Truncation of a portion of the coda has a negligible effect on the results.

(5) The free vibration part of the response is filtered after the input motion becomes zero. But, when its amplitude is relatively small, the effect of this motion is eliminated by making

the error covariance, R, larger. Use of the Kalman filter requires *a priori* information about the noise that contaminates the responses. If the noise level can be accurately assessed, this procedure can be put to practical use.

(6) The efficiency of the Kalman error filter for a multi-degree-of-freedom system was investigated in order to estimate the input motion from the structural response and to identify the structural parameters. In this procedure, even when the identified structural parameters deviate by about 10%, the effect of this error on the estimated input motion is negligible.

(7) The input accelerogram obtained from the error filter shows a decrease in amplitude for an increase in frequency beyond 10 Hz. But even for an accelerogram for which the identification is more difficult than that of velocity and displacement, the difference is only about 4% - 5% .

(8) The procedure was extended to a multi-input system. Although high-frequency components above 5 - 6 Hz are eliminated as observation and system noises, the estimated results of the input motions at points with observed responses are fairly good, even when the number of observations is smaller than the number of degrees of freedom.

References

[1] Toki, K., T. Sato and Y. Oiki. Detection of Dynamic Properties of Structural Systems by the Autoregressive Moving Average Method, Annuals Disas. Prev. Res. Inst., Kyoto University, No.21B-2, pp.57-68, 1987 (in Japanese).

[2] Hoshiya, M. and E. Saito. Identification Problem of Some Seismic Systems by Extended Kalman Filter, Proc. JSCE, No.339, pp.59-67, 1983 (in Japanese with English abstract).

[3] Hoshiya, M. and E. Saito. Estimation of Dynamic Properties of a Multiple Degree of Freedom Linear System, Proc. JSCE, No.334/I-1, pp.289-298, 1984 (in Japanese with English abstract).

[4] Hoshiya, M. and O. Maruyama. Identification of Restoring Force Characteristics of Nonlinear Systems during Earthquakes, Proc. JSCE, No.386/I-8, pp.397-405, 1987 (in Japanese with English abstract).

[5] Murakami, A. and T. Hasegawa. Back Analysis by Kalman Filter-Finite Elements and a Determination of Optimal Observed Points Location, Proc. JSCE, No.388, III-8, pp.227-235, 1987 (in Japanese with English abstract).

[6] Toki, K., T. Sato, J. Kiyono and K. Ichihara. Identification of the Fault Rupture Process by Use of the Kalman Filter, Annuals Disas. Prev. Res. Inst., Kyoto University, No.29B-2, pp.1-16, 1986 (in Japanese with English abstract).

[7] Toki, K., T. Sato and J. Kiyono. Identification of the Input Ground Motion of a Multi-Input System by use of the Kalman Filter, Annuals Disas. Prev. Res. Inst., Kyoto University, No.33B-2, pp.23-37, 1989 (in Japanese with English abstract).

[8] Ott, N. and H. G. Meder. The Kalman filter as a Prediction Error Filter, Geophysical Prospecting 20, pp.549-560, 1970.

[9] Wiener, N. Extrapolation, Interpolation and Smoothing of Stationary Time Series, with Engineering Applications, John Wiley & Sons, 1949.

[10] Kalman, R. E. and R. S. Bucy. New Results in Linear Filtering and Prediction Theory, Trans. ASME, Ser. D: J. Basic Eng. 83, pp.95-108, 1961.

[11] Jazwinski, A. H. Stochastic Processes and Filtering Theory, New York, Academic Press, pp.269-270, 1970.

[12] Wen, Y.K. Approximate Method for Nonlinear Random Vibration, Jour. of the Eng. Mech. Div., ASCE, Vol.101, No.EM4, pp.389-401, 1975.

[13] Jazwinski, A. H. Stochastic Process and Filtering Theory, Academic Press, 1970, pp.272-281.

[14] Toki, K., T. Sato, J. Kiyono, N. Kishi Garmroudi, S. Emi and M. Yoshikawa. Hybrid Experiment on Non-linear Earthquake-induced Soil-structure Interaction, Earthq. Eng. and Struc. Dyn., Vol.19, pp.709-723, 1990.

[15] Toki, K., T. Sato, J. Kiyono, N. Kishi Garmroudi and M. Yoshikawa. Hybrid Experiment on Nonlinear Earthquake-induced Soil-structure Interaction of Soil-pile System, Annuals Disas. Prev. Res. Inst., Kyoto University, No.33B-2, pp.13-23, 1990 (in Japanese with English abstract).

[16] Toki, K., T. Sato, J. Kiyono, N. Kishi Garmroudi, S. Emi and M. Yoshikawa. Hybrid Experiment of Pile Groups Taking into Account Earthquake-induced Nonlinear Soil-structure Interaction, Proc. 8th Japan Earthq. Eng. Symp., pp.1491-1496, 1990.

[17] Toki, K., T. Sato and J. Kiyono. Identification of Structural Parameters and Input Ground Motion from Response Time History, Proc. JSCE, Structural Eng./Earthquake Eng., Vol.6, No.2, 413s-421s, 1989.

[18] Toki, K. and M. Kubota. Nonlinear Response of Continuous Bridge to Traveling Seismic Wave, Proc. 5th Japan Earthq. Eng. Symp., pp.1065-1072, 1978 (in Japanese with English abstract).

CHAPTER 3

INVESTIGATION OF THE LOCAL SITE EFFECT ON GROUND MOTION

3.1 General Remarks

For civil structures that extend in a horizontal direction, such as suspension bridges, buried pipelines, and bank reinforcements, change in the phase of the seismic wave along the propagation path is important for assessing the safety of such structures in a seismic environment. Knowledge of the phase velocity of the seismic wave, in particular, is indispensable for seismic response analyses of structures for which the relative displacement between two supporting points is crucial. Several methods for calculating the appropriate phase velocity from a seismic wave are compared. Phase velocity usually is very sensitive to the noise level contained in a signal; therefore, a new method that eliminates this noise by use of the Kalman filter is developed. Phase velocities are detected from a noise-contaminated motion simulated with an artificial dispersion curve.

Most early phase and group velocity studies have been concerned with measuring the velocities of long-period surface waves and understanding the physical properties of the earth's interior from the dispersion characteristics of seismic waves. Many different schemes have been developed that measure phase and group velocities. Two stations on the same azimuth from the epicenter can be used to determine phase velocities by computing the phase differences from their spectra ratios. Group velocities can be calculated by differentiating the phase velocity curve or by measuring the group arrival time at each station and dividing the group delay by the separation distance. Sato [1] suggested the application of the Fourier transform in analyzing dispersed surface waves and gave a formula for the two-station method. Landisman et al. [2] measured interstation phase velocities from a windowed cross-correlogram. Dziewonski [3] developed a multiple-filter technique by which to calculate interstation group velocities. The measurement of phase velocities originated from the "peak-and-trough" technique that developed into the cross-

multiplication and sums and differences techniques of Blouch and Hale [4]. Nakanishi [5] and Steven [6] established Wiener filter techniques.

For engineering studies these methods are used to detect phase velocities because short period surface waves of less than 10 sec have been studied since the 1967 Matushiro and 1968 Tokachi-oki earthquakes. Shima [7] investigated short period surface waves in terms of engineering concerns and showed the necessity of further studies. Sato and Sawada [8] used Love-wave propagation to determine the phase velocities in frequency ranges of engineering interest. Kamiyama [9] calculated the dispersion characteristics of the Rayleigh wave using a multi-filter technique based on microtremor records. These studies focus on explanations of wave propagation in soil. Other studies consider structures and seismic waves in terms of engineering concerns. Kotsubo et al. [10] made a model analysis of bridge foundations that have different input accelerations. Toki [11] examined the frequency dependence of phase velocities based on strong ground accelerograms and considered the seismic-resistance property of structures. Toki and Kubota [12] and Toki and Imamura [13] calculated the seismic response of a multi-input bridge taking into account the apparent velocity of the wave propagating along the ground surface. Werner et al. [14] analyzed the bridge response for inputs P-, S-, and Rayleigh waves taking into account the phase difference for earthquake motion. Array observation systems are now well organized and many studies of the characteristics of wave propagation that use array data are being made.

The effect of the difference in the frequency range on the estimation of phase velocity is clarified here because frequency ranges that must be considered in engineering differ from those considered in other scientific disciplines. For engineering purposes, the wave length concerned varies from a few tens of meters to a few kilometers, and the frequency range varies from a few tenths to several tens of seconds. The dispersion curve of the phase velocities is derived from observational data. Phase delay curves that are calculated from seismograms are greatly affected by noise. The deconvolution method that includes the Kalman filter therefore is used to separate the signal and noise from the noise-contaminated records.

Seismic ground motions on layered media with an irregular interface are not uniform because of the effects of focusing and scattering. Long structures such as pipelines and subways are effected by differential ground motion rather than by inertial force. Such structures, which extend for long distances along or below ground surface, are heavily damaged if the relative displacement between two points on the ground becomes large during an earthquake.

The studies done on spatial variation in seismic ground motion have been deterministic and stochastic. The deterministic ones are based on the recorded time histories of two arbitrary points for which the phase delay is considered, and the differential motion calculated. The stochastic studies involve calculation of the correlation function. Ground motion is assumed to be a random, stationary process. Of the stochastic studies published, Kawakami [15] has modeled the cross-spectrum between two points and investigated the effect of the deformation of seismic waves. Harada [16] has given a probabilistic description of spatial variation in strong earthquake-generated ground displacement by modeling the spatial correlation function statistically. He also proposed a stochastic mode [17] for soil parameters by which motion on the ground surface can be simulated. Hoshiya [18] has modeled the cross-spectrum and simulated a spatially and temporally variable earthquake using an autoregressive model. Loh [19] has made an empirical study through direct statistical analysis that uses SMART-1 array [20] data.

The characteristics of the spatial variation in seismic ground displacement on irregular profiles is described. The procedure used to simulate ground motion is the Discrete Wave-number Method developed by Aki and Larner [21], which was devised to calculate the elastic wave field in layer-over-half-space media with an irregular interface. Power spectra densities are not constant at any of the surface points if the layered media has irregular interfaces. Simulated waves have been used to investigate the characteristics of the mean powers and the cross-correlation functions. The shape of the irregular boundary is identified from the mean powers and the spatial correlation coefficients. A simple procedure by which the relative displacement on an irregular profile can be calculated is proposed by replacing the basin model with layered media models.

3.2 Detection of the Phase Velocity

3.2.1 Techniques for Measuring Phase Velocity

(1) Phase velocity

Velocity measurement techniques are roughly divisible into two groups: In one the phase difference is calculated from the phase spectrum using the Fourier transform of earthquake records; e.g. by phase difference cross-correlation, and the sums and differences techniques. The other involves analysis in the time domain, as in the peak-and-trough and cross-multiplication techniques. Phase difference and cross-correlation are simple techniques, but they do not provide information about wave amplitude because only

the phase spectrum is used. Sums and differences, and cross-multiplication techniques can be used to assess the correlation of waves for two points. A deconvolution method that uses the Kalman filter is presented here. Two techniques, the Wiener and Kalman filters, are added to the standard techniques described above and are compared to each other. In this study, three criteria are assumed in order to detect phase velocities:

1. Two or more stations in the set that lies along the same radial line from the epicenter (Fig.3.1).
2. The instrumental characteristics (phase shift) of the seismographs are the same at all stations.
3. Noise is white and contained additionally.

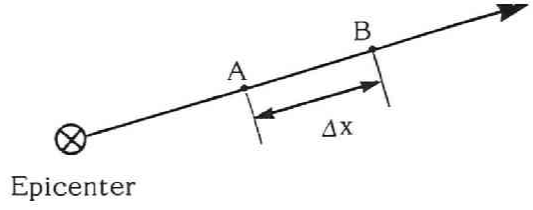

Fig. 3.1 Relation between the epicenter and observation points.

Based on these assumptions, the phases at points of A and B are represented as the sum of four terms;

$$\phi_A(x_A,\theta,\omega) = k(\omega)x_A + \phi_0(\theta,\omega) + \phi_I(\omega) + \phi_{NA} \tag{3.1}$$

$$\phi_B(x_B,\theta,\omega) = k(\omega)x_B + \phi_0(\theta,\omega) + \phi_I(\omega) + \phi_{NB} \tag{3.2}$$

in which x_A and x_B are the epicentral distances, θ is the azimuth, ω the angular frequency, and k the wave-number. $\phi_0(\theta,\omega)$ is the source phase shift, $\phi_I(\omega)$ the instrumental phase shift, and ϕ_{NA} and ϕ_{NB} are the phase shifts caused by instrumental and background noises, and the wave distortion induced by certain physical disturbances.

The phase difference between two points is given by subtracting Eq.(3.1) from Eq.(3.2)

$$\begin{aligned}\phi_A - \phi_B &= k(\omega)\Delta x + (\phi_{NA} - \phi_{NB}) \\ &= \phi + \Delta\phi\end{aligned} \tag{3.3}$$

in which ϕ is the phase difference that is in accord with wave propagation, $\Delta\phi$ the phase error produced by noise, and Δx the distance between the two points.

Seismological techniques for the detection of the phase velocities have been developed in order to measure the phase velocity of the long-period surface wave and to understand the physical properties of the Earth's interior. Before these techniques can be applied to the analysis of dispersed surface waves in ranges important for engineering, the effects of the objective period, wave length, and distance between two points must first be clarified in order to calculate the phase velocities. The error in phase velocity caused by noise is derived as

$$c = \Delta x / (\frac{\phi}{2\pi} T) \tag{3.4}$$

$$c^* = \Delta x / (\frac{\phi + \Delta\phi}{2\pi} T) = c\,(1+\frac{\Delta\phi}{\phi})^{-1} \tag{3.5}$$

$$\Delta c = c - c^* = c - c(1+\frac{\Delta\phi}{\phi})^{-1} \approx c\frac{\Delta\phi}{\phi} = \frac{c\Delta\phi}{2\pi\,\Delta x/\lambda} \tag{3.6}$$

$$\frac{\Delta c}{c} = \frac{\lambda}{2\pi\,\Delta x}\Delta\phi \tag{3.7}$$

in which c is the exact value of the phase velocity, c^* the phase velocity contaminated by noise, λ the wave length, and T the period of the wave. The fact that the r.m.s. (root mean square) of the phase shift is proportional to the signal-noise ratio is derived as follows: The time history of the earthquake, d(t), is assumed to be composed of the signal, s(t), and noise, n(t);

$$d(t) = s(t) + n(t) \tag{3.8}$$

The Fourier transform of Eq(3.8) is

$$D(\omega)\exp(i\phi_d) = S(\omega)\exp(i\phi_s) + N(\omega)\exp(i\phi_n) \tag{3.9}$$

in which $D(\omega)\exp(i\phi_d)$, $S(\omega)\exp(i\phi_s)$ and $N(\omega)\exp(i\phi_n)$ are the respective Fourier transforms of d(t), s(t) and n(t). If $N(\omega)/S(\omega)$ is small, Eq(3.9) is approximate to

$$\phi_d(\omega) \approx \phi_s(\omega) + \frac{N(\omega)}{S(\omega)} \sin(\phi_n(\omega) - \phi_s(\omega)) \qquad (3.10)$$

If the phase shift caused by the noise in Eq.(3.10) is assumed to change randomly, between 0 and 2π the r.m.s. of $\phi_d(\omega)$ becomes $N(\omega)/2S(\omega)$ and the r.m.s. of $\Delta\phi$ in Eq.(3.7) is directly related to the S-N ratio. Therefore, the conditions under which the measurement error of phase velocity decreases are (i) make $\Delta\phi$ small, or make the S-N ratio large; (ii) make the wavelength short; (iii) make the interstation distance, Δx, long. As for (iii), the wavelength used in the analysis of the long-period surface wave is from a few tens of to a few hundred kilometers, and the wavelength important for engineering purposes is less than a few kilometers. If $\Delta\phi$ in Eq.(3.7) is assumed to be constant, the wavelength for engineering purposes reduces the measurement error of phase velocity. One problem in detecting the phase velocity is to discriminate the periodicity in the phase difference. The phase difference is between 0 and 2π, but information about the integer multiple of 2π can not be obtained. Conditions (ii) and (iii) increase the measurement error of phase velocity because the wavelength and interstation distance must be short for engineering concerns. Moreover, as the period range considered in this engineering study is relatively short, it becomes difficult to measure the phase difference as the interstation distance is extended. Consequently, the measurement error of phase velocity is reduced by making $\Delta\phi$ as small as possible.

The following ratios of the wavelength to interstation distance, $\lambda/\Delta x$, have been adopted: Brune and Dorman (1983) 1/10 -1/40; Dziewonski (1969) 1/2 - 1/20; and Steven and Toksoz (1982) 1/5 - 1/30. A wave length of a few hundred meters and a period of less than ten seconds is dealt with in this study. The range of $\lambda/\Delta x$ is 10 - 1/10. If the classical techniques developed in long-period seismology to measure phase and group velocities are used, the sensitivity of the analysis will decrease if a constant $\Delta\phi$ is assumed. Therefore, the measurement error of phase, $\Delta\phi$, contained in the observed waves must be lessened.

(2) Detection techniques

(i) Phase difference method

The Fourier transform of the recorded signal f(t) is

$$F(\omega) = \int_{-\infty}^{\infty} f(t)\, e^{-i\omega t} dt \qquad (3.11)$$

The complex spectrum of the signal $F(\omega)$ is represented by its amplitude and phase functions:

$$F(\omega) = A(\omega) \exp\{i\phi(\omega)\} \tag{3.12}$$

The phase is represented as

$$\phi(\omega) = -\mathrm{Im}\{\log F(\omega)\} \tag{3.13}$$

Phase information can be extracted, and a phase delay curve constructed. Because the Fourier transform gives phase information only for the angle interval of 0 - 2π (rad). The exact phase difference is

$$\phi_B(\omega) - \phi_A(\omega) + 2n\pi \quad (n = 0,1,2\cdots) \tag{3.14}$$

The phase velocity is calculated from

$$c(\omega) = \frac{\Delta x}{\dfrac{\phi_B(\omega) - \phi_A(\omega) + 2n\pi}{\omega}} \tag{3.15}$$

in which Δx is the distance between points A and B. The integer, n, can be estimated from information on the possible range of the phase velocity values.

(ii) Cross-correlation method

The cross-correlation operation of the signals, $f_A(t)$, and $f_B(t)$, is defined in the time domain as

$$f_{AB}(t) = \int_{-\infty}^{\infty} f_A(\tau) f_B(t+\tau) d\tau \tag{3.16}$$

The Fourier transform of Eq.(3.16) is

$$F_{AB}(\omega) = \int_{-\infty}^{\infty} \int_{-\infty}^{\infty} f_A(\tau) f_B(t+\tau) d\tau \, e^{-i\omega t} dt$$

$$= F^*_A(\omega) \, F_B(\omega) \qquad (3.17)$$

in which $F_{AB}(\omega)$ is the Fourier transform of $f_{AB}(t)$, and $F^*_A(\omega)$ is the complex conjugate of $F_A(\omega)$. The complex spectrum of $F(\omega)$ is represented by the amplitude $R(\omega)$ and phase $\phi(\omega)$ as

$$F(\omega) = R(\omega) \exp\{-i\phi(\omega)\} \qquad (3.18)$$

By substituting Eq.(3.18) into Eq.(3.17);

$$F_{AB}(\omega) = R_A(\omega) \exp\{i\phi_A(\omega)\} \, R_B(\omega) \exp\{i\phi_B(\omega)\}$$

$$= R_A(\omega) \, R_B(\omega) \exp\{-i(\phi_B(\omega) - \phi_A(\omega))\} \qquad (3.19)$$

The phase difference is

$$\phi_B(\omega) - \phi_A(\omega) = -\mathrm{Im}\{\log F_{AB}(\omega)\} \qquad (3.20)$$

There is no difference in the calculation process for the phase difference method and this cross-correlation method if the records do not contain noise. The advantage of using the cross-correlation method is that the effect of random noise can be substantially reduced by the summation of a number of cross-correlograms, $F_{AB}(\omega)$.

(iii) Sums and differences method [4]

When two functions are in phase for a given frequency, their sum is the maximum value, and their difference the minimum value. The calculation is done by taking the direct Fourier transform of the sums and differences of the two functions;

$$H(\tau,\omega)_+ = \int_{-\infty}^{\infty} \{f_A(t+\tau) + f_B(t)\} \, e^{-i\omega t} dt \qquad (3.21)$$

$$H(\tau,\omega)_- = \int_{-\infty}^{\infty} \{f_A(t+\tau)-f_B(t)\}\, e^{-i\omega t}dt \qquad (3.22)$$

in which τ is the time delay. The logarithmic ratio of $H(\tau,\omega)_+$ to $H(\tau,\omega)_-$ is

$$G(\tau,\omega) = \log \{H(\tau,\omega)_-/H(\tau,\omega)_+\} \qquad (3.23)$$

If the two waves are in phase, G has a maximum negative value. The time delay, τ, of a sinusoidal wave with the frequency, ω, is obtained.

(iv) Cross-multiplication method [4]

If the two seismograms are narrow-band filtered so that they are effectively single-frequency seismograms, they then may be described as $A\cos(\omega t)$ and $B\cos(\omega t+\Delta\phi)$, $\Delta\phi$ being the relative phase of the two. The product seismogram then is

$$A\cos\omega t \cdot B\cos(\omega t+\Delta\phi) = \frac{AB}{2}\{\cos(2\omega t+\Delta\phi) + \cos\Delta\phi\} \qquad (3.24)$$

Thus, the seismogram consists of a wave with twice the original frequency that has been superimposed on a D. C. shift proportional to $\cos\phi$. Clearly, the D. C. shift is maximum when ϕ is zero. It is customary in cross-correlation to remove the oscillated component by integration, but integration leads to the undesirable loss of time resolution. Instead, the value of the D. C. shift is determined by finding the value of the maximum amplitude of the product seismogram X_{max} and the following minimum X_{min}. The D. C. level for a particular time shift (or phase velocity) is then $(X_{max}+X_{min})/2$.

(v) Wiener filter

Given two seismograms located on the same azimuth from a source, the interstation medium response function can be estimated. The amplitude spectrum of this medium response function gives a measurement of the spectral ratio between the two stations. This can be used to determine Q. The phase gives the phase delay of the system. The interstation phase velocities are calculated from this phase delay. The relation between the signals at the two stations and the transfer function is

$$f_B(t) = \int_0^t f_A(\tau) h_{AB}(t-\tau)\, d\tau \tag{3.25}$$

in which $f_A(t)$ is the seismogram at point A (assumed to be an input motion), $f_B(t)$ the seismogram at point B (assumed to be an output motion, and $h_{AB}(t)$ the transfer function.

The frequency domain representation of Eq(3.25) is

$$F_B(\omega) = F_A(\omega)\, H_{AB}(\omega) \tag{3.26}$$

$$H_{AB}(\omega) = F_B(\omega) / F_A(\omega) \tag{3.27}$$

in which $F_A(\omega)$, $F_A(\omega)$, and f_A are the Fourier transforms of $f_A(t)$, $f_A(t)$, and $h_{AB}(t)$. Eq.(3.27) is rewritten

$$H_{AB}(\omega) = \frac{R_B(\omega)}{R_A(\omega)} \exp\{i\,(\phi_B(\omega) - \phi_A(\omega))\} \tag{3.28}$$

The Wiener filter determines the transfer function by minimizing the difference between the calculated and observed output, $f_B(t)$, according to the least-square method.

D(t) is designed such that

$$D(t) = \int_0^t h_{AB}(\tau) f_A(t-\tau)\, d\tau \tag{3.29}$$

The expectation of the square of the difference is

$$e(t) = E[\{D(t) - f_B(t)\}^2] \tag{3.30}$$

$h_{AB}(t)$ is determined by minimizing e(t) in Eq.(3.30). The transfer function, $h_{AB}(t)$, the partial differentiation of which is zero, $\frac{\partial e(t)}{\partial h_{AB}}$, has the following relation to f_A and f_B;

$$\int_0^\tau \int_0^\tau h_{AB}(s)\, \{f_A(t-s)\, f_A(t-\tau) dt\}\, ds = \int_0^\tau f_A(t-\tau)\, f_B(t) dt \tag{3.31}$$

The Fourier transform of Eq.(3.31) is

$$H_{AB}(\omega)\, A(\omega) = G(\omega) \tag{3.32}$$

in which $H_{AB}(\omega)$, $A(\omega)$, and $G(\omega)$ are respectively the Fourier transform of $h_{AB}(t)$, the autocorrelation function of f_A, and the cross-correlation function of $f_A(t)$ and $f_B(t)$. As $H(\omega)$ coincides with the left side of Eq.(3.28), the phase difference is

$$\phi_B - \phi_A = \mathrm{Im}\,\{\log H(\omega)\} \tag{3.33}$$

and in Eq.(3.32)

$$A(\omega) = F_A(\omega)\, F_A^*(\omega) \tag{3.34}$$

$$G(\omega) = F_A^*(\omega)\, F_B(\omega) \tag{3.35}$$

Then

$$H(\omega) = F_B(\omega) / F_A(\omega) \tag{3.36}$$

in which $*$ is the complex conjugate . It turns out that this Wiener filter method is the same as dividing the output by the input in the frequency domain and that the noise contained in the signal can not be eliminated.

(vi) Kalman filter

The formulation of the Kalman filter is the same as Eqs.(2.1) and (2.2) in the continuous types

$$\frac{d\mathbf{x}(t)}{dt} = \mathbf{A}\cdot\mathbf{x}(t) + \mathbf{B}\cdot\mathbf{w}(t) \tag{3.37}$$

$$\mathbf{y}(t) = \mathbf{H}\cdot\mathbf{x}(t) + \mathbf{v}(t) \tag{3.38}$$

and in the discrete types

$$\begin{aligned} \mathbf{x}_{t+1} &= \Phi_{t+1|t}\mathbf{x}_t + \mathbf{G}_t\mathbf{w}_t \\ \mathbf{y}_t &= \mathbf{H}_t\mathbf{x}_t + \mathbf{v}_t \end{aligned} \tag{3.39}$$

The Kalman filter algorithm is shown in Fig.2.2. This Kalman filter is applied to the deconvolution problem. Let r(k) represent the input (signal at station A) to the system h(k), and y(k) be the output (signal at station B). The relation of r(k), y(k) and h(k) is

$$y(k) = \sum_{j=N}^{k} [r(j)\, h(k-j)] + v(k) \tag{3.40}$$

$$N = \begin{cases} 1 & (k < L) \\ k - L + 1 & (k \geq L) \end{cases} \tag{3.41}$$

in which v(k) is the Gaussian white noise and L the sampling number for input motion.

Eq.(3.40) is rewritten in matrix style

$$\begin{aligned} \mathbf{y}(k) &= \mathbf{H}(k)\mathbf{x}(k) + \mathbf{v}(k) \\ \mathbf{H}(k) &= [h(k)\ h(k-1) \cdots h(L-1)] \\ \mathbf{x}(k) &= [r(k)\ r(k-1) \cdots r(k-L+1)]^T \end{aligned} \tag{3.42}$$

The transfer function is assumed to be

$$h(k) = \sum_{i=1}^{L} \{b_i(k-l)\, h(k-i)\} \tag{3.43}$$

Eq.(3.43) is rewritten in matrix style

$$\mathbf{x}_k = \Phi_{k|k-1}\mathbf{x}_{k-1} \tag{3.44}$$

in which Φ is state transition matrix (see section **5.2**). As the convolution equation (Eq.[3.25]) is formulated into the linear stochastic system (Eq.[3.39]), the transfer function can be estimated by executing the Kalman filter algorithm.

3.2.2 Phase Velocity from Simulated Waves

Waves at two stations with the same azimuth from the source are simulated. The wave at station A (point closer to the source) has a maximum acceleration of 250 gal. It is simulated by generating the white noise and multiplying the envelope function given as

$$y = \frac{t}{t_p} \exp\left(1 - \frac{t}{t_p}\right) \tag{3.45}$$

Fig.3.2 shows this envelope function. The dispersion curve of the phase velocity is assumed to be

$$c = \begin{cases} 500 & (0 < \omega \leq 4\pi) \\ \dfrac{6280}{\omega} & (4\pi < \omega) \end{cases} \tag{3.46}$$

Fig.3.3 shows the dispersion curve. The Fourier transform of the wave at point A, $F_A(\omega)$ is

$$F_A(\omega) = \int_{-\infty}^{\infty} f_A(t)\, e^{-i\omega t} dt \tag{3.47}$$

As the phase difference between points A and B can be calculated from the interstation distance between the two points and the phase velocities when the wave propagates from point A to B, the Fourier spectrum of point A can be determined by using the amplitude, the phase of point A, and this phase difference. The attenuation of amplitude, however, is not considered. The wave at point B is computed from the inverse Fourier transform of $F_A(\omega)$ as

$$f_B(t) = \frac{1}{2\pi} \int_{-\infty}^{\infty} F_B(\omega)\, e^{i\omega t} d\omega \tag{3.48}$$

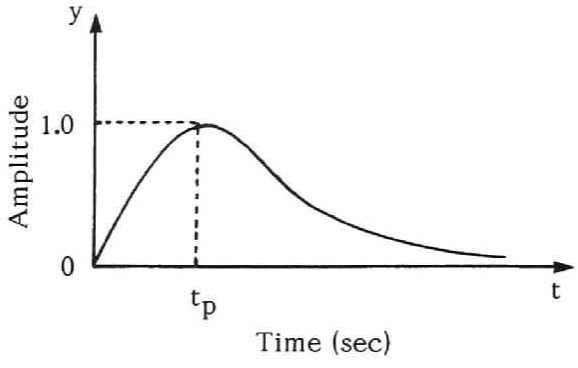

Fig. 3.2 Envelope function.

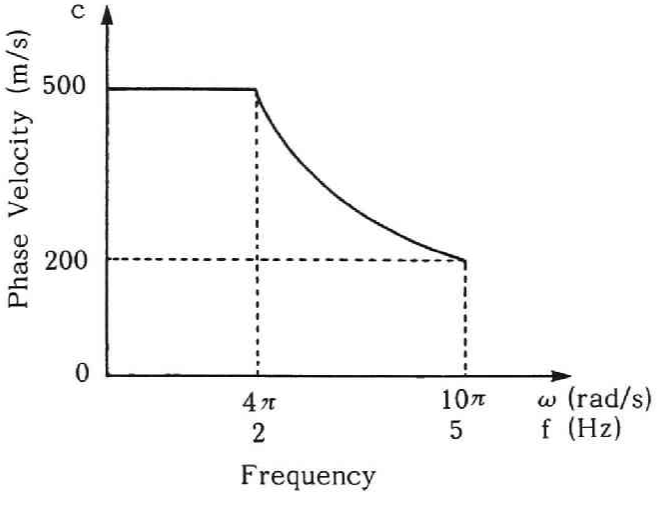

Fig. 3.3 Assumed dispersion curve.

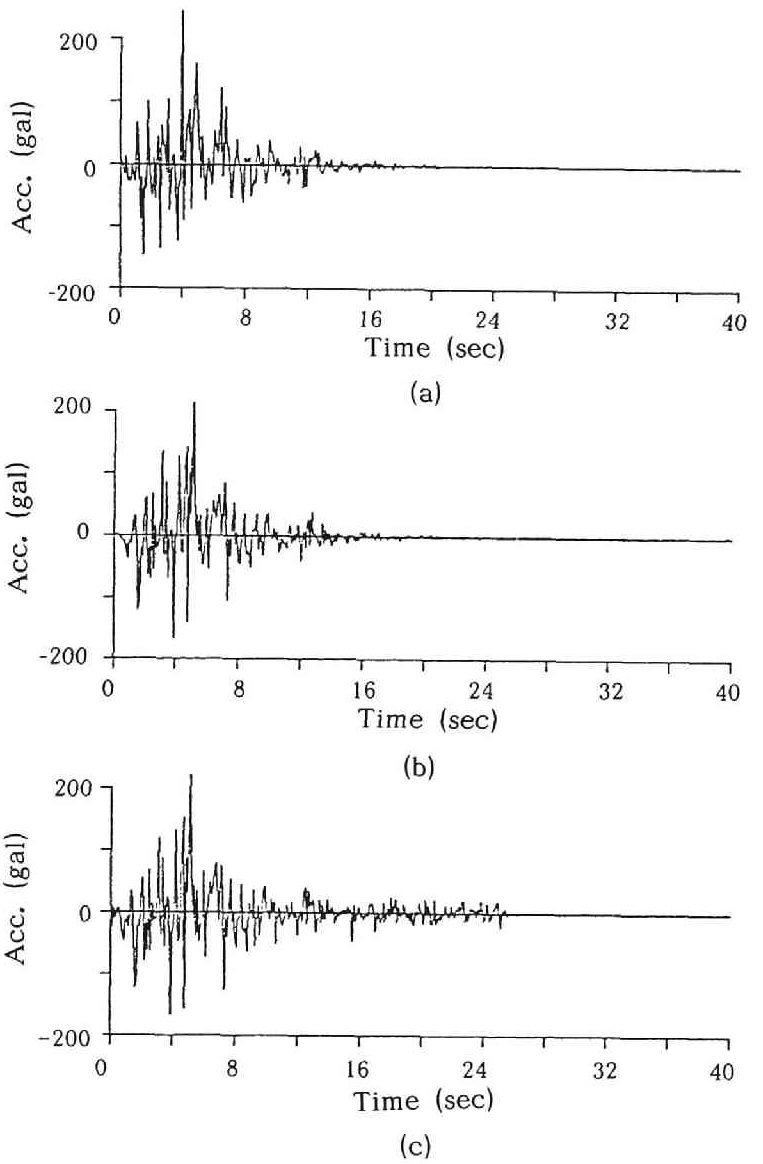

Fig. 3.4 Synthesized waveforms (interstation distance 100 m)
(a) waveform at point A, (b) waveform at point B (noise free)
(c) waveform at point B (noise contaminated)

White noise of the intensity of 10% of the mean square value is added to the wave at point B. The synthesized waveforms for an interstation distance of 100 m are shown in Fig.3.4, in which (a) is the wave at point A, (b) the wave at point B without noise, and (c) the wave at the point B with noise. The interval is 0.1 sec and the number of data 512. Waves for which the interstation distances are 300, 500, and 700 m also are synthesized to compare the effect of interstation distance on the detection of phase velocities.

(1) Phase difference and cross-correlation methods

These two methods use the same process to calculate phase differences from the records of two points; hence, the obtained phase velocities are identical. Fig.3.5 shows the phase velocities detected from records. The interstation distance for the left part is 100 m, and for the right 300 m. The upper part is noise free, but the lower part is noise contaminated. The solid line shows the exact values. The small circles (o) are the detected phase velocities. Other phase velocities are calculated using the increment of the integer, n, in Eq.(3.14). The larger the integer, the smaller the phase velocities. If the record is contaminated by noise, the measurement errors of the phase velocities become large, especially in the range of ω smaller than 15 rad/sec (period T=0.4 sec). This is because the noise contained in the small circular frequency range markedly affects the measurement of phase velocities because the phase delay is obtained by dividing the phase difference by the circular frequency, ω. Comparison of the results for interstation distances of 100 and 300 m shows that the measurement error of phase velocity is small, but recognition of the integer becomes difficult in the range of ω greater than 20 rad/sec (T=0.3sec). Table 3.1 shows r.m.s. errors in phase velocities for each interstation distance. These were computed by taking the difference between the exact value (solid line) and the closest values calculated from the simulation waves contaminated by noise. The larger the interstation distance, the smaller the measurement error of the phase velocity because Eq.(3.7) has the term Δx in its denominator.

Table 3.1 R.M.S. error in phase velocity for interstation distances

Δx (m)	R.M.S. Error (m/sec)
100	109.73
200	57.45
500	38.02
700	22.26

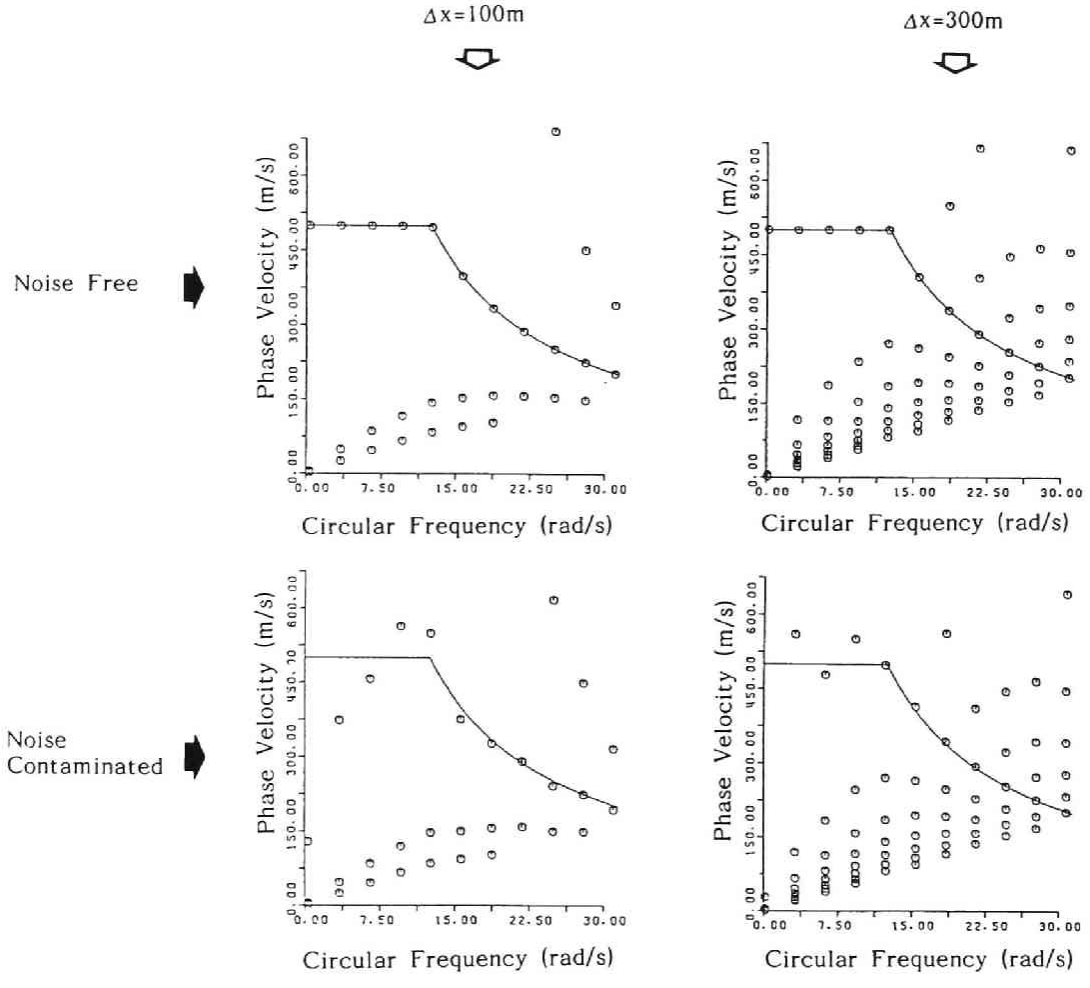

Fig. 3.5 Phase velocities calculated by the phase difference and cross-correlation methods.

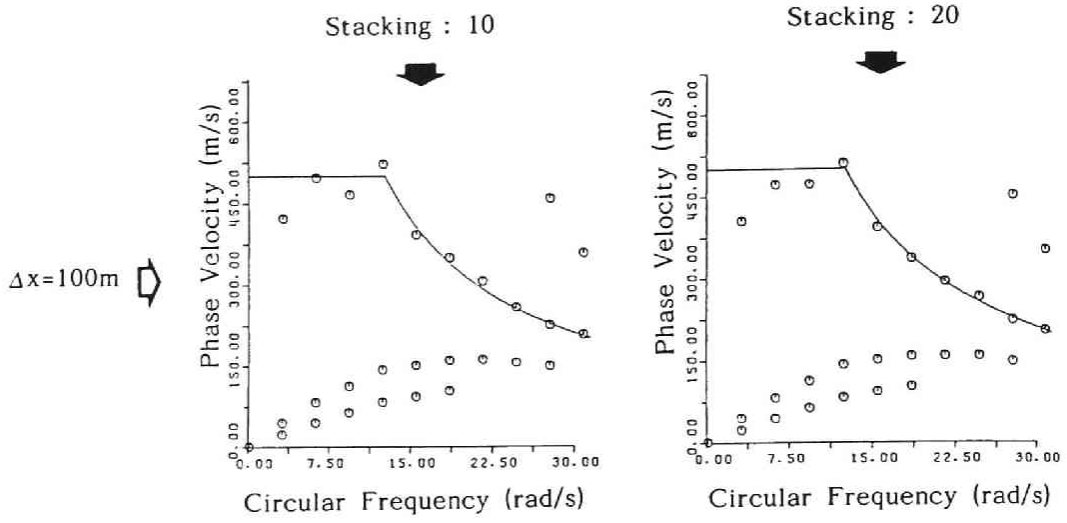

Fig. 3.6 Phase velocities calculated by data stacking

Table 3.2 R.M.S. error in phase velocity obtained by stacking cross-correlation functions

Superposed Number of Earthquakes	R.M.S. Error (m/sec)
1	109.73
10	66.00
20	55.79

If many earthquakes are recorded at two stations, the effect of random noise can be reduced by stacking a number of cross-correlograms. The waveforms used here are the same if the random noise is taken out. Fig.3.6 shows calculated phase velocities for which the stacking numbers were 10 (upper) and 20 (lower). The interstation distance is 100 m. The r.m.s. errors for the measured phase velocities obtained by stacking cross-correlograms are shown in Table 3.2. The r.m.s. error is reduced as the number of summations increases.

(2) The Sums and differences and cross-multiplication methods

The delayed time curves computed by the sums and differences (left) and cross-multiplication (right) methods are shown in Fig.3.7. The upper part is calculated from noise-free data and the lower part from noise-contaminated data. The abscissa is the circu-

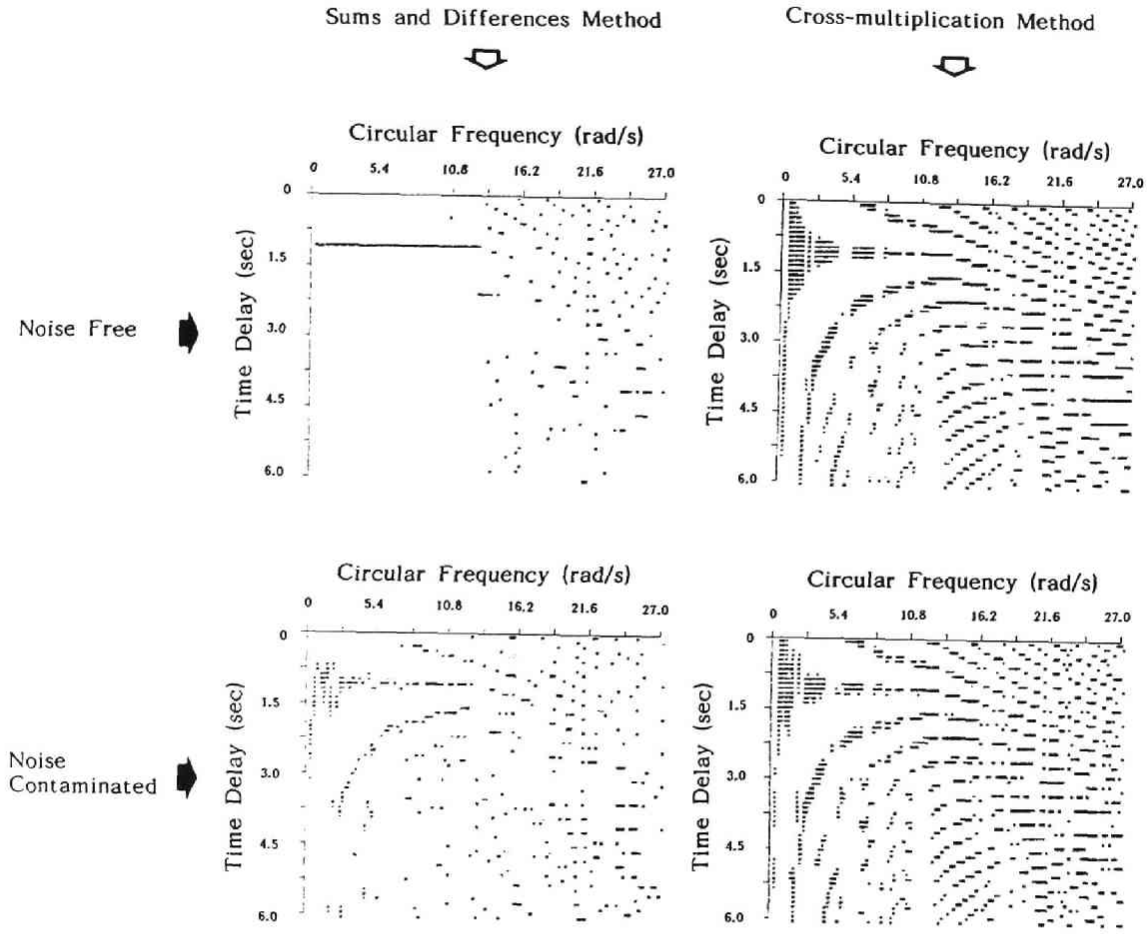

Fig. 3.7 Delayed time curves calculated by the sums and differences and cross-multiplication methods.

lar frequency, ω. The interstation distance is 500 m. If the phases of the waves at two points become closer, the G-value in Eq.(3.23) takes a larger negative value. These negative values are divisible into 4 classes: the ranges being 10% or less of all the data (#); 10 - 20% (*); 20 - 30% (+); and 30 - 40% (o). The upper limit of the phase velocity of the simulated wave is 500 m/sec, and the lower limit 200 m/sec. It takes 1.0 sec for the fastest wave to arrive and 2.5 sec for the slowest. As the sampling interval is 0.1 sec, 16 values for delayed time can be calculated by shifting waves every 0.1 sec. In the sums and differences method, judgement of the phase delay is easy in the range of ω less than 15 rad/sec (T=0.4 sec). It becomes difficult in the range of ω greater than 15 rad/sec because the interval of the delay time is very short. Because phase velocities only can be calculated at individual sampling times, velocities are estimated very roughly, especially when very large or the interstation distance very short. Thus, if the sampling interval for observed data is of the order of 10^{-2}, and detection of phase velocities of the order of a few km/sec is wanted, an interstation distance of a few hundred meters is not sufficient. An interstation distance of at least 500 m or a few kilometers is needed. A comparison of the results of the cross-multiplication method with those of the sums and differences method shows that the values in the cross-multiplication method scatter and the accuracy of the detection of phase velocities is low. As the seismograms must be passed through a narrow band-pass filter and the cross-product of the seismogram after time shifting taken, more CPU time is used than with the sums and differences method.

(3) Detection of phase velocities using the Kalman filter

The medium impulse response between two points, $f_{AB}(t)$ is represented by

$$f_{AB}(t) = \frac{1}{2\pi} \int_{-\infty}^{\infty} \frac{F_B(\omega)}{F_A(\omega)} e^{i\omega t} d\omega \qquad (3.49)$$

in which $F_A(\omega)$ is the Fourier transform of the waves at points A and B. Fig.3.8 shows the calculated medium impulse responses obtained with Eq.(3.49). The left part shows responses for an interstation distance of 100 m and the right part for 300 m. The upper part shows the results for a noise-free situation, and the middle for noise contamination. The medium impulse responses in the middle part contain much noise; in particular, in the range from 4 to 25 sec. The lower part shows the medium impulse responses calculated by the deconvolution method that uses the Kalman filter. After 4 sec the noise is markedly reduced. Fig.3.9 shows the phase velocities calculated from the phases of the medium re-

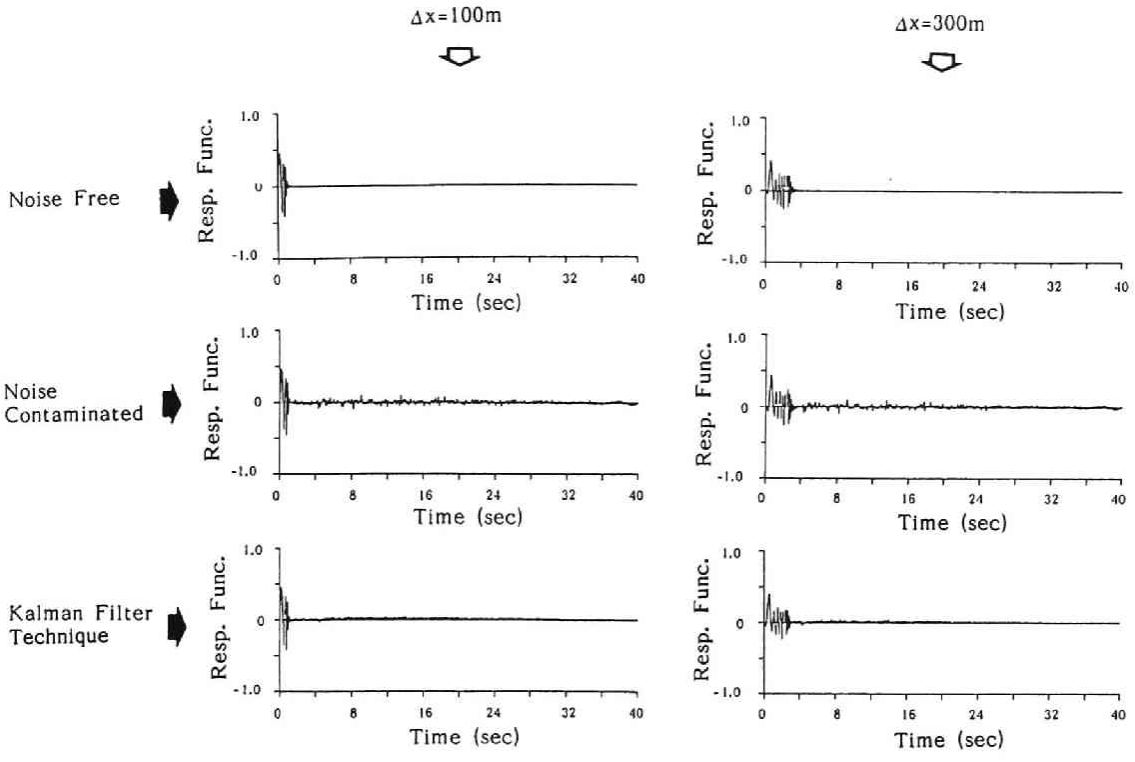

Fig. 3.8 Calculated medium impulse responses.

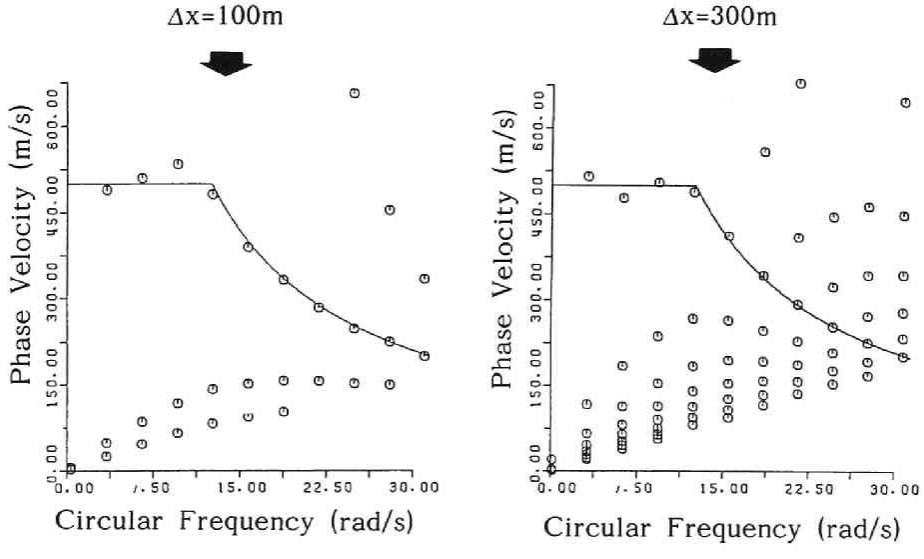

Fig. 3.9 Phase velocities detected by the Kalman filter technique.

sponses given by the medium response function deconvoluted by the Kalman filter. Compared with the lower part of Fig.3.5, the deviation from the exact value is smaller for a circular frequency of less than 15 rad/sec (2.4 Hz). Table 3.3 shows a comparison of the r.m.s. error from the exact value (Table 3.1). The estimated values of the phase velocities are improved. In Table 3.2, the r.m.s. error when the stacking number is one is 110 m/sec. When it is 10, it is 66 m/sec. As the r.m.s. error obtained when the Kalman filter is used is 77 m/sec, its efficiency is the same as the stacking of 7 to 8 cross-correlograms. The mean power of the noise contained in the wave at point B, simulated by convolution of the wave at point A and the medium impulse response from the Kalman filter, is half of the power of the assumed noise.

Table 3.3 Comparison of R.M.S. errors in phase velocity obtained by the cross-correlation and Kalman filter techniques

Δx (m)	R.M.S. Error Noise Contaminated (m/sec)	R.M.S. Error The Kalman Filter (m/sec)
100	109.73	77.10
200	57.45	12.98
500	38.02	10.73
700	22.26	8.45

3.2.3 Phase Velocity From Observed Records

(1) Earthquake records

Observation points were chosen from pairs which lie on the same azimuth from the source and for which the interstation distance is several hundred meters. The objective earthquake is the 1970 San Fernando earthquake (1970), the records being from Los Angeles, California, U.S.A. As the seismograms are set up independently at each site, the horizontal components are corrected for epicentral direction. The pairs of observation sites are

a) 1760 N. Orchid Avenue, ground floor, Hollywood (Q236)
   Hollywood Storage, basement, Los Angeles (F057)
b) 535 S. Fremont Avenue, basement, Los Angeles (R253)
   808 South Olive Street, street level, Los Angeles (F089)
c) 535 S. Fremont Avenue, basement, Los Angeles (R253)

646 South Olive Avenue, basement, Los Angeles (F098)

The interstation distances are 1000 m between Q236 and F057, 760 m between R253 and F089, and 580 m between R253 and F098. The epicentral distances at these stations range from 30 to 40 km. The horizontal components of the accelerations at these three stations are synthesized taking into account the azimuth from the epicenter.

(2) Analytical results

Phase velocities are detected by the cross-correlation method and the Kalman filter technique. Fig.3.10 (a), (b) shows the cross-correlogram and cross-spectrum between two observation points, Q236 and D057. The frequency of 2.4 Hz (15 rad/sec) is dominant. Phase velocities corresponding to the time delay of the peaks in Fig.3.10 (a) are shown in Table 3.4. As the peaks in the cross-correlogram denote the coincidence of the phases of the two waves, an adequate phase velocity is given in Table 3.4. The dispersion curves of the phase velocities obtained by the cross-correlation and Kalman filter techniques are shown in Fig.3.11 (a), (b). There are five dispersion curves in each figure, the two broken lines ① and ② being recognizable at the frequency of 2.4 Hz. The time delay which corresponds to the maximum value for the cross-correlogram is 1.7 sec, and its phase velocity is 590 m/sec. Broken line ② therefore is judged to be an exact dispersion curve. The dispersion curves calculated by the two techniques are shown in Fig.3.12 (a). There is a similar general tendency for the two lines. Above 10 rad/sec, the lines almost overlap; but, below it the difference is a few hundred meters per seconds in some cases.

Dispersion curves for the other pairs, R253-F089 and R253-F098, obtained by the same procedure are shown in Fig.3.12 (b), (c). The tendency of the curves also is similar in these pairs; but, phase velocities are improved when the Kalman filter is used. The largest difference is 500 m/sec.

Table 3.4 Phase velocity corresponding to time delay (Q236-D057)

Broken Line	Time Delay (sec)	Phase Velocity (sec)
-	0.40	2500
-	1.10	910
①	1.35	740
②	1.70	590

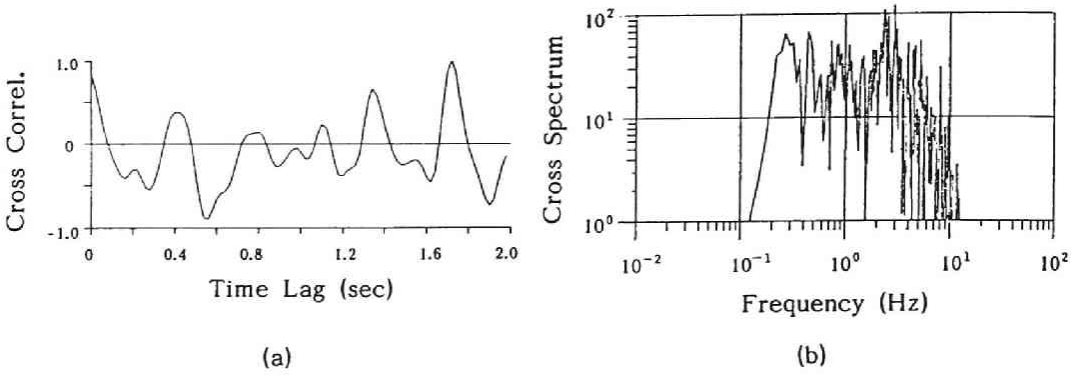

Fig. 3.10 Cross-correlogram and cross-spectrum (Q236-D057).

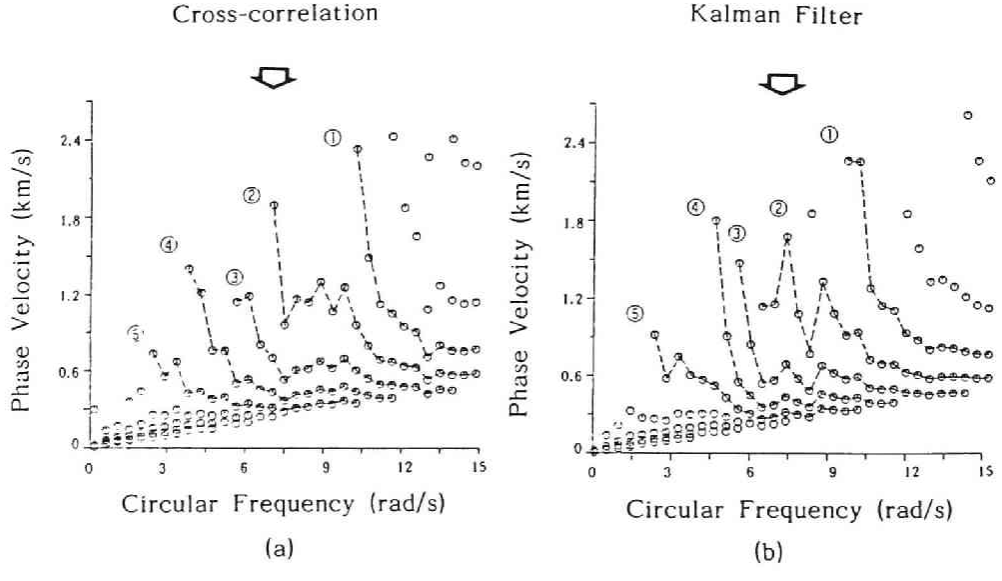

Fig. 3.11 Dispersion curves of phase velocities obtained by the cross-correlation (upper) and Kalman filter (lower) techniques

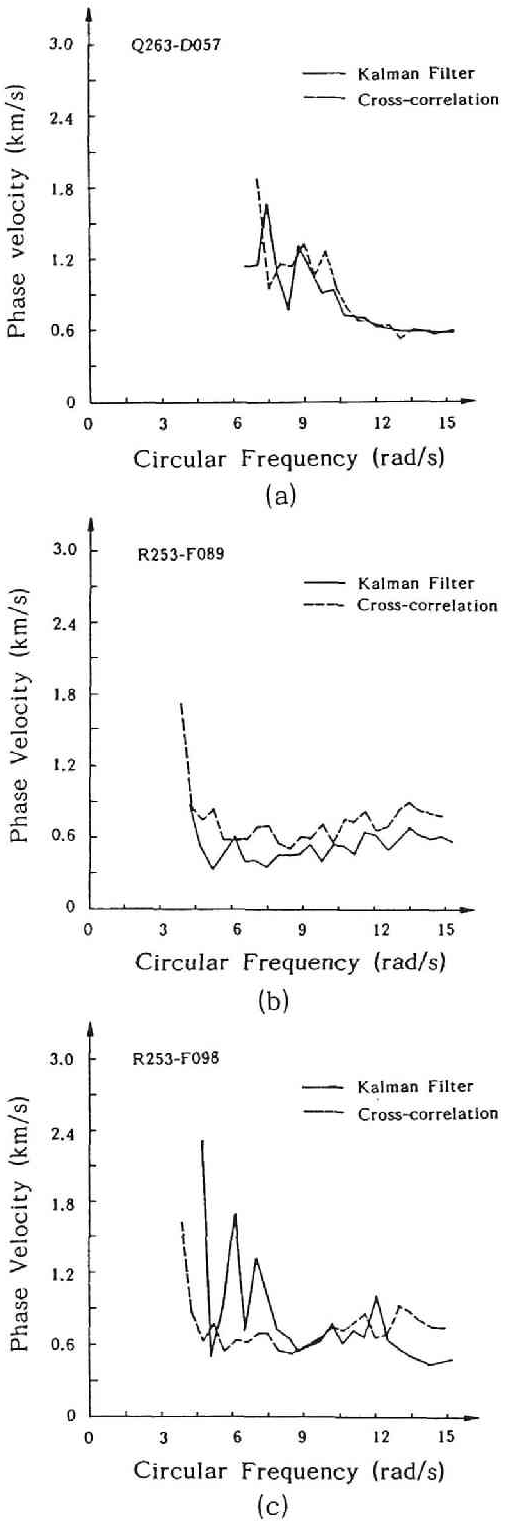

Fig. 3.12 Dispersion curves calculated from the cross-correlation and Kalman filter techniques for the observation station pairs Q263-D057, R253-F089, and R253-F098.

3.3 Identification of Layered Media with an Irregular Interface

3.3.1 Ground Motion with an Irregular Interface

A subsurface soil profile with several curved interfaces is shown in Fig.3.13 [22]. The problem is to find the motion at the free surface, z=0, when plane SH waves with the frequency ω are incident parallel to the x-z plane at the angle of θ from the z direction. The scattered wave field is represented by the combination of the plane wave, and the coefficients that satisfy the boundary condition approximately are determined. The Discrete Wave-number method [21] is adopted for this analysis. Hereafter, irregular ground means non-uniform layered ground.

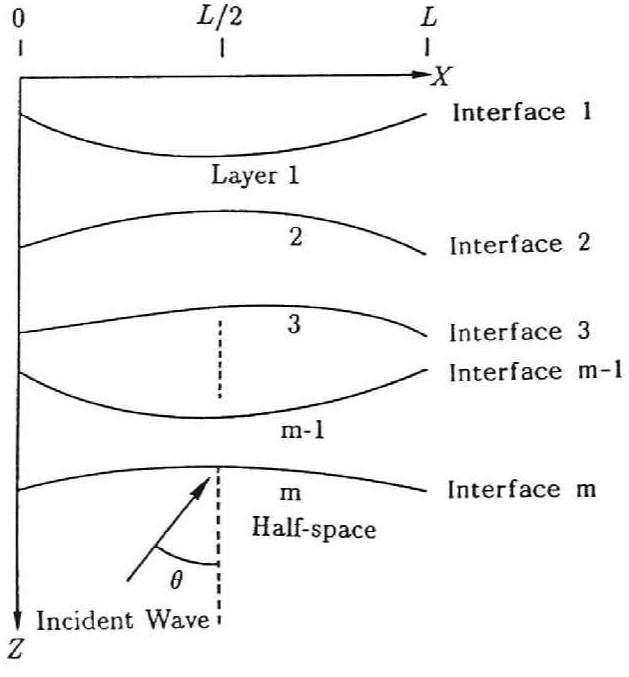

Fig. 3.13 Subsurface structure with curved interfaces [22].

The medium consists of isotropic (m-1)-th layers with a shear wave velocity, β_j (j=1,...,m-1), and the density, ρ_j (j=1,...,m-1), that overlie a isotropic half-space with a shear wave velocity of β_m and density of ρ_m. The depth to the j-th interface, $\zeta^{(j)}(x)$, is a function of x alone. Displacements in the j-th layer and in the lowest half-space are

$$U_j = \int_{-\infty}^{\infty} (A_j(k)e^{i\nu_j z} + B_j(k)e^{-i\nu_j z})e^{ikx}dk \tag{3.50}$$

$$U_m = e^{i(k_0 x - \nu_0 z)} + \int_{-\infty}^{\infty} A_m(k)e^{i(kx+\nu_m z)}dk \tag{3.51}$$

in which k is the x-component of the wave-number, A_j, B_j, and A_m are unknown coefficients, and k_0 and ν_0 are the x and z components of the wave-number of the incident wave.

The interface conditions of displacement and stress are

$$U_{j-1}(x,\zeta^j(x)) = U_j(x,\zeta^j(x)) \tag{3.52}$$

$$\tau_{j-1}(x,\zeta^j(x)) = \tau_j(x,\zeta^j(x)) \tag{3.53}$$

The two integral equations, given by substituting Eq.(3.50) in Eqs.(3.52) and (3.53), are converted into infinite-sum equations. These infinite-sum equations are derived by assuming a periodicity in the interface depth, $\zeta^{(j)}(x)$. They are valid for the discrete wave-number

$$\mathbf{G}_s^{(j)}\mathbf{A}^{(j)} = \mathbf{G}_d^{(j-1)}\mathbf{A}^{(j-1)} \tag{3.54}$$

in which **A** is the unknown coefficients matrix and **G** is the known matrix containing interface conditions. After approximating the infinite-sum equations by use of the finite-sum equations, they are expressed as

$$k_n = k_0 + \frac{2\pi n}{L} \qquad (n = 0, \pm 1, \pm 2, \cdots) \tag{3.55}$$

in which **G** is the matrix which depends on the wave-number and shape of the interface. The free surface and interface conditions between the (m-1)-th and m-th layers can be used to rewrite the linear equation;

$$\mathbf{D}\cdot\mathbf{A} = \mathbf{H} \tag{3.56}$$

in which

$$\mathbf{D} = \begin{bmatrix} \mathbf{G}^{(1)} & 0 \\ \mathbf{G}_d^{(m-1)}\mathbf{E} & -\mathbf{G}^{(m)} \end{bmatrix} \tag{3.57}$$

$$\mathbf{A}^T = \left\{(\mathbf{A}^{(1)})^T, (\mathbf{A}^{(m)})^T\right\} \tag{3.58}$$

$$\mathbf{H}^T = \left\{(\mathbf{H}^{(1)})^T, (\mathbf{H}^{(m)})^T\right\} \tag{3.59}$$

$$\mathbf{E} = \mathbf{R}^{(m-1)}.\mathbf{R}^{(m-2)}.\ldots.\mathbf{R}^{(2)} \tag{3.60}$$

$$\mathbf{R}^{(j)} = \left[\mathbf{G}_s^{(j)}\right]^{-1} \mathbf{G}_d^{j-1} \tag{3.61}$$

Substitution of $A_n^{(1)}$ and $B_n^{(1)}$ in the following equation gives the approximate solution, $U(\omega)$, of the wave field in the frequency domain;

$$U(\omega) = \sum_{n=-N}^{N} (A_n^{(1)} e^{i\nu_n^{(1)}\zeta^{(1)}(x)} + B_n^{(1)} e^{-i\nu_n^{(1)}\zeta^{(1)}(x)})\, e^{ik_n x} \tag{3.62}$$

3.3.2 Identification of a Curved Interface

The arrangement of an array of seismographs set up by Osaka Gas Co., Ltd. [23] is shown in Fig.3.14 (a), and the ground profile of the area in (b). These layered media have non-uniform soil layer as judged from the boring data. The media can be divided approximately into two layers. The respective shear wave velocities and densities of the upper and lower layers are 360 m/sec, 430 m/sec, and 1.7 t/m^3, 1.8 t/m^3. This ground profile was modeled as shown in Fig.3.15, the shape of the interface being like a basin because the Discrete Wave-number method requires the assumption of the periodicity of interface width, $\zeta(x)$. Examples of calculated transfer functions at points 10, 20, and 30 in Fig.3.15 are shown in Fig.3.16 (a), (b), (c).

Once transfer functions are obtained, the response time histories of the surface ground can be calculated (Fig.3.17). The input motion is Ricker's wavelet, of which

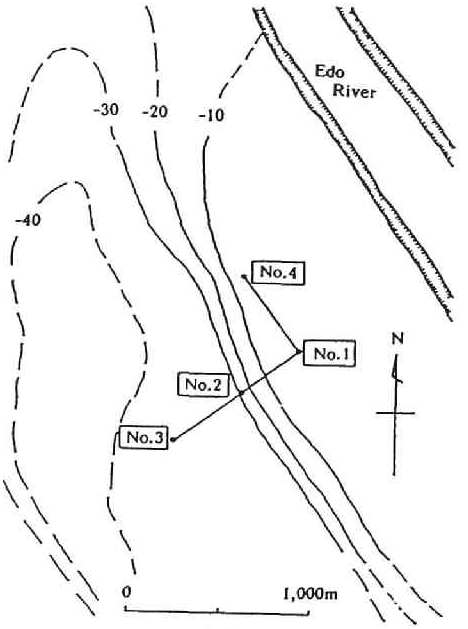

(a)

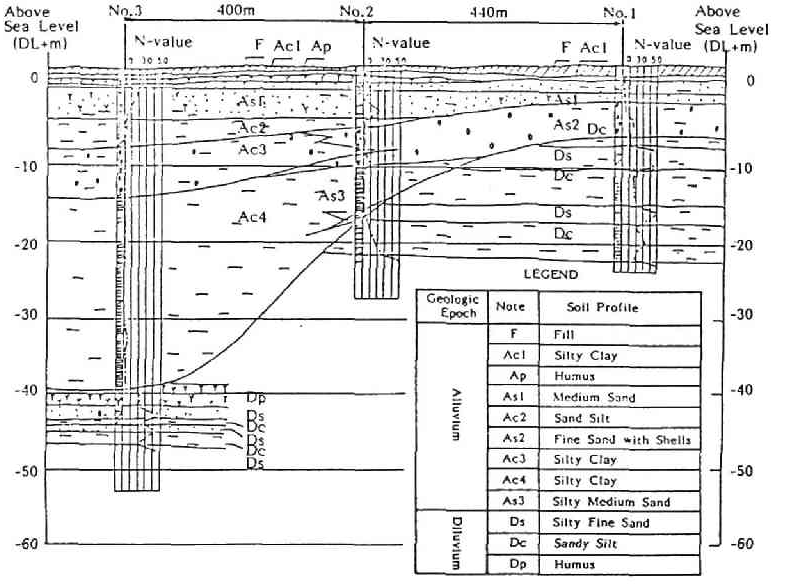

(b)

Fig. 3.14 Observation points: (a) arrangement of the seismograph array, (b) ground profile.

predominant period is 0.5 sec. The number of imaged observation points is 64, and each point is arranged in the same interval.

The mean powers and spatial correlations are computed in order to determine the spatial variation of ground motion on the irregular profile. The mean power, $P_m(x)$, as expressed by the response waves, is

$$P_m(x) = \frac{1}{N} \sum_{n=0}^{N} u^2(x, n\Delta t) \tag{3.63}$$

in which u(x,t) is the displacement time history of a point. Spatial variations in the mean power for different incident angles are shown in Fig.3.18. The abscissa is the separation distance from the fixed origin. Mean power has a peak at a point above the irregular part of the interface because of the focusing of scattering waves; therefore, spatial stationary ground motion can not be assumed.

The spatial correlation function is

$$R_{XT}(x_1,x_2,\frac{x_1-x_2}{c}) = \frac{1}{T}\int_0^T u\,(x_1,t)\; u\,(x_2,t+\frac{x_2-x_1}{c})dt \tag{3.64}$$

in which T is the duration and c the apparent velocity of the wave. The correlation coefficients obtained for three incident angles are shown in Fig.3.19. The values are normalized by R(0,0,0). Plot data for the incident angle of 1° in Fig.3.19 suggest that these correlation coefficients contain information about the shape of the irregular interface. Thus, this shape of the irregular interface can be identified by the use of the mean powers and correlation functions. The spatial correlation functions shown in Fig.3.19 include the effect due to the phase delay caused by lateral wave propagation. This effect is eliminated by shifting the time axis of the response as much as $(x_2-x_1)/c$ in Eq.(3.64). The functions obtained after this effect is eliminated are given in Fig.3.20. The coefficients express the approximate shape of the irregular boundary, but they still contain the effect of the mean powers which is not constant at each point. The responses can be divided by their own mean powers to eliminate this. The spatial correlation coefficients after normalization are shown in Fig.3.21: The effects of both phase delay and mean power are eliminated. The functions show the shape of the irregular interface regardless of the incident angle.

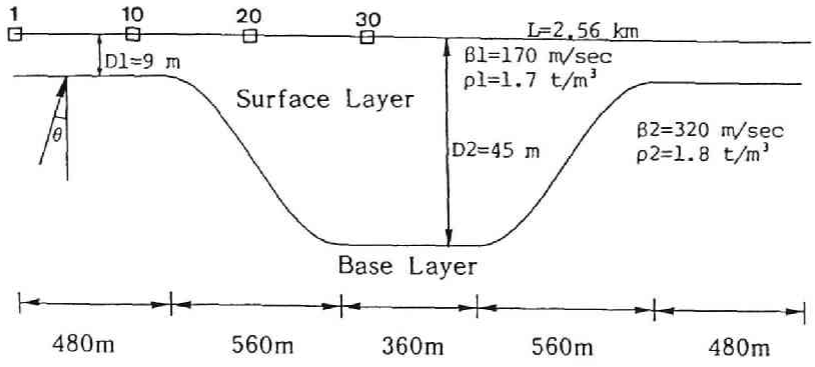

Fig. 3.15 Ground model.

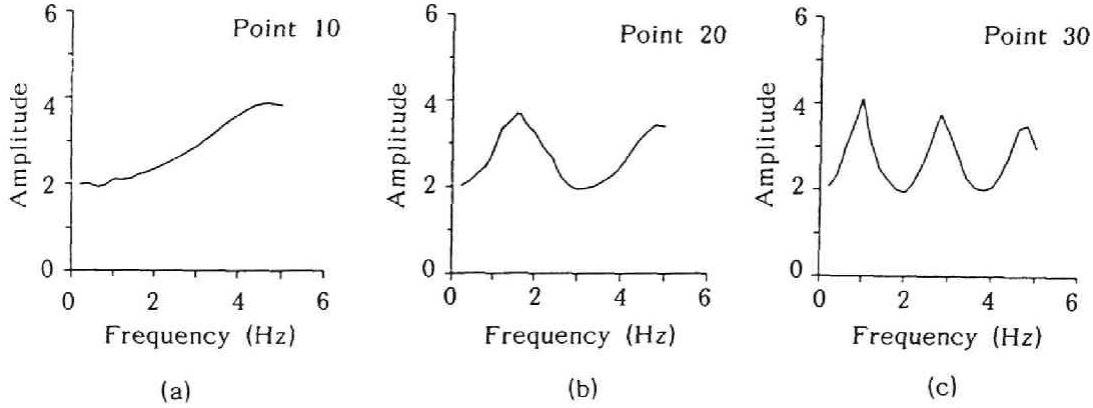

Fig. 3.16 Transfer functions calculated by the D-W method.

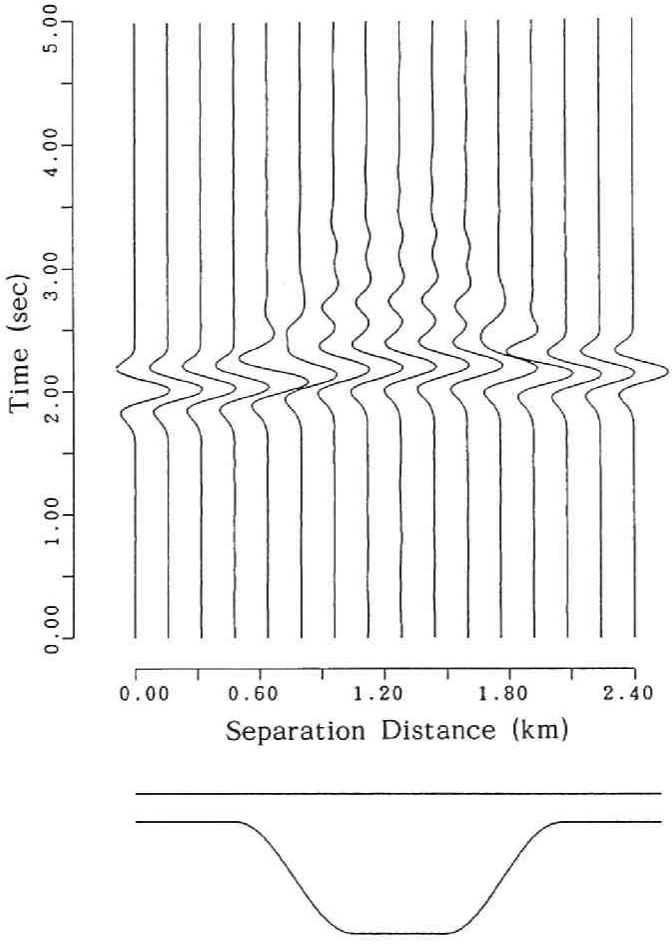

Fig. 3.17 Response time histories of the surface ground (Ricker's wavelet input)

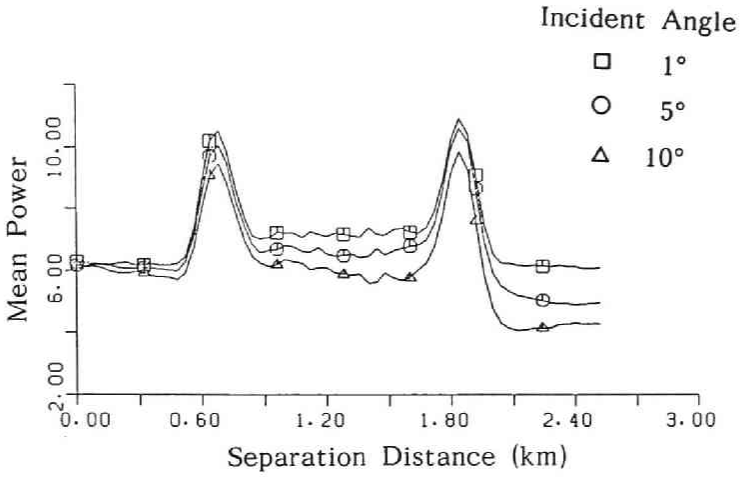

Fig. 3.18 Spatial variation of mean powers.

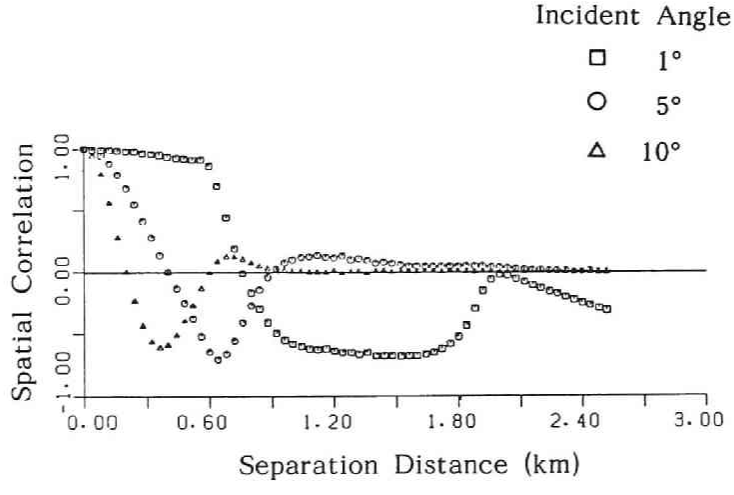

Fig. 3.19 Spatial correlation coefficients.

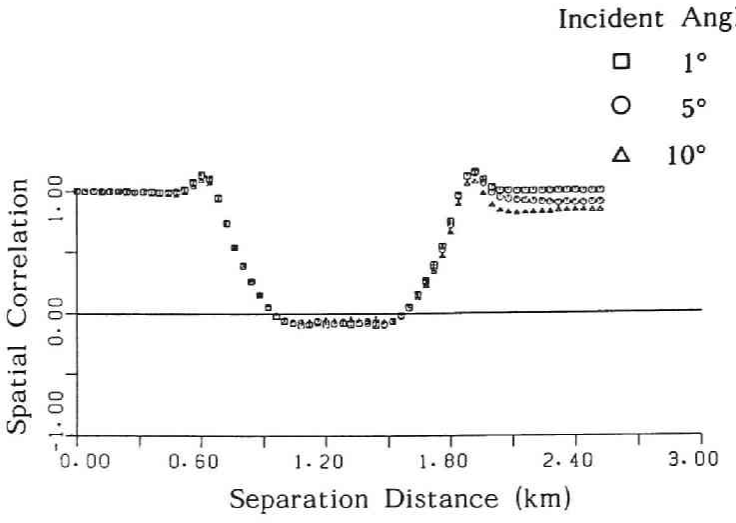

Fig. 3.20 Spatial correlation coefficients (no time delay)

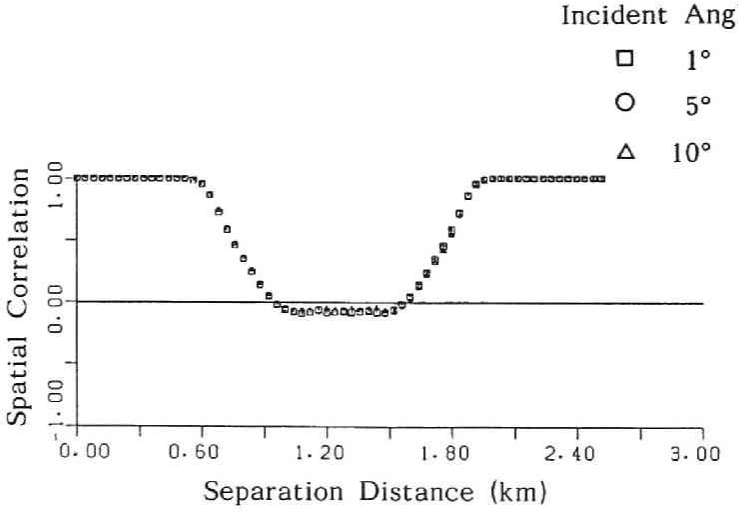

Fig. 3.21 Spatial correlation coefficients (no time delay, constant mean power)

3.3.3 Identification of Non-uniformity of Subsurface Ground

In the previous section, the non-uniformity of the interface in the soil media was shown to cause variation in surface ground motion; therefore, the search for irregular boundaries in layered media is an important engineering concern. Autoregressive pattern recognition is here applied to specify the irregular part of the interface. This method was first developed by Bois [24] to delimit the boundaries of oil and gas reservoirs. Pattern-recognition involves two phases; a descriptive phase and a decision rule. The auto-regressive process here is used in the first phase, and cluster analysis in the second. On the assumption that the response time history on the surface ground is an output of a linear filter for which the input is white noise, the path from the source to the site is a kind of linear filter.

Consider a time series taken from a random process, y(t). It can be expressed by the M-th order autoregressive process defined from the sequence of M coefficients, α_k.

The M-th order autoregressive process is

$$y_t = - \alpha_1 y_{t-1} - \alpha_2 y_{t-2} - \cdots - \alpha_M y_{t-M} + a_t \tag{3.65}$$

in which α_k(j=1,2,...,M) is the AR coefficient, and a the input data.

There are two general techniques for estimating the unknown coefficients a_1,..., a_m: One, the Yule-Walker [25] method, involves solving the Toeplitz equations, and requires explicit knowledge of the autocorrelation function, ϕ_τ, of the input y_t. The other, developed by Burg [26] estimates AR parameters without *a priori* knowledge of the autocorrelation function. This latter method is used here. Its qualitative description is as follows:

The average of the sum of the mean square prediction and mean square hindsight errors for the (m+1)-length prediction error (PE) filter is

$$P_m = \frac{1}{2(N-m)} \sum_{i=1}^{N-m} \left[(x_{i+m} + \sum_{s=1}^{m} a_{ms} x_{i+m-s})^2 + (x_i + \sum_{s=1}^{m} a_{ms} x_{i+s})^2 \right]^2 \tag{3.66}$$

To obtain a recursive solution, the coefficients a_{m1}, a_{m2}, ..., $a_{m,m-1}$ of the (m+1)-length PE filter are written in terms of the coefficients $a_{m-1,1}$, $a_{m-1,2}$, ..., $a_{m-1,m-1}$ of the m-length PE filter which is known from step m-1. This is accomplished by use of the Toeplitz recursion;

$$a_{ms} = a_{m-1,s} + a_{mm}a_{m-1,m-s}\,, \qquad s = 1, 2, \cdots, m\text{-}1 \tag{3.67}$$

Next, this recursion Eq.(3.67) is substituted in Eq.(3.66), after which P_m is minimized with respect to the last coefficient a_{mm} by setting

$$\frac{\partial P_m}{\partial a_{mm}} = 0 \tag{3.68}$$

In this manner, the coefficient a_{mm} is obtained in the form

$$a_{mm} = -\frac{2\sum_{i=1}^{N-m} b_{mi}b'_{mi}}{\sum_{i=1}^{N-m} (b_{mi}^2+b'^2_{mi})} \tag{3.69}$$

in which

$$b_{mi} = \sum_{s=0}^{m} a_{m-1,s}\, x_{i+s} \tag{3.70}$$

$$b'_{mi} = \sum_{s=0}^{m} a_{m-1,s}\, x_{i+m-s} \tag{3.71}$$

and where $a_{m0}=1$ and $a_{ms}=0$ for $s>m$. Once a_{mm} has been computed, the remaining coefficients a_{m1}, a_{m2}, ..., $a_{m,m-1}$ are determined from the recursion.

The optimal order is obtained by minimizing the FPE (final prediction error) proposed by Akaike.

$$E[(\hat{x}_t - x_t)^2] \rightarrow \min. \tag{3.72}$$

An estimate, FPE_M, of the FPE for an autoregressive model of order M is calculated from the definition

$$(FPE)_M = \frac{N + (M+1)}{N - (M+1)}\,\sigma_M^2 \tag{3.73}$$

The estimation of the power spectrum density, $\hat{S}(f)$, is given by the use of order M;

$$\hat{S}(f) = \frac{\sigma_M^2}{\left|1 - \sum_{m=1}^{M} a_M(m) \exp(-i2\pi fm)\right|} \qquad (3.74)$$

Eq.(3.60) shows that an estimated value for S(f) can be obtained merely by knowing the coefficient $a_M(m)$. As AR coefficients completely determine the shape of the power spectrum, these coefficients can be used as feature extractors. Response time histories are calculated for the case when Ricker's wavelet is incident to the model ground of the irregular profile at an angle of 1° . Values for AR coefficients of responses at three points are shown in Fig.3.22. The abscissa is the j-th AR coefficient α_j (j=1, 2 ,... , 8). Because of the large fluctuations for α_3 and α_4, these two coefficients are plotted on a Cartesian graph.

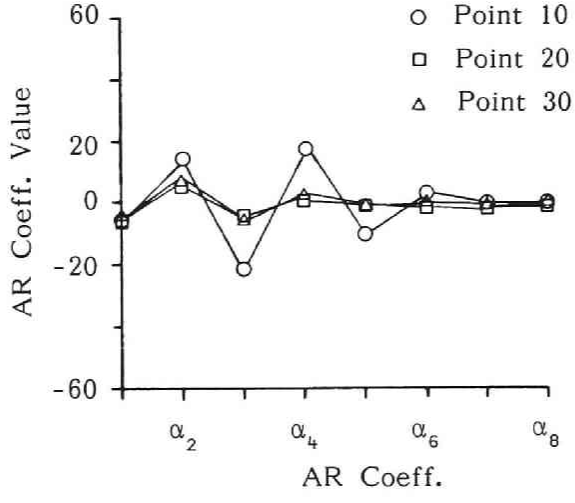

Fig. 3.22 AR coefficient values at three points.

The dots corresponding to the values at these observation points are classified in clusters. This is the second phase, or decision rule. The cluster analysis method classifies groups without subjective information and according to the algorithm [27]:

a) The whole group initially is divided into n_g clusters. The center coordinates, (x_k, y_k), of each cluster, C_k, (the number of elements is n_k) then is determined.

b) The summation of the square of the distance between the element and the gravity center

is calculated from the following Eq.(3.75)

$$S_e = \sum_{k=1}^{n_g} \sum_{i=1}^{n_k} \left\{ (x_i - \bar{x}_k)^2 + (y_i - \bar{y}_k)^2 \right\} \tag{3.75}$$

c) Select an arbitrary element (x_r, y_r) from cluster C_k.

d) Move element (x_r, y_r) from cluster C_k to cluster C_p. If the S_e value increases, the element (x_r, y_r) remains in C_k. If not, the element transfers to cluster C_p.

e) Renew the number of elements, n_k, and the gravity center (x_k, y_k).

f) If there are no transferred elements after n trials, go to stop.

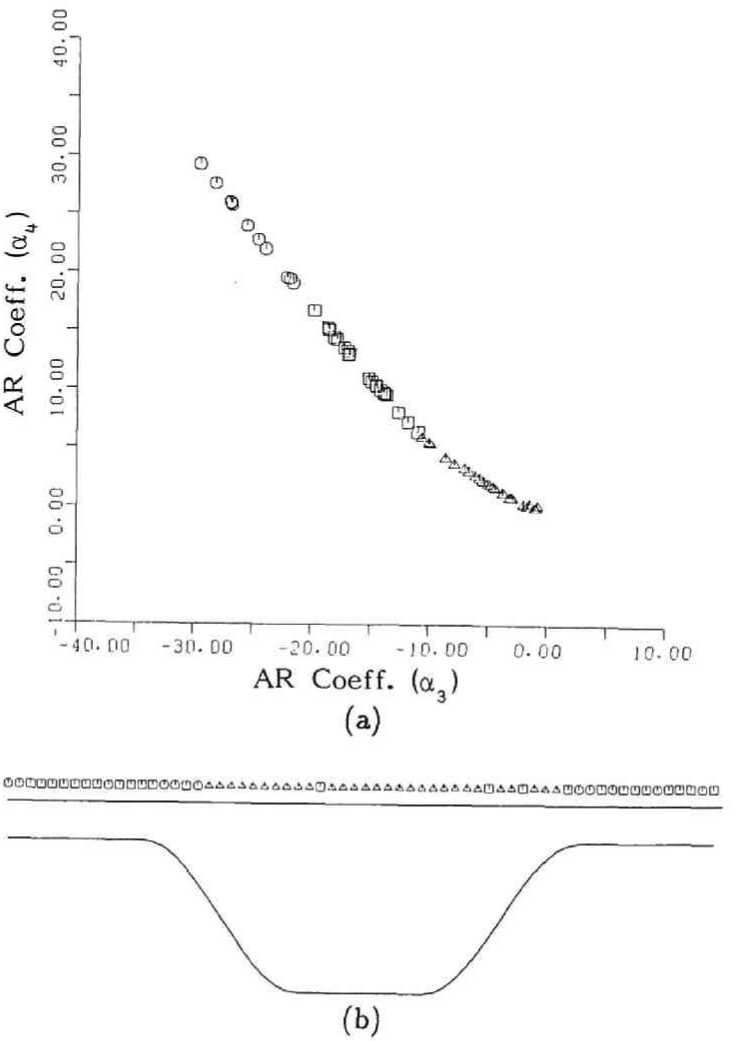

Fig. 3.23 Clustered AR coefficients and their projection to ground surface.

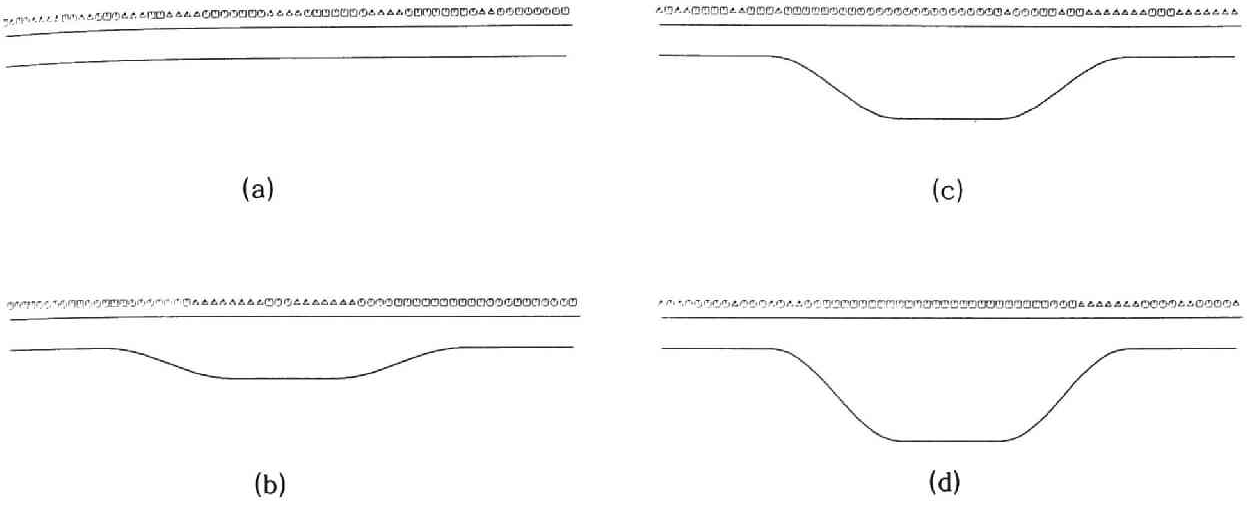

Fig. 3.24 Recognition of the subsurface irregular part for various depths of the thick layer.

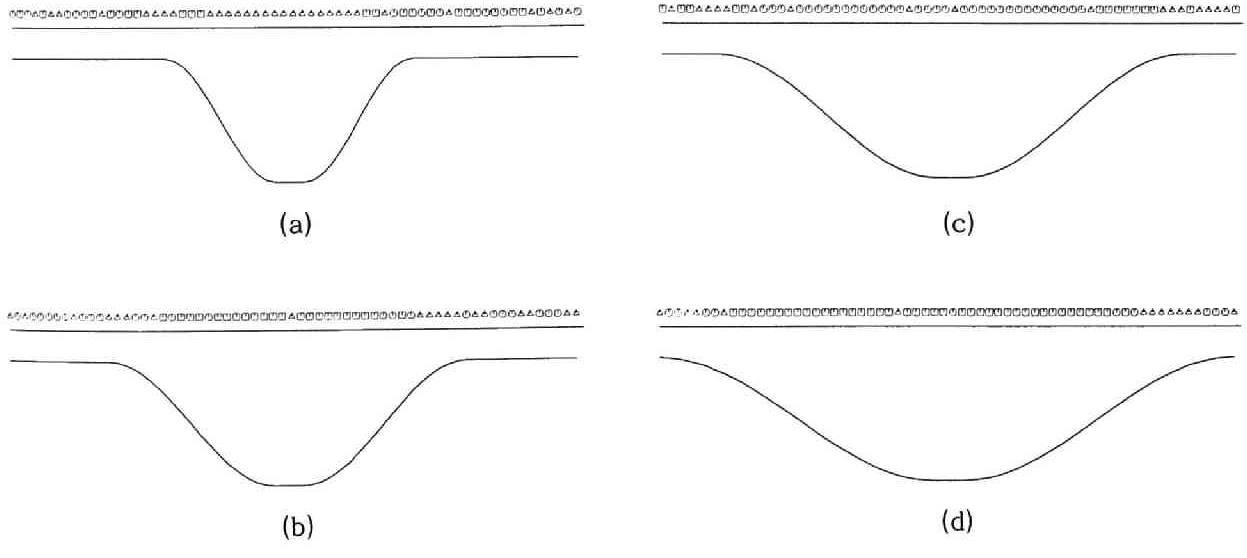

Fig. 3.25 Recognition of the subsurface irregular part for various interface shapes.

On the assumption that the number of clusters is three, AR coefficients are plotted on a Cartesian graph (Fig.3.23 [a]), the clustered elements arranged on the irregular profile being shown in Fig.3.23 (b). Triangular symbols can be seen on the thick layer. Circles and squares on the thin layer indicate the transit part between the thin and thick layers. Results obtained when the ratio of the depth of the thick layer to that of the thin layer is changed are shown in Fig.3.24. The ratios of (a) (d) are 1.0, 2.0, 3.0 and 4.0. It becomes difficult to recognize the transit part as the ratio becomes smaller. The case for when the length of the irregular part is changed is shown in Fig.3.25. The lengths of the irregular part of (a) - (d) are 480, 720, 960, and 1200 m. The transit part can be determined and the existence of the irregular interface recognized. The AR coefficient recognition method that incorporates cluster analysis therefore is useful for detecting the existence of an irregular profile.

3.4 Modeling Relative Displacement on Ground with a Non-uniform Profile

3.4.1 Modeling Ground Motion

The power spectrum of relative displacement, $S_{\Delta u \Delta u}(\omega)$, between two points, x and y, is

$$S_{\Delta u\, \Delta u}(\omega) = S_{xx}(\omega) + S_{yy}(\omega) - 2\mathrm{Re}[S_{xy}(\omega)] \tag{3.76}$$

in which $S_{xx}(\omega)$ and $S_{yy}(\omega)$ are the power spectra of the responses of the points, x and y, and $S_{xy}(\omega)$ is the cross-spectrum. The mean square of the relative displacement is obtained by integrating Eq.(3.76).

$$E[\Delta u^2] = \int_{-\infty}^{\infty} S_{xx}(\omega)\, d\omega + \int_{-\infty}^{\infty} S_{yy}(\omega)\, d\omega - 2\int_{-\infty}^{\infty} \mathrm{Re}[S_{xy}(\omega)]\, d\omega \tag{3.77}$$

The cross-correlation function, $R(x,y,\tau)$, is given by

$$R(x,y,\tau) = \int_{-\infty}^{\infty} S_{xy}(\omega)\, e^{-i\omega\tau} d\omega \tag{3.78}$$

The third term on the right side of Eq.(3.77) is rewritten substituting zero for τ as

$$R(x,y,0) = \int_{-\infty}^{\infty} S_{xy}(\omega)\, d\omega \tag{3.79}$$

The autocorrelation function, $R(x, \tau)$, is

$$R(x,\tau) = \lim \frac{1}{T} \int_{-\frac{T}{2}}^{\frac{T}{2}} u_x(t)\, u_x(t+\tau)\, dt \tag{3.80}$$

The power spectra, $S_{xx}(\omega)$ and $S_{yy}(\omega)$, are expressed by

$$S_{xx}(\omega) = \int_{-\infty}^{\infty} R(x,\tau)\, e^{-i\omega\tau} d\tau \tag{3.81}$$

The spatial correlation coefficients of the responses and those of two kinds of layered media are given in Fig.3.26 (a). The thicknesses of the layered media are 9 and 45 m for the shallow and deep layers. Solid line 1 corresponds to the shallow layer and line 2 to the deeper one. Square symbols, show the exact values of the spatial correlation coefficients calculated from the response time histories. The letters A - H indicate points on the irregular interface shown in Fig.3.26 (c). The spatial correlation coefficients shift from the line for the shallow layer (A - B, G - H) to the line for the deep layer (D - E) at the transit part of the interface. The following spatial correlation model that uses the correlation function of two-layered media is proposed: The chain line in Fig.3.26 (a) represents the average of two solid lines. The proposed correlation function is assumed to cross this line at the center of the transit part of the irregular interface (C and F). The broken line in Fig.3.26 (a) represents the proposed spatial correlation coefficients. Fig.3.26 (b) gives the autocorrelation coefficients of the responses and those of the two kinds of layered media. The time lag, τ, is 0.2 sec. The solid lines and square symbols are the same as in Fig.3.26 (a). From the case studies, if the predominant frequency of the input motion is higher than the first natural frequency of the deeper layer ($\beta_1/4D_2$), the autocorrelation coefficients have two peaks at the transit parts. If lines, 1, 2 and 3 in Fig.3.26 (b) are replaced with a, b and c, the proposed line 3 is

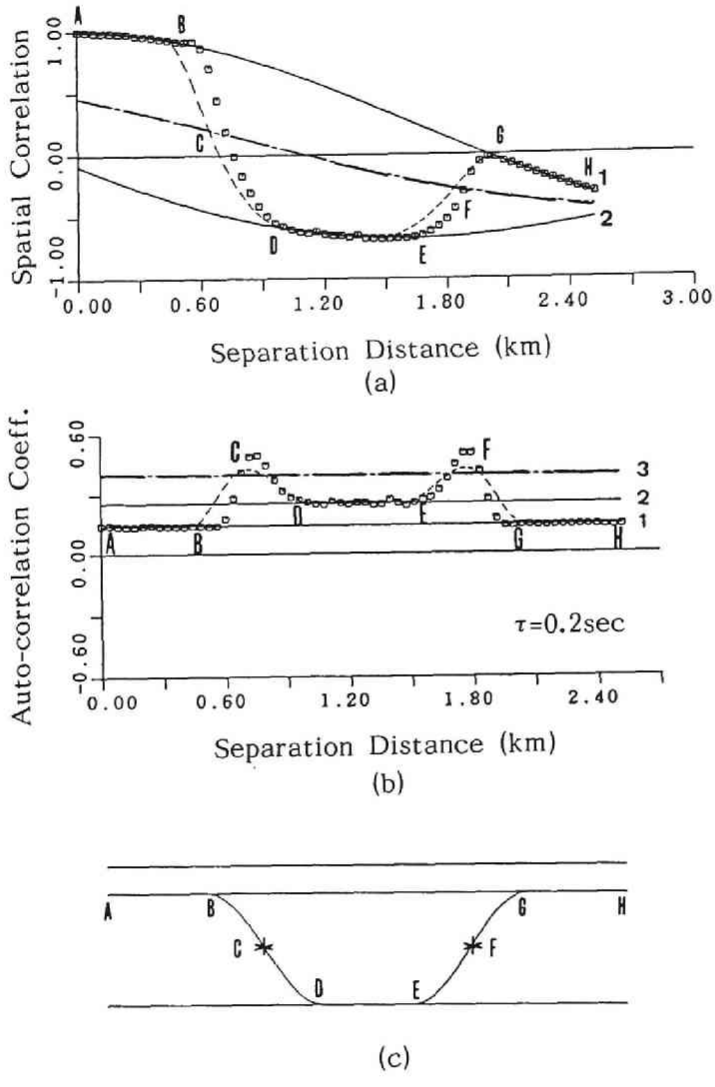

Fig. 3.26 Modeling of spatial correlations (a) and autocorrelation coefficients (b).

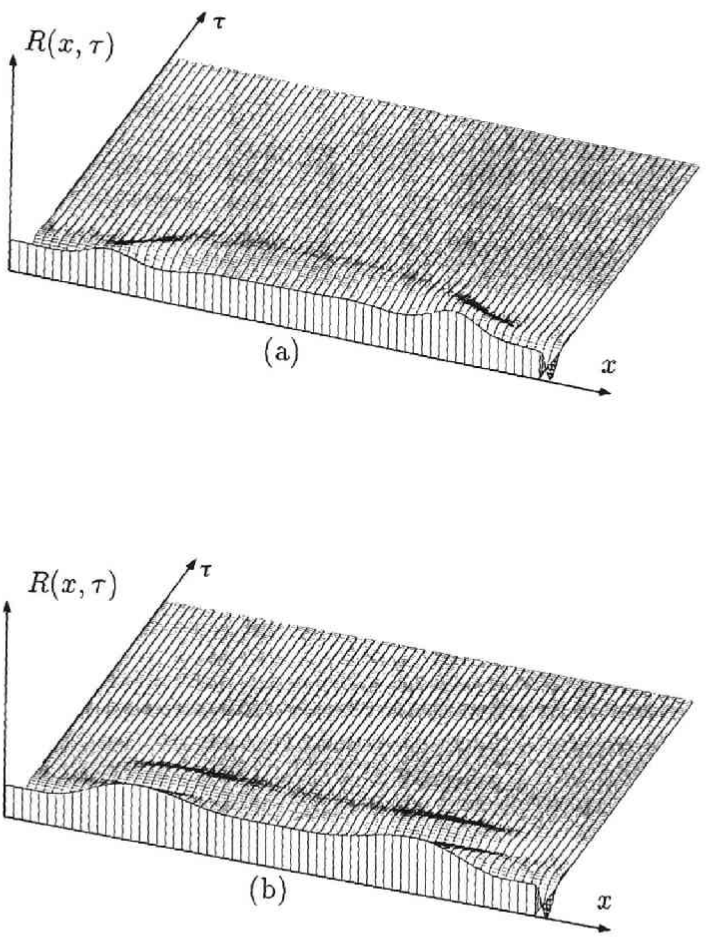

Fig. 3.27 Autocorrelation function: (a) exact values calculated directly from the responses, (b) values estimated by the proposed method.

$$c = |b - a| + \max(a, b) \tag{3.82}$$

The autocorrelation coefficients are assumed to cross line 3 at the center of the transit part of the irregular interface (C and F). This model approximates the peaks of the autocorrelation coefficients. If lines 1 and 2 coincide, line 3 will approach those lines. The broken line shown in Fig.3.26 (b) is the proposed one. Autocorrelation functions for each time lag are shown in Fig.3.27. This figure gives the exact values calculated directly from the responses and (b) the autocorrelation function according to the proposed model. The power spectrum of an arbitrary point, x, is obtained by Fourier transformation of the time history, R(x,t).

3.4.2 Relative Displacement

The first and second terms on the right side of Eq.(3.77) are computed by integrating these power spectra. This autocorrelation function and the spatial correlation shown in Figs.3.26 (a) and 3.27 (b) are used to calculate the mean square of the relative displacement (Fig.3.28). The square symbols represent exact values, the solid line estimated ones. The estimated values show the features of the curves of the exact relative displacements.

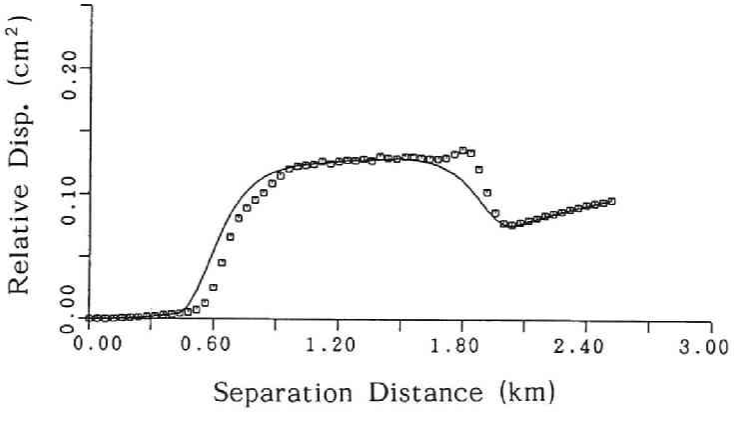

Fig. 3.28 Comparison of the mean squares of the relative displacements.
(squares: exact values, solid line: estimated values)

Observed records are used to check the validity of above procedure. The arrangement of the seismograph array is shown in Fig.3.29, in which (a) is the cross-section and (b) the plane. The mean square of the relative displacement can be calculated if earthquake records observed at the two points, No.1 and No.3 in Fig.3.29 are used. Many earthquakes have been recorded at this site. Of these, the record of the earthquake which occurred off of Ibaragi Prefecture on 22 February, 1981 is used. Its magnitude was 4.7, epicentral distance 95 km, and maximum acceleration 4.72 gal. The observed seismograms of the NS- and EW-components are synthesized to the transverse direction for the epicenter. The synthesized displacement waves of three observation points: Nos.1, 2 and 3, are shown in Fig.3.30. The estimated relative displacements based on the records at Nos.1 and 3 are shown as a solid line in Fig.3.31. The mean squares of the relative displacements of Nos.2 and 3 to No.1 are plotted as circles (o). The observation points are too few to discuss the outline of the estimated relative displacement. But, for the two observation pairs used, the line estimated by modeling the spatial correlation and auto-correlation function approximates the relative displacement calculated directly from observed waves.

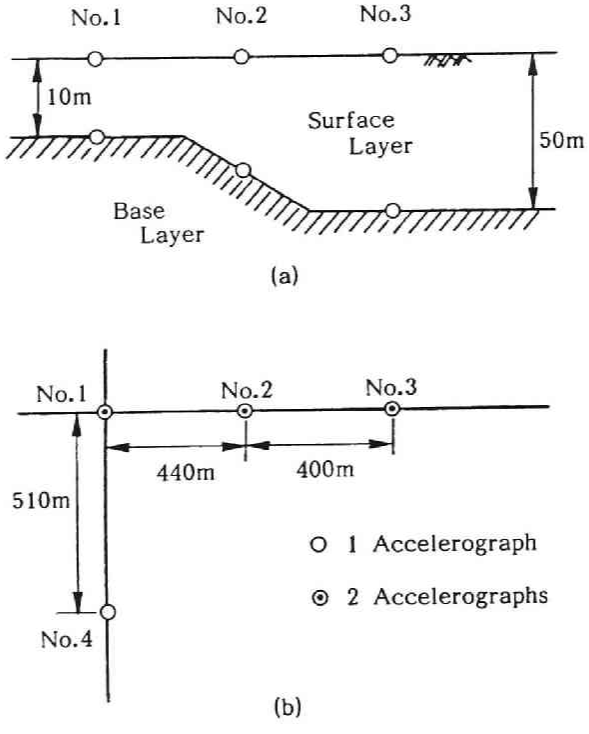

Fig. 3.29 Arrangement of the seismograph array:
(a) cross-section, (b) plane.

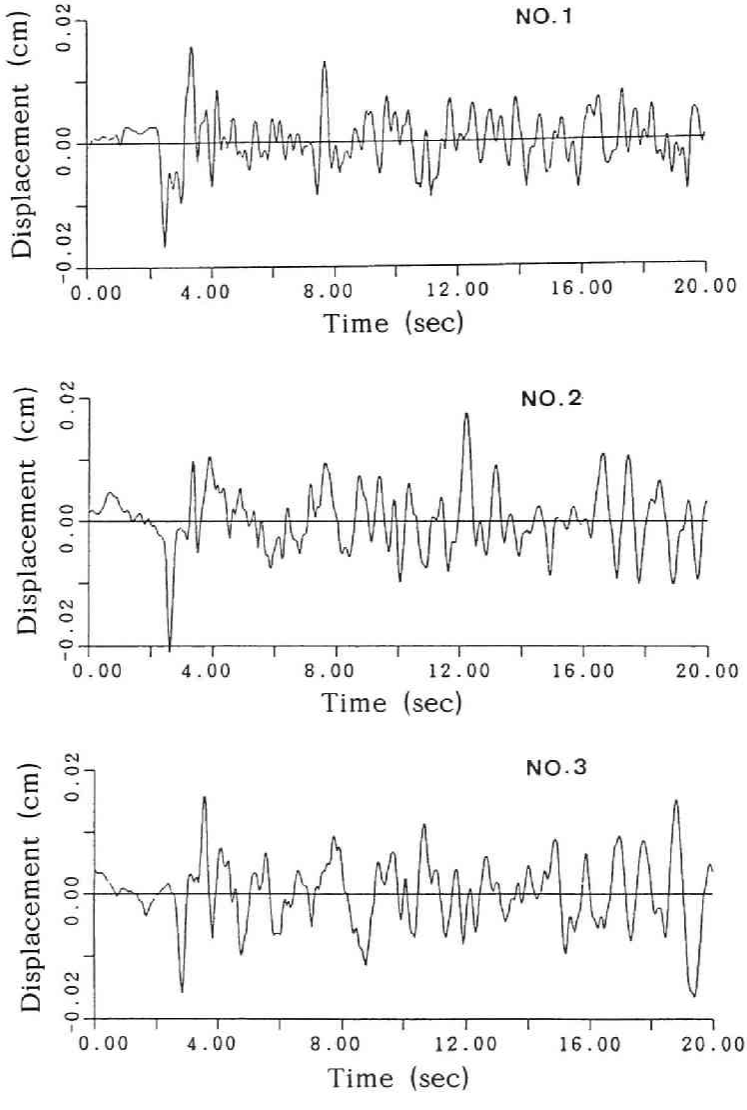

Fig. 3.30 Displacement records at three points: Nos.1, 2 and 3.

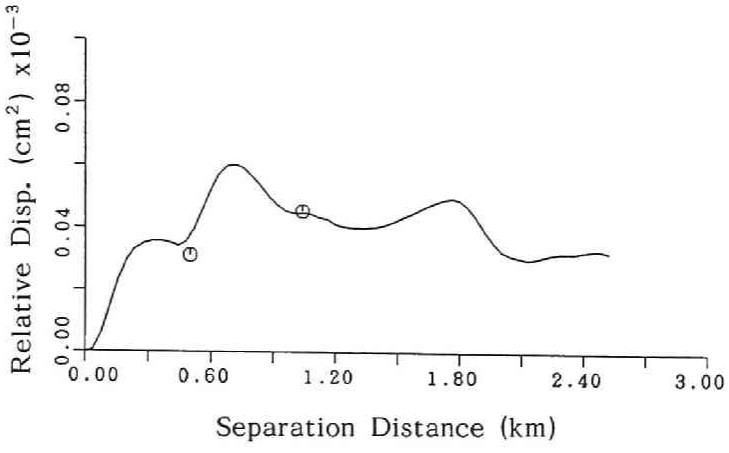

Fig. 3.31 Comparison of calculated (solid line) and observed (circles) relative displacements.

3.5 Conclusions

In this chapter, the site effect was investigated by focusing on the characteristics of the propagating wave and layered media with an irregular interface. The procedures used and results are

(1) The principal techniques for detecting phase velocities were compared and investigated in order to develop a new technique. The phase difference and cross-correlation methods give stable results under noise-free conditions. But, results become unstable if the signal is contaminated by noise. The sums and differences and cross-multiplication methods do not give as instable results as the first two methods. But, as these latter methods calculate phase velocities from the delay time of the phase, the sampling interval of the signal must be as small as possible when the interstation distance is short and the wave velocity fast. Even if the waves at two points satisfy the relation between the input and output signals in the Wiener filter, noise is not eliminated in the filtering process based on least square criteria.

(2) If the classical techniques developed for measuring the phase and group velocities in the field of long period seismology are used to detect the phase velocities in engineering terms, the measurement error of the phase becomes large when noise exists. Therefore the S/N

ratio must be appropriately improved. The estimation error of the phase velocities is improved by use of the Kalman filter. For example, when the interstation distance is 100 m, the mean power of the noise is decreased by half by use of this filter which corresponds to the stacking of eight cross-correlograms.

(3) Phase velocities are detected from the observed records by use of the Kalman filter. The general tendencies for dispersion curves obtained by the cross-correlation and the Kalman filter techniques are similar, but a difference of 500 m/sec can be seen at some frequencies.

(4) The shape of an irregular interface can be identified by the use of AR coefficients and is obtained by analyzing the observed record on the surface ground. The AR coefficient recognition method that incorporates cluster analysis is useful for detecting the existence of an irregular profile.

(5) Simulation of ground motion on layered media that have an irregular interface and the investigation of the characteristics of spatial variations in ground motion make possible derivation of the shape of the irregular interface when the spatial correlations and mean powers of the response time histories are taken into account.

(6) The relative displacements can be calculated by modeling the spatial correlations and autocorrelation coefficients. The estimated relative displacements are in good agreement with the exact values.

References

[1] Sato, Y. Theory of Elastic Waves, Iwanami-Shoten, 1978, pp.220-292 (in Japanese).

[2] Landisman, M., A. Dziewonski and Y. Sato. Recent Improvement in the Analysis of Surface Wave Observation, Geophys. J. R. Astr. Soc., 17, pp.369-403, 1969.

[3] Dziewonski, A., S. Bloch and M. Landisman. A Technique for the Analysis of Transient Seismic Signals, Bull. Seism. Soc. Am., Vol.59, No.1, pp.427-444, 1969.

[4] Bloch, S. and A. L. Hales. New Techniques for the Determination of Surface Wave Phase Velocity, Bull. Seism. Soc. Am., Vol.58, No.3, pp.1021-1034, 1968.

[5] Nakanishi, I. Phase Velocity and Q of Mantle Rayleigh Waves, Geophys. J. R. Astr. Soc., 58, pp.35-59, 1979.

[6] Steven, R. T. and M. N. Toksoz. Measurement of Interstation Phase Velocity and Group Velocity and Q Using Wiener Filtering, Bull. Seism. Soc. Am., Vol.72, No.1, pp.73-91, 1982.

[7] Shima, E. Seismic Surface Waves Detected by the Strong Motion Acceleration Seismograph, Proc. 3rd Japan Earthq. Eng. Symp., pp.277-284, 1970 (in Japanese with English abstract)

[8] Sato, T. and Y. Sawada. Experimental Investigations on Propagation of Seismic Surface Wave, Proc. 3rd Japan Earthq. Eng. Symp., pp.263-267, 1970 (in Japanese with English abstract).

[9] Kamiyama, M. Estimation of Velocity Structures of the P- and S-wave from Measurements of Microtremors, Proc. 25th Japan National Conf. on Soil Mech. and Foundation Eng., pp.833-836, 1976 (in Japanese).

[10] Kotsubo, S. and J. Harada. Response Analysis of Bridges Subjected to Different Earthquake Waves at Each Support, Proc. JSCE, No.175, pp.39-48, 1970 (in Japanese with English title).

[11] Toki, K. Detection of Phase Velocity from Strong-Motion Accelerograms, Proc. 4th Japan Earthq. Eng. Symp., pp.265-272, 1970 (in Japanese).

[12] Toki, K. and M. Kubota. Nonlinear Response of Continuous Bridge to Travelling Seismic Wave, Proc. 5th Japan Earthq. Eng. Symp., pp.1065-1072, 1978 (in Japanese).

[13] Toki, K. and S. Imamura. Response of a Continuous Bridge to Seismic Waves with Phase Differences, Proc. Annual Conf. of Kansai Branch of JSCE, I-54, 1979 (in Japanese).

[14] Werner, S. D., C. Lee, H. L. Wong and M. D. Trifunac. Structural Response to Travelling Seismic Waves, Jour. Struc. Dev., ASCE, ST12, pp.2547-2564, 1979.

[15] Kawakami, H. and Y. Sato. Effect of Deformation of Seismic Waves on the Estimated Value of Ground Relative Displacement or Strain, Proc. JSCE, No.337, pp.37-46, 1983 (in Japanese with English abstract).

[16] Harada, T. Probabilistic Modeling of Spatial Variation of Strong Earthquake Ground Displacement, Proc. 8th World Conf. of Earthq. Eng., pp.605-612, 1984.

[17] Harada, T. and M. Shinozuka. Stochastic Analysis of Ground Response Variability for Seismic Design of Buried Lifeline Structures, Proc. 7th Japan Earthq. Eng. Symp., pp.595-600, 1986.

[18] Hoshiya, M., K. Ishii and H. Kurita. Simulation of Spatial and Temporally Variable Earthquake Ground Motions, Proc. JSCE, No.386/I-8, pp.359-367, 1987 (in Japanese with English abstract).

[19] Loh, C. H. and Y-H. Yeh. Spatial Variation and Stochastic Modeling of Seismic Differential Ground Movement, Earthq. Eng. and Struc. Dyn., Vol.16, pp.583-596, 1988.

[20] Loh, C. H., A. H-S. Ang and Y. K. Ang. Spatial Correlation Study of Strong Motion Array Data with Application to Lifeline Earthquake Engineering, Structural Research Series No. 533, Univercity of Illinoi, 1983.

[21] Aki, K. and K. L. Larner. Surface Motion of a Layered Medium Having an Irregular Interface Due to Incident Plane SH Waves, Jour. Geophys. Res., Vol.75, No.5, pp.933-954, 1970.

[22] Horike, M. Extension of the Aki and Larner Method to Absorbing Media with Plural Curved Interfaces and Several Characteristics of a Seismic response on a Sedimentary Basin, Zishin 2, Vol.40, pp.247-259, 1987 (in Japanese).

[23] Toki,K., Y. Fukumori, M. Sako and T. Tsubakimoto. Recommended Practice for Earthquake-resistant Design of High Pressure Gas Pipeline, Proc. International Symposium on Lifeline Earthquake Engineering, pp.349-356., 1983.

[24] Bois, P. Autoregressive Pattern Recognition Applied to the Delimitation of Oil and Gas Reservoirs, Geophysical Prospecting, Vol.28, pp.572-591, 1980.

[25] Walker, G. On Periodicity in Series of Related Terms, Proc. Roy. Soc. London, Ser.A, 131, pp.518-532, 1931.

[26] Burg, J. P. The Relationship between Maximum Entropy Spectra and Maximum Likelihood Spectra, Geophysics, Vol.37, pp.375-376, 1972.

[27] Ohsaki, Y. Guidelines for the Estimation of Seismic Ground Motion for Aseismic Design of Nuclear Power Plants, ORI Report 84-01, Ohsaki Research Institute, 1984 (in Japanese).

CHAPTER 4

ESTIMATION OF PEAK GROUND MOTION TAKING INTO ACCOUNT THE SOURCE, PATH, AND SITE EFFECTS

4.1 General Remarks

A multi-variable regression analysis that includes the magnitude of the earthquake, M; the epicentral distance, Δ; and the parameter that expresses the site condition generally is made when investigating the attenuation of peak acceleration. Because of the importance for engineering, a number of regression equations have been proposed, but the regression curve is affected by the characteristics of the data base used. Although the numbers of observed earthquake records are increasing, consistent data that show homogeneous distributions of epicentral distance and magnitude are rare, especially over a short distance and for a large magnitude. A simplified analytical method is presented with which to predict peak accelerations near the source region where the effect of the fault extent can not be ignored. To account for the fault extent, a large event is synthesized from small events that occur in part of the fault plane. This type of method was proposed first by Hartzell in a somewhat simple formula, and researchers have attempted to improve on his method in order to synthesize a large event from small events ([1], [2], [3]). Here Irikura's revised model [4], which is based on the idea that slips on the fault plane during a large event can be replaced by the spatial distribution of slips that take place during small events, is used. Therefore, sufficient high frequency components can be generated.

The equation of superposition is transformed into the frequency domain to obtain the power spectrum of the large event. The expected peak ground motion then can be evaluated in terms of three spectral moments. Peak accelerations near the fault region are expressed as a function of the fault parameters and the relative collocation between the fault and the observation site. This gives a new attenuation law that shows near-field attenuation with a flat part in the source area.

As a wave propagates through soil, its amplitude attenuates because of inertial friction. This friction effect is expressed by the dimensionless quantity, Q, which, in general,

depends on the frequency. Many equations have been proposed to express the frequency dependence of the Q-value for Japan ([5], [6], [7], [8], [9]). Using an inversion method, Iwata and Irikura [10] obtained the Q-value of the shear wave from the 1983 Nihonkai-Chubu earthquake.

The effect of the site itself also is important when predicting surface ground motion. On the assumption of seismic bed rock for which the shear wave velocity is about 3km/sec, the amplification factor between the deep bed rock and the ground surface is needed. Midorikawa et al. [11] defined the relation between the geological conditions and the amplification factor for the peak acceleration value of deep seismic bed rock. The damping effect of the propagation path and the amplification effect of the surface ground are here considered in order to obtain a realistic predicted acceleration.

Next, the time term is incorporated in the estimation of ground motion. This shows what the probability of the occurrence of an earthquake is and when one occurs. The historical records preserve information for the past few hundred years, whereas active fault data is based on seismic activity over a few million years [12]. Assuming that the stochastic populations for the historical earthquake records and active fault data are the same, both data can be combined by use of Bayes' theorem. Seismic hazard is evaluated from the combination of information. The procedure developed is used to introduce the attenuation equation of peak acceleration. The area analyzed is the Kinki district in western Japan.

The attenuation equation is derived from the simulation of the maximum response acceleration for a single degree of freedom system. The risk spectrum at bed rock level for the return period is found from the attenuation of the response spectrum. As the case study, the expected ground motion for a return period of 100 years at Osaka City is simulated using the spectrum-fitting method.

4.2 Attenuation of Peak Ground Motion

4.2.1 Method for Predicting Peak Acceleration

A fault model of the Haskell type is assumed in this analysis. The model is described by a rectangular fault with five factors: the fault length, L; fault width, W; rise time, τ; final offset of dislocation, D; and the rupture velocity, v_r. Assuming that small events are caused by the dislocation of a small area on the fault, a large event can be synthesized

by superposing these small events and taking into account the time delay caused by the propagation of rupture.

The fault model is shown in Fig.4.1. The fault plane is divided into n elements, each of which corresponds to the area of a small event. The motion of the large event, $g_L(t)$, at observation point Q is expressed by the motion of a small event, $g_S(t)$, as

$$g_L(t)=\sum_{l=1}^{N_L}\sum_{m=1}^{N_W}\sum_{n=1}^{N_D} g_S(t-t_{lmn}) \qquad (4.1)$$

in which N_L, N_W, and N_D are the number of subdivisions that respectively correspond to the fault length, fault width, and dislocation, and t_{lmn} is the time delay of the element wave. The following relation is assumed; $N_L = N_W = N_D = n$, in which n is the number of superpositions calculated by use of the ratio of the seismic moments for the large and small events.

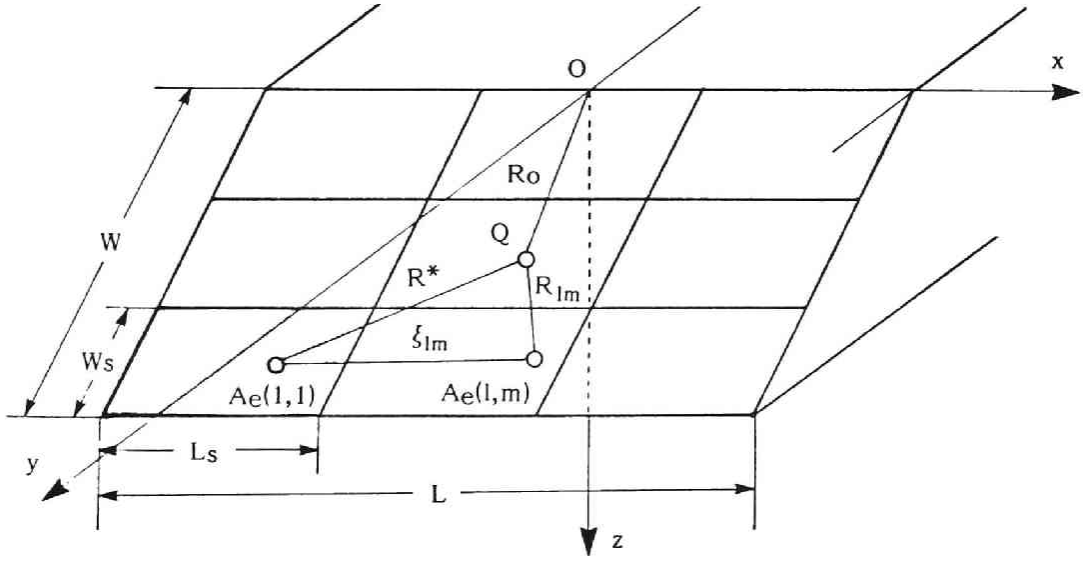

Fig. 4.1 Fault model.

Earthquake motion produced by a small event is given by

$$g_S(t) = \frac{R_{\theta\phi}}{4\pi\rho v_s^3} \frac{s(t)}{R_{lm}} \tag{4.2}$$

in which $R_{\theta\phi}$ is the radiation pattern, ρ the density of the medium, v_S the shear wave velocity, R_{lm} the distance from a fault element to the site, and s(t) the source time function. The Fourier transform of Eq.(4.2) becomes

$$G_S(f) = \frac{R_{\theta\phi}}{4\pi\rho v_s^3} \frac{S(f)}{R_{lm}} \tag{4.3}$$

in which S(f) is the source spectrum. Taking the Fourier transform of Eq.(4.1) and multiplying by its conjugate, the power spectrum of the earthquake motion of a large event is

$$P_L(f) = \frac{2}{T}\left(\frac{R_{\theta\phi}}{4\pi\rho v_s^3}\right)^2 S(f)S^*(f)\left(\sum_{l=1}^{n}\sum_{m=1}^{n}\sum_{n=1}^{n} e^{-i2\pi f t_{lmn}}/R_{lm}\right)\left(\sum_{l=1}^{n}\sum_{m=1}^{n}\sum_{n=1}^{n} e^{i2\pi f t_{lmn}}/R_{lm}\right) \tag{4.4}$$

in which T is the duration of the stationary part of the ground motion and $*$ indicates the complex conjugate.

The duration, T, is defined as

$$T = T_e - T_b + T_\alpha \tag{4.5}$$

in which T_b and T_e are the arrival times of the seismic waves originating from the initial and last rupture elements. T_α is the duration of the seismic wave generated in the last rupture element. The duration, T, is given by the empirical formula proposed by Kawashima et al. [13]. Because Irikura's revised model is used to superpose the small events, the source spectrum, S(f), has a slope of -2 in the logarithmic form for the high frequency region.

The source spectrum of acceleration becomes flat in the high frequency region because the spectrum of displacement has a slope of -2 with respect to the frequency. Therefore, the integration of the spectral moment in Eq.(4.4) becomes infinite. To eliminate this inconsistency, f_{max} is introduced. This is the corner frequency of the acceleration spectrum in the high frequency region. It has been defined by Hanks [14] and studied in detail by Aki [15]. According to Hanks, the value of f drops to a value between 20 - 30 Hz at the rock site. An f_{max} of 25 Hz was selected.

Once the power spectrum of the large event is given, the expected peak ground motion, A_{max}, is calculated as follows [16]:

$$A_{max} = p\sqrt{\lambda_0}\ , \quad p = f\ (\nu_e, \lambda_0, \lambda_1, \lambda_2) \tag{4.6}$$

in which p is the peak coefficient; λ_i (i=0, 1, 2), the spectrum moments of zero and the first and second orders; and ν_e the reduced ratio of the zero-crossing.

The expected peak accelerations were computed for several combinations of the dip angle, δ; the direction of the observation site, θ; and the starting point of rupture. The respective values of v_s , v_r, and the radiation pattern $R_{\theta\phi}$ are 3.4 km/sec, 3.0 km/sec, and 0.4. The values of the parameters used in the numerical calculations are given in Fig.4.2.

The attenuation of peak acceleration when the direction of the observation site is varied is shown in Fig.4.3. Because the starting point of rupture is fixed at element 1 (see Fig.4.2), the peak acceleration expected is highest for θ=90°, the direction of rupture propagation, and is lowest in the opposite direction. This phenomena is a kind of Doppler effect.

The attenuation of peak acceleration at various dip angles is shown in Fig.4.4. The starting point of rupture is at element 1. θ=45° means that the observation site is on the same side of the fault plane, and θ=135° that it is on the opposite side. There are no remarkable differences in peak acceleration when the observation sites are on the opposite side of the fault plane; but, when the sites are on the same side of the plane there are differences in the short distance range. These occur because the distance between the observation site and the fault plane becomes short as the dip angle approaches 0°.

The attenuation of the peak accelerations for magnitudes 6, 7, and 8 is shown in Fig.4.5. In the figure, each peak acceleration has an upper bound. In the direction of θ=90°, the peak acceleration has a constant value for the distance range that coincides with the length of the fault.

A comparison of values obtained from the attenuation law with the observed peak accelerations is shown in Fig.4.6. The equations in the caption are the regression equations derived from data for a rock site that contains 24 components from 8 earthquakes that took place in Japan between 1968 and 1982 (solid circles in Fig.4.6). The solid line (1) was calculated by the proposed method (θ=45°, δ=90°; the starting point of rupture, 1). The chain line is given by equation (3), which is proposed by the Public Works Research Institute, Ministry of Construction, Japan [17]. The broken line is given by equation (2)

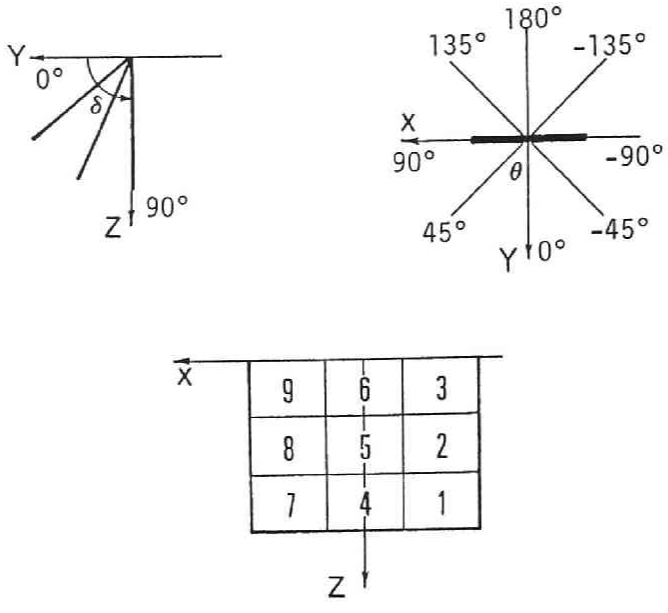

Fig. 4.2 Classification of parameters.

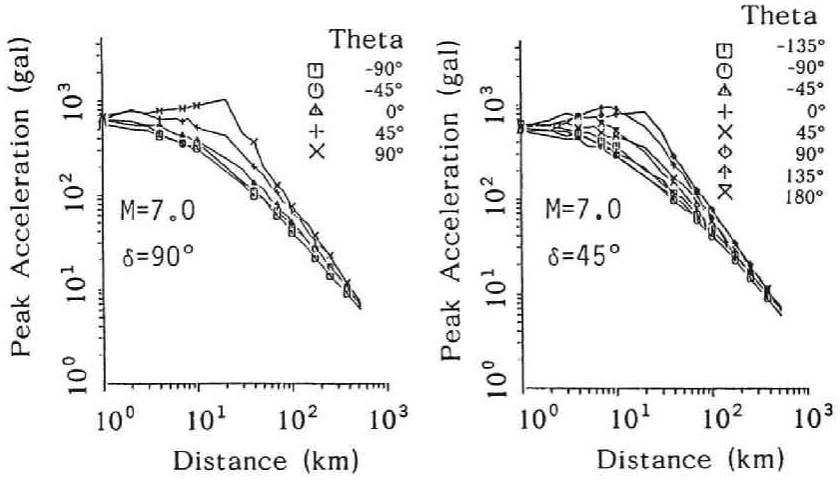

Fig. 4.3 Attenuation of peak acceleration when the direction of the observation site is varied.

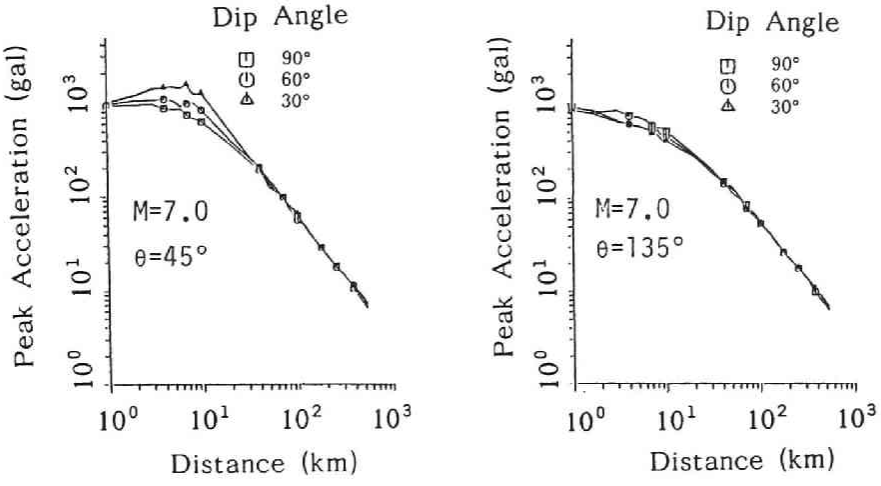

Fig. 4.4 Attenuation of peak acceleration for the dip angles 90°, 60°, and 30°.

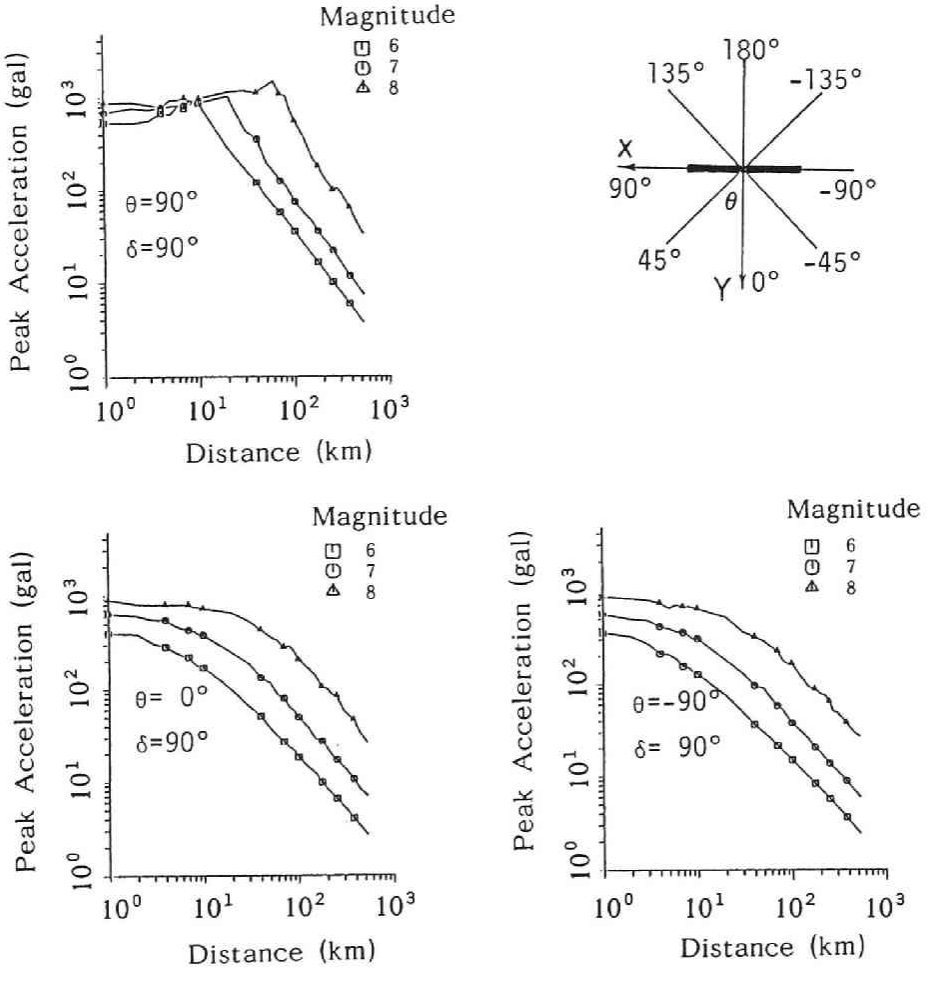

Fig. 4.5 Attenuation of peak acceleration for magnitudes 6, 7, and 8.

obtained by regression analysis of earthquake records with epicentral distances larger than half the fault length, a constant value of peak acceleration being assigned within the fault length. The fault length is derived from Geller's equation based on the magnitude of the earthquake. The broken line agrees better with line (1) than with line (3).

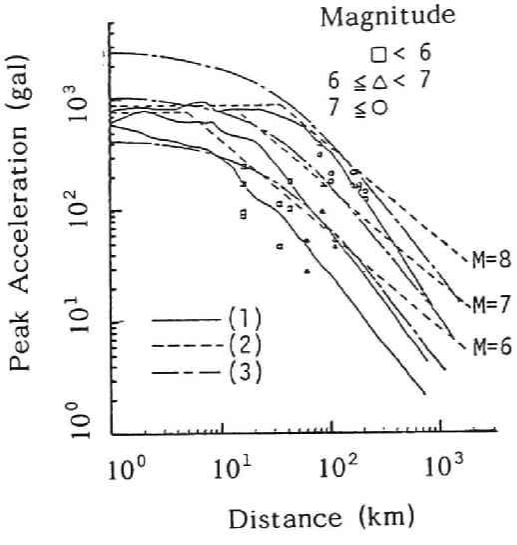

(1) Starting Point of Rupture: 1
θ=45°, δ=90°

(2) $a_{max} = 13.56 \times 10^{0.3925M} \times \Delta^{-0.9503}$ (this study)

(3) $a_{max} = 166.6 \times 10^{0.3973M} \times (\Delta + 30)^{-1.323}$ [17]

Fig. 4.6 Comparison of the attenuation curves.

4.2.2 Adoption of Path and Amplification Effects

(1) Path effect

In Eqs.(4.3) and (4.4) only the radiation damping that is proportional to the reciprocal of the distance, 1/R, is considered. The damping caused by the internal friction of the material, the Q-value, must, however, be accounted for in order to approach the real phenomena. From the spatial decay of the propagating wave, the exponential decaying function for G(f) is defined as follows [18]:

$$G'(f) = G(f) \exp\left[\left(-\frac{\pi f}{cQ}\right)R_{lm}\right] \qquad (4.7)$$

in which G(f) is the Fourier transform of earthquake motion as in Eq.(4.3), c the wave propagation velocity.

Fig.4.7 shows the frequency-dependent Q-values in the full logarithmic scale obtained for the Japanese archipelago ([5], [6], [7], [8], [9], [10]). The gradients of the lines are steep in the northern and gentle in the southern part of the islands. The Q-value for this region is approximated by the average of these straight lines, as expressed by

$$\log Q^{-1} = -0.7 \log f - 2.2 \qquad (4.8)$$

The effect of internal damping is incorporated by substituting Eq.(4.8) in Eq.(4.7).

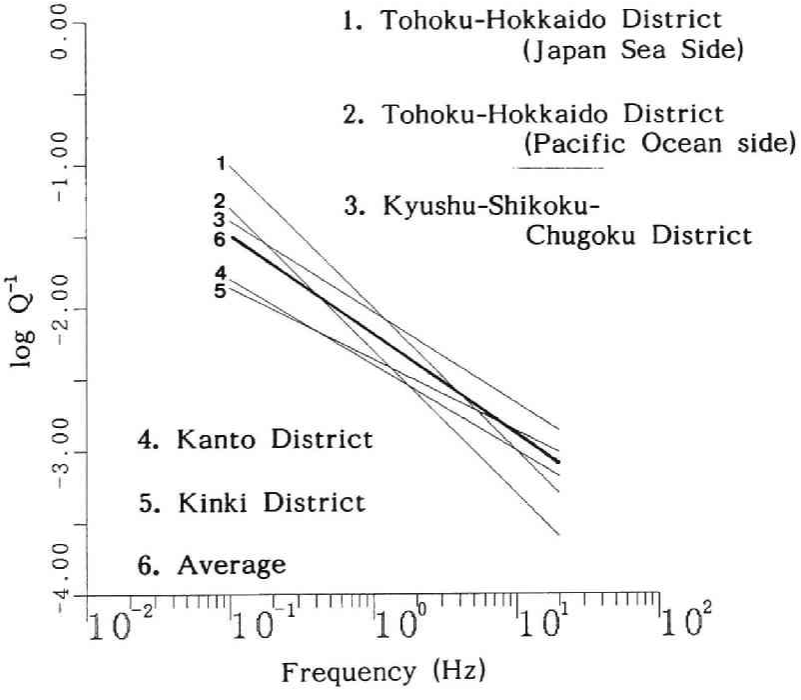

Fig. 4.7 Frequency-dependent Q-values in Japan.

(2) Amplification effect

The amplification effect of the surface ground also is an important factor in the accurate prediction of the intensity of surface ground motion.

Midorikawa [11] investigated the correlation between geological conditions and shear wave velocities and defined the amplification factor based on the geological conditions. The amplification factor, α_i, is defined as

$$\begin{aligned} \alpha_1 &= 5.5 && \text{(Quaternary)} \\ \alpha_2 &= 4.0 && \text{(Quaternary Extrusives)} \\ \alpha_3 &= 5.0 && \text{(Neogene to Quaternary)} \\ \alpha_4 &= 3.5 && \text{(Neogene)} \\ \alpha_5 &= 2.5 && \text{(Pre-neogene)} \end{aligned} \tag{4.9}$$

The peak acceleration on the ground surface, A_{max}^{surf}, is obtained by multiplying one factor of Eq.(4.9) by the maximum acceleration of the bed rock, A_{max}:

$$A_{max}^{surf} = \alpha_i \, A_{max} \tag{4.10}$$

4.2.3 Estimation of Peak Acceleration

The values of the peak accelerations during the 1988 Nepal-India earthquake are estimated taking into account the damping of the traveling path and the amplification factor of the surface ground.

On the basis of the preliminary report of the U.S.G.S. [19], three source mechanisms for the Nepal-India earthquake are proposed. In each model two planes (the fault plane and its auxiliary) are identified. The distribution of the aftershocks is used to determine the actual fault plane. The P- and S-wave arrival times for 97 microearthquakes recorded at five stations from the mainshock until October 3, 1988 were provided by Dr. M. R. Pandey, Director of the Seismological Laboratory of the Department of Mines and Geology, Nepal. Fig.4.8 shows the epicenter distribution of these 97 microearthquakes. The upper and lower curved lines respectively represent the borders between China and India. The positions of the observation stations are shown by crosses (+). A P-wave velocity of 7.0 km/sec was assumed in order to derive the figures. The hypocentral depths of the microearthquakes projected in the A-B and C-D sections of Fig.4.8 are shown in Fig.4.9 (a) and (b). The distribution of microearthquakes in the A-B section is homogeneous, whereas that in the C-D section is concentrated on the surface with a dip angle

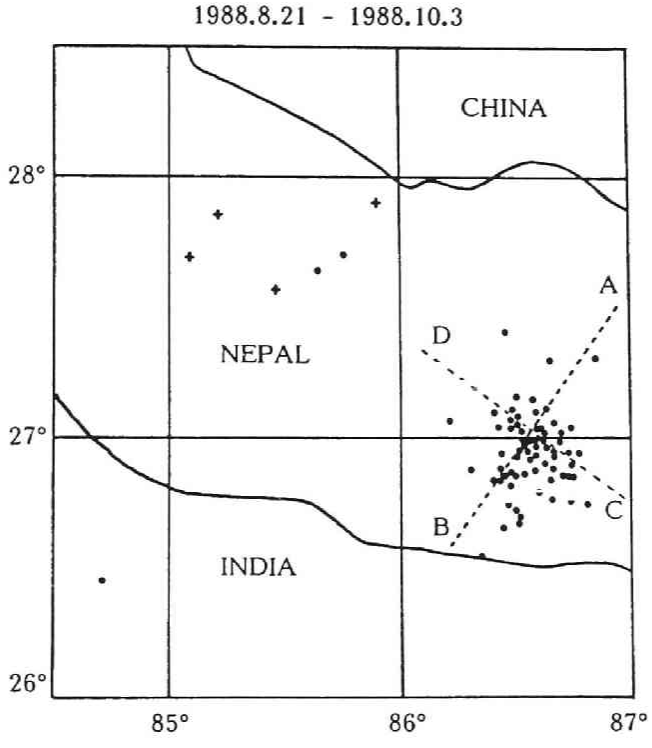

Fig. 4.8 Epicenters of microearthquakes in Nepal and India (P-wave velocity: 7.0 km/s)

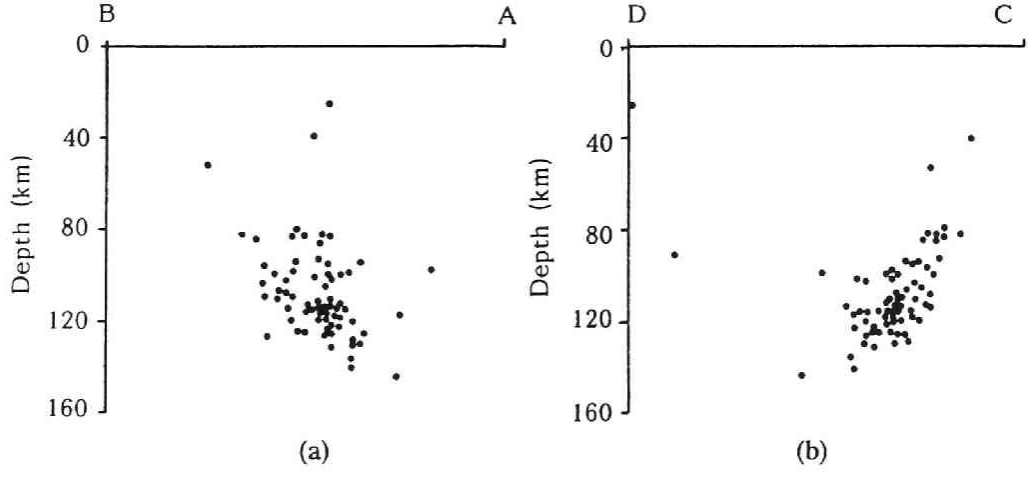

Fig. 4.9 Distribution of microearthquake depth in Nepal and India.

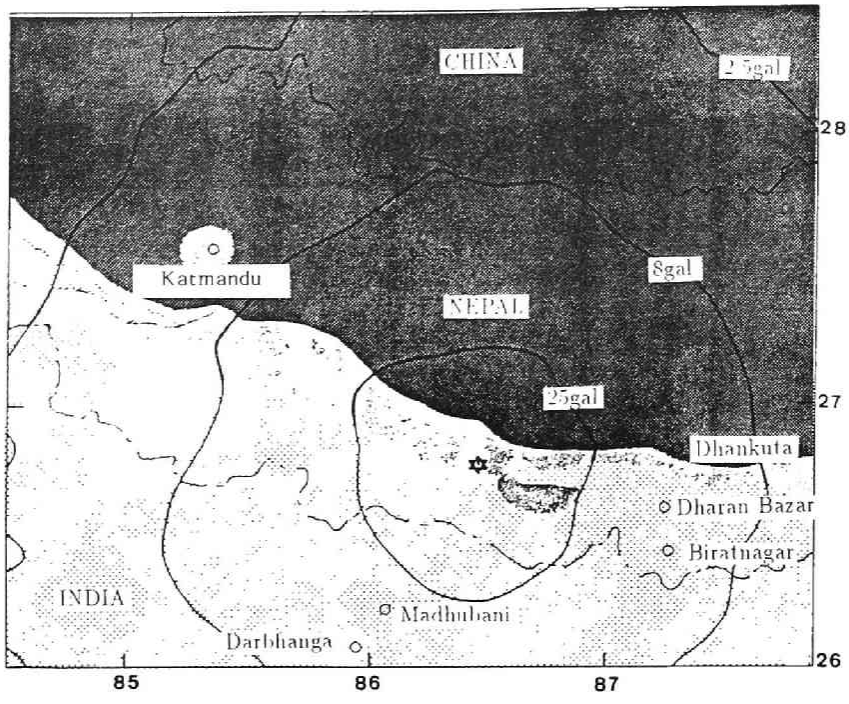

Fig. 4.10 Contours of peak acceleration at bed rock level in the 1988 Nepal-India Earthquake.

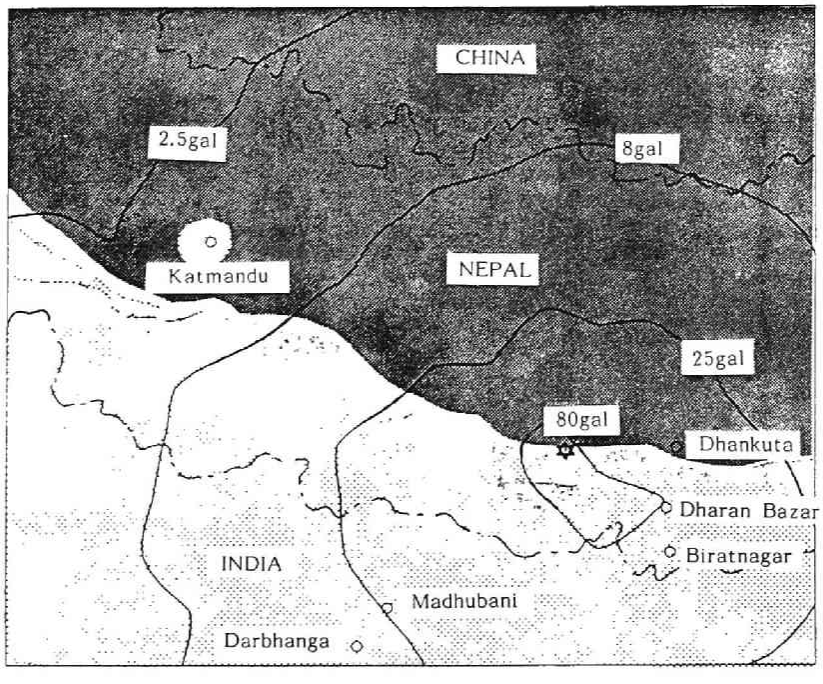

Fig. 4.11 Contours of peak acceleration at bed rock level in the 1988 Nepal-India Earthquake. (Rupture is assumed to have started at the left edge of the fault.)

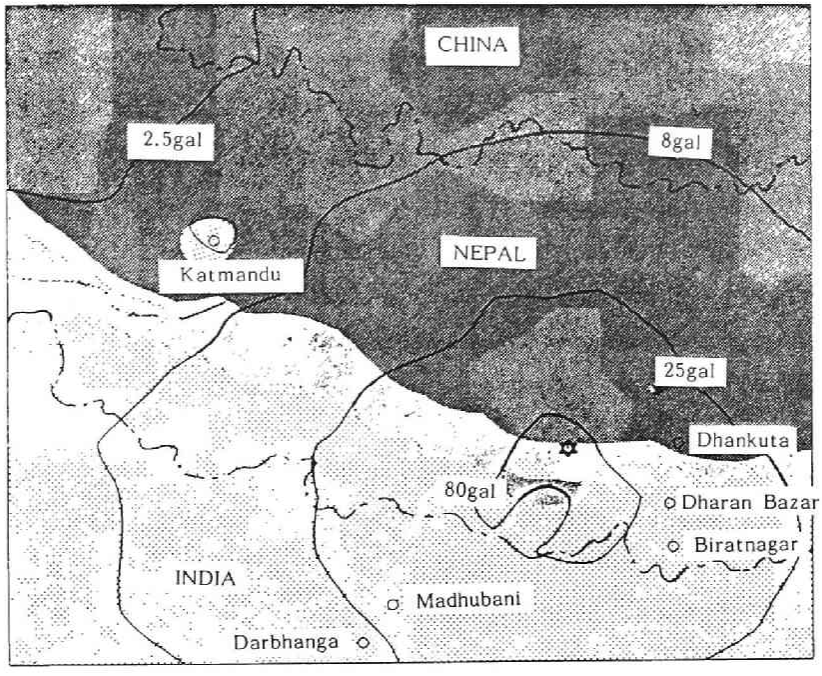

Fig. 4.12 Contours of peak acceleration at bed rock level in the 1988 Nepal-India Earthquake. (Rupture is assumed to have started at the right edge of the fault.)

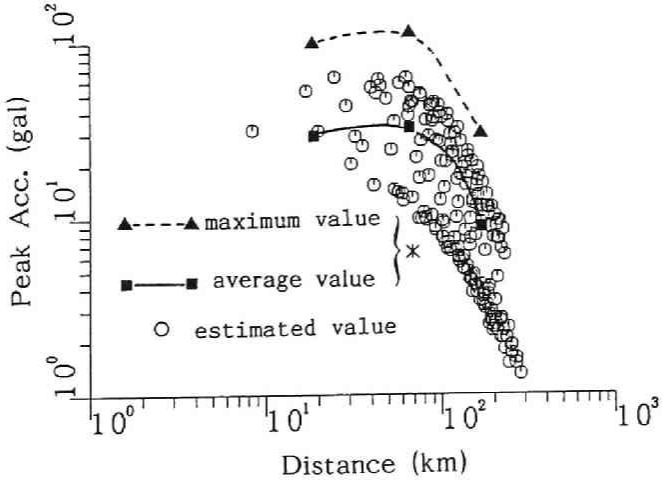

Fig. 4.13 Comparison of peak accelerations from theoretical solutions and questionnaire data.

between 50° and 60°. This distribution is supporting evidence for the model of dislocation of a fault with a strike angle of 217° and a dip angle of 54° (the Hovered model). These values and a slip direction of 0° are assumed in the following analyses.

The great earthquakes that occur in this region are related to a north-dipping detachment fault that marks the tectonic plate boundary between India and Asia. According to the Seeber model [20], the detachment lies no more than 20 km below the region concerned. Accuracy in defining the focal depth is not as good as in showing the distribution of the mainshock (57 km) because only data recorded at five stations are used, the hypocenters of the microearthquakes being outside of the network of stations. The hypocenters of almost all the microearthquakes are distributed at depths between 80 to 125 km. This suggests that the 1988 earthquake may not have been related to the existing detachment. Because the relative positions of the hypocenters obtained from microearthquake data are reasonably accurate, a dip angle of 54° was selected.

Contours of the estimated peak accelerations at base rock level during the 1988 Nepal-India earthquake obtained by the proposed method are shown in Fig.4.10. A seismic moment of 2.3×10^{26} dyne∗cm [20] is assumed. Although the estimated values were for the base rock level, they were modified by the amplification effect produced by the soft surface deposit and the damping effect of the propagation path.

The fault parameters are the same for both figures, but the starting point of rupture on the fault differs: In Fig.4.11, the rupture is assumed to start from the left edge of the fault and to propagate homogeneously to the right edge. In Fig.4.12, it starts in the middle of the fault and propagates homogeneously in both directions. In comparison with Fig.4.10, the peak accelerations are larger as a whole, and the contour of the estimated peak acceleration extends to outer space. A comparison of the intensities of ground shaking obtained from calculations and from a questionnaire [21] is shown in Fig.4.13. The estimated average value from the questionnaire data gives a low intensity for a short epicentral distance, but is in good agreement with the calculated value as the epicentral distance increases.

Eq.(4.4) can be extended to multiple fault rupture mechanisms. If a fault is composed of two fault planes and the time delay of rupture propagation from one fault to the other is assumed to be t_0, the power spectrum of the multiple faults is

$$P_L(f) = 2\left(\frac{R_{\theta\phi}}{4\pi\rho v_s^3}\right)^2\left\{\frac{S_1(f)}{\sqrt{T_1}}\frac{S_1^*(f)}{\sqrt{T_1}}XX^* + \frac{S_1(f)}{\sqrt{T_1}}\frac{S_2^*(f)}{\sqrt{T_2}}XY^* + \frac{S_2(f)}{\sqrt{T_2}}\frac{S_1^*(f)}{\sqrt{T_1}}YX^* + \frac{S_2(f)}{\sqrt{T_2}}\frac{S_2^*(f)}{\sqrt{T_2}}YY^*\right\}\cdot\left\{\right. \tag{4.10}$$

in which T_1 and T_2 are duration times of event 1 and 2, X and Y are

$$X = \sum_{l=1}^{n} \sum_{m=1}^{n} \sum_{n=1}^{n} \exp\{-i2\pi f t_{lmn}\} / R_{lm} \qquad (4.11)$$

$$Y = \sum_{l=1}^{n} \sum_{m=1}^{n} \sum_{n=1}^{n} \exp\{i2\pi f (t_{lmn}+t_0)\} / R_{lm} \qquad (4.12)$$

The estimated peak acceleration is obtained from Eq.(4.6).

The 1983 Nihonkai-Chubu earthquake involved two fault planes, and its magnitude was 7.7 on the Japan Meteorological Agency Scale. Values for the observed peak accelerations during this earthquake and the contours of the estimated peak accelerations at base rock level are shown in Fig.4.14. The seismic moment of the southern fault plane is assumed to be 3.6×10^{27} dyne*cm and that of the northern one 2.2×10^{27} dyne*cm. The dip angles are 40° and 20° , and the depths of the fault planes 2 and 3km. There is a fairly large discrepancy between the estimated and recorded values, which is lessened by considering the damping effect of the propagation path and the amplification effect produced by the soft surface deposit.

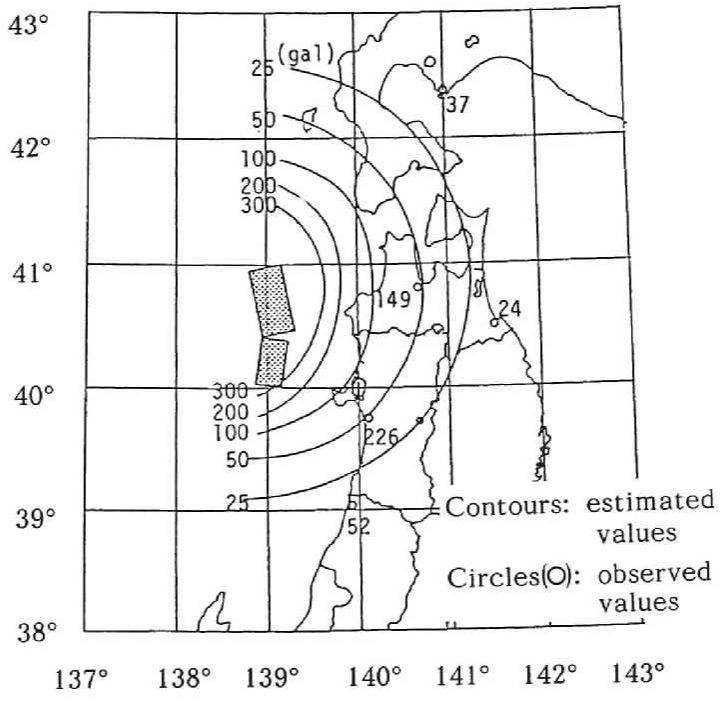

Fig. 4.14 Contours of peak accelerations at bed rock level.

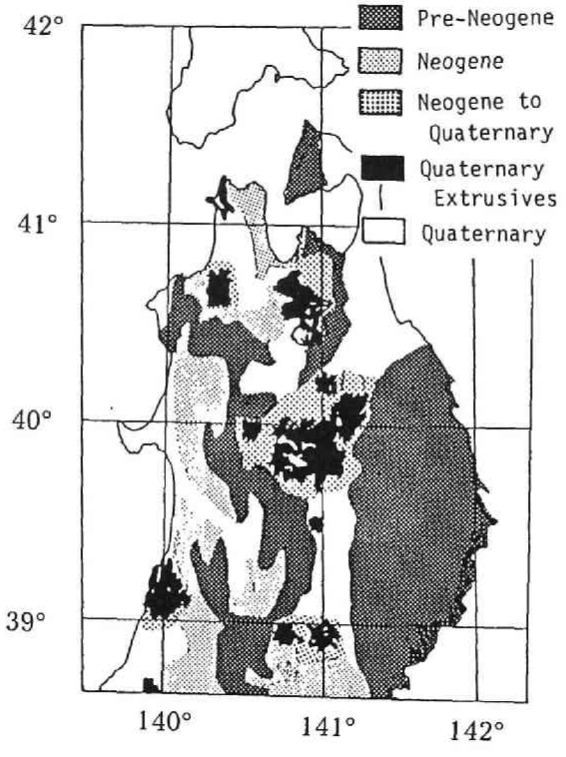

Fig. 4.15 Geological conditions in the Tohoku district.

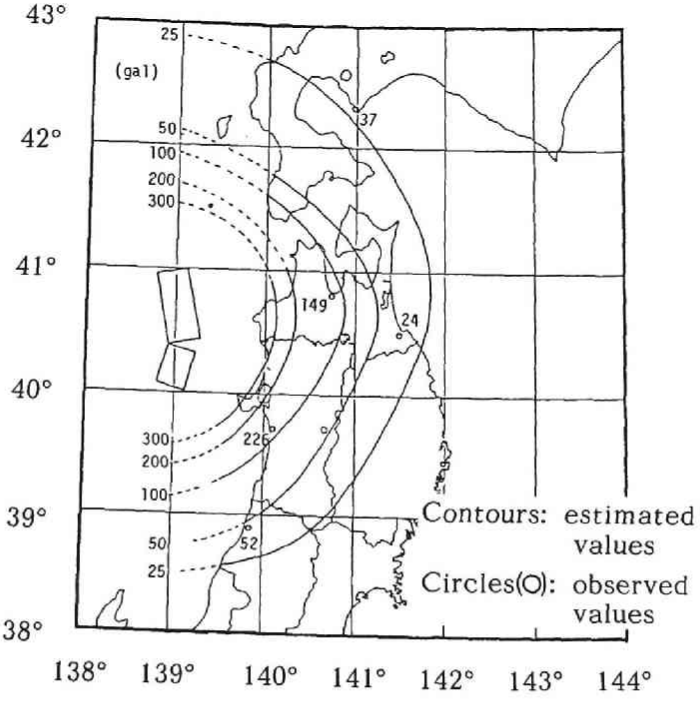

Fig. 4.16 Contours of peak accelerations: path and site effects taken into account.

Incorporation of the damping and amplification effects give a Q-value that is the same as line 1 in Fig.4.7. The geological conditions in this region are shown in Fig.4.15. An amplification factor was assigned each site according to Eq.(4.9). The estimated peak accelerations in the 1983 Nihonkai-Chubu earthquake with the damping of the traveling path and the amplification factor of the surface ground taken into account are shown in Fig.4.16. The fault parameters are the same as in Fig.4.14, but the peak accelerations in general are larger, and the contour of the estimated peak accelerations extends into outer space. The estimated peak accelerations as improved by the revised method are in good agreement with the recorded values.

4.3 Peak Ground Motion Obtained by Seismic Risk Analysis

4.3.1 The Earthquake Occurrence Rate Based on Historical Earthquake Records

The historical information used are mainly from the lists published by Usami [22] and Utsu [23]. The quality of the data varies with the period. Katayama's classifications [24] are used for the following classified periods for every magnitude. Data recorded before 1600 were omitted because of the question of reliability. The historical records used are shown in Fig.4.17. The multiplication symbols, triangle, circle, and square in the figure respectively correspond to the ranges of magnitude 5 - 6, 6 - 7, 7 - 8 and 8 ~.

Suppose that n_h historical records are obtained during T years in a region within a 300 km radius of a site. The earthquake occurrence rate, ν_h, for which the acceleration exceeds the value α^* at the site is

$$\nu_h = P(\alpha<\alpha^*)\ \nu'_h \qquad (4.13)$$

in which $P(\alpha<\alpha^*)$ is the probability of the acceleration exceeding α^* at an arbitrary site in the region, and ν'_h the average occurrence rate of earthquakes in that region.

Attenuation equations are needed to assess the probability, $P(\alpha<\alpha^*)$, various ones having been proposed for different conditions. The attenuation equation at the base rock level proposed by Ejiri [25], in which the shear wave velocity is about 3 km, is used here because, in the proposed procedure, peak accelerations at the base rock level are calculated first after which the amplification factors of the site are considered.

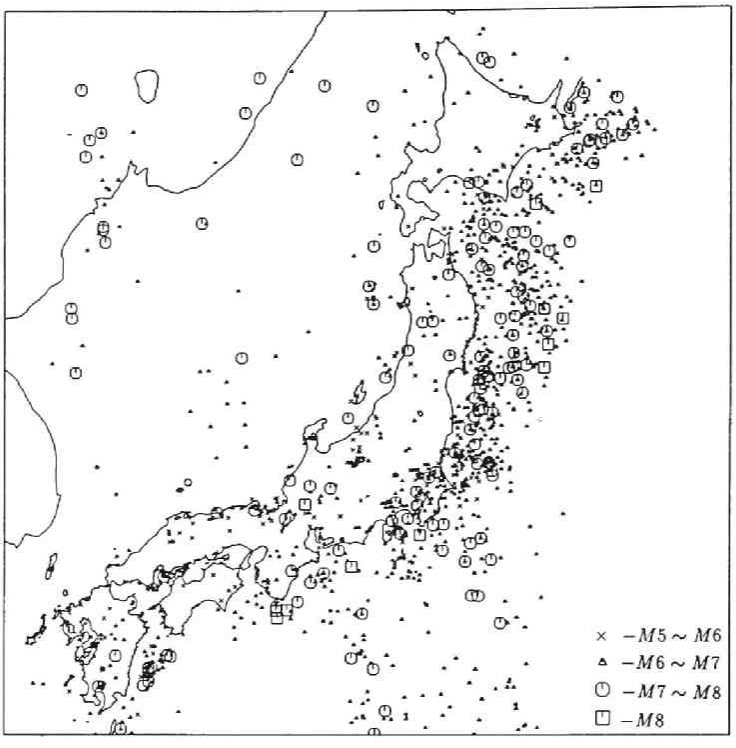

Fig. 4.17 Historical earthquake records in Japan.

The regression curve [26] with magnitude M and the distance from the source Δ is expressed by

$$\log \overline{\alpha}_h = c_{h_1} + c_{h_2}M + c_{h_3}\log \Delta \qquad (4.14)$$

in which c_{h1}, c_{h2}, and c_{h3}, are 2.07, 0.180, and 0.180. $\overline{\alpha}_h$ is an average value around which the observed data are scattered.

When the index of scattering, $S_{\alpha h}$, is defined as $\alpha_h/\overline{\alpha}_h$, the logarithmic value of $S_{\alpha h}$ obeys a standard normal distribution, the mean value, m_{sh}, being zero and the variance, σ_h^2, 0.259. When an earthquake of magnitude M_i and distance Δ_i occurs, the probability of the acceleration, α, exceeding α^* is

$$P_i(\alpha>\alpha^*|M_i,\Delta_i) = P(\log S_{\alpha h} > \log \alpha_h^* - \log \overline{\alpha}_h)$$

$$= 1 - \Phi\left(\frac{\kappa_h - m_{sh}}{\sqrt{2}\sigma_h}\right) \tag{4.15}$$

in which Φ is the distribution function and κ_h denotes $\log \alpha_h^* - \log \overline{\alpha}_h$.

Therefore when an earthquake occurs at an arbitrary point in a region, the probability that the acceleration, α ,exceeds α^* is given by averaging P_i (i=1, ..., n_h) as

$$P(\alpha>\alpha^*) = \sum_{i=1}^{n_h} P_i/n_h \tag{4.16}$$

The average earthquake occurrence rate, ν'_h, is given from n_h historical data during T years;

$$\nu'_h = \frac{n_h}{T_h} \tag{4.17}$$

The average earthquake occurrence rate in which the acceleration α exceeds α^* is obtained by substituting Eqs.(4.16) and (4.17) for Eq.(4.13);

$$\nu_h = \frac{1}{T_h}\sum_{i=1}^{n_h} P_i \tag{4.18}$$

in which

$$P_i = \frac{1}{2}\left\{1 - \mathrm{erf}\left(\frac{x_h}{\sqrt{2}\sigma_h}\right)\right\} \tag{4.19}$$

$$x_h = \log \alpha_h^* - (c_{h1} + c_{h2}M_i + c_{h3} \log \Delta_i) \tag{4.20}$$

Assuming that this rate obeys the Poisson process with an average of ν_h, the probability of having n events in period T is

$$P(N=n) = \frac{(\nu_h T_h)^n}{n} \exp(-\nu_h T_h) \tag{4.21}$$

As the probability that no special events exceeding α^* occur in a year is $\exp(-\nu_h)$, the annual exceedance, F_{ph}, and the average return period, T_{rh}, are

$$F_{ph} = 1 - \exp(-\nu_h) \tag{4.22}$$

$$T_{rh} = \frac{1}{F_{ph}} \tag{4.23}$$

The calculated hazard curve for Osaka City (34.7°N, 135.5°E), Japan is shown in Fig.4.18. The amplification factor at that site is 5.5 for the input wave at base rock level based on the geological conditions. The historical records for a 300 km radius of Osaka City are shown in Fig.4.19. Many earthquakes have occurred in the ocean off the southern coast of the Kii Peninsula. No earthquake is recorded on the median tectonic line. The hazard map of the Kinki district, determined by the above procedure, is shown in Fig.4.20. The return period is 100 years. A peak acceleration of more than 100 gal is expected in the southern Kii Peninsula, in the area from Osaka Bay to Lake Biwa, and in the vicinity of Ise Bay.

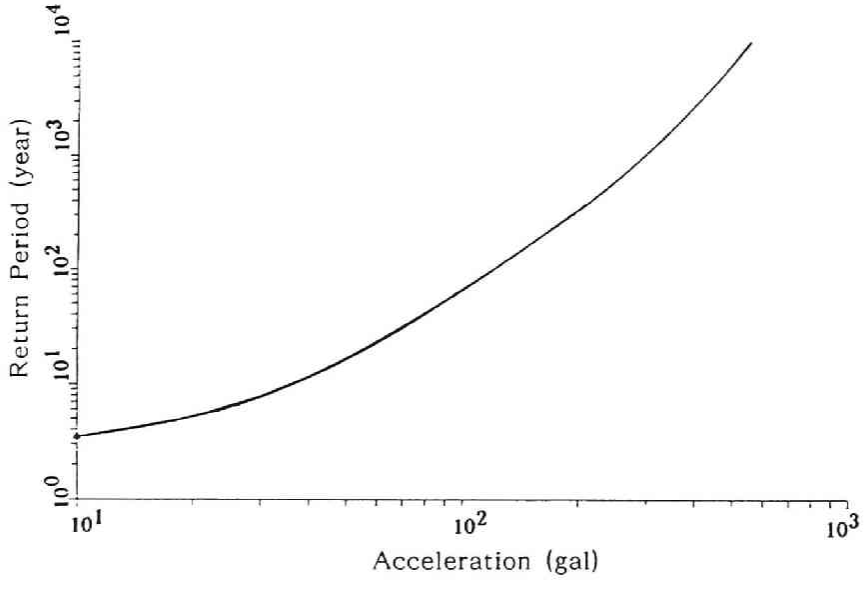

Fig. 4.18 Estimated hazard curve for Osaka City based on historical earthquake records.

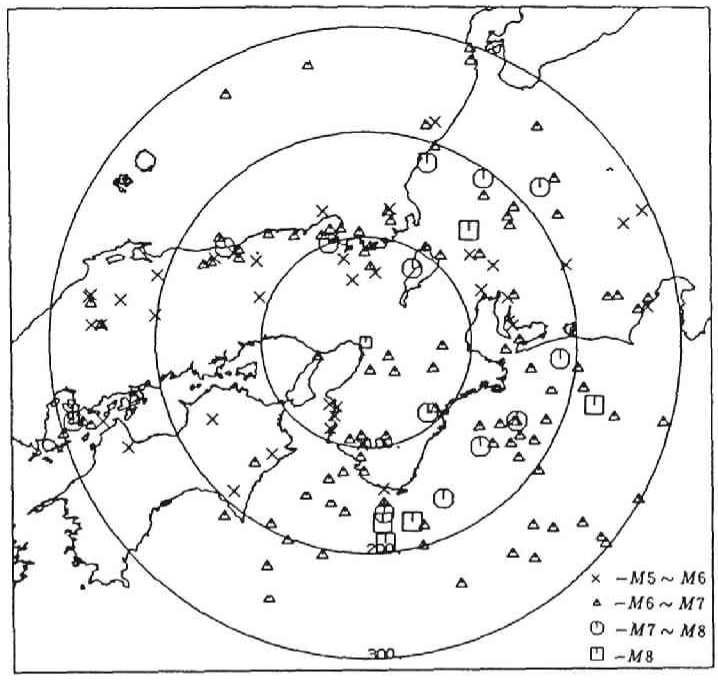

Fig. 4.19 Historical earthquake records for the Kinki district.

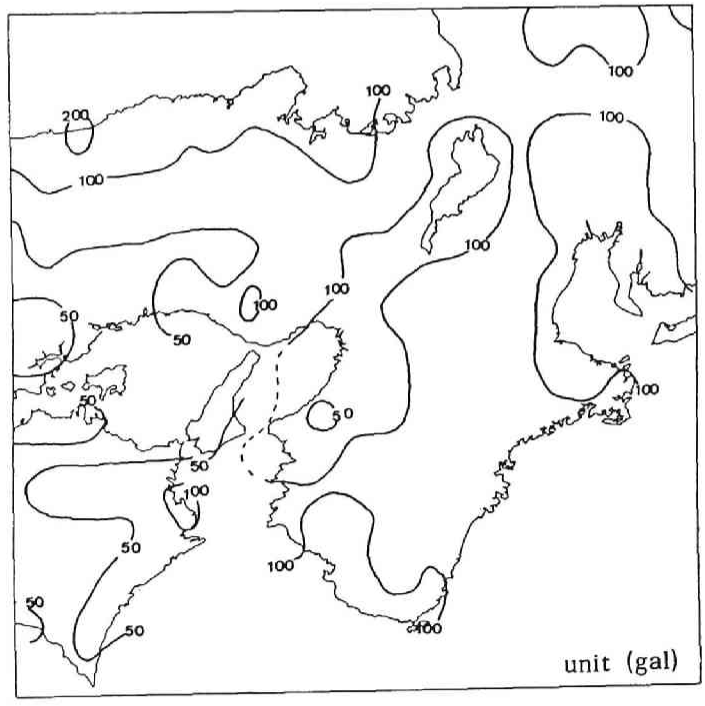

Fig. 4.20 Risk map for the Kinki district based on historical earthquake records. (return period, 100 years)

4.3.2 Earthquake Occurrence Rate Based on Active Fault Data

Data on active intraplate faults are taken from a map published by the Research Group on Active Faults in Japan. There are three reliability classes (I, II, III) that express seismic activity based on traces of Quaternary displacement. The ranked data from groups I and II, which are the most reliable, were used. As for digitization of fault data, the active fault is idealized as a straight line. The total number of faults in this data set is 887 [25]. The faults located in the Kinki district are shown in Fig.4.21. The fault mechanism used is the maximum moment model [27], in which the earthquake occurrence rate, ν_i, on a fault, i, is assumed to be equal to the ratio of the geologically determined rate of moment release, $\dot{M}_0$, to the seismic moment of the maximum expected earthquake, M_0^{max}, on the fault;

$$\nu_i = \frac{\dot{M}_0}{M_0^{max}} \tag{4.24}$$

Fig. 4.21 Active faults in Japan.

This equation suggests that the fault periodically releases its inherent seismic moment, M_0^{max}. The seismic moment is proportional to the length of the fault. The rate of moment release is determined from the shear modulus, μ; the area of the fault plane, S; and the average slip rate, $\dot{D}$, as

$$\dot{M}_0 = \mu \dot{D} S \tag{4.25}$$

An earthquake occurrence rate for which the acceleration, α, exceeds the value α^* at a given site is supposed. The smallest magnitude, m_0, is 5.0, and the radius for the region affected is assumed to be 300 km. The occurrence of earthquakes in this area would affect engineering sites. The conditional earthquake occurrence rate, $\hat{\nu}_i$, on a fault, *i*, in the region is

$$\hat{\nu}_i = P(\alpha > \alpha^* | E_i)\, \nu_i \tag{4.26}$$

in which $P(\alpha<\alpha^*|E_i)$ is the conditional probability of the acceleration, α, exceeding α^* at the site when an event with $m>m_0$ occurs on that fault.

The probability $P(\alpha<\alpha^*|E_i)$ is closely related to an attenuation equation based on the procedure described in the previous section. The expected peak accelerations are calculated from simulations in which the fault parameters of magnitude, distance from the fault, dip angle, the starting point of rupture, and the collocation between the fault and site are considered to be random values. The combinations of generated random values number are 1000. The shear wave velocity of the base rock is assumed to be about 3 km/sec. The regression curve for the average peak acceleration in terms of the magnitude, M, and the distance from the center of the fault line, Δ, is

$$\log \overline{\alpha}_f = c_1 + c_2 M + c_3 \log (\Delta + 30) \tag{4.27}$$

in which c_1, c_2, and c_3 are 5.57, 0.252, and 2.92. Results of regression analysis for a magnitude of 6.0 and its standard deviation, $\pm\sigma$, are shown in Fig.4.22, in which the data are scattered around the regression curve, $\overline{\alpha}_f$. When the index of scattering, $S_{\alpha f}$, is defined as $\alpha_f/\overline{\alpha}_f$, the logarithmic value of $S_{\alpha f}$ has a standard normal distribution with a mean value, m_{sf}, of zero and a variance, σ_f^2, of 0.023. The probability of the acceleration exceeding α^* therefore is

$$P(\alpha>\alpha^*|E_i) = P(\log S_{\alpha f}>\log \alpha_f^* - \log \overline{\alpha}_f)$$

$$= 1 - \Phi\left(\frac{\kappa_f - m_{sf}}{\sqrt{2}\sigma_f}\right) \tag{4.28}$$

in which Φ is the distribution function, and κ_f denotes $\log \alpha_f^* - \log \overline{\alpha}_f$. The average occurrence rate is obtained by substituting Eqs.(4.24) and (4.28) in Eq.(4.26). The corresponding occurrence rate in the region, ν_f, then is

$$\nu_f = \sum_{i=1}^{n_f} \hat{\nu}_i \tag{4.29}$$

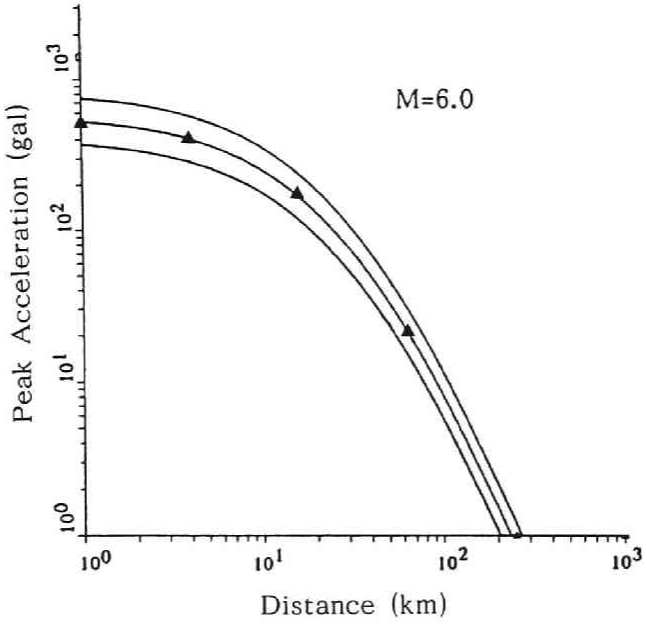

Fig. 4.22 Attenuation curve and the standard deviation of peak acceleration at base rock level obtained by regression analysis of calculated theoretical data.

Assuming that the occurrence of earthquakes in the region obeys the Poisson process with an average occurrence rate of ν_f, the number of events of interest in that region in the interval T_f years is

$$P(N=n) = \frac{(\nu_f T_f)^n}{n!} e^{-\nu_f T_f} \tag{4.30}$$

As the probability that no special events exceeding α^* occur in a year is $\exp(-\nu_h)$, the annual probability of exceedance, F_{pf}, and the average return period, T_{rf}, are

$$F_{pf} = 1 - \exp(-\nu_f) \tag{4.31}$$

$$T_{rf} = \frac{1}{F_{pf}} \tag{4.32}$$

The calculated hazard curve for Osaka City (34.7°N, 135.5°E) is shown in Fig.4.23. The estimated peak acceleration is more than 200 gal for a return period of 100 years.

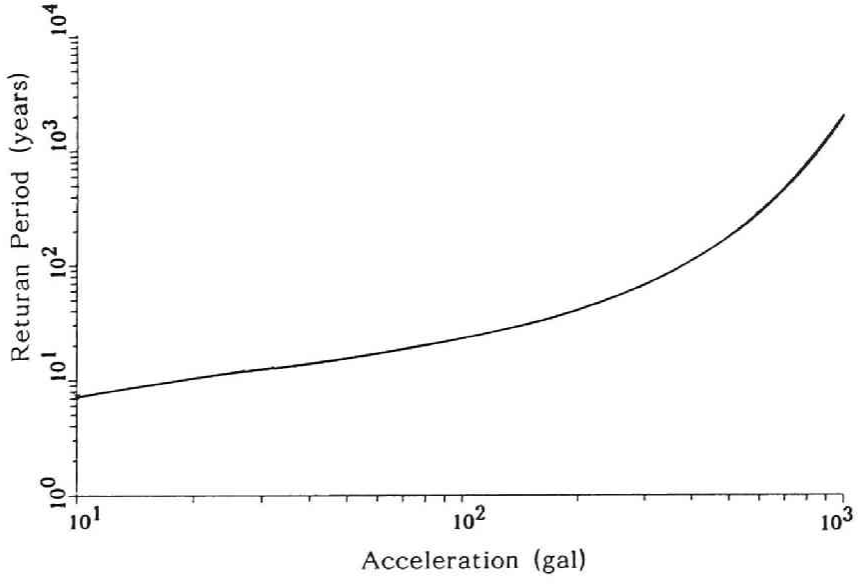

Fig. 4.23 Estimated hazard curve for Osaka City based on active fault data.

Active fault data within a of 300 km radius of Osaka City are shown in Fig.4.24. The risk map for the Kinki district for a return period of 100 years is shown in Fig.4.25. The southern part of the district usually is pointed out as an area at risk because a major fault runs along the Pacific rim, and large interplate earthquakes occur periodically in the region. For example, such severe earthquakes as the 1854 Ansei Nankai and 1946 Nankai earthquakes, occurred in the Nankai Trough, the interface between the Eurasian and Philippine Plates. This study, however, deals only with intraplate earthquakes and mappable Quaternary faults. That is why the southern part of the Kii Peninsula is not shown as

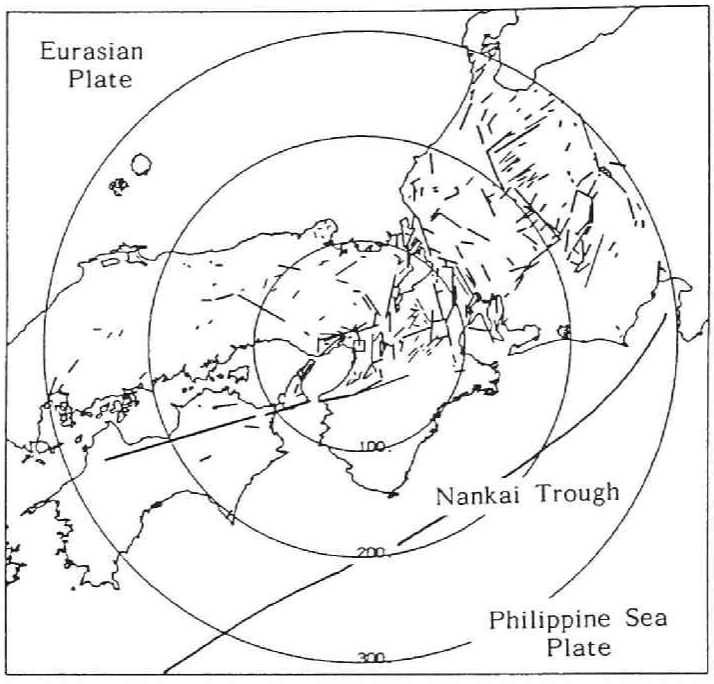

Fig. 4.24 Active faults in the Kinki district.

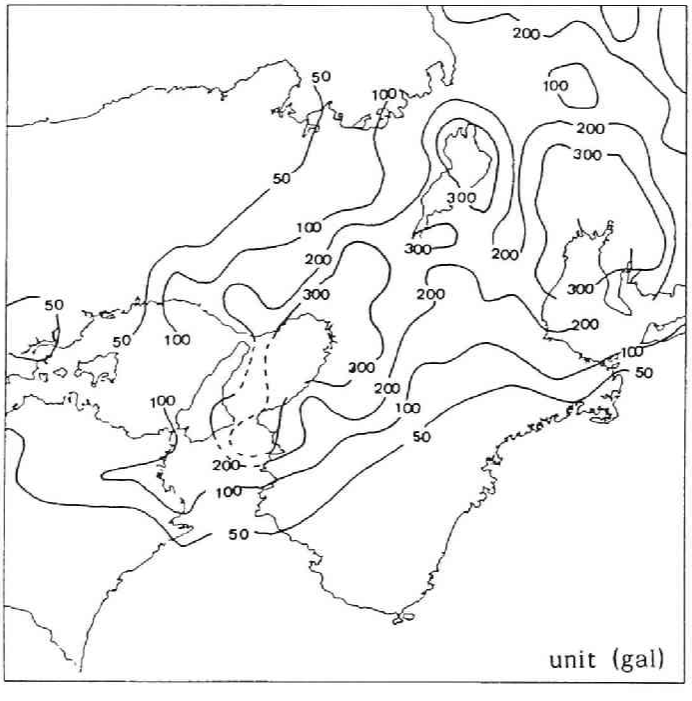

Fig. 4.25 Risk map for the Kinki district based on active fault data.
(return period, 100 years)

having a high intensity level. Estimated accelerations in the Osaka Bay area, the vicinity of Lake Biwa, and the Ise Bay area exceed 300 gal. This is because these areas have large deposit amplification factors and are adjacent to a group of intraplate faults.

4.3.3 Combination of Historical Earthquake Records and Active Fault Data

In previous sections, the annual earthquake occurrence rates, for which the acceleration, α, exceeds the value α^* were calculated as ν_i for historical data and as the logarithmic normal distribution for active fault data. Bayes' theorem here is used to combine the active fault and historical data .

Bayes' theorem, which incorporates a prior distribution of probabilities and statistical data, leads to a new, posterior distribution [28]. The prior probability density function of parameters of the random variable Θ is assumed to be $f'(\theta)$. The probability that Θ is between θ_i and $\theta_i+d\theta$ is $f'(\theta)d\theta$. If an event, ε, occurs in an experiment (or recorded observations), the prior distribution is modified by Bayes' theorem and the posterior distribution is

$$f''(\theta_i)d\theta = \frac{P(\varepsilon|\theta_i)\, f'(\theta_i)\, d\theta}{\sum_{i=1}^{n} P(\varepsilon|\theta_i)\, f'(\theta_i)\, d\theta} \tag{4.33}$$

in which $P(\varepsilon|\theta_i)$ is the conditional probability of the occurrence of ε on θ_i and $P(\varepsilon|\theta_i) = P(\varepsilon|\theta_i < \Theta < \theta_i+d\theta)$. The infinity on the n of Eq.(4.33) is

$$f''(\theta) = \frac{P(\varepsilon|\theta)\, f'(\theta)}{\int_{-\infty}^{\infty} P(\varepsilon|\theta)\, f'(\theta)\, d\theta} \tag{4.34}$$

$P(\varepsilon|\theta_i)$, called the likelihood function, is written $L(\theta)$. The denominator of Eq.(4.34) is independent of θ and the coefficient for normalization. Then the posterior distribution is rewritten

$$f''(\theta) = k\, L(\theta)\, f'(\theta) \tag{4.35}$$

$$k = \left[\int_{-\infty}^{\infty} L(\theta) f'(\theta) d\theta \right]^{-1} \tag{4.36}$$

The expected parameter θ is

$$\hat{\theta} = E(\Theta|\varepsilon) = \int_{-\infty}^{\infty} \theta f''(\theta) d\theta \tag{4.37}$$

(1) Prior distribution

Assuming that the probability density function of the earthquake occurrence rate, based on active fault data, obeys a logarithmic normal distribution, (μ, σ^2), the prior distribution is

$$f'(\nu) = \frac{1}{\sqrt{2\pi}\,\xi} \exp\left[-\frac{1}{2} \left\{ \frac{\ln \nu - \lambda}{\xi} \right\}^2 \right] \frac{1}{\nu} \tag{4.38}$$

in which

$$\xi = \ln\left\{ 1 + \frac{\sigma^2}{\mu^2} \right\} \tag{4.39}$$

$$\lambda = \ln \mu - \frac{1}{2}\xi^2 \tag{4.40}$$

(2) Likelihood function

The average earthquake occurrence rate, ν_k, in the region was obtained from historical records. This means that earthquakes occur ν_k times a year, equivalent to one earthquake per $1/\nu_k$ year. As the event-generating process is assumed to be a Poisson process, the likelihood function on ν is

$$L(\nu) = \frac{\nu}{\nu_h} \exp\left(-\frac{\nu}{\nu_h} \right) \tag{4.41}$$

(3) Posterior function

Combining the prior distribution and the likelihood function by means of Bayes theorem, the posterior distribution on $f''(\nu)$ is

$$L(\nu) = \frac{\nu}{\nu_h} \exp\left(-\frac{\nu}{\nu_h}\right) \tag{4.42}$$

The average earthquake occurrence rate after combining the historical and active fault data is

$$\hat{\nu} = \int_0^\infty \nu f''(\nu) d\nu \tag{4.43}$$

The annual probability of exceedance and the average return period can be calculated from Eqs. (4.31) and (4.32)

An example of data combination using Bayes' theorem is shown in Fig.4.26 for Osaka City. The prior distribution obeys the logarithmic normal distribution. Its mean value, ν, is 2.0×10^{-3} and variance, σ^2, 3.6×10^{-6}. The squares show the posterior distribution. The mean occurrence rate is 2.6×10^{-3}. The calculated hazard curves for Osaka (34.7°N, 135.5°E) and Tottori (35.6°N, 134.2°E) cities are shown in Fig.4.27 (a) and (b). The abscissa gives the expected horizontal peak acceleration, the ordinate the return period. The peak accelerations for a return period of 100 years are estimated to be 225 gal for Osaka and 25 gal for Tottori.

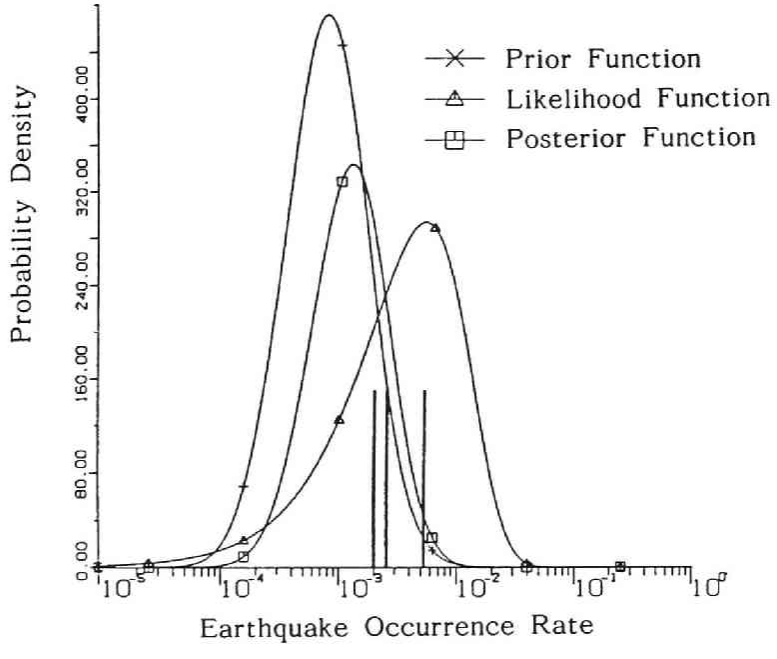

Fig. 4.26 Combined earthquake occurrence rates according to Bayes' theorem.

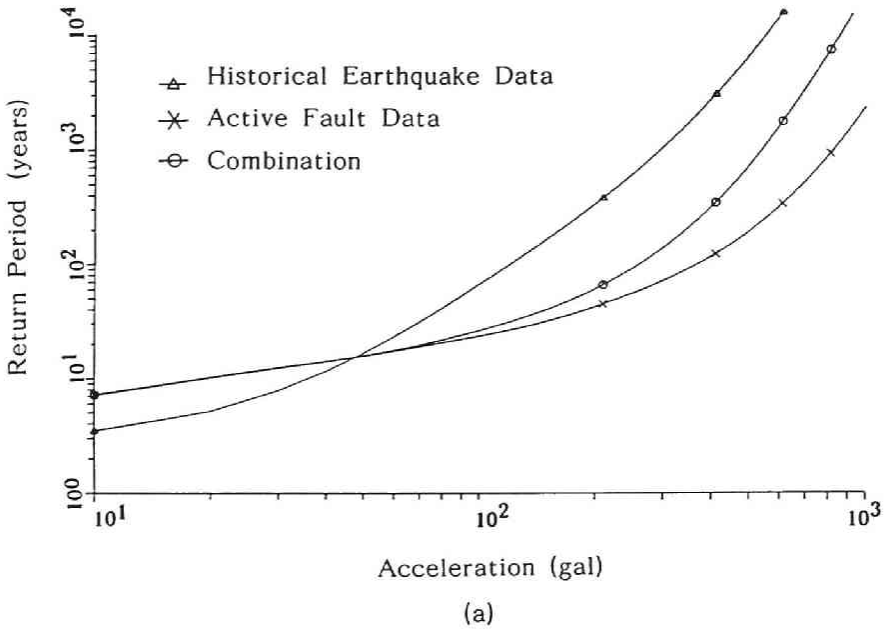

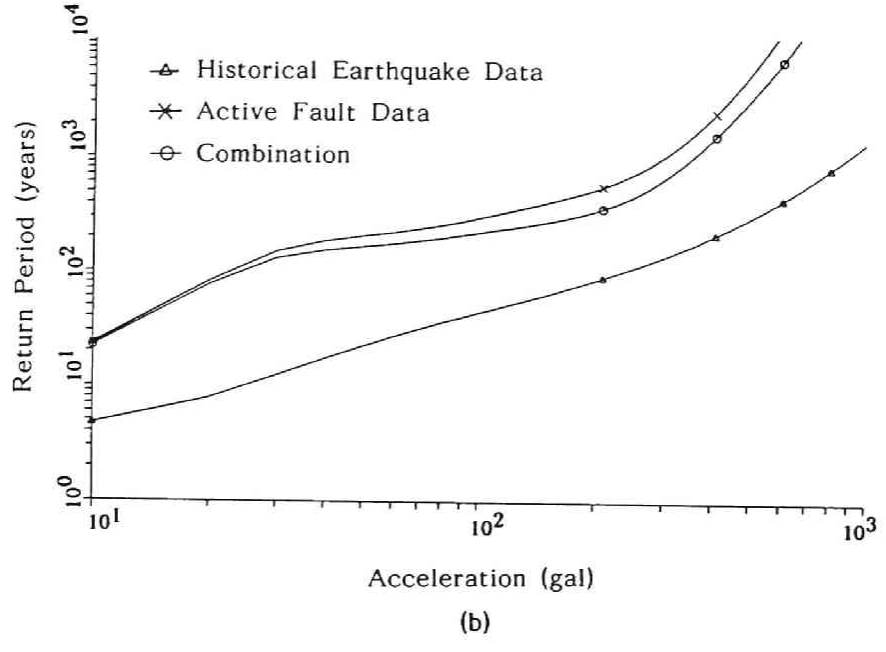

Fig. 4.27 Estimated hazard curves. (a) Osaka City, (b) Tottori City

The hazard map for the Kinki and Chugoku districts is shown in Fig.4.28. In this analysis, the prior distribution is assumed to be a logarithmic normal one and its deviation to be very small. If the distributions of ν, based on historical records and active fault data, separate mutually, then the distribution of ν when these types of data are combined tends to come close to the prior distribution for the active fault data. The estimated acceleration for the Chugoku district (as at Tottori) is small because of the lack of active fault data. As the moment release rate for this area is very low, the hazard curve estimated from historical records alone may well be much in error. For that reason the results obtained, which are greatly affected by the active fault data, are reasonable for the Chugoku district.

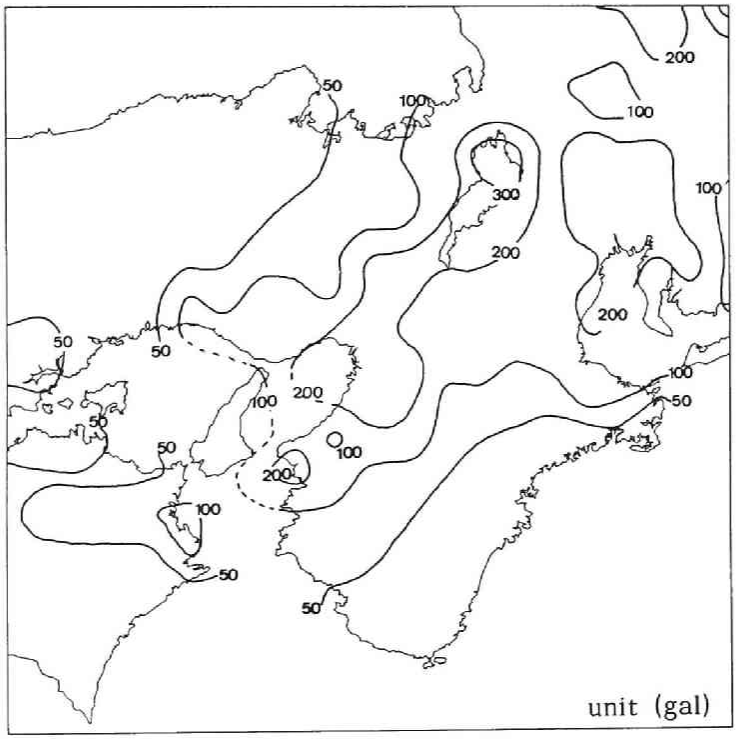

Fig. 4.28 Risk map for the Kinki and Chugoku districts obtained by combining historical earthquake and active fault data. (return period, 100 years)

4.3.4 Risk Spectrum at the Base Rock Level

The response spectrum at the base rock level (v_s=3km) is simulated theoretically and an attenuation equation for maximum response acceleration is established for each natural period of that spectrum. Seismic risk analysis is made on the basis on this attenuation law, and the risk spectrum for Osaka City calculated.

A large event is synthesized by superposing small events. The motion of the large event is basically the same as that expressed by Eqs.(4.1) and (5.17), but the equation is improved to take into account the high frequency component. The motion of the large event is

$$g_L(t) = \sum_{i=1}^{N_L} \sum_{j=1}^{N_W} g_S(t-t_{ij}) + \sum_{i=1}^{N_L} \sum_{j=1}^{N_W} \sum_{k=1}^{(N_D-1)N'} \frac{1}{N'} g_S(t-t_{ijk}) \qquad (4.44)$$

in which t_{lm} and t_{lmn} are the time delays caused by the superposition of the small events. N_L, N_W, and N_D are the same as in Eq.(4.1).

Multiplying the Fourier transform of Eq.(4.44), $G_L(f)$, by its conjugate gives the power spectrum of the large event, $P_i(f)$. The path effect is accounted for by averaging the Q-value (see Fig.4.7). Once the power spectrum of the earthquake motion at the bed rock level for a given M_i and Δ_i is obtained, the response power spectrum is gotten by multiplying that spectrum by the response function, $H_{jk}(f \mid T_j, h_k)$, of a single degree-of-freedom system in which the natural period is T_j and the damping constant h_k;

$$R_{ijk}(\omega) = P_i(\omega)\, H_{jk}(\omega)\, H^*_{ij}(\omega) \qquad (4.45)$$

Once the power spectrum of the large event is known, the maximum response acceleration can be estimated using the same procedure as Eq.(4.6).

The approximate value of the maximum response acceleration is

$$S(T_j, h_k) = p\sqrt{\lambda_0} \qquad (4.46)$$

in which p is the peak coefficient and a function of the m-th order spectrum moment (m=0,1,2). Magnitude, M_i, and epicentral distance, Δ_i, are generated randomly in the ranges of $5.0 < M_i < 8.0$ and $0 < \Delta_i < 500$ km. The maximum response acceleration is

computed for the paired magnitude and epicentral distance varying T_j (0.1, 0.2, 0.5, 0.8, 1.0, 2.0, 5.0 sec) and h_k (0.02, 0.05, 0.10). The regression equation is

$$\log \overline{S}_A(T_j,h_k) = c_1 + c_2M - c_3\log (\Delta+30) \qquad (4.47)$$

The regression coefficients obtained for seven natural periods are shown in Table 4.1. The damping constant is 5%. The attenuation curves for the maximum response acceleration for these natural periods are shown in Fig.4.29.

Table 4.1 Regression coefficients for natural periods (damping const.: 5%)

C \ T	0.10	0.20	0.50	0.80	1.00	2.00	5.00
c_1	6.16	5.41	4.01	3.34	3.08	2.59	1.28
c_2	0.24	0.25	0.30	0.37	0.37	0.38	0.48
c_3	3.06	2.76	2.32	2.24	2.17	2.05	1.95

The attenuation equations for peak acceleration (Eqs.(4.14) and (4.27)) are replaced by the attenuation equations for the maximum response accelerations (Eq.(4.47)). Taking into account the scattered data around the mean value of the attenuation equation, S_{SA}, the annual occurrence rate, ν, for a response acceleration, S_A, that exceeds the value for a natural period, S^*_A, is obtained by the same procedure. Assuming that the occurrence of earthquakes obeys the Poisson process with an average occurrence rate, ν, obtained by combining the occurrence rates based on historical earthquake records and active fault data, the return period for the objective site at the base rock level can be calculated. Three hazard curves for T=0.8 sec and h=5% for Osaka City are shown in Fig.4.30. Hazard curves based on the combined occurrence rate for seven natural periods are shown in Fig.4.31. The risk spectrum found from these hazard curves is shown in Fig.4.32. The return period is 100 years. This risk spectrum is compared with the one proposed by Sugito et al. [29] that was calculated from the attenuation equation proposed by Sugito [30]. The risk spectrum developed is smaller than theirs, especially in the low frequency range, because they define the base rock level as the layer in which the shear wave velocity is 700 - 800 m. If the amplification characteristics between the base rock layer (v_s=3km) and upper layer can be obtained, the risk spectrum at the layer of concern can be approximated.

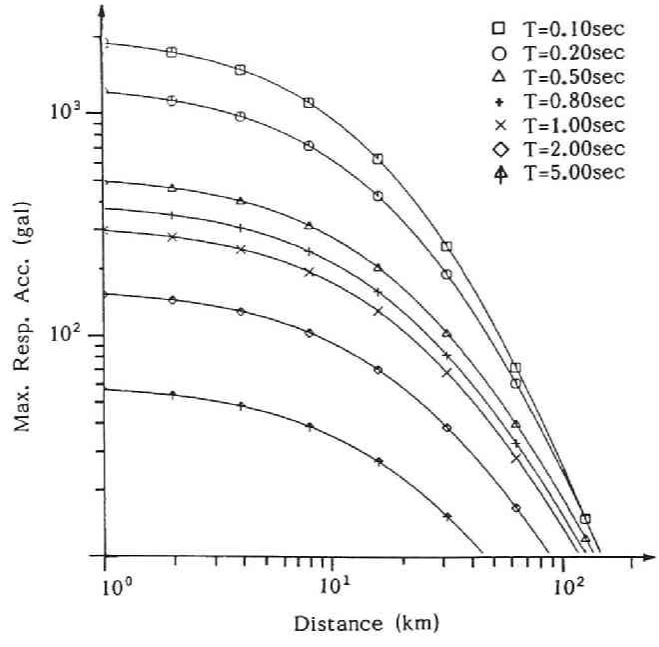

Fig. 4.29 Attenuation curves for the maximum response acceleration for seven natural periods.

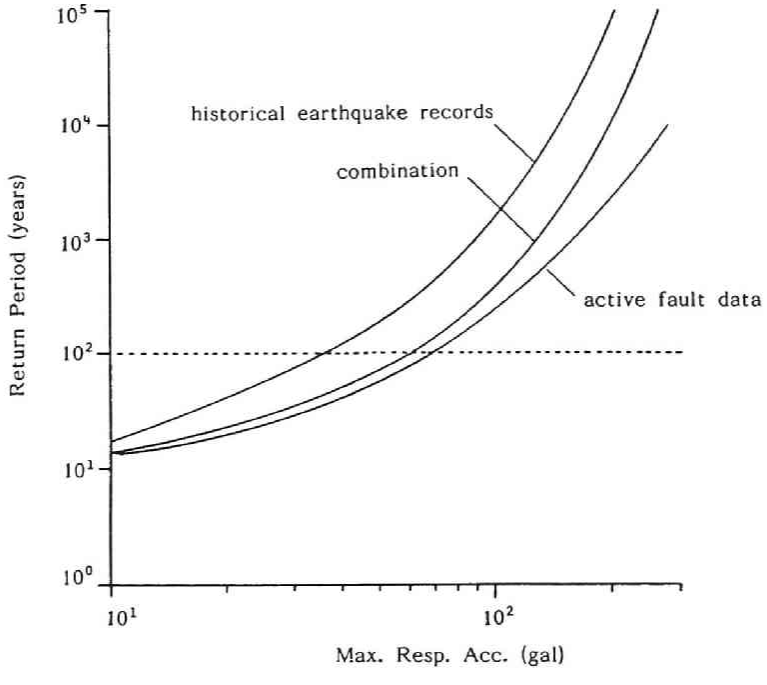

Fig. 4.30 Three hazard curves for T=0.8 sec and h=5% for Osaka City.

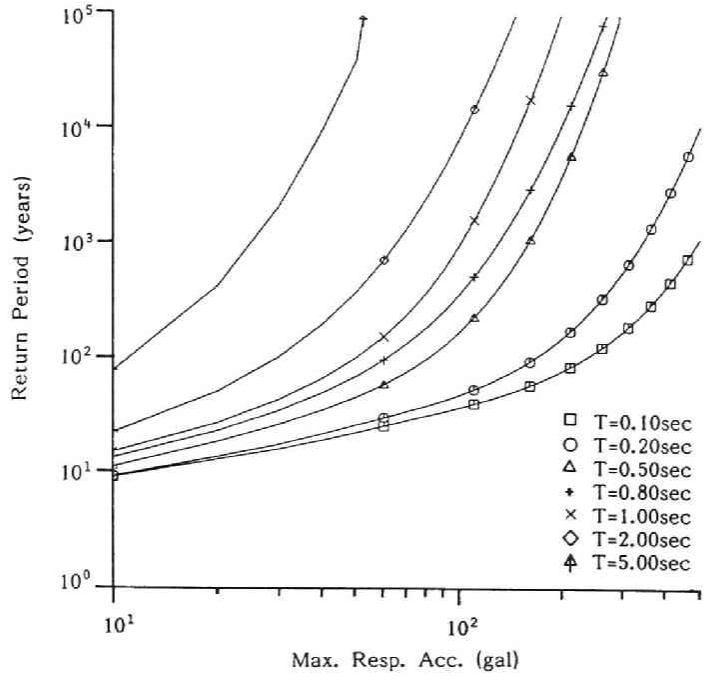

Fig. 4.31 Hazard curves based on the combined occurrence rate for seven natural periods.

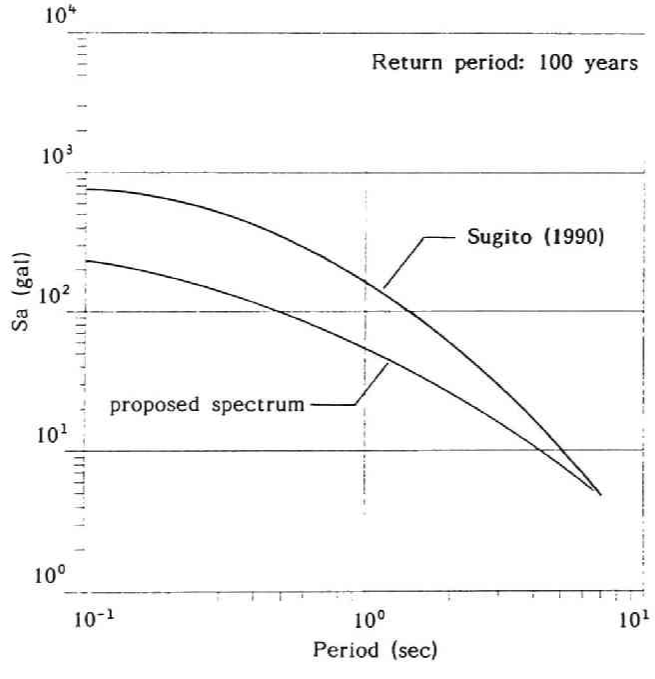

Fig. 4.32 Estimated risk spectrum at base rock level for Osaka City.
(return period, 100 years)

4.4 Conclusions

A new theoretical attenuation law that includes the effect of the fault extent was derived. The peak acceleration was determined in terms of the source mechanisms, damping of the traveling path, and amplification at the site. A risk map for the Kinki district was calculated by combining historical earthquake records and active fault data using Bayes' theorem. The risk spectrum of the bed rock level was estimated using the proposed attenuation equation of the response spectrum. The following are the procedure used and results obtained in this chapter:

(1) Attenuation of the peak acceleration is affected greatly by the rupture process and the direction of the observation site. Peak acceleration was highest at observation sites located in the direction of rupture propagation and lowest at sites in the opposite direction. When the effect of the fault extent was included, the attenuation curves had upper bounds near the source region, and the range was, at most, the fault length.

(2) If an outline of the fault mechanism can be obtained, the peak ground motions for an area without earthquake records, such as the area of the Nepal-India earthquake, can be estimated.

(3) The proposed method also can be used to estimate peak accelerations of an earthquake with multiple fault events, such as the Nihonkai-Chubu earthquake. To obtain the peak accelerations, the damping of the traveling path and the amplification at the site must be accounted for. Estimated values obtained with the improved method are in good agreement with recorded values.

(4) Data from historical earthquake records and active fault data are combined by the use of Bayes' theorem. A seismic risk map for the Kinki district was estimated from hazard curves at several hundred nodal points in a 20 x 20 km mesh that covered the district. The peak acceleration for a return period of 100 years is 225 gal for Osaka.

(5) The response spectrum at base rock level (v_s=3km) was simulated theoretically, and an attenuation equation of the maximum response acceleration for each natural period of that spectrum formulated. A seismic risk analysis was made using this attenuation law, and the risk spectrum for Osaka City calculated. If the amplification characteristics between the base rock (v_s=3km) and upper layer are known, the risk spectrum at the layer being consideration can be approximated.

References

[1] Hartzell, S. H. Earthquake Aftershock as Green's Function, Geophys. Res. Letters, Vol.5, No.1, pp.1-4, 1978.

[2] Matsumura, I. and K. Irikura. Estimation of Strong Ground Motion during a Large Earthquake Using Observed Seismograms of Small Events: A Study of Predicting Damage for a Large Earthquake in the Tokai District, Research Report of Japanese Group for the Study of Natural Disaster Science, No.A-56-3, pp.33-46, 1981 (in Japanese).

[3] Iida, M. and M. Hakuno. The Synthesis of the Acceleration Wave in a Great Earthquake by Small Earthquake Records, Proc. JSCE, No.329, pp.57-68,1983 (in Japanese with English abstract).

[4] Irikura, K. Semi-Empirical Estimation of Strong Ground Motions during Large Earthquake, Bull. Disas. Prev. Res. Inst., Kyoto Univ.,Vol.33, Part 2, No.297, pp.63-104, 1983.

[5] Umino, N. and A. Hasegawa. Three-dimensional Qs Structure in the Northeastern Japan Arc, Zisin 2, No.39, pp.241-249, 1986 (in Japanese with English abstract).

[6] Tsujiura, M. Special Analysis of the Coda Waves from Local Earthquakes, Bull. Earthq. Res. Inst., Univ. of Tokyo, 53, pp.1-48, 1978.

[7] Sato, H. and S. Matumura. Q-values (2-32Hz) of S-waves in the Kanto District, Zisin, 33, pp.541-543, 1980 (in Japanese with English abstract).

[8] Akamatu, J. Seismic Observation at the Sumiyama Seismic Station (2)- On the Natures of Attenuation and Spectra of Coda Parts of Local Earthquakes, Annuals Disas. Prev. Res. Inst., Kyoto University, Vol.23B-1, pp.107-114, 1980 (in Japanese with English abstract).

[9] Hoshiba, K. Regional Study of Coda Q-1 in the Kyushu District, Japan, Abstracts, Annual Convention of the Seismological Society of Japan, 1987.

[10] Iwata, T. and K. Irikura. Separation of Source, Propagation and Site Effects from Observed S-Wave, Zisin 2, No.39, pp.579-593, 1986 (in Japanese with English abstract).

[11] Midorikawa, S. and H. Kobayashi. Isoseismal Map in Near-Field with Regard to Fault Rupture and Site Geological Conditions, Trans. of A. I. J., No.290, pp.83-94, 1980 (in Japanese with English abstract).

[12] Kameda, H. and T. Okumura. Seismic Hazard Estimation Based on Active Fault Data and Historical Earthquake Data, Proc. JSCE, Vol.362/I-4, pp.407-415, 1985 (in Japanese with English abstract).

[13] Kawashima, K., K. Aizawa and K. Takahashi. Attenuation of Peak Ground Motion and Absolute Acceleration Response Spectra, Proc. 8th World Conf. on Earthq. Eng., 1984.

[14] Hanks, T. C. f_{max}, Bull. Seism. Soc. Am., 72, pp.1867-1879, 1982.

[15] Aki, K. Origin of f_{max}, Preliminary Report, 1984 (prepublication manuscript).

[16] Kiureghian, A. D. Structural Response to Stationary Excitation, Jour. Eng. Mech. Div., EM6, pp.1195-1213, 1980.

[17] Ministory of Construction. New Seismic Design Method, Technical Note of PWRI, No.1185, Public Works Research Institute, 1977.

[18] Aki, K. and Richard P. G. Quantitative Seismology, Vol.1, FREEMAN, 1980, pp.168-169.

[19] USGS. Preliminary Determination of Epicenters, Monthly Listing, National Earthquake Information Center, U. S. A., August, 1988.

[20] Seeber, L. and J. G. Armbruster. Great Detachment Earthquake along the Himalayan Arc and Long-term Forecasting in Earthquake Prediction, An international Review, Maurice Ewing Ser., 4, American Geophysical Union, pp.259-277, 1981.

[21] Fujiwara, T., T. Sato, T. Kubo and H. Murakami. Reconnaissance Report on the 21 August 1988 Earthquake in the Nepal-India Border Region, Research Report on Natural Disaster, Japanese Group for the Study of Natural Disaster Science, 1989.

[22] Usami, T. Descriptive Catalogue of Disaster Earthquakes in Japan, Univ. of Tokyo Press, Tokyo, 1975 (in Japanese).

[23] Utsu, T. Seismicity of Japan from 1885 through 1925: A New Catalogue of Earthquakes M<6 in Japan and Smaller Earthquake which Caused Damage, Bull. Earthq. Res. Inst., Univ. of Tokyo, 54, pp.223-308, 1979 (in Japanese).

[24] Katayama, T. An Engineering Prediction Model of Acceleration Response Spectra and its Application to Seismic Hazard Mapping, Earthq. Eng. and Struc. Dyn., Vol.10, pp.149-163, 1982.

[25] Ejiri, J. and Y. Goto. Database of Seismic Information and Waves, Technical Report, Obayashi Co.,Ltd., 1990 (in Japanese).

[26] Ejiri, J. and Y. Goto. Characteristics of Seismic Ground Motion at Base Rock Level: Peak Acceleration, Proc. 45th Annual Conference of JSCE, I, pp.1028-1029, 1990 (in Japanese)

[27] Wesnousky, S. G., C. H. Scholz, K. Shimazaki and T. Matsuda. Earthquake Frequency Distribution and the Mechanics of Faulting, Jour. Geophys. Res., Vol.88, No.B11, pp.9331-9340, 1983.

[28] Alfredo H., S. Ang and W. H. Tang. Probabilistic Concepts in Engineering Planning and Design, John Wiley and Sons, Inc., New York, 1975, pp.323-332.

[29] Goto, H., M. Sugito, H. Kameda, H. Saito and T. Ootaki. Prediction of Nonstationary Earthquake Motions for Moderate and Great Earthquake on Rock Surface, Annuals Disas. Prev. Res. Inst., Kyoto Univ., No.27B-2, 1984 (in Japanese with English abstract).

[30] Furuta, H. Research Report on Safety and Reliability Estimation of Bridges, Research Group organized by the Kansai Branch of JSCE, pp.176-186, 1990 (in Japanese).

CHAPTER 5

SYNTHESIS OF GROUND MOTION FOR SEISMIC RESPONSE ANALYSES

5.1 General Remarks

The fundamental step in producing earthquake-resistance designs of structures is to estimate the amount of seismic input to a structure. Many discussions and studies have been published, the results of which are reflected in the existing earthquake-resistance design codes.

Classical earthquake-resistance designs have been based on the seismic coefficient method because of its simplicity and practicability; but, as structure size increases this method no longer is suitable for assessing the safety of a structure in a seismic environment. For sensitive structures, such as nuclear power plants, sophisticated dynamic response analyses are required; therefore, comprehensive knowledge of the earthquake motion input to structures is indispensable.

The procedures available for determining input earthquake motions can be classified under three methods: The first uses actual earthquake records directly for the input ground motion. For example, the El Centro accelerograms for the Imperial Valley earthquake (1940), the Taft records for the Kern County earthquake (1952), and the Hachinohe records for the Tokachi-Oki earthquake (1968) frequently are used. The second method, which assumes that earthquake motion is the output from filters, has two parts; a system response for a white noise input [1] and the superposition of harmonic waves of different amplitudes and phase angles [2]. The third method synthesizes earthquake motion by the use of a fault dislocation model. In this approach, fault rupture in an infinite or semi-infinite homogeneous elastic medium usually is modeled and analyzed by the theory of elastodynamics.

In the first method, it is essential to use records obtained at a site that has the same conditions as the site being considered. In actuality, it is difficult to obtain matching conditions. In the second method, the simple filter used can not represent the propagation path

of seismic waves from the source to the observation site. Moreover, as a point source is assumed, the effect of the source extent is not considered when evaluating ground shaking. Because of these defects, the third method has proven the most useful. As the rupture process on a fault plane has yet to be thoroughly investigated, the source parameters and fault rupture process are here identified by deconvoluting seismic waves.

The large event usually is synthesized by superposing small events and taking into account the time lags caused by delays in the rupture of the fault plane. This means that the large event is expressed by the convolution of impulses and the time history of the small events. The impulses contain information about the rupture process. If these impulses are deconvoluted from the large event, the rupture process can be identified. Bayless and Brigham [3] were the first to apply the Kalman filter to the deconvolution problem. In this study, an analytical procedure based on Crump's method [4], developed for blasting seismology, is established

The Kalman filter is applied to deconvolute seismic waves into system response functions and trains of impulses. A method with which to identify the rupture process of a fault, which is based on several criteria of minimum error and which uses the deconvoluted trains of impulses, is proposed. Simulated waves and recorded blasting waveforms are analyzed in order to examine the validity of this deconvolution method. Records obtained at seven local JMA (Japan Meteorological Agency) stations during the 1983 Nihonkai Chubu earthquake are examined in order to identify the fault mechanism. Because seven deconvoluted trains of impulses contain information about the fault mechanism, the rupture process which expresses the focal parameters of rupture velocity, the starting point of rupture, the direction of rupture propagation, and the rise time can be identified by minimizing the error between the deconvoluted trains of impulses and the calculated ones based on theoretical fault rupture mechanisms.

When earthquake motion is synthesized using the analytical Green function, a simple, layered homogeneous ground profile usually is assumed. For greater accuracy, strong ground motions are simulated by replacing the Green function with such records of small events as the foreshocks and aftershocks that have taken place within the area on the fault plane of the mainshock ([5], [6]). A method for synthesizing ground motion that uses earthquake and microearthquake records is presented. The merits of using microearthquakes are that many records can be obtained during a short observation period (about 1000 records per year in the Kinki District) and that records for short epicentral distances can be obtained. The characteristics of microearthquakes that have taken place in the Kinki District were investigated and the recorded waveforms analyzed by the AR-MA (autoregressive-moving average) process. Regression analyses of the AR-MA parameters

then were derived from each record, after which a statistical simulation model for micro-earthquake motion was developed. A simulated waveform can be regarded as a kind of Green function; therefore, this statistical Green function can be superposed and large earthquake motion synthesized. A new scaling law is proposed for superposing micro-earthquakes.

5.2 Identification of the Fault Rupture Process by Use of the Kalman Filter

5.2.1 Deconvolution Method with the Kalman Filter

When a system consists of elements, each of which is expressed by a governing equation (such as Newton's for a kinematic system), that equation is entirely described by the differential equation and the initial condition [7].

Consider the signal generation and observation processes written by the linear stochastic differential equation

$$\frac{d\mathbf{x}(t)}{dt} = \mathbf{A}\cdot\mathbf{x}(t) + \mathbf{B}\cdot\mathbf{w}(t) \tag{5.1}$$

and

$$\mathbf{y}(t) = \mathbf{H}\cdot\mathbf{x}(t) + \mathbf{v}(t) \tag{5.2}$$

in which vectors **x**, **w**, **y** and **v** are the stochastic process, and the matrices **A**, **B** and **H** are deterministic. By solving Eq.(5.1), both equations can be written as a discrete linear system;

$$\begin{aligned} \mathbf{x}_{t+1} &= \Phi_{t+1|t}\mathbf{x}_t + \mathbf{G}_t\mathbf{w}_t \\ \mathbf{y}_t &= \mathbf{H}_t\mathbf{x}_t + \mathbf{v}_t \end{aligned} \tag{5.3}$$

in which

$\mathbf{x}_t$: n-dimensional state vector at t

$\mathbf{y}_t$: p-dimensional measurement vector at t

$\mathbf{w}_t$: m-dimensional Gaussian white noise

$\mathbf{v}_t$: p-dimensional Gaussian white noise

$\mathbf{F}_{t+1|t}$: state transition matrix from t to t_{t+1} with the dimensions $n \times n$

$\mathbf{G}_t$: system noise coefficient matrix with the dimensions $n \times n$

$\mathbf{H}_t$: measurement matrix with the dimensions $p \times n$

$E\{\mathbf{w}_t\mathbf{w}_s^T\}=\mathbf{Q}_t\times\delta_{ts}$

$\mathbf{Q}_t$: system noise covariance matrix

$E\{\mathbf{v}_t\mathbf{v}_s^T\}=\mathbf{R}_t\times\delta_{ts}$

$\mathbf{R}_t$: measurement noise covariance matrix

where E represents the expectation and Kronecker's delta. If the dynamic system model is constructed as Eq.(5.3), filter computations can proceed in accordance with Fig.2.2 [8].

The deconvolution method frequently is used in blasting seismology to map the interior of the earth from recorded observations. Seismic waves repeat reflections and refractions at the interface of soil layers, and the seismogram on the surface ground is the result of these reflections and refractions. The seismic record therefore is expressed by the convolution of the reflection coefficients and reflection waves. Deconvolution leads to the problem of separating the reflection coefficients and reflection wave from the seismogram. This is the same problem as separating a train of impulses and a response function from a seismic wave. The Kalman filter is applied to this deconvolution.

The seismic wave, y(k), is described as the convolution of a train of impulses, r(k), and the response function, h(i), expresses information about the traveling path between a source and a site;

$$y(k) = \sum_{j=N}^{k} [\, r(j)\, h(k-j)\,] + v(k) \tag{5.4}$$

in which L is the sampling number, v(k) the white noise and N is

$$N=\begin{cases} 1 & (k < L) \\ k - L + 1 & (k \geq L) \end{cases} \tag{5.5}$$

Eq. (5.4) is rewritten

$$\begin{aligned} &\mathbf{y}(k) = \mathbf{H}(k)\mathbf{x}(k) + \mathbf{v}(k) \\ &\mathbf{H}(k) = [\, h(k)\ h(k-1) \cdots h(L-1)\,] \\ &\mathbf{x}(k) = [\, r(k)\ r(k-1) \cdots r(k-L+1)\,]^T \end{aligned} \tag{5.6}$$

Suppose r(k) is described by the autoregressive process

$$r(k) = \sum_{i=1}^{L} \{b_i(k\text{-}l)\, r(k\text{-}i)\} + \mathbf{G}w(k\text{-}1) \qquad (5.7)$$

Then Eq.(5.4) is rewritten

$$\mathbf{x}(k) = \Phi_{k/k\text{-}1}\mathbf{x}(k\text{-}1) + \mathbf{G}w(k\text{-}1) \qquad (5.8)$$

in which

$$\Phi_{k/k\text{-}1} = \begin{bmatrix} b_1(k\text{-}1) & b_2(k\text{-}1) & \cdots & \cdots & b_L(k\text{-}1) \\ 1 & 0 & \cdots & \cdots & 0 \\ 0 & 1 & \ddots & \cdots & 0 \\ \vdots & \vdots & \cdots & \ddots & 0 \\ 0 & 0 & \cdots & 1 & 0 \end{bmatrix} \qquad (5.9)$$

Because Eqs.(5.6) and (5.7) have the same style as the linear stochastic system given by Eq.(5.3), the state variable, $\mathbf{x}(k)$, can be estimated by executing the Kalman filter algorithm. A train of impulses, r(k), can be deduced directly from $\mathbf{x}(k)$. When filter computation proceeds from step (1) to (7) in the Kalman filter algorithm (shown in Fig.2.2), the window of the filter moves at every time interval, Δt. Consequently, the signal at time t, which is greater than (L-1) Δt, is filtered L times.

5.2.2 Deconvolution of Simulated Waves

The newly developed procedure is checked by the use of simulated and artificial blast waves. The waves used are simulated by superposing element waves. The artificial blast waves used are those recorded at a limestone excavation site. These waves are deconvoluted to check the validity of the developed procedure.

(1) Formulation

Initial values must be given for the following matrices and vectors in order to start filtration:

(i) state transition matrix

$\Phi_{k/k+1}$, or $b_i(k-1)$ $(i = 1, \cdots, L)$

(ii) error covariance matrix

$\mathbf{Q}_t$ (=q**I**) , $\mathbf{R}_t$ (=r**I**)

(iii) initial condition

$\mathbf{x}_{0|0}$, $\mathbf{P}_t$ (=p**I**)

The effects of the initial values on filtering accuracy are examined. Element waves are shown in the upper part of Fig.5.1 (a), (b) and (c). The sampling intervals, Δt, for these waves are 0.1, 0.02, and 0.01 sec. The duration is 2 sec. Seven element waves are superposed at the times 0.0, 1.0, 3.0, 4.0, 5.0 and 6.0 sec (shown in the middle part of Fig.5.1). These waves are combined with white noise of an intensity of 1% of the mean square value of the waves. The sampling numbers of the moving window, L, for (a), (b) and (c) are 20, 100, and 200. The values of p, q, and r are 10^{-2}, 10^{-4}, and 1/L. Identification accuracy improves as the time interval, Δt, becomes smaller (in the lower part of Fig.5.1 [a], [b] and [c]). This means that a Δt of at least 0.02 sec is necessary for the sampling interval.

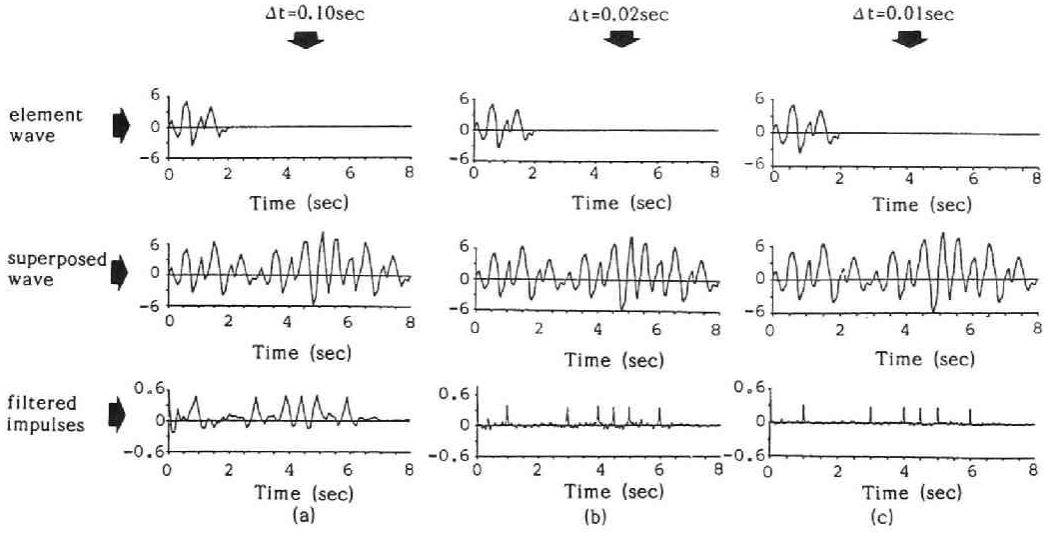

Fig. 5.1 Dissolution of a train of impulses for three sampling intervals. Upper: fundamental wave. Middle: superposed wave. Lower: estimated train of impulses. Sampling time interval: (a) 0.10 sec, (b) 0.02 sec, (c) 0.01 sec.

For the coefficients, $b_i(k)$, three types of models are considered: i) the impulse at time k is expressed as the summation of the impulses in the window that have been multiplied by weights proportional to their amplitudes; ii) the impulse at time k is expressed as the summation of the impulses in the window that have been multiplied by equal weights; and iii) the impulse at time k is expressed as the summation of impulses in the window, in which the impulse close to time k has much more weight, and each weight decreases linearly. Good results are obtained when ii) is assumed.

The values of p, q, and r are varied to examine the effect on filtering accuracy. The ratios of p to q and p to r have no affect on the filtering results. Peaks show up clearly even when the ratio of q to r becomes small.

(2) Deconvolution of blasting records

The robustness of the procedure is here examined by the use of observed records. Blasting records are used because the physical characteristics of the source are clear. Kunimatsu et al. [9] proposed criteria for the level of blasting vibration. More detailed studies are necessary to make blasting more efficient and to restrict its vibration effects.

Two kinds of blasting are used; single shot and a series of single shots with time delay. The time delays in the series of single shots must be considered when blasting data are analyzed. The nominal time delay for a series of single shots is known because the trigger time is measured in the field where the tests are carried out, but it is not exact. The Kalman filter is used to determine the time delay for a series of single shots. Blasting data for the limestone quarry of Ube Industries Ltd., recorded at the sand and rock site, were used. The parameters for these data are shown in Table 5.1. The single shot and series of single shots travel the same path from the source to the site. The single shot is considered to represent the Green function. The series of single shots are expressed as the convolution of a single shot and the train of impulses, for which the times of occurrence coincide with the blasting times. This relation between a single shot and a series of single shots is the same as that between an aftershock and a mainshock.

The identified time intervals of the delayed blastings for three sets of data are shown in Fig.5.2. The upper part of the figure is for single shots and middle part for the series of single shots. The times of the estimated impulses correspond to the blasting times. The number of blastings is given as *a priori* information. The Kalman filter algorithm is applied to the waves shown in Fig.5.2 (a) and (b). Fig.5.2 (c) shows the identified trains of impulses. The arrows in this figure indicate selected impulses of large amplitude. A comparison of nominal and estimated time delays is given in Table 5.2, and superposed waves with nominal and identified time delays is given in Fig 5.3. The upper part of this figure

shows the original waves observed in situ, the middle part waves superposed with nominal time delays, and the lower part waves superposed with estimated time delays. As judged from the peak phases, the waves synthesized with the identified time delays (lower) agree well with the observed waves (upper). This procedure therefore is robust enough to be used to analyze observed records.

Table 5.1 Blasting data

Soil Condition	Shot Data	Nominal Time Delay (msec)	Distance (m)
Rock	TEST00A	60 65 75	100
	TEST00D	60 65 70	150
Sand	ISA16	20 20	5.19

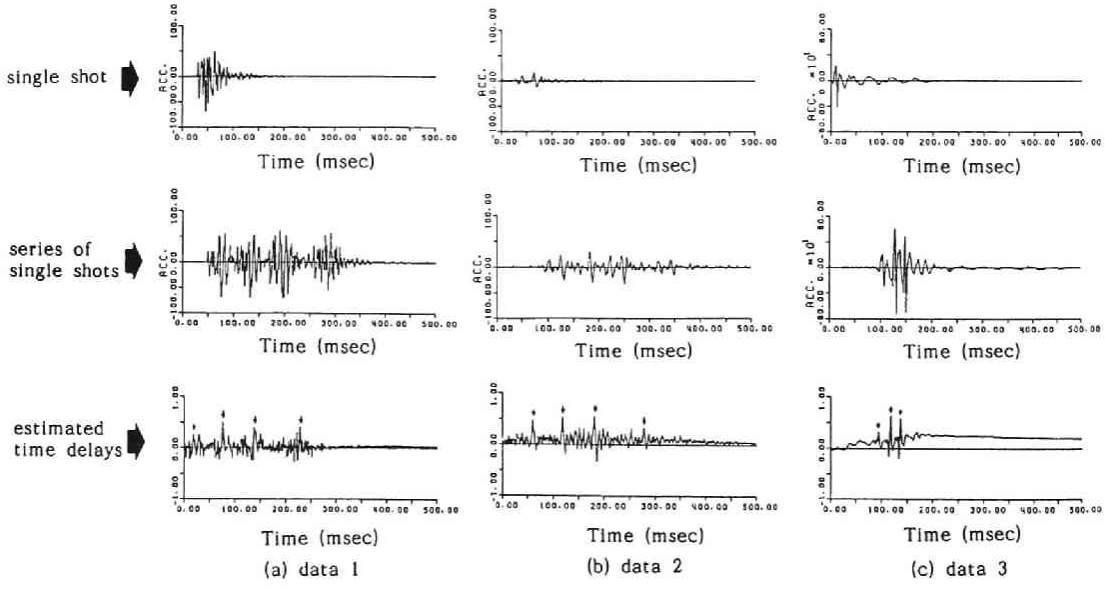

Fig. 5.2 Time intervals in delayed blastings estimated from observed records
(a) single shot, (b) series of single shots, (c) estimated time delay

Table 5.2 Comparison of nominal and estimated time delays

Soil Condition	Shot Data	Nominal Time Delay t_1 (ms)	Estimated Time Delay t_2 (ms)	Δt(ms) $t_2 - t_1$
Rock	TEST00A	60	57	- 3
		65	62	- 3
		75	90	+15
	TEST00D	60	57	- 3
		65	63	- 2
		70	97	+27
Sand	ISA16	20	19	- 1
		20	24	+4

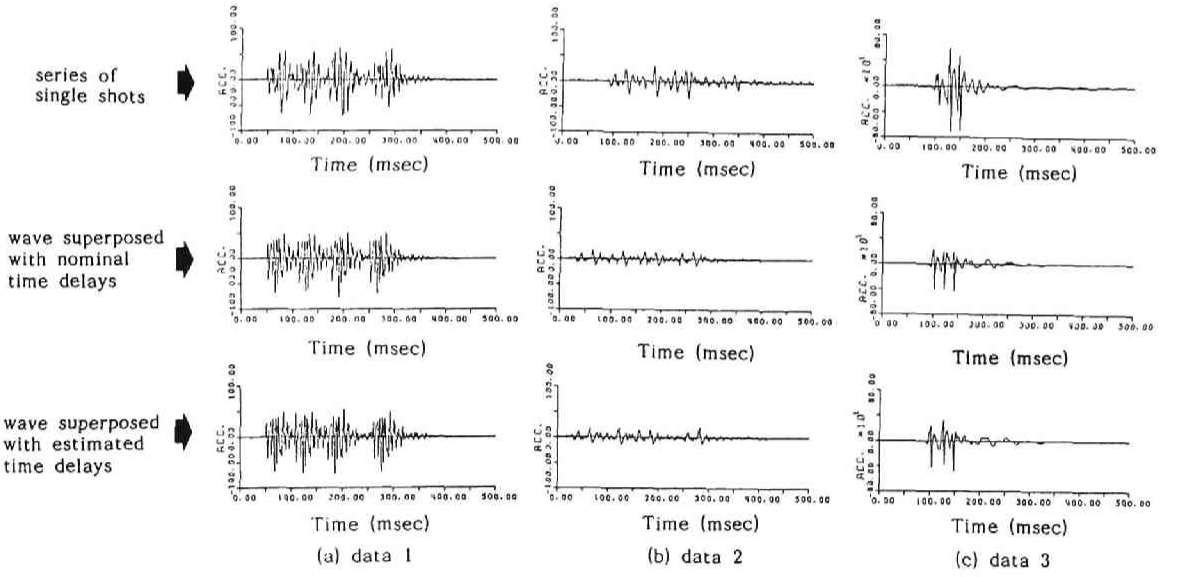

Fig. 5.3 Comparison of waves superposed with the nominal time delay and those superposed with the estimated time delay: (a) a series of single shots, (b) wave superposed with the nominal time delay, (c) wave superposed with the estimated time delay.

5.2.3 Identification of the Fault Rupture Mechanisms

The mainshock is expressed by the convolution of an aftershock and a train of impulses according to Eq.(5.4). The train of impulses can be obtained by the use of the Kalman filter algorithm. Fault rupture mechanisms are identified by taking into account the time intervals of extracted trains of impulses. The identified parameters are the starting point of the rupture; the rise time of the aftershock, τ_a; the rupture velocity, v_r; and the shear wave velocity, v_s. Records obtained at seven local JMA stations: Muroran, Mori, Hachinohe, Miyako, Akita, Sakata, and Niigata during the 1983 Nihonkai Chubu earthquake are used to identify the fault mechanisms.

(1) Fault model

If the small event is given, earthquake motion that takes into account the fault extent can be synthesized by superposing the small event on the assumed fault with the time lags caused by the delays in rupture on the fault plane. A rectangular fault plane that has the length, L, and width, W, is treated. Three additional parameters are needed to define the rupture mechanics of the fault: the rupture velocity, v_r; the final dislocation, D; and the rise time, τ. The outline of this fault model is given in Fig.4.1. The ground surface is the x-y plane, on which the observation station, Q, is located. The distance from point, O, to the observation station represents the distance from the source to the site. Rupture is assumed to begin at point $A_e(1,1)$, to propagate in all directions with a uniform velocity, and to stop at the periphery of the fault plane.

If the fault plane is divided into n^2 elements, n small events must occur in each element to satisfy the scaling law for rise time. Green's function is used to generate these small events; but, because it does not satisfy the scaling law for stress drop when microearthquakes are used as the Green function, a new scaling law that accounts for this effect in fault dislocation is proposed.

On the basis of the scaling law, the following relation between the displacement time function of a large event, g_L, and that of a small event, g_S, can be formulated [5]:

$$g_L(Q, t) = \sum_{l}^{N_L} \sum_{m}^{N_W} \sum_{n}^{N_D} g_S(Q, t-\tau_{lmn}) \tag{5.10}$$

in which

$$\tau_{lmn} = \xi_{lm}/v_r + (R_{lm}-R^*)/v_S + (k-1)\tau_S \tag{5.11}$$

Eq.(5.11) gives the time delay of the superposition for each small event. τ_S is the rise time of the small event; ξ_{lm}/v_r the time delay due to rupture propagation from the point at the initial element, $A_e(1,1)$, to the point at the other element, $A_e(l,m)$; and $(R_{lm}-R^*)/v_S$ is the time delay between the wave arriving from the initial element and the one arriving from the rupture front.

The relation between magnitude and seismic moment as proposed by Geller [10] is

$$\begin{array}{cc} \log M_0 = 18.89 & (M_s < 6.76) \\ \log M_0 = 1.5M_s + 5.51 & (6.76 < M_s < 8.12) \\ \log M_0 = 3.0M_s + 3.33 & (8.12 < M_s < 8.22) \\ M_s = 8.22 & (28.0 < \log M_0) \end{array} \qquad (5.12)$$

According to the scaling law of Kanamori and Anderson [11], the ratio, n, between the source parameters of the large event (fault length, L, fault width, W, and average dislocation, $\overline{D}$.) and the parameters of the small event is written in terms of the seismic moments of the large event, M_{0L}, and the small event, M_{0S}, as

$$n = \sqrt[3]{\frac{M_{0L}}{M_{0S}}} \qquad (5.13)$$

The mainshock of the Nihonkai Chubu earthquake occurred on 26 May 1983 and the maximum aftershock on 21 June 1983, the respective JMA magnitudes being 7.7 and 7.1. The geographic locations of the seven recording sites and the epicenters are shown in Fig.5.4. The main characteristics of crustal activity in this region as reported by Hirasawa et al. [12] are 1) The aftershock area is narrowly spread N-S, extending from 40°1'N to 41°3'N according to the aftershock data processing done at the Tohoku University and Hirosaki University. The width of the aftershock area is 30-35 km and the source depth less than 70 km. The fault plane inclines to the island arc side with a dip angle of about 20°. 2) The analysis of the P-wave radiation pattern indicates that the fault is the dip-slip fault with E-W compression. 3) From the near field records, the fault is seen as being composed of two parts. The time interval for this multiple shock is about 24 sec, and the distance between the two starting points of the ruptures is about 50 km. The respective magnitudes of the main and after shocks are 7.7 and 7.1. Solving Eqs.(5.12) and (5.13) for the number of superpositions, n, gives the approximate value of 2.

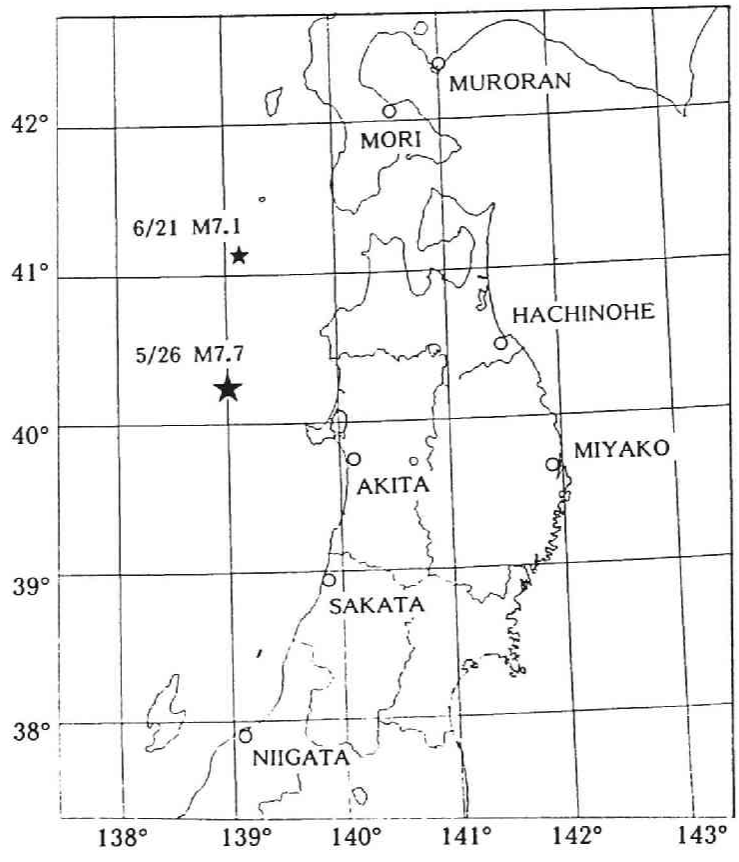

Fig. 5.4 Epicenters of the mainshock and maximum aftershock in the 1983 Nihonkai-Chubu earthquake.

The aftershock area for the Nihonkai Chubu earthquake observed at Hirosaki University is shown in Fig.5.5. The fault shape, modeled to be rectangular, covers the aftershock area. The rectangular fault model determined from Fig.5.5 is shown in Fig.5.6. It includes the aftershock area and extends N-S. The fault length is 150 km, the width 50km, the depth 10 km, and the dip angle 20°. The fault plane is divided into four elements according to the scaling law. Small events occur eight times because individual small events occur two times in each element to satisfy the scaling law of rise time. Consequently, the mainshock is expressed by the superposition of eight aftershocks.

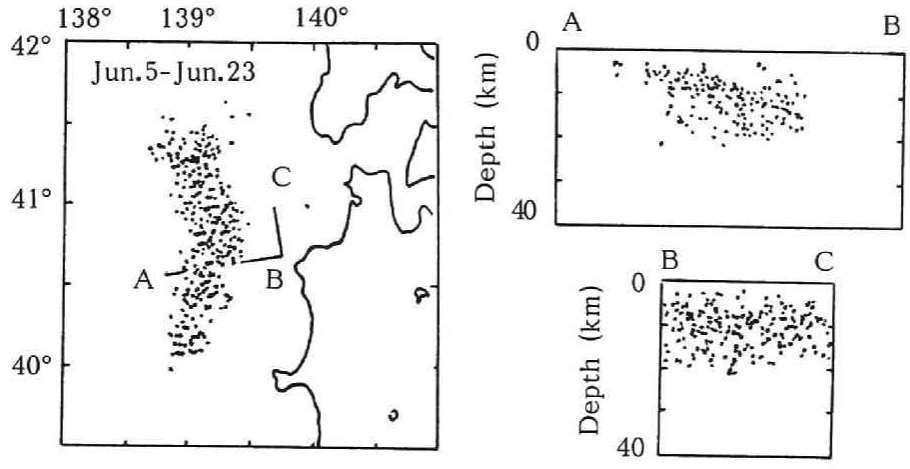

Fig. 5.5 Aftershock area and distribution of hypocenters of the 1983 Nihonkai-Chubu earthquake.

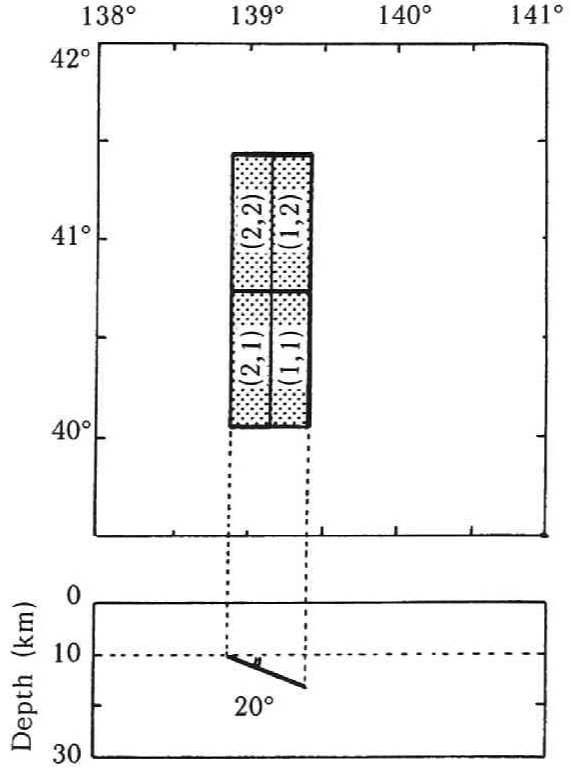

Fig. 5.6 Fault model of the 1983 Nihonkai-Chubu earthquake.

(2) Correction of observation records

The records used in the analysis are those recorded at seven sites: Akita, Hachinohe, Miyako, Mori, Muroran, Niigata, and Sakata on the JMA's displacement type seismographs. The magnification factor, natural periods of horizontal and vertical motion, and damping constant of this type of instrument respectively are 1, 6.0, 5.0 and 0.55. In general, the sensitivity of the displacement type seismograph decreases markedly in the long period range, and the phase delays decrease in the short period range. The amplitude characteristics of the JMA seismograms are shown in Fig.5.7. The amplitude and phase characteristics are corrected after Noda et al. [13]

The records are corrected with a digital filter [14] using the Fourier transform. The amplitude and phase characteristics of this filter are given in Fig.5.8. This filter, however, does not satisfy the causality. This means that an unexpected wave appears before the initial part of the wave. In this study, the Chebychev filter with an equi-ripple pass-band, $F_c(f)$, which is a recursive digital filter that satisfies causality, is used for the instrument correction. This filter is

$$F_c(f) = \frac{\exp\{i\phi(f)\}}{R(f)} A(f) \tag{5.14}$$

$$R(f) = \frac{1}{\sqrt{\{(f_0/f)^2-1\}^2 + 4h^2(f_0/f)^2}} \tag{5.15}$$

$$\phi(f) = \tan^{-1}\{\frac{2h(f_0/f)}{(f_0/f)^2-1}\} \tag{5.16}$$

The observed wave, the wave corrected with the correction filter, F(t), and the wave corrected with the correction filter, $F_c(t)$, are shown in Fig.5.9 (a), (b) and (c).

After correcting the main- and aftershock records by the above procedure, the trains of impulses for each of the seven stations are calculated (Fig.5.10). The upper part of the figure shows the wave of the mainshock, the middle the wave of the aftershock, and the lower part the estimated trains of impulses for each site. As the mainshock is composed of eight superpositions of aftershocks, the eight impulses which have the largest amplitudes are selected. Fault rupture mechanisms are estimated on the basis of the identified trains of impulses at eight stations generally fit the assumed rupture process. Four parameters are to be identified: the starting element of the rupture; the rise time of the aftershocks, τ_a; the rupture velocity, v_r ; and the shear wave velocity, v_s. The center of the element is specified as the representative point of rupture. These four parameters are varied independently within an adequate range. The starting point of rupture varies for 4 elements, (1,1) - (2,2).

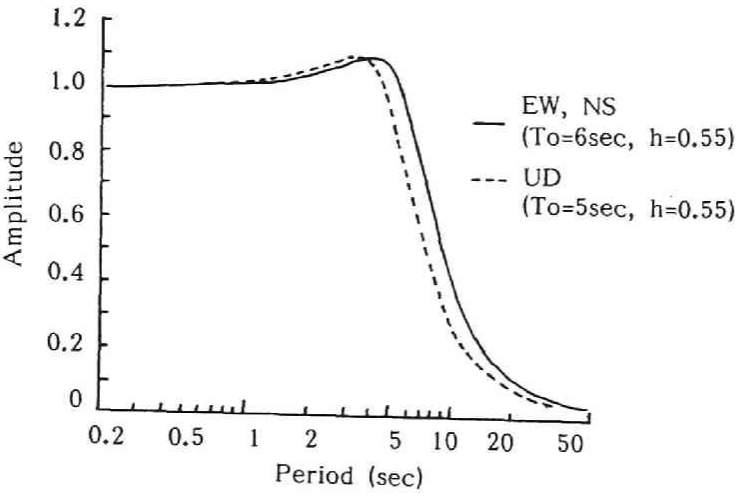

Fig. 5.7 Amplitude characteristics of JMA seismograms.

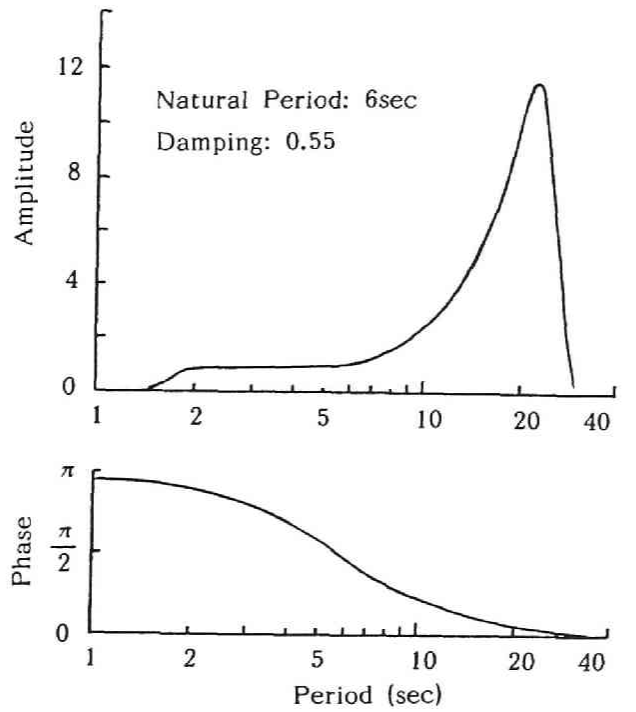

Fig. 5.8 Amplitude and phase characteristics of the correction filter.

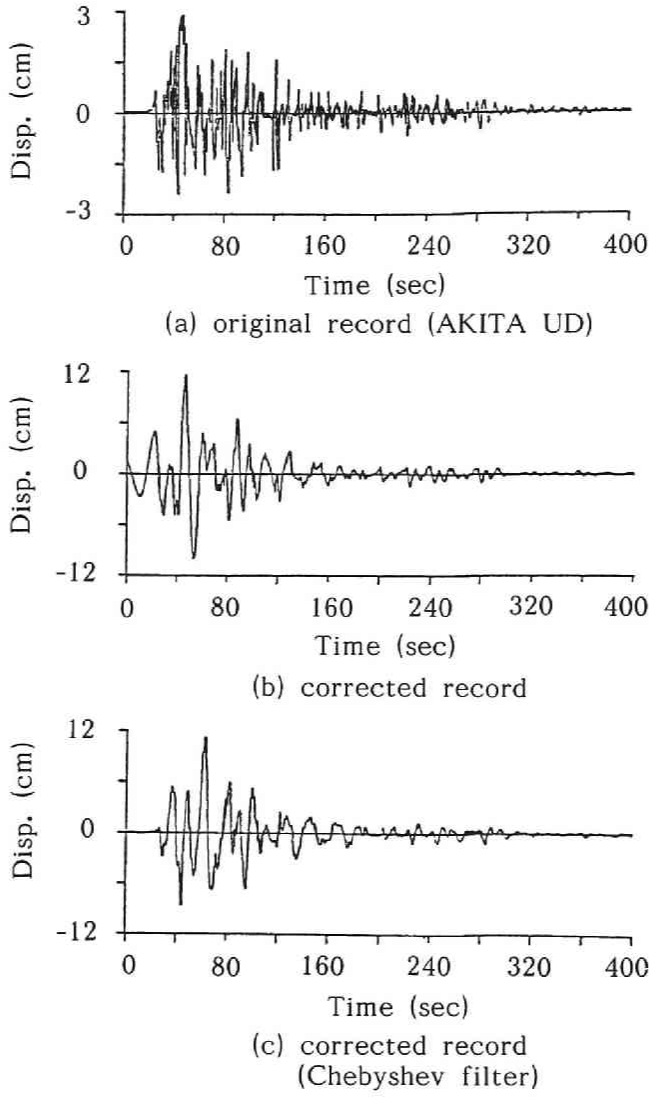

Fig. 5.9 Example of a corrected seismogram.

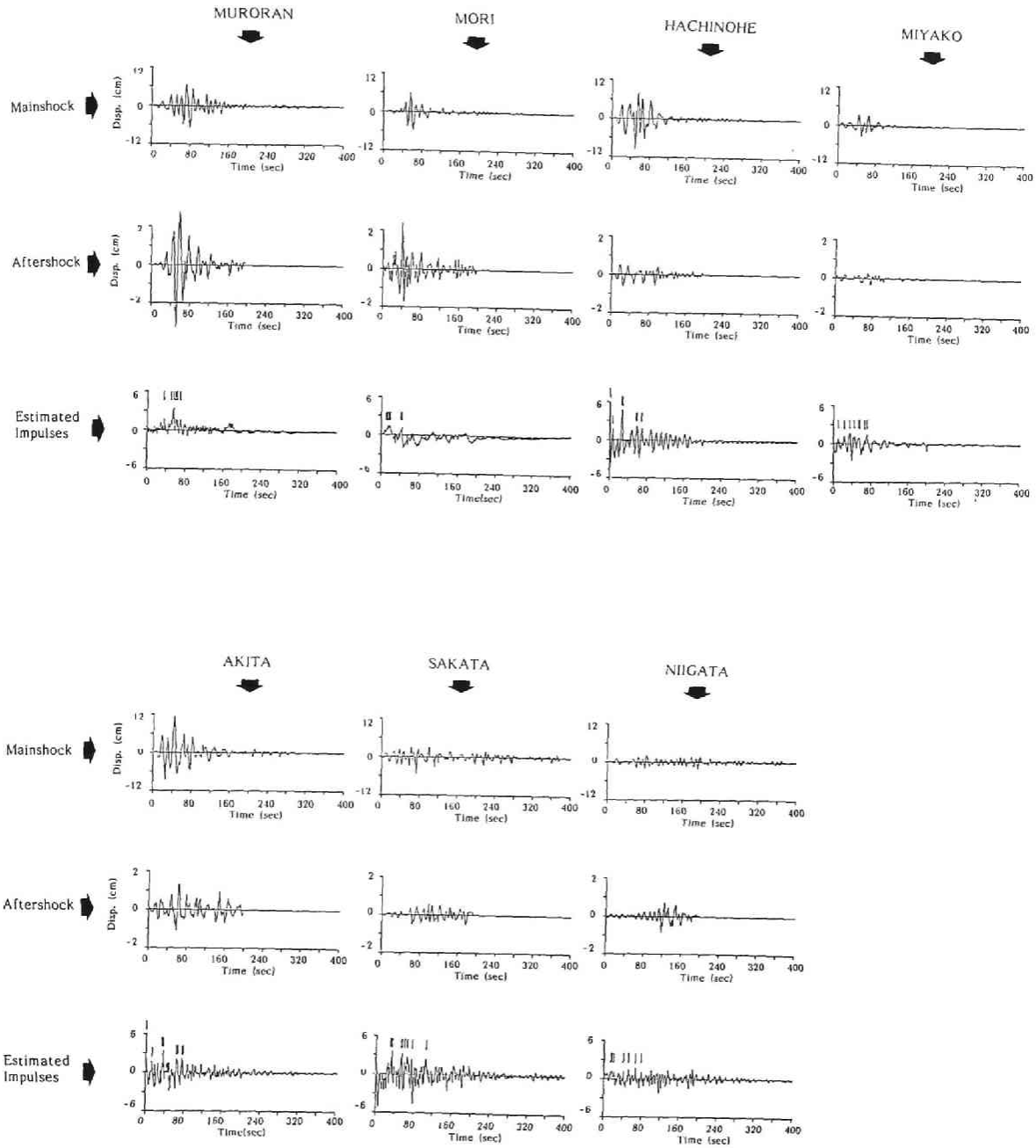

Fig. 5.10 Deconvoluted trains of impulses (arrows: bottom row) at selected stations obtained from mainshock and aftershock records.

The rise time of the aftershock varies from 1.0 to 10 sec in 0.1 sec increments. The rupture velocity varies from 1.0 to 5.0 km/sec in 0.1 km/sec increments. The shear wave velocity varies from 1.0 to 6.0 km/sec in 0.1 km/sec increments. The trains of impulses for all the combinations of these parameters are compared. The computed intervals of the impulses are compared with the identified impulses according to the following relative criteria;

$$J = \frac{1}{N}\sum_{i=1}^{N} \frac{|Q_{oi} - Q_{ci}|}{Q_{oi}} \tag{5.17}$$

in which Q_{oi} is the time of occurrence of the i-th impulse estimated from observed data at the j-th site; Q_{ci} the time of occurrence of the i-th impulse computed from a parametric study; and J_j the criteria of judgment for the j-th site. The optimal combination of parameters is

$$\sum_{j=1}^{N} J_j \rightarrow \min. \tag{5.18}$$

The ten best-fitted sets of optimum parameters calculated with Eq.(5.18) are shown in Table 5.3. A comparison of the trains of impulses calculated from optimum fault parameters and those identified by use of the Kalman filter is shown in Fig.5.11.

Table 5.3 Identified optimum fault parameters

No.	Starting Point of Rupture	Rise Time (sec)	Rupture Velocity (km/sec)	Shear Wave Velocity (km/sec)	Judgment
1	(1, 1)	2.00	2.40	3.60	0.40222
2	(1, 1)	2.00	2.40	3.50	0.40222
3	(1, 1)	2.00	2.40	3.40	0.40259
4	(1, 1)	2.00	2.40	3.70	0.40266
5	(1, 1)	2.00	2.40	3.60	0.40269
6	(1, 1)	2.00	2.40	3.50	0.40269
7	(1, 1)	2.00	2.50	4.00	0.40272
8	(1, 1)	2.00	2.50	3.90	0.40278
9	(1, 1)	2.00	2.50	3.80	0.40284
10	(1, 1)	2.00	2.50	4.10	0.40285

As judged from the identified optimum fault parameters, rupture started in the southern part of the fault and propagated northward at the velocity of 2.4 km/sec. The rise time of the aftershock was 2.0 sec. These results agree with those of Hirasawa [12] showing two fault ruptures that occurred at a time interval of 24 sec and a distance of about 50 km. Irikura estimated the rise time of the mainshock from the trough frequency of the near field acceleration spectrum as 4.7 sec which corresponds to a rise time of 2.35 sec for the aftershock. The shear wave velocity of the crust is generally said to be 3.0 4.5 km/sec. The rupture velocity, v_r , satisfies the condition $v_r < v_s$ and is equal to $0.7v_s$.

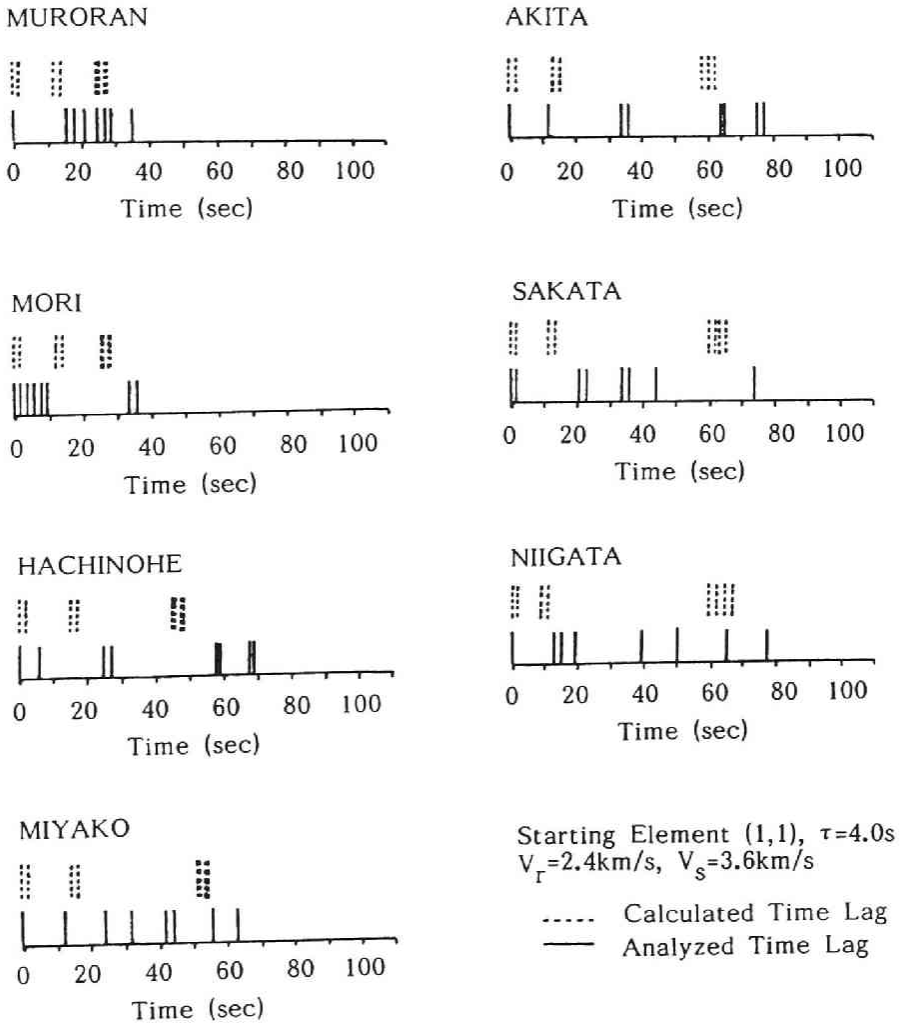

Fig. 5.11 Comparison of trains of impulses calculated from optimum fault parameters with those obtained using the Kalman filter.

5.3 Synthesis of Ground Motion by the Statistical Green Function

5.3.1 The AR-MA process

The autoregressive moving average (AR-MA) process was used to construct a stochastic time series model of earthquake motion. Earthquake motions are assumed to be synthesized by the second-order AR-MA process. This means that a synthesized motion is the output of a single degree-of-freedom system excited by a nonstationary white noise, as shown in Fig.2.1. Such nonstationary characteristics of the filter as the natural frequency, f_0, and the damping constant, h, of a single degree-of-freedom system can be calculated from AR-MA parameters that have been determined by the two-stage least square method [15] from a sequence of data segmenting an earthquake record. Regression analysis then is done for the nonstationary characteristics of the filter in order to set up an attenuation law given as a function of the magnitude and epicentral distance.

The AR-MA process of order (2, 2) is

$$y_t = - \alpha_1(t)y_{t-1} - \alpha_2(t)y_{t-2} + \varepsilon_t + \beta_1(t)\varepsilon_{t-1}\ \ \beta_2(t)\varepsilon_{t-2} \qquad (5.19)$$

in which $\varepsilon(t)$ is the input white noise; y(t) the observed waveform of the earthquake; and $\alpha_i(t)$ and $\beta_i(t)$ (i=1,2) nonstationary AR-MA parameters identified from observation records alone if the input is assumed to be nonstationary white noise [16]. Eq.(5.19) is similar in form to the stationary process, except that its parameters are functions of time, t. To obtain a reasonable estimate of this nonstationary trend, the rectangular time window is multiplied for a given data series, and the center point of the window is assumed to be the time at which the model parameters are specified. For the window length, T_w, 1 sec is adopted [17].

The parameters $\alpha_i(t)$ (i=1,2) are related to the natural frequency and the damping of the single degree-of-freedom system as follows [18]:

$$\lambda^2 + \alpha_1\lambda + \alpha_2 = 0\ , \quad \left.\begin{matrix}\lambda \\ \lambda^*\end{matrix}\right\} = \exp\left(-2\pi f_0 h T_m \pm i2\pi f_0 T_m\sqrt{1-h^2}\right) \qquad (5.20)$$

in which $i=\sqrt{-1}$, λ and λ^* are conjugate complex solutions of the quadratic equation, and T_m is the sampling interval. Eq.(5.20), is used to describe the equivalent nonstationarity of the single degree-of-freedom system from nonstationary AR-MA parameters. To pro-

duce a model with which to simulate earthquake motion, the nonstationarity of the parameters must be expressed by simple mathematical formulas. These nonstationarities are given in Table 5.4 [17], in which $\sigma(t)$ is the input white noise intensity, and σ_{max} and t_p the maximum values of the intensity and occurrence time. The regression equations are given by

$$P = c_1 + c_2M + c_3\log R \tag{5.21}$$

in which P stands for the parameters in Table 5.4, M is the magnitude, and R the distance. A regression analysis is made for each parameter in Table 5.4 using the earthquake magnitude and the epicentral or hypocentral distance.

Table 5.4 Modeling of nonstationarity

$\sigma(t) = \sigma_{max}(t/t_p)\exp(1-t/t_p)$
$f(t) = f_A\exp(-f_Bt)$
$h(t) = h_A\exp(h_Bt)$
$\beta_1(t) = \beta_1$ (const.)
$\beta_2(t) = \beta_2$ (const.)

5.3.2 Simulation of Ground Motion

Waveforms are simulated by the second order AR-MA process. Two data bases are used to obtain the difference for epicentral distance. Because there is so little wide-spread data, the data base has an epicentral distance that ranges from a few kilometers to a few hundred kilometers. One data base is composed of the 57 earthquakes that occurred in California, U. S. A. between 1933 and 1971. The other consists of the microearthquakes that took place between May 1980 and December 1981 at Kamigamo, Abuyama, Myoken, and Rokko in the Kinki district of Japan. The respective numbers of records in these data bases are 116 and 192. The former data base is designated DB-1 and the latter DB-2. The relations between magnitude and epicentral distance for DB-1 and DB-2 is shown in Fig.5.12 (a) and (b).

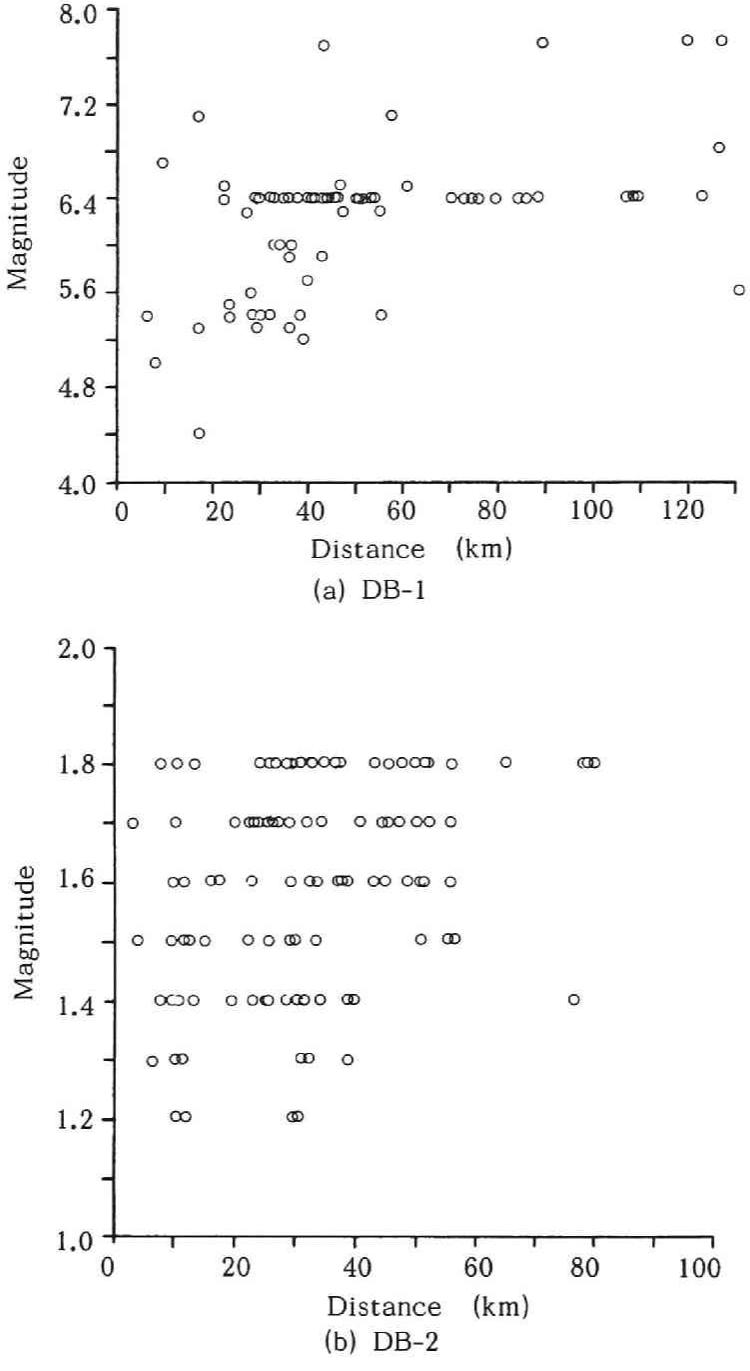

Fig. 5.12 Relation of magnitude to epicentral distance.

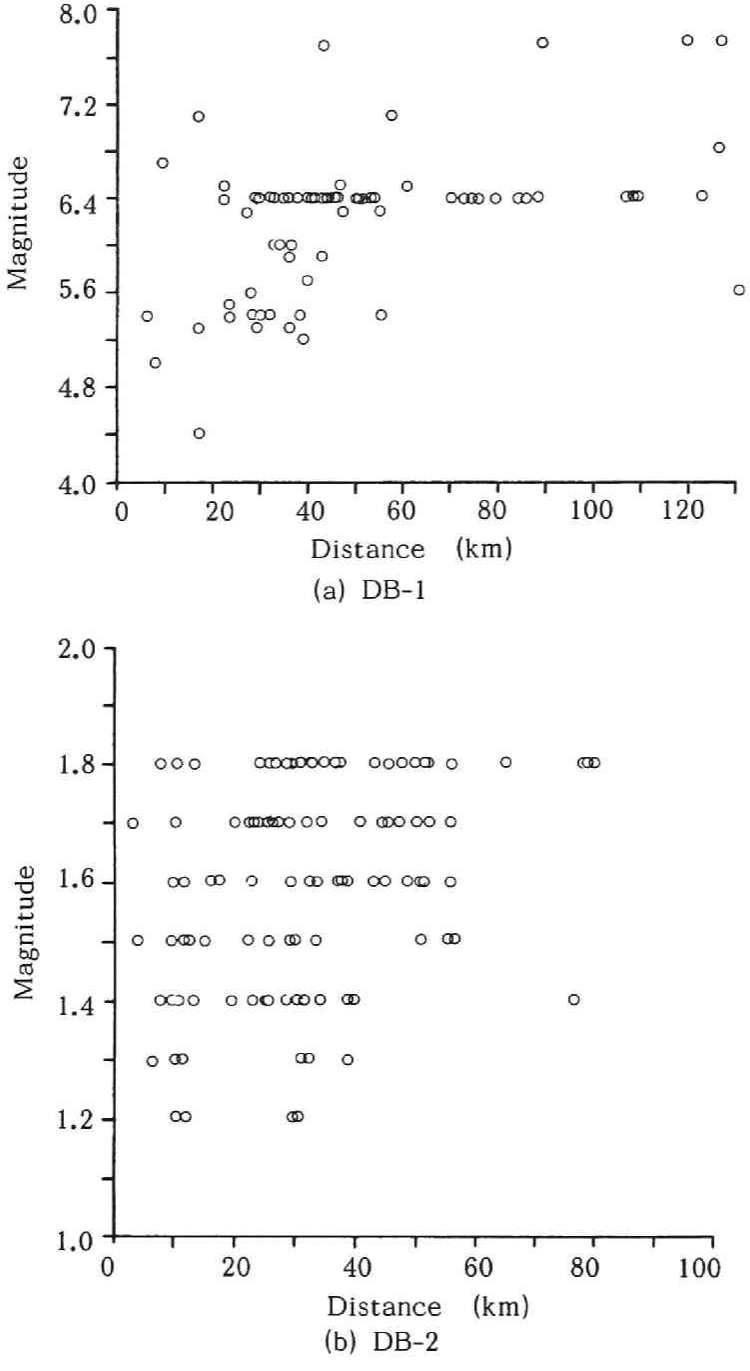

Fig. 5.12 Relation of magnitude to epicentral distance.

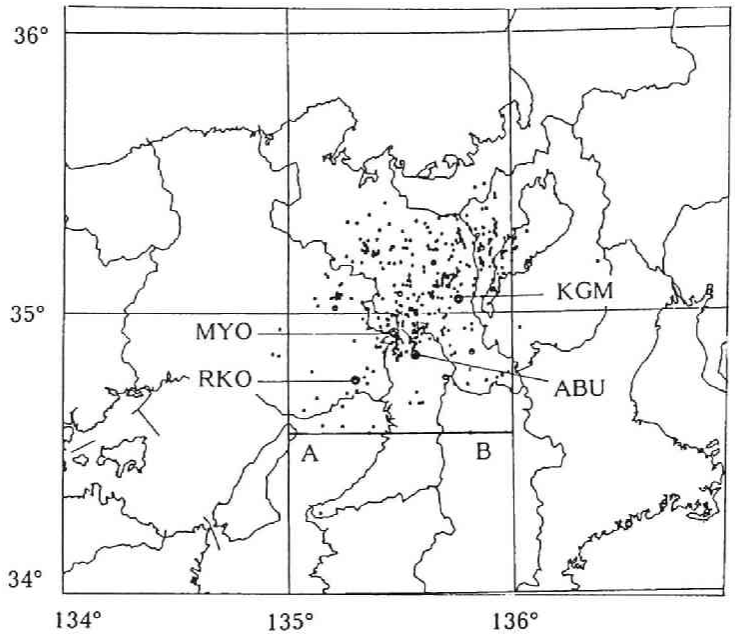

(a)

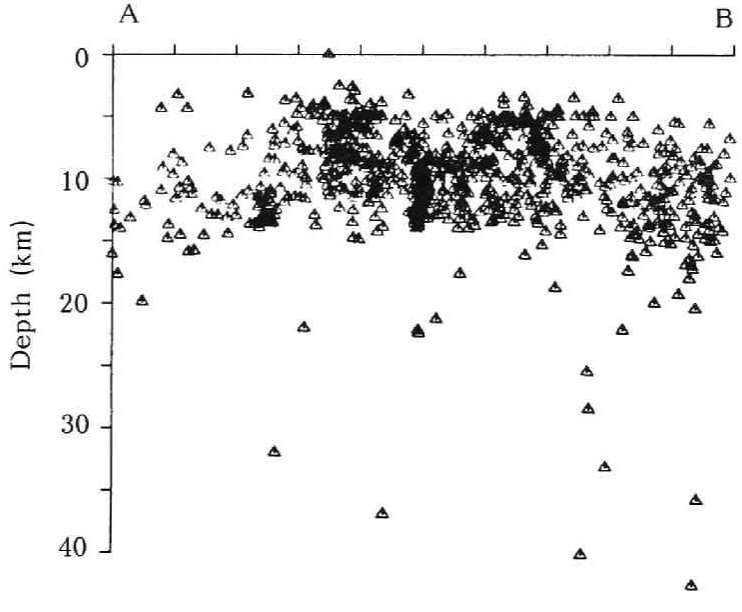

(b)

Fig. 5.13 (a) Locations of observation stations and epicenters.
(b) Source depth.

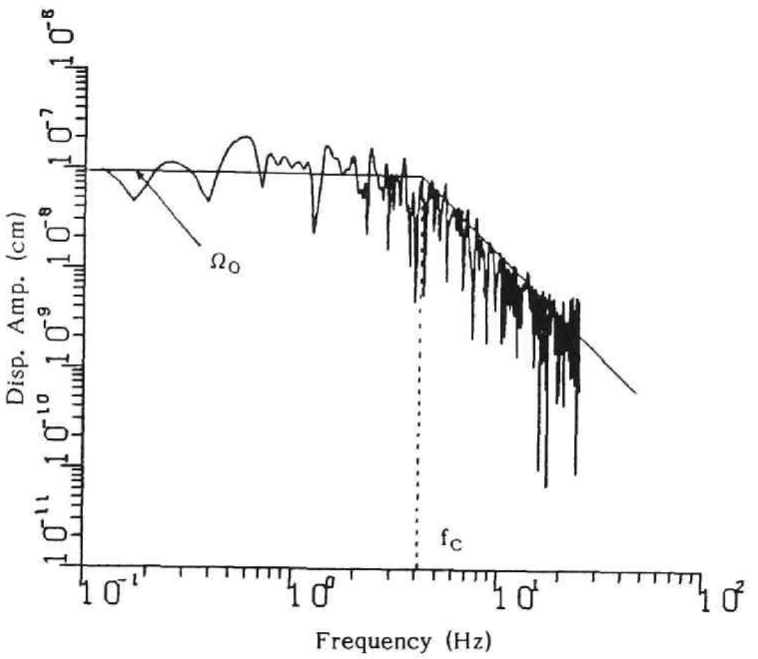

Fig. 5.14 Typical displacement amplitude spectrum of an observed microearthquake.

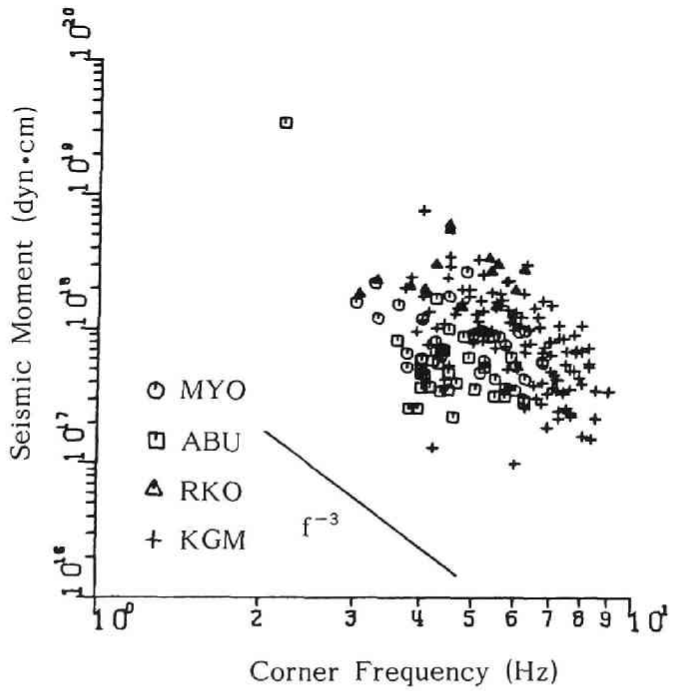

Fig. 5.15 Relation of the corner frequency to the seismic moment.

in which δ is the dip angle. In logarithmic form the spectra defined by Eq.(5.22) consist of four straight line asymptotes with slopes of zero, one, two, and three. The frequencies that correspond to the intersections of these straight lines are

$$\begin{aligned} f_1 &= 1/(2\pi\chi_L) \\ f_2 &= 1/(2\pi\chi_\tau) \\ f_3 &= 1/(2\pi\chi_W) \end{aligned} \tag{5.24}$$

Considering an earthquake motion that has a k times larger f_1 value, it is evident from Eqs.(5.22) and (5.23) that L is 1/k times the original value. According to the scaling law (given later), D and W also have a linear relation to L ($W=c_1L$, $D=c_2L$); therefore, the values of D, W and L are 1/k times the original value. Because the seismic moment is proportional to DWL, it decreases k^3 times when the f_1 value increases k times; consequently, the relation between the corner frequency and the seismic moment in logarithmic form has a slope of -3. The relation between the corner frequency and seismic moment obtained from the microearthquakes is shown in Fig.5.15. The distribution of data obtained from the microearthquake records has the slope of -3 to -2.

The seismic moment, M_0, is related to the amount of displacement in the low frequency region. The displacement spectrum in this region usually has a constant value called the flat level, Ω_0. Therefore, the seismic moment is

$$M_0=\frac{\Omega_0}{R_{\theta\phi}}(4\pi R\rho c^3) \tag{5.25}$$

The chosen values of ρ and c were 2.6 t/m^3 and 3.4 km/s. The chosen value of $R_{\theta\phi}$ was 0.4, the average value of the S-wave radiation pattern.

The effective fault radius, r, is given by considering circular rupture [20];

$$\begin{aligned} r_p &= 0.21\ v_s / f_{cp} \\ r_s &= 0.32\ v_s / f_{cs} \end{aligned} \tag{5.26}$$

in which the rupture velocity, v_r, is equal to 0.9 v_s, r_p and r_s the effective fault radii for the P- and S-wave portions of the record, and f_{cp} and f_{cs} are the corner frequencies for the P- and S-wave portions. The effective fault radius, r, is the average of r_p and r_s. The rise time, τ, is expressed in terms of the fault area S ($=\pi r^2$):

$$\tau = \frac{16S^{1/2}}{7\pi^{3/2}v_s} \tag{5.27}$$

and the average dislocation D is given by

$$D = \frac{16}{7\pi\mu} \; r \; \Delta\sigma \tag{5.28}$$

The relation between the seismic moment and average dislocation is

$$M_0 = \mu DS = \mu D\pi r^2 \tag{5.29}$$

Substituting Eq.(5.28) in Eq.(5.29) and solving for $\Delta\sigma$, the stress drop is

$$\Delta\sigma = \frac{7M_0}{16r^3} \tag{5.30}$$

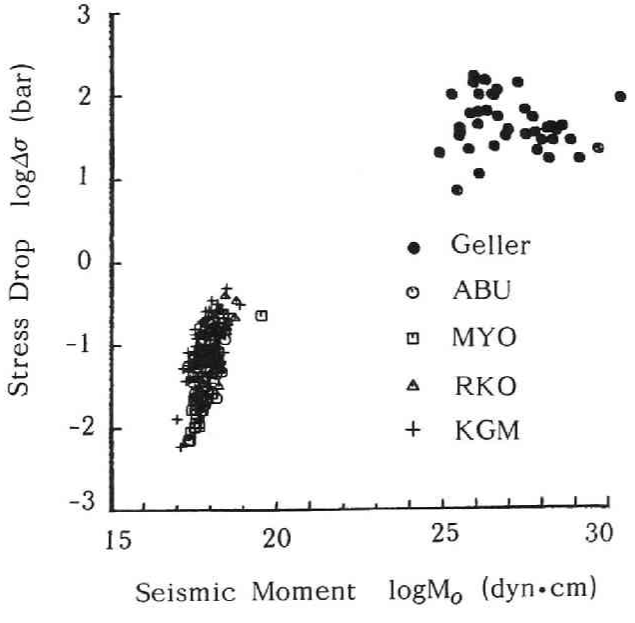

Fig. 5.16 Relation of the seismic moment to the stress drop.

Using these equations Madariaga [20], Brune [21], and Marion [22] determined many fault radii and stress drops for microearthquakes. Relations between the seismic moments, M_0, and the stress drops calculated from Eqs.(5.29) and (5.30) are shown in Fig.5.16 which includes the plots for the large earthquake records (●) reported by Geller [10] as well as those for microearthquakes recorded at Kamigamo (+), Abuyama (○), Myoken (□) and Rokko (Δ).

The average stress drops of the large earthquakes are hundreds of times larger than those of the microearthquakes. For earthquakes of relatively large magnitude, stress drops usually are of the order of several tens of bars regardless of the scale of the event. The stress drops of microearthquakes, however, differ considerably from those of large earthquakes.

(2) Simulation of ground motion

The AR-MA parameters are calculated from Eqs.(5.19) and (5.20). The modeling of the nonstationary parameters is given in Table 5.4. The regression coefficients of DB-1 and DB-2 are shown in Tables 5.5 and 5.6. In DB-1, R in Eq.(5.21) is replaced with Δ+C, in which Δ is the epicentral distance, and C a constant that expresses the effect of the spatial extent of the fault. The value of C is 40 km. In DB-2, R is expressed by the epicentral distance. The waveforms simulated from DB-1 are shown in Fig.5.17. The magnitude used was 5.5 and the epicentral distances 50, 100, and 150 km.

Table 5.5 Regression coefficients (DB-1)

	B_1	B_2	B_3	σ_p
log σ_{max}	2.5451	0.3870	2.1422	0.3516
t_p	-21.2477	1.0849	9.9054	2.6788
log f_A	0.8590	0.0976	0.4007	0.1470
f_B	0.0495	0.0046	0.0253	0.0299
log h_A	-0.8191	0.0532	-0.0631	0.2170
log h_B	0.0665	0.0042	0.0355	0.0503
β_1	-0.1617	0.2004	0.2814	0.2794
β_2	-0.0595	0.0395	0.0202	0.1093
T	-65.1381	2.1087	41.0481	12.2636

Table 5.6 Regression coefficients (DB-2)

	B_1	B_2	B_3	σ_p
log σ_{max}	-4.9100	0.6590	-1.4800	0.2880
t_p	-6.5800	-0.4080	7.8500	1.6500
log f_A	0.3660	0.0895	0.0301	0.0202
f_B	0.0632	0.0193	-0.0396	0.0077
log h_A	0.2340	-0.1370	-0.1320	0.0453
log h_B	0.0448	0.0126	-0.0203	0.0040
β_1	0.0442	0.2660	0.0090	0.0493
β_2	-0.1890	0.2830	-0.1490	0.0483
T	10.4000	-11.0000	27.0000	5.2500

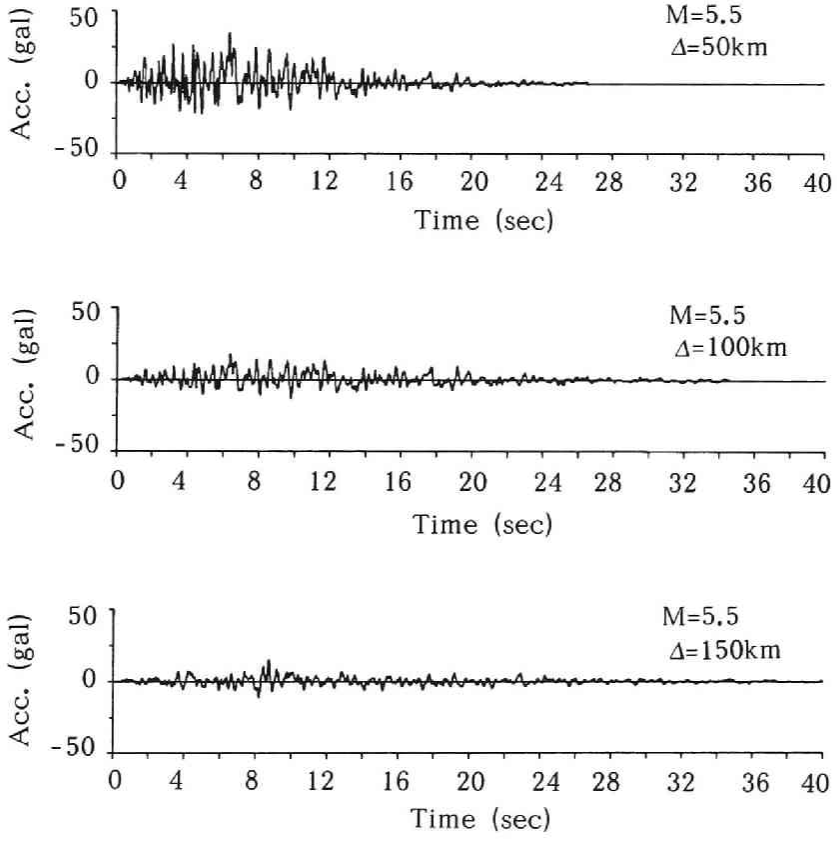

Fig. 5.17 Samples of simulated waves. (DB-1)

The waveforms simulated from DB-2 are shown in Fig.5.18. The magnitude was 1.8 and the epicentral distances 10, 30, and 50 km. Fig.5.18 (a), (b), (c) and (d) shows the respective waveforms that correspond to the Kamigamo, Abuyama, Myoken, and Rokko observation sites. Because the records for the Rokko site were concentrated around an epicentral distance of 30 km, only the waveform at 30 km, is shown. Because waveforms calculated by the above procedure include the influence of the propagation path as well as the geological conditions under the observation site, they can be considered Green functions. Such waveforms are here called the statistical Green function.

A comparison of the waveforms at each observation site shows differences in the high-frequency components and maximum amplitudes even when the magnitudes and epicentral distances are the same. This means that each site shows its particular inherent, vibration characteristics when excited by seismic waves and that the waveform predicted at a site reflects the geological conditions below that site.

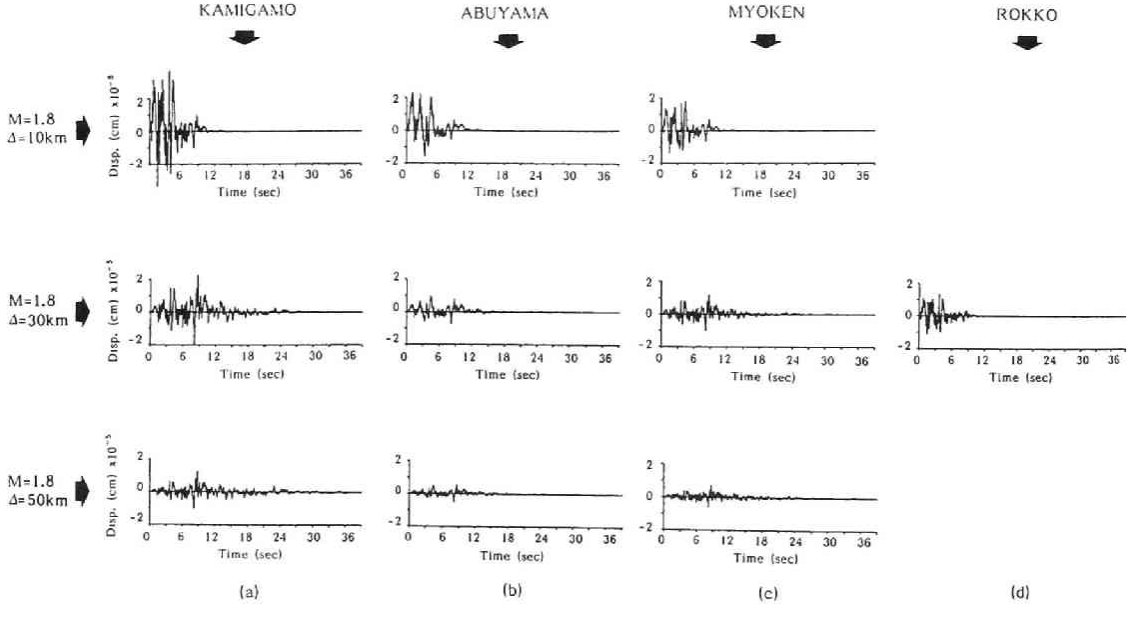

Fig. 5.18 Samples of simulated waves. (DB-2)

5.3.3 Superposition of Small Earthquakes

Earthquake motion that takes into account the fault extent can be synthesized by superposing a small earthquake on the assumed fault based on time lags produced by delays in rupture on the fault plane. The formulation of superposition has been described in section 5.2.3.

The statistical Green function calculated from DB-2 (microearthquakes) can not be superposed directly because of the marked difference in stress drops between large events and microearthquakes. The stress drops of large events are several hundred fold larger than those of the microearthquakes calculated by Eq.(5.30).

A plot of the magnitude, M_S, against the logarithmic seismic moment, M_0, that is based on results obtained by Geller [10], Frankell [23], and McGarr [24] is shown in Fig.5.19. The solid line shows Geller's results, the broken line the results of regression analyses of the data from Frankell and McGarr and this study.

If the statistical Green functions of the microearthquakes are used for superposing, the number of superpositions given by Eq.(5.13) becomes very large because of the substantial difference in the stress drops of the large events and microearthquakes. For example, although the seismic moment, M_0, that corresponds to magnitude M=6.4 is $10^{25.3}$ dyn*cm in Geller's expression, a value of M_S=1.8 is $10^{18.7}$ dyn*cm is seen from the broken line in Fig.5.19. The value of n becomes 157 when these M_0 values are substituted in Eq.(5.13). The microearthquake records used gave an equivalent rectangular fault length of 500 600 m, as calculated from the radius of the fault given by Eq.(5.26) on the assumption that L=2W. The estimated fault length for M_S=6.4 therefore is about 100 km; several times the actual fault length. To eliminate this inconsistency, the difference in stress drop is attributed to dislocation. The Fourier spectrum amplitude of the statistical Green function is magnified by the ratio of the stress drops of the large event to that of the microearthquake. The waveform obtained by using the inverse Fourier transform for the magnified Green function is used as the small event for superposition.

The notations of the source parameters of the large event, small event and the statistical Green function are given in Table 5.7. A stress drop of 30 bars is assumed for the large event and 0.103 bar for the statistical Green function which is the average of the stress drops of all the microearthquake records. The value of m, the ratio of the stress drops of the large event to the statistical Green function therefore is approximately 291. This means that the small event is derived by magnifying the statistical Green function by 291.

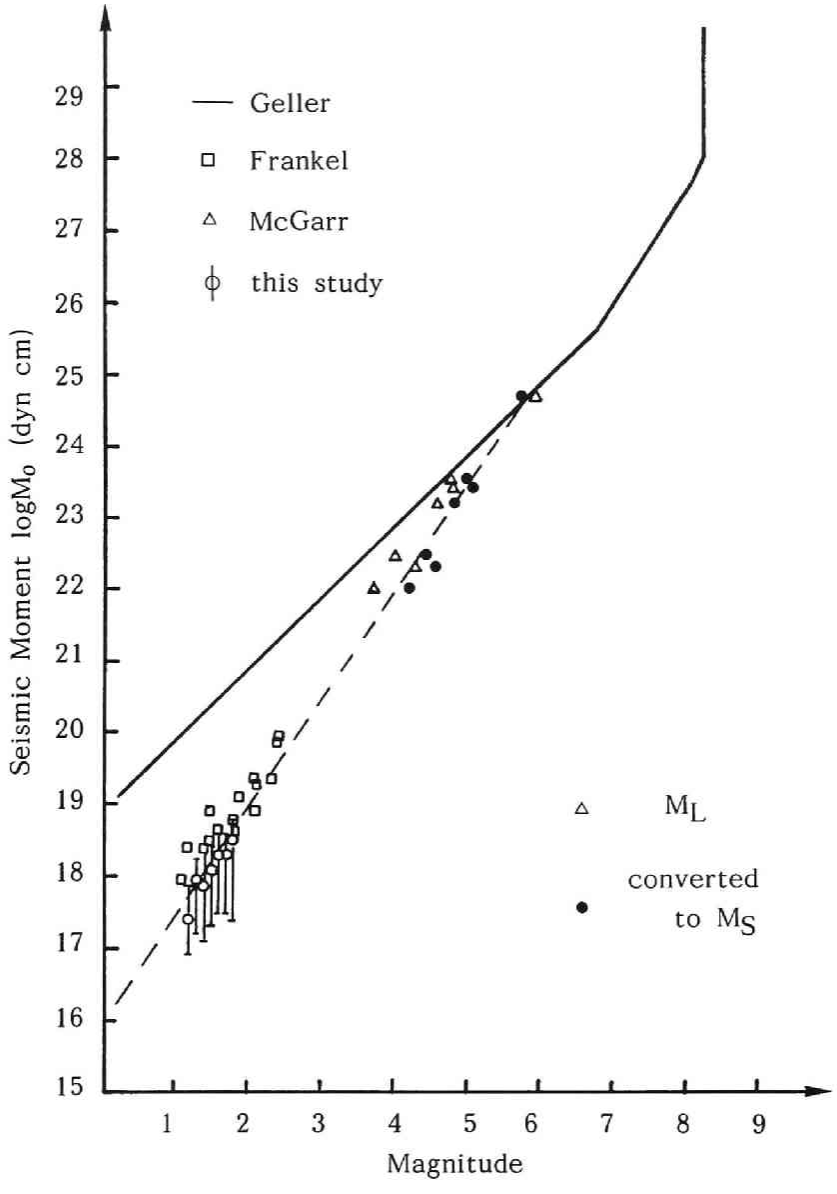

Fig. 5.19 Relation of magnitude to the seismic moment.

Table 5.7 Definitions of source parameters

	Seismic Moment	Width	Length	Dis-location	Stress Drop
Large Event	M_{0L}	W_L	L_L	D_L	$\Delta\sigma_L$
Small Event	M_{0S}	W_S	L_S	D_S	$\Delta\sigma_S$
Micro-Earthq.	M^*_{0S}	W^*_S	L^*_S	D^*_S	$\Delta\sigma^*_S$

Using these parameters, the newly defined scaling law [25] is written

$$\begin{aligned} \Delta\sigma_L &= \Delta\sigma_S = m\Delta\sigma_S^* \\ D_S &= mD_S^* \\ L_S &= L_S^* \\ W_S &= W_S^* \\ M_{0S} &= mM_{0S}^* \end{aligned} \tag{5.31}$$

From these equations

$$\begin{aligned} L_L &= nL_S = nL_S^* \\ W_L &= nW_S = nW_S^* \\ D_L &= nD_S = nmD_S^* \end{aligned} \tag{5.32}$$

The value of the superposition, n, from Eqs.(5.13), (5.31) and (5.32) is obtained from the relation $M_0=\mu DLW$.

$$n = \sqrt[3]{\frac{M_{0L}}{m\ M_{0S}^*}} \tag{5.33}$$

Once n is determined, superposition of the small event is made through Eqs.(5.10) and (5.11).

The superposition procedure in the frequency domain is shown in Fig.5.20. If the large event is synthesized by the general scaling law without considering the difference in

stress drops between large events and microearthquakes, the spectrum for the statistical Green function is shifted along line A-D. This line relates the corner frequency of the large event to that of the statistical Green function. Because the spectrum in the high-frequency range has an f^{-3} asymptote, the decease for the high-frequency component is extreme.

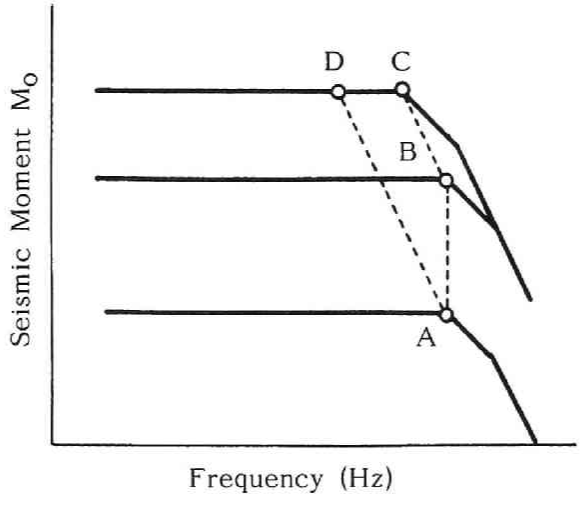

Fig. 5.20 Superposition procedure in the frequency domain.

In the newly proposed scaling law, the statistical Green function is amplified several hundred times and is defined as the small event for superposition. The spectrum of this function is raised on line A-B to compensate for the difference in stress drop between the large event and the microearthquake, then it is shifted along line B-C which is parallel to line A-D. The shift along line B-C takes into account the seismic moment ratio. Consequently, sufficient high-frequency components are incorporated in the simulated waveform. When the spectrum is lifted up along line A-B, the noise also is amplified. This high-frequency noise can be cut off by the following procedure: Because of the relation between the cut-off frequencies and peak accelerations of the simulated waveforms, the cut-off frequency determined just before the peak acceleration varies markedly [26]. This relation is plotted in Fig.5.21. The acceleration is obtained by differentiating each statistical Green function. The magnitude is 1.8 and the epicentral distance 10 km for the KGM, ABU and MYO stations. For the RKO station, the epicentral distance is 30 km as stated previously. Results show that the peak acceleration amplitude becomes large as the cut-off

frequency increases and that there is a flat area between 15 and 20 Hz at every station. A cut-off frequency of 15 Hz therefore was used.

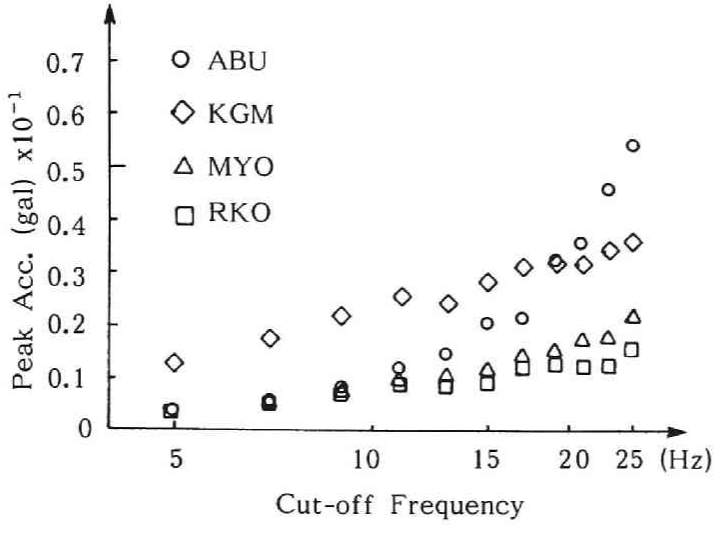

Fig. 5.21 Relation of the peak acceleration to the cut-off frequency.

The statistical Green functions calculated from DB-1 are used to synthesize the large event. The scaling law used corresponds to m=1 in Eqs.(5.31) and (5.32). The obtained accelerations are shown in Fig.5.22. The magnitude chosen was 6.4, the magnitude of the San Fernando earthquake. Epicentral distances were 50, 100, and 150 km. The modified statistical Green function calculated from DB-2 is superposed using the new scaling law to give a synthesized displacement waveform. Acceleration waveforms are calculated by twice differentiating the displacement waveforms. The magnitude is 6.4, and only the three epicentral distances 10, 30, and 50 km are considered. The epicentral distance for Rokko, however, is only 30 km. The acceleration waveforms calculated for the KGM station are shown in Fig.5.23.

Peak accelerations for each distance at the four sites are shown in Fig.5.24 together with the observed peak accelerations for the 1971 San Fernando earthquake. The general attenuation trend for the simulated peak accelerations is similar to that for the observed accelerations, but the differences in peak acceleration for these sites become marked as the epicentral distance shortens (Δ=10 km). At such distances, the effect of the fault extent can not be neglected. This means that it is difficult to obtain a unique estimation of peak

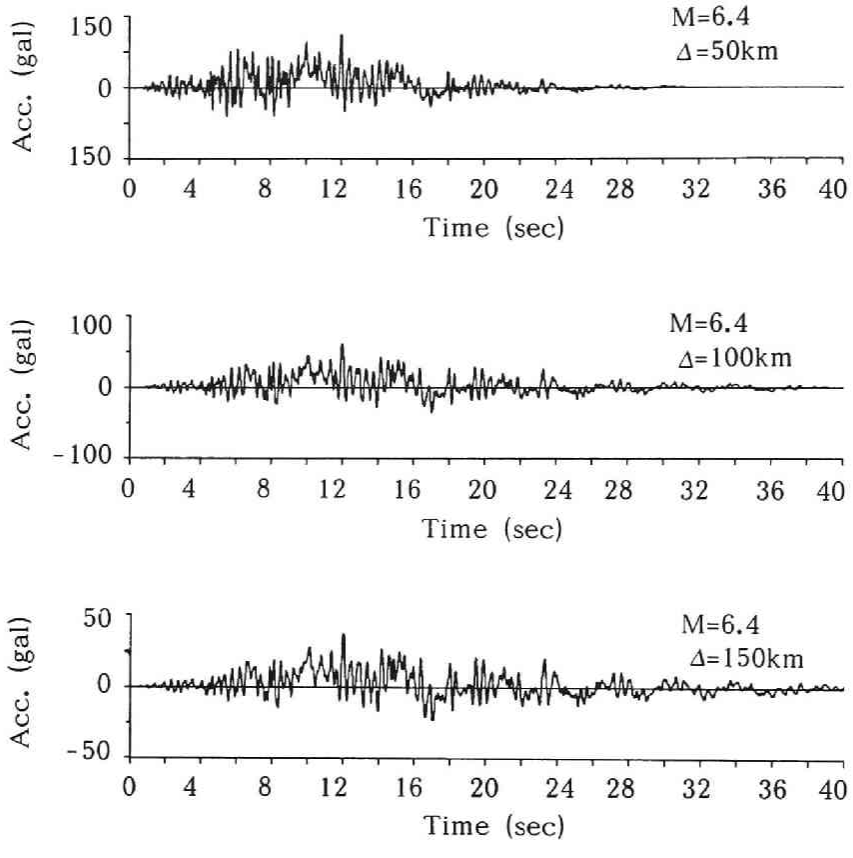

Fig. 5.22 Synthesized waves. (DB-1)

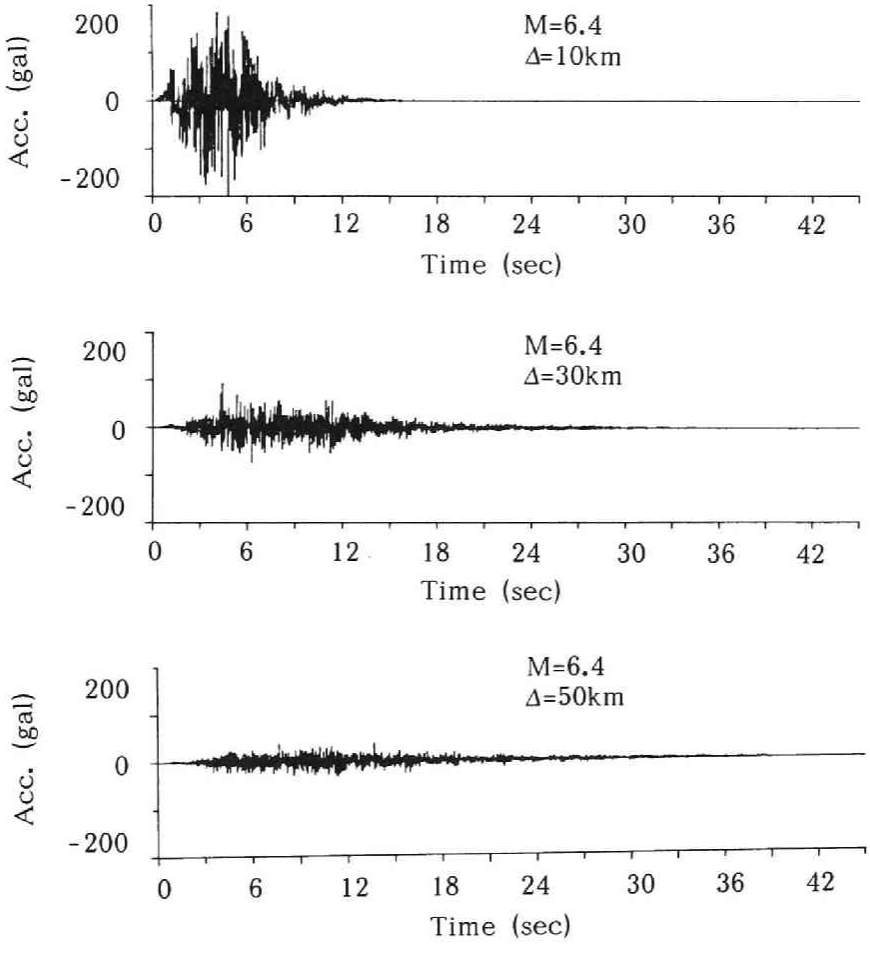

Fig. 5.23 Synthesized waves at Kamigamo. (DB-2)

acceleration with the existing attenuation law. Acceleration response spectra for epicentral distances of 10, 30, and 50 km at each site are shown in Fig.5.25 (a), (b) and (c). The damping ratio chosen was 5% of the critical value. The solid lines in these spectra represent values from synthesized accelerograms, and the lines with circles the spectra proposed by Katayama et al. [27]. From the results of their analysis, a magnitude range of 6.1 - 6.7 and epicentral distance ranges of 6 - 19 and 20 - 59 km were chosen for the two groups. The ground classification is base rock. The spectral values calculated from our synthesized accelerograms are markedly larger than those calculated from Katayama's model, with a particularly marked difference for 10 km. This difference may be attributable to the fact that the sensitivity for the period range around 0.1 sec strongly decreases in the SMAC accelerograph and that the analysis of Katayama et al. is based on records made by that accelerograph. The trend at all sites is such that the spectral amplitude is higher for the short period range. Response peaks, which appear in the vicinity of 0.06 - 0.07 and 2.0 - 4.0 sec, correspond to the source spectrum peaks that depend on the focal parameters (rise time, fault length, fault width, rupture velocity, etc.). The predicted maximum responses in the vicinity of 0.1 - 0.3 sec are 600 - 1500 gal at Δ =10 km, 400 - 700 gal at Δ=30 km, and 200 - 400 gal at Δ =50 km.

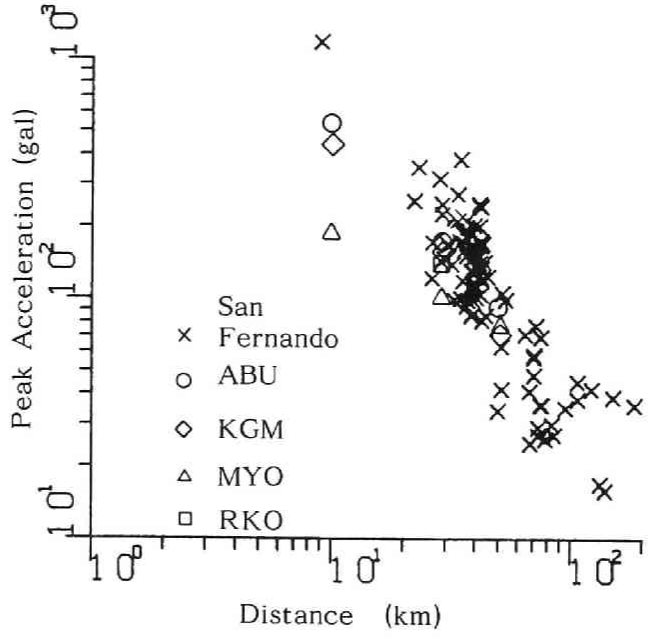

Fig. 5.24 Attenuation law for peak acceleration and epicentral distance.

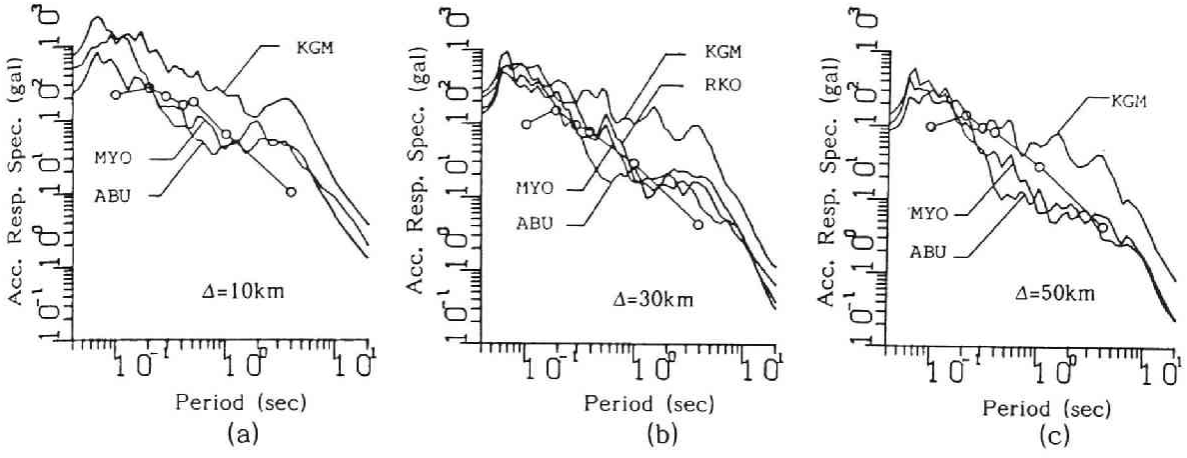

Fig. 5.25 Acceleration response spectra.

5.4 Conclusions

A convolution method that includes the Kalman filter was used to analyze the Nihonkai Chubu earthquake, the fault rupture mechanisms being identified. A prediction model for strong ground motion was presented and checked by use of peak accelerations and response spectra. The procedure used and results obtained are as follows:

(1) A UD filter is incorporated in the deconvolution method by use of the Kalman filter. This filter is stable and very useful in engineering studies. The components of the first row of the transition matrix, Φ, were investigated to accurately identify the impulses. Good results are obtained when an impulse has been obtained from equally weighted preceding impulses. The initial value of the estimated error covariance, p, has little effect on the results. Good results are obtained when a small ratio of observation noise covariance to system noise covariance is used.

(2) The proposed identification algorithm was used to determine the time delay in blasting records. The delay time was identified accurately, evidence that this procedure is robust enough to be used for identifications based on observed records.

(3) The identification results for the 1983 Nihonkai Chubu earthquake are as follows: Rupture originated in the southern part of the north-south prolonged fault and propagated to the north at 2.4 km/sec. The rise time of the mainshock was about 4 sec, and the average shear wave velocity was 3.6 km/sec. These results are in good agreement with the results

of other studies of the Nihonkai Chubu earthquake. This procedure is a powerful tool with which to identify the outline of fault mechanisms from the mainshock and aftershock records.

(4) A numerical database for microearthquakes of magnitude 1.2 to 1.8, that occurred in the Kinki district of Japan over an 18-month period was established and compared with a database for earthquakes that occurred from 1933 to 1971 in California, U.S.A.

(5) The microearthquakes showed the tendency of an earthquake swarm, and their hypocentral depths were distributed at a depth of 10 km. Most of their displacement spectra had corner frequencies of from 3 to 9 Hz. Spectrum amplitudes higher than these corner frequencies decayed at the rate of f^{-3} - f^{-2}.

(6) The AR-MA process was used to analyze two databases (DB-1 and DB-2), and the filter characteristics of the process were detected. A regression analysis was made of the AR-MA parameters to obtain attenuation laws for the filter characteristics. The simulated waveform based on the result of the regression analysis was used as the Green function which was predicted statistically. If strong earthquake motion is synthesized using the number, n, of Eq.(5.13), the fault dimension becomes large because assumption of a constant stress drop, regardless of the seismic scale, is not valid for microearthquakes. To correct this, a new scaling law was proposed in which the difference in the stress drop between a large earthquake and a microearthquake is attributed to the difference in dislocation.

(7) The properties of synthesized strong earthquake motion were examined by comparing the synthesized peak acceleration amplitudes with those found in the 1971 San Fernando earthquake records. Scattering of the amplitudes became small as distance from the fault increased. Amplitudes at sites near the source, however, showed distinct differences from site to site. A comparison with the acceleration response spectrum proposed by Katayama et al. showed that the responses obtained in this study had larger values, especially in the region near the fault.

References

[1] Shinozuka, M. and Y. Sato. Simulation of Earthquake Ground Motion and the Response of Structures, Proc. Japan Earthq. Eng. Symp., pp.167-172, 1966 (in Japanese with English abstract).

[2] Toki, K. Simulation of Earthquake Motion and its Application, Annuals Disas. Prev. Res. Inst., No.11A, pp.291-303, 1968 (in Japanese).

[3] Bayless, J. W. and E. O. Brigham. Application of the Kalman Filter to Continuous Signal Restoration, Geophysics, Vol.35, pp.2-23, 1970.

[4] Crump, N. A Kalman Filter Approach to the Deconvolution of Seismic Signals, Geophysics, Vol.39, pp.1-13, 1974.

[5] Muramatu, I. and K. Irikura. Estimation of Strong Ground Motion during a Large Earthquake Using Observed Seismograms of Small Events: Predicting Damage for a Large Earthquake in the Tokai District, Japanese Group for Study of Natural Disaster Science, No.A-56-3, pp.33-46, 1981 (in Japanese).

[6] Iida, M. and M. Hakuno. The Synthesis of the Acceleration Wave in a Great Earthquake by Small Earthquake Records, Proc. JSCE, No.329, pp.57-68, 1983 (in Japanese with English abstract).

[7] Toki,K., T. Sato and J. Kiyono. Identification of Input Ground Motion of a Multi Input System By Use of the Kalman Filter, Annuals Disas. Prev. Res. Inst., Kyoto Univ., No.33B-2, pp.1-16, 1986 (in Japanese with English abstract).

[8] Jazwinski, A. H.: Stochastic Processes and Filtering Theory, New York, Academic Press, 1970, pp.269-270.

[9] Kunimatsu, S., K. Nakagawa, F. Miura, T. Imamura and M. Sakamoto. Estimation of the Vibration Level Caused by Open Pit Blasting, Report of the Faculty of Engineering, Yamaguchi Univ., Vol.36, No.1, pp.89-96, 1985 (in Japanese).

[10] Geller, R. J. Scaling Relation for Earthquake Source Parameters and Magnitudes, Bull. Seism. Soc. Am., Vol.66, No.5, pp.1501-1523, 1976.

[11] Kanamori, H. and D. L. Anderson. Theoretical Basis of Some Empirical Relations in Seismology, Bull. Seism. Soc. Am., Vol.65, No.5, pp.1073-1095. 1975.

[12] Hirasawa, T. Synthetic Investigation of Seismic Damage in the 1983 Japan Sea Earthquake, Report of Special Research on Natural Disasters, pp.17-68, 1984 (in Japanese).

[13] Yamada, Y., S. Noda and M. Tomimoto. Characteristics of Relatively Long-period(5 to 15sec) Ground Motions Using JMA's Seismograph Records during the 1983 Nihonkai-chubu Earthquake, Annuals Disas. Prev. Res. Inst., Kyoto Univ., No.28B-2, pp.33-61, 1985 (in Japanese with English abstract).

[14] Saits, M. An Automatic Design Algorithm for Band-selected Recursive Digital Filters, Butsuri-Tansa, Vol.31, No.4, pp.112-135, 1978.

[15] Gersh, W. and R. S. Z. Livj. Time Series Method for the Synthesis of Random Vibration Systems, Jour. Appl. Mecha., pp.159-165, 1976.

[16] Toki, K. and T. Sato. Detections of Nonstationary Filtering Properties of Strong Motion Seismograms, Annuals Disas. Prev. Res. Inst., Kyoto Univ., No.22B-2, pp.25-36, 1979 (in Japanese with English abstract).

[17] Toki,K., T. Sato and J. Ejiri. Simulation of Strong Motion Seismograms by Autoregressive Moving Average Process, Annuals Disas. Prev. Res. Inst., Kyoto Univ., No.23B-2, pp.1-12, 1980 (in Japanese with English abstract).

[18] Toki, K., T. Sato and Y. Oiki. Detection of Dynamic Properties of Structural Systems by the Autoregressive Moving Average Method, Annuals Disas. Prev. Res. Inst., Kyoto Univ., No.21B-2, pp.57-68, 1978 (in Japanese with English abstract).

[19] Watanabe, A. Determination of Earthquake Magnitude at Regional Distance In and Near Japan, Zisin II-24, pp.189-200, 1971 (in Japanese with English abstract).

[20] Madariaga, R. Dynamics of an Expanding Circular Fault, Bull. Seism. Soc. Am., Vol.66, No.3, pp.639-666, 1976.

[21] Brune, J. N. Tectonic Stress and the Spectra of Seismic Shear Waves from Earthquakes, J. Geophys. Res. Vol.75, pp.4997-5009, 1970.

[22] Marion, G. E. and L. T. Long. Microearthquake Spectra in the Southeastern United States, Bull. Seism. Soc. Am., Vol.70, No.4, pp.1037-1054, 1980.

[23] Frankell, A. Source Parameters and Scaling Relationships of Small Earthquakes in the Northeastern Caribbean, Bull. Seism. Soc. Am., Vol.71, No.4, pp.1173-1190, 1981.

[24] McGarr, A., R. W. E. Green and Spottiswoode. Strong Ground Motion of Mine Tremors; Some Implications for Near-source Ground Motion Parameters, Bull. Seism. Soc. Am., Vol.71, No.1, pp.295-319, 1981.

[25] Toki, K., T. Sato and J. Kiyono. Synthesizing Design Ground Motions from Microearthquake Records, Proc. JSCE, Struc. Eng./Earthq. Eng., Vol.2, No.2, pp.423s-433s, 1985.

[26] Goto, H., H. Kameda, and M. Sugito. Correction of SMAC-B2 Accelerograph Records by Digital Filter, Proc. JSCE, No.277, pp.57-69, 1978 (in Japanese with English title).

[27] Katayama, T., T. Iwasaki and M. Saeki. Statistical Analysis of Earthquake Acceleration Response spectra, Proc. JSCE, No.275, pp.29-40, 1978 (in Japanese with English title).

CHAPTER 6

CONCLUDING REMARKS

The local conditions, travel path, and source factors that affect seismic motion have been identified, and input ground motions synthesized. The important conclusions of each chapter of this dissertation are summarized below.

The purpose of this research and general remarks on the estimation of seismic ground motion are given in chapter 1. A review of past studies of earthquake ground motions also is presented there.

In chapter 2, a procedure was established for identifying input motion from structural response records that takes into account kinematic interaction. The extended Kalman filter method was shown to be valid for identification problems of nonlinear dynamic structural characteristics. Input motion and structural parameters can be identified merely from the coda part of the response time history, information on input motion not being necessary. The efficiency of the Kalman error filter was investigated in a multi-degree-of-freedom system in order to estimate the input motion from the structural response and identify the structural parameters. In this procedure even when the identified structural parameters deviated by about 10%, the effect on the estimated input motion was negligible. The input accelerogram obtained from the error filter showed a decrease in amplitude for an increase in frequency beyond 10 Hz. But, even for this accelerogram, for which identification usually was more difficult than for velocity and displacement, the difference was only 4 - 5% .

The site effect was investigated in chapter 3, focus being on the characteristics of the propagating wave and layered media with an irregular interface. Estimation error for the phase velocity was reduced by use of the Kalman filter which made it possible to detect phase velocities in the time domain using observed records. The shape of the irregular interface was identified by the use of AR coefficients obtained by analyzing observed records at ground surface. The AR coefficient recognition method combined with cluster analysis provided a way to detect the existence of an irregular profile. The shape of the irregular

interface was derived by taking into account the spatial correlations and mean powers of the response time histories. The relative displacements could be calculated by modeling the spatial correlation and the autocorrelation function. The estimated relative displacements were in good agreement with the simulated values.

In chapter 4, a simplified analytical procedure was developed with which to estimate the attenuation of peak ground motion taking into account the fault extent. Peak acceleration was determined in terms of the source mechanisms, damping of the traveling path, and amplification at the site. When the effect of the fault extent was included, the attenuation curves had upper bounds near the source region, and the range was at most the fault length. The proposed method also could be used to estimate the peak accelerations in such earthquakes with multiple fault events as the Nihonkai Chubu earthquake. The estimated values obtained with this improved method were in good agreement with the recorded values. A risk map for the Kinki district was calculated from combination of historical earthquake records and active fault data by the use of Bayes' theorem under an assumption of the common stochastic population. The peak acceleration for a return period of 100 years is 225 gal for Osaka City. A seismic risk analysis was made according to this new attenuation law, and the risk spectrum at Osaka City was calculated. If the amplification characteristics between the base rock (v_S=3km) and upper layers are known, the risk spectrum at the level of the layer under consideration can be obtained.

Lastly, in chapter 5, seismic ground motion was synthesized after identifying the source mechanisms. A deconvolution method that includes the Kalman filter was used to analyze the fault rupture process imprinted in the earthquake motion records of site responses. The Kalman filter is stable, and robust enough for making identifications from observed records. The identification results for the 1983 Nihonkai Chubu earthquake were in good agreement with the results of other studies of that event. The proposed procedure offers an efficient means of identifying the outline of fault mechanisms from mainshock and aftershock records. A new scaling law also was proposed in which the difference in the stress drop between a large earthquake and a microearthquake is attributed to a difference in dislocation. Superposition of the statistical Green function made possible the synthesis of large earthquake motion.